2016

Laboratory Fatigue Evaluation of a Full Scale Steel Orthotropic Bridge Deck with Round Bottom Ribs and Fitted Floor Beams

Soham Mukherjee
Lehigh University

Laboratory Fatigue Evaluation of a Full Scale Steel Orthotropic Bridge Deck with Round Bottom Ribs and Fitted Floor Beams

by

Soham Mukherjee

A Thesis
Presented to the Graduate and Research Committee
of Lehigh University
in Candidacy for the Degree of
Master of Science

in

Structural Engineering

Lehigh University

January 2016

This thesis is accepted and approved in partial fulfillment of the requirements for the Master of Science.

_____

Date

_____

Dr. Sougata Roy
Thesis Advisor
Former Principal Research Scientist
ATLSS Engineering Research Center,
Lehigh University

_____

Dr. Richard Sause
Thesis Advisor
Department of Civil and Environmental
Engineering, Lehigh University

_____

Dr. Panayiotis (Panos) Diplas
Chairperson
Department of Civil and Environmental
Engineering, Lehigh University

ACKNOWLEDGEMENT

The author would like to express his sincere gratitude to his thesis advisors Dr. Sougata Roy and Dr. Richard Sause, for their valuable guidance and insight into this research. The author particularly appreciates the effort put forward by Dr. Roy in helping the author to complete his thesis. This thesis is based on a research project that was conducted at the ATLSS Engineering Research Center of Lehigh University. The author gratefully acknowledge the funding provided by the sponsor of the research project. The author also gratefully acknowledge the contributions of High Steel Structures, the fabricator of the specimen. Special thanks are due to Mr. Ronnie Medlock, VP technical Services of High Steel Structures for valuable input on fabrication of this deck and to Dr. John W. Fisher for sharing his vast experience with orthotropic decks. The author is also thankful to research assistants Mr. Xudong Zhao, Mr. Philipp Keller, Mr. Frank Artmont, Mr. Yeun Chul Park, Ms. Katelyn Kitner, and Mr. Juan Tzoc, and the laboratory support staff of ATLSS Engineering Research Center for their help with successful execution of the project.

Finally, the author would like to thank his parents, girlfriend and friends for all the support they provided throughout his graduate studies.

CONTENTS

LIST OF TABLES

LIST OF FIGURES

ABSTRACT

A steel orthotropic deck integrated with steel box girders is proposed for a replacement vertical lift bridge. In contrast to the orthotropic bridge decks implemented in the United States over the past two decades with ribs passing through matching cutouts in floor beams with extended cutout under the rib soffit, the subject deck incorporates a $^{3}/_{4}$ in. (19 mm) deck plate stiffened by $^{5}/_{16}$ in. (8 mm) thick rounded bottom ribs (U-shaped) passing continuously through matching cutouts in the floor beams without any extended cut-out under the rib soffit. Perceived to be cost-effective, the fitted rib-to-floor beam connection is proposed to be fillet welded, however, performance of this connection requires careful fit-up, which can incur additional fabrication costs. In addition, the lift bridge serves as a key element of a portway corridor carrying the main trucking route and hence the expected high volume of Average Daily Truck Traffic (ADTT) on the lift bridge was a concern. Accordingly, the connection details of the subject deck was evaluated for infinite fatigue life by testing a full-scale prototype of the part-bridge deck at the ATLSS Engineering Research Center of Lehigh University. This thesis pertains to the fatigue performance of the proposed rib-to-floor beam connection design.

Multi-level 3D linear elastic finite element analyses (FEA) of the proposed bridge deck were performed that identified the rib-to-floor beam connection adjacent to a box girder as the most critically stressed region of the deck, when the rear tandem axle of the AASHTO fatigue design truck was symmetric with the floor beam and the rib was located in the shear span of the floor beam. Based on the analyses, a full-scale prototype of the part bridge deck comprising 5 ribs and 3 floor beams, and a test setup that would adequately replicate the boundary conditions were decided for assessing the in-service fatigue

performance of the proposed deck by testing in the laboratory under simulated conditions. The prototype deck was fabricated in two panels, which were spliced (transverse to the ribs) in the laboratory by a complete joint penetration (CJP) weld at the deck plate and bolted splices at the ribs and the girder, simulating the field splice in the actual bridge construction. During assembly of the deck panels in the laboratory, significant lack of fit was noted between the panels due to the distortion from welding heat effects on asymmetric cross section of the specimen. The CJP deck plate splice was performed using a brass backing bar to facilitate removal of after the welding. Use of a brass backing bar, however, resulted in significant lack of fusion (LOF) at the weld root, which could not be effectively repaired due to the access restrictions.

The fatigue testing was performed using a pair of above-deck hydraulic actuators, which were attached to spreader beams and loading pads, simulating the rear tandem axles of the AASHTO fatigue truck for orthotropic deck design and the tire contact with the deck plate. The deck was loaded as per the Fatigue I limit state load of the AASHTO LRFD Bridge Design specifications (BDS) 6th edition to verify infinite life performance, which resulted in a total load range of 82.8 kip (368.4 kN) or 41.4 kip (184.2 kN) per axle (or actuator). In addition, an under-deck actuator provided at the inner floor beam was cycled for a displacement range of 0.1 in. (2.5 mm), synchronous with the above-deck actuators to simulate the global displacement boundary condition. The deck was extensively instrumented with strain gauges and displacement transducers to evaluate the response of the deck and the various connection details, with majority of the instrumentation concentrated at the critical connection between the floor beam at the midspan and the rib adjacent to the girder. The deck response was also determined under a rolling tandem axle

bogie load moved across the deck at a slow rate.

The fatigue testing was run-out at 8 million cycles without any detectable fatigue cracking in the deck. The measured stress ranges at all critical connections were less than the CAFT of their respective detail categories. The test results would indicate infinite life performance of the rib-to-floor beam connection detail of the proposed deck design, as long as the site specific overloads do not exceed the AASHTO Fatigue I limit state load more than 1 in 10000 occurrences. The test results also demonstrated that the large deviation from the specified fabrication tolerances and the rejected welding procedures, which were noted during the specimen fabrication and installation, did not affect the fatigue resistance of the connection details. This suggests that the specified fabrication tolerances are arbitrary. In addition, the study provided critical information on issues related to fabrication and installation of the proposed orthotropic deck design for the lift bridge.

1 INTRODUCTION

1.1 Background

A steel orthotropic deck integrated with steel box girders is proposed for a replacement vertical lift bridge (Figure 1). The orthotropic deck was an ideal choice for the movable bridge because of its light weight and inherent redundancy that reduced demand on the prime movers and reduced dead load stresses, and thereby allowed increased span length. In addition, if adequately designed and properly fabricated, an orthotropic deck is a bridge deck system likely to provide a service life exceeding 100 years with minimum maintenance (Fisher and Roy 2010). In contrast to the orthotropic bridge decks implemented in the United States over the past two decades with ribs passing through matching cutouts in the floor beams with extended cutout under the rib soffit, the subject deck incorporates a $^{3}/_{4}$ in. (19 mm) deck plate stiffened by $^{5}/_{16}$ in. (8 mm) thick rounded bottom ribs (U-shaped) passing continuously through matching cutouts in the floor beams without any extended cut-out under the rib soffit. Perceived to be cost-effective, the fitted rib-to-floor beam connection is proposed to be fillet welded, however, performance of this connection requires careful fit-up, which can incur additional fabrication costs.

In addition, the lift bridge serves as a key element of a portway corridor carrying the main trucking route and hence is expected to experience significant truck traffic. In terms of time dependent deterioration such as corrosion and fatigue, the deck is the most vulnerable element of a bridge, and in-service fatigue cracking of steel bridges is caused primarily by the truck traffic in the vehicular spectrum. Moreover, for deck elements the number of load cycles from truck traffic is multiplied by the number of axles. As such, the

expected high volume of ADTT on the lift bridge was a concern. To ensure long term durability of the bridge, the design and fabrication of the proposed deck detail needed to be verified for infinite fatigue life, i.e., no in-service fatigue cracking during the design life of the bridge.

The rib-to-floor beam and the rib-to-deck plate connections are the most critical among all the welded connections in an orthotropic deck. This thesis pertains to the fatigue performance of the proposed rib-to-floor beam connection design.

1.2 Proposed Replacement Orthotropic Deck

The framing plan (without the cross frames) and a typical cross section of the proposed replacement bridge deck are shown in Figures 2 and 3 respectively. The lift span is 324 ft. (99 m) long and 110 ft. (34 m) wide. The deck comprises three box girders identified as BG-1, BG-2 and BG-3, with an integrated orthotropic deck. The box girders are 12 ft. (3.7 m) wide and 14 ft. 9 in. (3.7 m) deep, having 2 $^{1}/_{4}$ in. (57 mm) thick bottom flange and $^{9}/_{16}$ in. (14 mm) thick web. The orthotropic deck consists of a ¾ in. (19 mm) thick deck plate stiffened by 46 ribs equally spaced at 2 ft. 4 in. (711 mm) centers in the longitudinal direction and 27 floor beams equally spaced at 11 ft. 9 in. (3.6 m) centers in the transverse direction. The floor beams vary in depth from 1ft. 6 in. (457 mm) at the edge to 4 ft. (1.2 m) in the middle with about an average nominal depth of 3 ft. 4 in. (1 m). The floor beam web is ½ in. (13 mm) thick.

The design details of the orthotropic deck are shown in Figure 4. The design uses trapezoidal round bottom (U-shaped) ribs. The ribs are 14 in. (356 mm) high having $^{5}/_{16}$ in. (8 mm) thick rib wall. The rib-to-deck weld is specified as 80% partial joint penetration (PJP) groove weld. The floor beam is fitted all around the ribs without any extended cutout

under the rib soffit, with the ribs passing continuous through the floor beam. All around $^{5}/_{16}$ in. (8 mm) fillet welds from both sides are specified between the floor beam web and the ribs, and the floor beam web and the deck plate.

The deck splice is proposed as a CJP groove weld at the deck plate and bolted splice at the ribs, the edge girders and the floor beams. The closed ribs are provided with access holes at the soffit at the splice location and are hermitically sealed by providing full-depth $^{3}/_{8}$ in. (9.5 mm) sealing plates on both sides of the access holes.

1.3 Review of Previous Studies

A preliminary search on steel orthotropic deck revealed more than 100 publications in English. These publications span a wide range of areas including: application (mostly in signature bridges) and case studies; general performance evaluation; analysis of stresses and design; experimental and analytical evaluation of fatigue resistance including effects of fabrication; fatigue assessment based on field monitoring and FEA; evaluation of in-service fatigue cracking and retrofit; strengthening mechanisms; performance of wearing surfaces; effect of wearing surfaces on stresses in the deck plate; evaluation for stability and ultimate loads; Life Cycle Cost (LCC) analysis, and new concepts of orthotropic deck forms. Out of these, publications related to: experimental and analytical evaluation of fatigue resistance; and in-service fatigue cracking and fatigue assessment were of primary interest.

Significant research was performed on fatigue resistance of welded details in orthotropic decks in the United States, in Europe (notably in the United Kingdom, the Netherlands and Germany), and in Japan. In Europe and Japan, the research efforts were limited to experimental and analytical evaluation of fatigue performance of orthotropic

decks that exhibited distress in service and developing effective retrofit details. These decks mostly employed thin deck plates of ½ in. (12 mm) or less that often exhibited fatigue cracking from the weld toe or the weld root due to significant localized distortion under wheel loads.

Kolstein (2007) discussed fatigue performance of rib-to-floor beam connections, where continuous ribs pass through matching cuts in the floor beam with or without additional cope hole around the soffit of the rib (cutouts), and discontinuous ribs fitted between crossbeams. Of particular interest to this study was the results of fatigue tests conducted by Kolstein et al. (1995) on trapezoidal rib-to-floor beam connections, where the ribs were continuous through matching cuts in the floor beam without any cutout, and fillet welded all around. A similar detail is proposed for the orthotropic deck for the current study. Although the salient dimensions of the test specimen may be significantly different than the proposed orthotropic deck, to the knowledge of the author it is the only full size test available to date for such detail. In the first test program, two single rib specimens containing a full-size rib-to-floor beam connection were tested under out-of-plane bending. While these tests are unlikely to reflect the true response of the rib-to-floor beam connection in a full deck, where the connection is subjected to complex combination of in-plane and out-of-plane stresses, the detail surpassed the fatigue performance of rib-to-floor beam connections where cutouts of two different geometries were provided. Fatigue cracks initiated at the fillet weld toe on the rib, near the corner rounding of the rib soffit, and propagated along the weld toe at the bottom of the rib and also through the weld into the floor beam. In the second test program, a full-size deck including eight ribs and a floor beam was tested under combined in-plane and out-of-plane loading to simulate passage of

axles over the floor beam. At four of the ribs the floor beam web was provided with a cutout and the other four ribs were welded all around. The rib-to-floor beam connections without cutouts exhibited significantly longer fatigue life. The crack growth in these connections was similar to the single rib specimens. The crack growth rate increased significantly when the cracks grew into the floor beam web. Kolstein also presented the results of FEA of the full-size specimen that was conducted by Leendertz (1995). The model consisted of eight node shell elements, which were capable of reproducing membrane as well as bending effects. Local effects due to the welds and plate thicknesses were not modelled. The analysis replicated the test loading and the boundary conditions. A comparison of numerical results with the experimental results showed that they coincided very well for the stresses in the web. The stresses in the ribs, however, were in less agreement in the vicinity of the floor beam web, probably due to the weld and the plate thickness effects that played an important role for these locations.

In the United States, fatigue resistance of orthotropic decks have been mostly evaluated by testing of full-size prototypes of replacement orthotropic decks for signature bridges in the laboratory, with realistic simulation of boundary conditions, moving loads and fabrication effects. These tests were conducted at the ATLSS Engineering Research Center, Lehigh University for the Williamsburg Bridge in New York City (Tsakopoulos and Fisher 2003, Kaczinsky et al. 1997), for the Bronx Whitestone Bridge in New York City (Tsakopoulos and Fisher, 2005), and the Verrazano Narrows Bridge in New York City (Roy et al. 2010, Roy et al. 2011a, Roy et al. 2011b, Roy et al. 2012a). For all these tests, the ribs were continuous at the rib-to-floor beam connections, and a cutout was provided in the floor beam under the rib soffit.

From the test conducted on the prototype of replacement orthotropic deck for the Williamsburg Bridge, it was concluded that a combination of full penetration weld and fillet weld at the rib-to-subfloor beam was more fatigue resistant than just a fillet welded connection that stopped short of the cutout. The combination consisted of 4 in. (102 mm) full penetration weld adjacent to the termination of the cutout and the rest fabricated with fillet welds. The fatigue resistance of this weld option was defined by AASHTO LRFD as Category C fatigue design curve.

The next study was carried out on the prototype of replacement deck for the Bronx-Whitestone Bridge. In this, the replacement orthotropic deck design incorporated the improvements identified from the Williamsburg Bridge deck testing and the bulkhead plate was replaced with two internal stiffeners at the rib-to-floor beam connection. The load level was equivalent to 3×HS15 and 4.6×HS15 (where HS15 is the AASHTO fatigue truck) including 15% impact for each of the two phases of testing. Even with the application of the maximum stress range in the random variable spectrum determined from field measurements by Connor and Fisher (2001) and Connor et al. (2003), the only fatigue cracking was observed at the deck plate at the floor beam locations. This test demonstrated the effectiveness of the design improvements adopted in the prototype replacement decks of these two bridges.

The next study was carried out on the prototype of replacement deck for the Verrazano Narrows Bridge. In contrast to conventional orthotropic deck designs, the sub-floor beams were made integral with the existing stringers, making them load bearing in the transverse direction. Based on the results of the first phase testing, improvements were made to the deck design and a second phase testing was conducted. The second phase

testing verified that the refurbished deck would provide a 75 years' service life under site specific loading. With the design improvements the stresses at the fatigue critical details reduced significantly. The measured stress ranges at all details except at the cutout edge were at or below the CAFT of their respective detail categories.

In this current study, the ribs are passed continuously through matching cut outs in the floor beam, and without any extended cutout under the rib soffit. To be cost-effective, the floor beam is fitted around ribs and is fillet welded.

1.4 Study Rationale

To ensure proposed orthotropic deck has required fatigue resistance for 100 years of service life, the deck design needed to be verified for infinite fatigue life.

The rib-to-floor beam connection details are among the most critical welded connections in an orthotropic deck, as they are subjected to complex in-plane and out-of-plane stresses under moving wheel load (Gajer et al. 1996). To reduce the cost of fabrication, the proposed orthotropic deck design has rib-to-floor beam connections without cutouts and fillet welded all around. Although limited studies (Kolstein 2007) showed promise, infinite life fatigue performance of this rib-to-floor beam connection (without cutout) for the proposed geometric parameters of the deck was not known.

In addition to these, the response of orthotropic decks under wheel loads is quite complex that creates in-plane and out-of-plane stresses at the welded details as functions of the relative geometry of the connecting elements. Thus, the fatigue design of critical orthotropic deck details cannot be performed based on simple strength of material calculations. The complex behavior of proposed orthotropic deck needed to be simulated both in analysis and experiments for accurate fatigue assessment of the welded

connections. Fatigue resistance of different welded details in orthotropic decks of varied configurations has not been established by laboratory testing, where the boundary effects have been adequately accounted for. Only a handful of such tests in the United States provided data on the rib-to-floor beam connections with cutout of particular geometric configuration, which were not readily applicable to the orthotropic deck details for the lift bridge. Similarly, the tests conducted in Europe and Japan were not applicable to the current project as they were mostly conducted on small specimens, where accurate boundary conditions were not replicated and deck sections employed antiquated practices and details. In addition, the newly introduced AASHTO provisions do not provide a reliable and consistent fatigue design methodology for infinite life of welded connections in orthotropic decks. Thus, full-scale testing that adequately captures the behavior of orthotropic decks was the only rational means of evaluating in-service fatigue performance of orthotropic decks.

Based on the understanding of research problem and the background information, it was apparent that verifying the infinite life fatigue performance of the rib-to-floor beam connection detail by testing a full-size part deck specimen (full-scale prototype) was the most rational approach for fulfilling the goals of this study.

1.5 Objectives and Scope of the Current Study

The objectives of this study were:

(i) to verify the infinite life fatigue performance of the proposed orthotropic deck based on experimental and analytical studies according to the latest provisions of the AASHTO LRFD BDS;

(ii) to determine the response of the proposed orthotropic deck under static and

moving wheel loads; and

(iii) to mockup fabrication and installation of the actual bridge deck, for generating critical information related to economic fabrication and installation of the proposed orthotropic deck using domestic resources.

1.6 Study Approach

The objectives of the study were achieved by adopting the following approach. Multi-level 3D linear elastic FEA were performed on the proposed orthotropic deck design for the lift bridge: (a) to determine the most critically stressed rib-to-floor beam connection in the deck; (b) to determine the disposition of loads that will produce the most critical stresses; and (c) to decide a suitable full-scale prototype and a test setup that will sufficiently replicate the behavior of an entire deck in service. A full-scale prototype consisting of three floor beams and five ribs and part of a box girder web was designed based on FEA, and was tested in the laboratory under simulated AASHTO rear tandem axle loading. The static and fatigue tests were conducted using two stationary above-deck hydraulic actuators. In addition, the global vertical displacement boundary condition was simulated using an under-deck hydraulic actuator. The deck response was also determined under moving load using a tandem axle bogie rolling across the deck at a slow rate. The deck was instrumented using about 250 sensors at critical locations. After fatigue testing, the rib-to-floor beam weld and the CJP deck splice was destructively evaluated. The full-scale prototype was used to mock-up the deck fabrication and installation of the lift bridge.

1.7 Outline

This thesis contains 7 chapters. The first chapter introduces the background and the

problem statement for the study. A relevant literature review, the rationale for the study, the study objectives and the study approach are also provided in the first chapter, in addition to the outline of the report.

The second chapter discusses the FEA of the full bridge deck identified as global model (GM) and FEA of the part of deck identified as submodel (SM). Determination of the most fatigue critical rib-to-floor beam connection and corresponding wheel load disposition based on FEA, and the corresponding fatigue critical stresses at the welded connection are discussed in this chapter.

The third chapter discusses the design of the prototype deck and the test setup for fatigue testing, including the development of the prototype deck from the FEA of the bridge deck. The chapter also presents the FEA of the prototype deck.

The fourth chapter discusses the fabrication of the prototype deck and the details of the test fixtures. The chapter also discusses installation of the deck specimen in the laboratory, and details of instrumentation, loading and the tests conducted.

The fifth chapter discusses the finding of the destructive evaluation of the rib-to-floor beam weld and the CJP deck plate splice.

The sixth chapter discusses the static test results of the prototype deck. It also provides the fatigue test results of the prototype deck including assessment of fatigue resistance. In addition, the response of the prototype deck under moving wheel load is also discussed.

The final chapter presents the conclusions, recommendations and requirements for further research.

2 ANALYTICAL STUDIES OF THE PROPOSED BRIDGE DECK

2.1 Analysis Plan

Multi-levels of 3D linear elastic FEA of the proposed orthotropic deck was conducted using ABAQUS (Dassault Systemes 2012), a commercially available FEA software. The purpose of the FEA was: (a) to determine the most critically stressed rib-to-floor beam connection in the deck; (b) to determine the disposition of loads that will produce the most critical stresses; and (c) to decide a suitable full-size specimen for fatigue testing that will sufficiently replicate the behavior of an entire deck in service. In the first level, a 3D FEA of the entire proposed lift span of the lift bridge superstructure was performed under vehicular live loads as specified in the AASHTO LRFD BDS (AASHTO 2012). This model is identified as Global Model (GM). The FEA of GM was performed using shell elements. Welds were not modelled in the GM. To obtain the fatigue critical stresses at the welded connections, a 3D submodel (SM) of the critically stressed region of the deck, as identified by the GM, was analyzed to obtain an improved resolution of the local stresses. This model consisted of solid elements and included all the weld details. The results of the GM and the SM analyses were used to design the full-scale prototype. The FEA of the GM and the SM are discussed in this chapter. 3D solid FEA of the full-scale prototype, which replicated the test specimen, is discussed in the next chapter.

2.2 Details of Global Model

The details of GM is shown in Figure 5. All components of the deck were included in this model. The global model consisted of a deck plate, 27 floor beams, 46 ribs, 3 box girders (BG-1, BG-2 and BG-3) and 2 end floor beams. The deck components were

modelled as per the design drawings for the deck. The components were modelled as separate parts and assembled together. The welds were not modelled; all welded connections were considered as integral. The effect of weld notch was studied in subsequent levels of FE models where the welds were incorporated. The ribs are numbered as Rib 1 to Rib 46 starting from the south deck edge towards BG-1. The rib adjacent to BG-1 towards BG-2 is identified as Rib 10 in Figure 5. The floor beams are numbered as FB 1 to FB 27, and the floor beam at the midspan is identified as FB 14 in Figure 5.

The GM was modeled using shell elements. Shell elements were preferred, keeping in mind the computational demand that would have resulted by use of solid elements. All components were modelled by defining the geometry at the middle surface. Figure 6 shows the cross section of a typical rib and a floor beam with the modelled mid surface identified. Figure 7 shows the cross section of a typical box girder and an end floor beam with the mid surface identified as modelled. As discussed earlier, the floor beams are of variable depth with 4 ft. (1.2 m) at the center and uniformly reducing towards the end to 1 ft. 6 in. (457 mm) at a slope of 2%. The average depth of the floor beams is about 3 ft. 4 in. However, an average nominal depth of 3 ft. (914 mm) was used for modelling the floor beam (inclusive of the deck plate), which was conservative as it reduced the shear area for in-plane stresses and also reduced out-of-plane rotational flexibility of the floor beam.

2.3 Details of Submodel

The FEA of GM identified the rib-to-floor beam connection (Rib 10-to-FB 14 connection) adjacent to one of the box girders (BG-1) as the most critically stressed connection in the deck. The tandem axles symmetric with respect to the floor beam in the longitudinal direction, and with the wheels nearest to the box girder placed centrally

between the adjacent pair of ribs produced the most critical stress state at the rib-to-floor beam connection. The response of the deck under the tandem axles in the most critical load disposition was localized and was significant only over three floor beams (FB 14 directly under the tandem axles, and the two adjacent FB 13 and FB 15) in the longitudinal direction as shown in Figure 8 (see discussions later). Based on this observation, it was decided to include three floor beams in the SM as shown in Figure 8. Figure 9 shows the undeformed and the deformed configuration of the GM under the critical loading. The deformation of the deck in the transverse direction was limited to a few ribs (Figure 9) locally where the load was applied. Accordingly, a submodel consisting of the ribs 10 to 20 between box girders BG-1 and BG-2 and ribs 9 and 21 on the other side of BG-1 and BG-2 respectively, and 3 floor beams were developed. This model is identified as SM. The extent of SM is shown in Figure 10 overlaid on the plan view of the GM. The SM was 35 ft. 3 in. (11 m) in length and 30 ft. 4 in. (9.2 m) in width. In the transverse direction the SM was symmetric about Rib 15. The boundaries of the SM in the longitudinal direction was 5 ft. 10 ½ in. (1.8 m) from the centerline of FB 13 and FB 15, which were respectively half the spacing between two consecutive floor beams. All the weld details were modeled in the SM as $^{5}/_{16}$ in. (8 mm) fillet welds with idealized zero notch radius at the weld toes and complete penetration at the weld root. The local stresses at the welded connections as obtained from SM were used for determining the size of the prototype. The SM was analyzed for the same critical disposition of the tandem axles as the GM analysis. The bolted connections in the deck at the splice locations were modelled as tie constraints, which rigidly connected the mating surfaces of the connected components by enforcing same displacement at the interface nodes.

2.4 Material Properties

Widely accepted linear elastic material properties of steel were used for analysis. The modulus of elasticity and Poisson's ratio of steel were assumed as 29000 ksi (2.0×10^5 MPa) and 0.3 respectively.

2.5 Details of Element Type and Meshing

The GM was meshed with doubly curved, thick shell elements having eight nodes and incorporating quadratic, reduced integration isoparametric formulation. In ABAQUS, this element is designated as S8R. Shell elements were chosen over solid elements in order to reduce the computational time considering the size of the model. Thick shell elements was chosen in order to capture the shear deformation in the structure, as transverse shear deformation was expected to occur near cutouts in the floor beam which is a geometric discontinuity. Each node of the element has 6 degrees of freedom with 3 translational and 3 rotational degrees of freedom. The mesh was generated automatically by ABAQUS with an average element size of approximately 7 in. (178 mm) resulting in 891,164 elements, 2,609,646 nodes, and 15,657,876 solution variables or nodal degrees of freedom. All the components were meshed separately using structured meshing technique. The meshed components were merged to form the meshed deck model. The average aspect ratio of the element was about 3 with the largest aspect ratio of about 7. The average maximum and minimum of the corner angles were about 91° and 89° respectively. The quality of the meshing was important, as poor distorted mesh would have resulted in singular matrix while inverting Jacobian of transformation from original space to isoparametric space. The mesh quality was also checked with recommendations of ABAQUS (Dassault Systemes 2012).

The SM was meshed with 3D continuum solid hexahedral elements, incorporating twenty node, quadratic, reduced integration and second order isoparametric formulation. In ABAQUS, this element is identified as C3D20R. The C3D20R element was used as it is known to provide accurate results for three dimensional stress analyses and is effective in capturing stress concentration effects (Dassault Systemes 2012). Each node of the element has 3 translational degrees of freedom.The mesh was generated automatically by ABAQUS with an average element size of approximately 1 in (25 mm) resulting in 160, 3140 elements, 823,1042 nodes and 2,469,3126 solution variables or nodal degrees of freedom (three displacement degrees of freedom per node). The average aspect ratio was about 6. The average maximum and minimum corner angles were about 85° and 95° respectively. As discussed earlier, the quality of the mesh was important to avoid singularity while inverting the Jacobian of isoparametric transformation.

Automatically generated non-uniform mesh for the models limited the freedom of propagation of spurious modes that are associated with these reduced integration elements.

2.6 Boundary Conditions

2.6.1 Global Model

The boundary conditions of the GM replicated the boundary conditions of the full bridge deck in service. As per the design drawings the lift span was supported at the east and the west towers by end floor beams resting on expansion and fixed bearings respectively. In the GM these bearings were simulated by consistent displacement boundary conditions imposed at the soffit of the end floor beams, coincident with the proposed bearing locations in the physical bridge (Figure 11). Displacement boundary

conditions restraining displacements in all three global coordinates were imposed at the underside of the west end floor beam to simulate fixed condition. Displacement boundary conditions releasing displacement in the longitudinal direction of the deck and restraining displacements in the other two directions, were imposed at the underside of the east end floor beam to simulate roller support or expansion bearing. All the displacement boundary conditions were applied at a node of the end floor beam flange aligned with the centerline of each box girder.

2.6.2 Submodel

The submodel analysis employed shell-to-solid sub-modelling, where the SM was driven by the displacement solution of the GM at the common interface.

2.7 Loading

2.7.1 Global Model

The GM was analyzed for 5 longitudinal positions of the AASHTO fatigue design truck for Fatigue I Limit State as recommended by the latest AASHTO LRFD BDS. These longitudinal load positions are shown in Figure 12, and identified as L1, L2, L3, L4 and L5. Corresponding to each longitudinal position, the transverse load positions were decided starting from the south edge (towards BG-1) of the bridge and gradually moving towards the north edge (towards BG-3). The transverse load positions are shown in Figures 13 to 22. The criticality of the load position was decided in terms of the fatigue critical stresses normal to the rib-to-floor beam welded connection both on the floor beam web and the rib wall. Only the critical load positions are presented. The load cases are identified by the longitudinal load position followed by the transverse load position (e.g. L1T29, L1T30,

etc.).

The loads were positioned about FB14, the floor beam at the mid span of the bridge deck, such as to produce the maximum global displacements of the deck, and any associated effect on the local deformations in the deck. The longitudinal load positions were chosen such as to simulate the passing of an AASHTO tandem axle over the span of the deck between FB 14 and FB 13. The first longitudinal load position was chosen such that the tandem axle was symmetric with respect to FB 14 to produce symmetric response of the FB 14. The subsequent load positions were chosen to represent the gradual passage of the axle over the span between FB 14 and FB 13 and to investigate the asymmetric response of FB 14 under the combined effects of in-plane and out of plane deformation of the floor beam due to the rib rotation.

The load from each wheel pair of the tandem axle was distributed over a rectangular area of 10 in. (254 mm) long and 20 in. (508 mm) wide, as specified by AASHTO LRFD BDS for simulating tire contact. The spacing between the tire contacts in the longitudinal direction and the transverse direction were 4 ft. (1.2 m) and 6 ft. (1.8 m) respectively. The spacing between the tire contacts were in accordance with the AASHTO LRFD BDS. The total load applied on the deck was 82.8 kip (368 kN), which is three times the AAHTO fatigue design load (0.75×HS20 + 15% impact) as specified by AASHTO for Fatigue I limit state design of orthotropic decks. This resulted in a total load of 41.4 kip (184 kN) per axle or 20.7 (92 kN) kip per wheel pair or load patch. For each load patch or tire contact, the wheel load was distributed as nodal loads to the elements in that contact area.

The load from the orthotropic deck is transferred to the box girder through the floor beam as shear. Consequently in the shear span, a diagonal tension field is formed from the

bottom flange (tension flange) of the floor beam to the top corner formed by the floor beam, the box girder and the deck plate. This tension field deviates around the rib cutout in the floor beam, and causes high stress concentration at the rib-to-floor beam connection near the rib rounding, where the principal tensile stress field is tangential to the cutout. Accordingly, the transverse load positions were chosen to simulate different shear spans, generating different stress concentration at the rib-to-floor beam connection. In addition, the transverse load positions also covered several cases of response of the deck components in the transverse direction. The truck was positioned such that either one wheel or both wheels of the left wheel pair was located symmetrically between the ribs, on a rib wall, or over a rib. These placements of the left wheel pair also resulted in different positions of the right wheel pair, where the deck plate over the ribs or between the ribs was loaded in different arrangements. As a result, the deck plate and the ribs, whose responses are driven by local effects of individual wheels, were subjected to several different load conditions, where the wheels (tire contacts) were positioned partially or fully between the rib walls, or on the rib walls. These load positions generated several stress states in the deck plate, the rib walls and rib-to-deck plate connections.

2.7.2 Submodel

The SM was analyzed for load case L1T29, which was determined from GM analysis to produce the most critical stress state at the rib-to-floor beam connection adjacent to the box girder (see discussions later). This load position in elevation and plan are shown in Figures 9 and 10 respectively. The load from each wheel pair of the tandem axle was uniformly distributed over a rectangular area of 10 in. (254 mm) long and 20 in. (508 mm) wide, as specified by AASHTO LRFD BDS for simulating tire contact. These load patches

are identified as LP in Figure 10. Each pair of load patches in the transverse direction represented one axle of the tandem. As seen from Figure 10, the tandem axles were symmetrically placed 2 ft. on either side of FB 14. The spacing between the load patches in the longitudinal and the transverse directions were consistent with the latest provisions of the AASHTO LRFD BDS. The total load applied on the deck was 82.8 kip (368 kN) , which is three times the AAHTO fatigue design load (0.75×HS20 + 15% impact) as specified by AASHTO for Fatigue I limit state design of orthotropic decks. This resulted in a total load of 41.4 kip (184 kN) per axle or 20.7 kip (92 kN) per wheel pair or load patch, producing a uniformly distributed pressure load of 0.104 ksi (0.72 MPa) per load patch.

2.8 Analysis

The GM and the SM were analyzed on distributed memory computer cluster of 8 nodes, each having 16 central processing units (cpu). All analyses were linear elastic. All analyses used the direct linear equation solver and converged in a single increment. The direct linear equation solver used a sparse, direct, Gauss elimination method that found exact solution of this system of linear equations (Dassault Systemes 2012).

2.9 Analysis Results

2.9.1 Comparison of Deck Response in GM under Different Load Cases

Figure 23 shows the principal stress contour in FB 14 web for the two most critical load cases as observed from the FEA of GM. The FEA of the GM showed high stress concentration in the floor beam and the rib wall at the Rib 10-to-FB 14 welded connection, in the shear span adjacent to the box girder (BG-1) web. Comparison of deck response as

obtained from different load cases are presented in Figures 24 to 27 in terms of variation of stresses normal to the Rib 10-to-FB 14 connection. The paths along which the stresses are plotted (the abscissa of the plots), and the direction of stresses are identified in the inset. The path originated at the soffit of the rib and proceeded counter-clockwise along the rib rounding as seen on east face of the floor beam (BG-1 on the left hand side). The results are plotted for those six transverse load positions that demonstrated the variation in stresses with the transverse positions. .

Figure 24 shows the circumferential variation of tensile stresses in the FB 14 web normal to the Rib 10-to-FB 14 connection for L1. The maximum tensile stress was observed for T29 and was about 4.3 ksi. The location of maximum stress was about 56° from the rib soffit. This load position generated higher shear forces in the floor beam web and the most critical stresses at the Rib 10-to-FB 14 connection. Figure 25 shows the circumferential variation of tensile stresses in the FB 14 web normal to the Rib 10-to-FB 14 connection for L2. The maximum tensile stress was observed for T29 and T30 and was about 3.7 ksi. Note that L2 produced both in-plane and out-of-plane stresses in the floor beam web. However, stresses due to L2 were less than L1. This is because sufficient floor beam depth was available below the soffit of the rib which provided the out-of-plane flexibility of the floor beam web. Also L1 produces more in-plane bending than L2.

Figures 26 and 27 show the circumferential variation of tensile stresses in Rib 10 normal to the Rib 10-to-FB 14 connection for L1 and L2 respectively.. The maximum tensile stress was observed for L1T29 and was about 3 ksi. The maximum tensile stress for L2 was lower and was about 1.8 ksi.

Figures 28 and 29 show the radial variation of tensile stress in FB 14 web normal

to the Rib 10-to-FB 14 connection for L1 and L2 respectively. The origin of the path corresponds to the maximum stress point location and proceeded radially outward from the connection. Similar behavior was observed for all the transverse load positions with high tensile stress at the connection that gradually became compressive away from the weld toe.

From the above evaluation it is evident that the load position L1T29 produced the most critical stresses normal to the Rib 10-to-FB 14 welded connection, when the tandem axles were symmetrically placed about the floor beam (Figure 12). For this load case, the wheels nearest to the box girder were placed centrally between the adjacent pair of ribs (ribs 10 and 11) and the center line of the tandem axle was 11 ft. from the center line of BG-1 (or 5 ft. 4 in. from the box girder web). Accordingly, the analysis of subsequent levels of FE models and also the fatigue testing were conducted for load case L1T29. The FEA results for this load case only are presented in the following sections.

2.9.2 Behavior of the Deck Plate and the Ribs

The maximum principal stress contour on the 3D deformed bridge deck is shown in Figure 30 for both GM and SM, scaled to 350x. As is seen from the figure, the deck deformation was characterized by global longitudinal bending of the ribs and transverse bending of the floor beams, and significant local transverse bending of the deck plate under the load patches. Deformation of the deck plate beyond the load patches was insignificant, as the black patches can only be seen on the deck plate under the load patches. The stress contours of the GM and the SM matched well, verifying the accuracy of the FE models.

The response of the deck plate and the ribs was investigated by comparing the defected shape of the deck at two transverse sections of the GM. These sections are identified in Figure 31. Transverse sections A-A and B-B are aligned with the centerline of

west pair of load patches and the centerline of FB 14 respectively.

Figure 32 shows the overlay plot comparing the deformed shapes of the deck at sections A-A and B-B, scaled to 50x. As also noted previously, the deck plate underwent local transverse bending at section through the load pads much more compared to the section through the centerline of floor beam. In addition, the deformation of the deck plate away from the load pads was negligible. Zoomed views of the portions of the deck around the load patch are shown in Figures 33 and 34. It could be seen that the deck plate deformed in a sagging curvature under the load pads between the rib walls and in a hogging curvature over the rib walls. The deformation of the deck plate and the rib wall was essentially local under the wheel loads and the rib walls and the rib-to-deck plate connections underwent local out-of-plane bending under the wheel loads. The details of the behavior of the deck plate and the ribs are discussed in Roy and Mukherjee (2015).

2.9.3 Behavior of the Floor Beams

Figure 35 compares the maximum principal stress contour in FB 14 web for GM and SM. As it can be seen from the figure, the distribution of the principal stress matched well for the two FE models. As discussed earlier, the floor beams were integral with the box girder and the wheel loads were transferred to the box girder (BG-1) through the floor beam by shear. In both the load cases, the transfer of wheel loads as shear to the box girder resulted in a diagonal tension field from the bottom (tension) flange of FB 14 to the top corner formed by the FB 14 web and the box girder web. The shear induced tensile stress in the FB 14 web was interrupted by the cutouts, and the stress field deviated around the cutout. As a result, high stress concentration developed in the web of FB 14 where the tension fields were approximately tangential to the cutout. The maximum stress occurred

along the diagonal tension field at Rib 10 adjacent to BG-1: in the floor beam web adjacent to the rib rounding at the Rib 10-to-FB 14 connection. Hence, the Rib 10-to-FB 14 connection was the most critical in terms of fatigue cracking. The magnitude of the principal stress was higher for the SM, as welds were modelled in the SM and the weld toe notch acted as stress raiser and further increased the stress at that connection. The maximum principal stresses in FB 14 web were about 11.3 ksi (78 MPa) and 13.9 ksi (93 MPa) for GM and SM respectively.

The deformed configurations of FB 13 and FB 14 are shown in Figure 36 for GM and SM, scaled to 500x. The deflected profiles of the floor beams matched well for GM and SM. As discussed in section 2.7, the loads were positioned around FB14, the floor beam at the mid span of the bridge deck, to produce the most critical global deformations. So, the displacement of FB 14 was more than the displacement of FB 13. The displacements of the floor beams were almost similar away from the load, but FB 14 displaced more under the wheel loads. FB 14 essentially deflected like a propped cantilever with the prop support at BG-1 and with support settlement at BG-1, however, FB 13 deflected like rigid body with support settlement. This can also be seen from Figure 37.

The in-plane bending moment diagrams of FB 14 and FB 13 as observed from FEA of GM is shown in Figure 38. FB 14 and FB 13 are identified as Inner FB and Outer FB respectively. The moment diagram is similar like a continuous beam supported by the box girders. The moment was maximum under the wheel loads, so the maximum displacement also occurred under the load. The moment at the edge of the BG-1 was almost zero verifying the propped cantilever deflection profile of FB 14. Figure 39 shows the distribution of transverse stresses along the bottom surface of the FB 14 flange at section

B-B for load cases L1T29 and L2T29, as observed from FEA of GM. The path along which the stress variation was plotted (the abscissa or the x-axis of the plots) and the direction of stress is identified in the section view of the deck. The origin of the path corresponds to the south wall of BG- 1 and ends at the north wall of BG-2. The maximum tensile stresses in the floor beam flange were about 4.8 ksi and 4.6 ksi for load cases L1T29 and L2T29 respectively. The stress envelope resembled the variation of bending moment in a continuous beam spanning between the box girders with sagging curvature in the span and hogging curvature over the support (or over the box girders).

As is evident from Figures 24 and 25, the stresses were higher for load case L1T29 when the loads were placed symmetrically on either side of FB 14. Out-of-plane bending of the floor beam web due to rotation of the rib was expected to occur at the rib-to-floor beam connection. In that case, load L2T29 would have been more critical. However, L2T29 was not critical as sufficient floor beam depth was available below the soffit of the rib which provided the out-of-plane flexibility of the floor beam web and reduced the out-of-plane stresses in the floor beam web. Figure 40 shows the variation of the stress normal to the Rib 10-to-FB 14 connection on the two faces of FB 14 web along a radial path as observed from FEA of GM. The origin of the path corresponds to the maximum stress point location and continues radially outward from the rib-to-floor beam connection. The stresses were primarily in-plane. The out-of-plane stress component was minimal in L2T29. The out-of-plane stress component was maximum at the connection and stayed constant for a distance of about 3 in. (76 mm). As the distance increased further, the out-of-plane component decreased rapidly and became primarily in-plane. For L1T29, there was no out-of-plane bending as the loading was symmetric to FB 14.

3 DESIGN OF SPECIMEN AND TEST SETUP

The specimen for laboratory testing (full-scale prototype) and the test setup was designed based on the FEA of the GM and the SM. FEA of the GM identified the most fatigue critical rib-to-floor beam connection and the corresponding disposition of the tandem axle. The solid SM with all the weld details modelled, provided the fatigue critical stresses at the welded connections. The specimen consisted of a deck plate, three floor beams, five ribs and a part of a box girder web. The specimen was tested in a novel test setup with adequate fixtures such that the critical stress state of the full-bridge deck could be reproduced in the specimen. Two above-deck actuators simulating AASHTO tandem axle loading and an under-deck actuator simulating the global displacement boundary condition, were used for loading the specimen.

3.1 Design of the Specimen

3.1.1 Longitudinal Extent of the Specimen

GM and SM analyses showed that the deformation of the deck was highly localized under the load patches and was limited within three floor beams in the longitudinal direction, FB 14 about which the loads were symmetrically placed and FB 13 and FB 15 on either side FB 14. FB 14 will be referred as the inner FB and the two other floor beams will be referred as the outer FB in the subsequent texts and figures. As seen from Figure 38, the moment in the outer FB was much less as compared to the inner FB. As observed from FEA, a diagonal tension field formed from the bottom flange of the floor beam to the top corner, due to transfer of load from floor beam to box girder as shear and was responsible for stress concentration at the rib-to-floor beam connection. Figure 41 clearly

shows that the shear force in the outer FB was negligible. As seen from Figures 36 and 37, the inner FB essentially deflected like a propped cantilever in between the BG-1 and BG-2 with support settlement at BG-1 while the outer FB essentially deflected like a rigid body with support settlement. The deflection in inner FB was also much higher than outer FB. As it can be seen from Figure 8, the deformation was mostly localized around inner FB and inclusion of three floor beams in the longitudinal direction of the specimen was the best choice. Hence, three floor beams was included in the longitudinal direction of the specimen.

3.1.2 Transverse Extent of the Specimen

Figure 36 shows that the curvature of the inner FB was restricted to few ribs locally around the load patches and inclusion of few ribs in the transverse direction was sufficient as the specimen, provided the stresses in the SM could be reproduced in the specimen by appropriate boundary condition. Accordingly, the transverse extent of the specimen was determined progressively by trial analyses of FE models of the part bridge deck. The in-plane bending moment and the shear in the inner FB web was compared with the GM analysis results to have the same curvature in the inner FB as the GM and the principal stress contour in the inner FB web was compared with the SM analysis results to have similar stress state at the fatigue critical rib-to-floor beam connection.

3.1.2.1 First and Second Trials

Figure 42 shows the 3D view of the first trial FE model. As discussed earlier, 3 floor beams were included in the longitudinal direction as the longitudinal extent of the FE model with 2 ft. overhang on both sides. Figure 43 shows the cross sectional elevation of the model at the inner FB section. Five ribs were included in the transverse direction to

accommodate the wheel loads in the transverse direction and the deck was extended beyond the fifth rib. The deck included a 7 ft. 4 in. (2.2 m) deep simulated box girder web with 1 in. (25 mm) thick flange, simulating the north web (right wall) of BG-1 adjacent to Rib 10. The transverse width of the specimen was 15 ft. (4.6 m). Figure 38 shows that the in-plane bending moment at the north wall of BG-1 (right wall) was about zero and there was non-zero in-plane moment at 15 ft. from the north wall. Accordingly, the simulated box girder web flange was given pinned boundary condition aligned with the centerline of the three floor beams and the end of the floor beams on the other side were given fixed boundary conditions to develop moment restraint at that section. Provision of moment restraint was avoided in the second trial FE model, where the deck was extended beyond the fifth rib such that the transverse width of the specimen was 20 ft. 8 in. (6.3 m) Figures 44 and 45 shows the 3D view and the sectional elevation of the second trial FE model. It can be seen from Figure 38 that the in-plane bending moment 20 ft. 8 in. from the north wall of BG-1 was about zero. Hence, in the second trial FE model the end of the floor beams on the other side of the box girder were given roller boundary condition to develop no moment restraint.

Figure 46 compares the principal stress contour in the inner FB web of the first and second trial FE models with the SM analysis results. The principal stress contour of second trial FE model matched well with the SM analysis results. However, the principal stress values in first trial FE model was lower than the SM analysis. Figures 47 and 48 compares the in-plane bending moment and shear in the inner FB of the two models with the GM respectively. It can be clearly seen that the bending moment in the first trial model was much lower than the GM. However, the moment and shear in the second trial model matched well with the GM results. Thus, the second trial FE model was the chosen

alternative. Further refinements were done in the next trial FE models to reduce the size of the specimen, at the same time simulating the critical stress state at the rib-to-floor beam connection.

3.1.2.2 Third Trial

It was observed for the first trial FE model that the in-plane moment was lower than the GM. Keeping the transverse width of the specimen model as 15 ft. (4.6 m), it was analyzed that an upward displacement of 0.07 in. (2 mm) at the box girder aligned with the centerline of the inner FB was creating a similar curvature in the inner FB. The 3D view and the sectional elevation of the third trial FE model is shown in Figures 49 and 50 respectively. The longitudinal and the transverse extents of this model was same as that of the first trial model, however, the simulated box girder web was trimmed matching the depth of the floor beam. Pinned boundary condition was applied at the simulated box girder web aligned with centerline of the two outer FB and the end of the floor beams on the other side was given fixed boundary condition. Figure 51 shows the comparison of the principal stress contour in the inner FB web with the SM analysis. The principal stress contour in the inner FB web matched well with the SM analysis results. This can also be seen from Figure 52, which shows a good correlation of the in-plane bending moment in the inner FB web of the trial model with the GM analysis results.

3.1.2.3 Fourth Trial

The third trial appeared to be better than the second trial as it restricted the transverse width of the specimen to 15 ft. However, the deck plate and the floor beams were extended beyond the fifth rib for the entire transverse width of 15 ft. To reduce the size of the specimen, in the fourth trial FE model the deck plate was not extended the full

transverse width after the fifth rib. The 3D view and the sectional elevation of the fourth trial FE model is shown in Figures 53 and 54 respectively. The floor beams were continued for the full width of the specimen, but the deck plate was cut 1 ft. 6 in. (457 mm) short. A 3 ft. 7 in. (1.1 m) deep simulated box girder web with 1 in. (25 mm) thick bottom flange was used, and similar to third trial an upward displacement of 0.07 in. (2 mm) was applied at the box girder flange aligned with the centerline of the inner FB. An 8 in. x ¾ in. (203 mm x 19 mm) thick plate was used after the fifth rib at a 1 ft. 6 in. (457 mm) from the specimen end, to simulate the stiffening effect of the sixth rib. Pinned boundary condition was applied at the simulated box girder web flange aligned with centerline of the two outer floor beams and the end of the floor beams on the other side was given fixed boundary condition. Figure 55 shows principal stress comparison with the SM analysis. The principal stress contour in the inner FB web matched well with the SM analysis results. This can also be seen from Figures 56 and 57, which show a good correlation of the in-plane bending moment and shear in the inner FB web of the trial model with the GM analysis results. Hence, the fourth trail was the best option for the specimen among all the four trials conducted.

3.1.2.4 Fifth Trial

Fourth trial involved the application of lift-up, and so it was investigated in the fifth trial whether this lift-up can be avoided by increasing the transverse width of the specimen. Recall that the second trial where the transverse width of the specimen was 20 ft. 8 in. gave a good correlation with the GM and SM analysis results. The fifth trial FE model was a modified version of the second trial model. The 3D view and the sectional elevation of the fifth trial FE model is shown in Figures 58 and 59 respectively. The applied boundary

conditions to the FE model was similar to the second trial model. The inner floor beam was continued to the full width of the specimen, but the outer floor beams and the deck plate were trimmed at 15 ft. (4.6 m) from the box girder web. Figure 60 shows the principal stress comparison with the SM analysis. The principal stress contour in the inner FB web matched well with the SM analysis results. This can also be seen from Figures 61 and 62 which shows a good correlation of the in-plane bending moment and shear in the inner floor beam web of the trial model with the GM analysis results. Hence, the fifth trail was also an alternative for the full-size specimen.

3.1.2.5 Option 1 and 2 for the Specimen

Fourth and fifth trial FE models were the two alternatives for the laboratory specimen. The fourth trial FE model and the fifth trial FE model will be referred as Option 1 and Option 2 respectively in the subsequent text and figures. The 3D views of the models are shown in Figures 63 and 64 respectively. Figure 65 shows principal stress comparison with the SM analysis. The principal stress contour in the inner FB web matched well for both the options with the SM analysis results. This can also be seen from Figures 66 and 67 which show a good correlation of the in-plane bending moment and shear in the inner FB of the options with the GM analysis results However, it was envisaged that installation of Option 2 in the lab would require more space than Option 1, which is shown in Figures 68 and 69. It was also realized that the steel required for fabricating Option 2 would be more than that of Option 1. So, Option 1 was selected for subsequent refinement to design the full-size specimen for laboratory testing.

3.1.2.6 Modified Option 1

Option 1 was modified keeping the transverse width of the deck as 15 ft. (4.6 m).

The deck plate was trimmed further and was cut 3 ft. 6 in. (1.1 m) short of the specimen end. The deck plate was extended 6 in. beyond the centerline of the simulated box girder web. The depth of the box girder was adjusted such that the total depth of the simulated girder web flange including the deck plate was 4 ft. 4 in. (1.3 m). The depth of the floor beams were increased from 3 ft. (914 mm) to 3 ft. 4 in. (1 m). The depth of the floor beams was variable as per the design drawings for the full-bridge deck and the average depth of the floor beam in the part of the deck under consideration was about 3 ft. 4 in. To accommodate this, the depth of the floor beam was increased. The sectional elevation at the inner floor beam section is shown in Figure 70. Figure 71 shows principal stress comparison with the SM analysis. The principal stress contour in the inner FB web matched well with the SM analysis results.

3.2 Determination of Design Lift-up

The upward vertical displacement or the design lift-up at the box girder flange at the centerline of the inner FB was determined both graphically and analytically. The procedures for determining the design lift-up are discussed in the following.

3.2.1 Determination of Design Lift-up Graphically

The steps for graphical determination of the design lift-up are shown in Figures 72 and 73. Figure 72 shows the deflected shape of the inner and outer FBs as determined from FEA of the GM. The box girder will be referred as edge girder in subsequent figures. The centerline of the box girder web is identified by point B and the other end of the specimen model is identified by point A. For making the peripheral plane (consisting of the longitudinal edges of the specimen and the two outer floor beams) horizontal, the chord

joining points A and B was made horizontal by giving a rigid body rotation to it. The deflected shape of the inner FB was corrected for the same rigid body rotation and the resulting deflected shape of the inner FB after correction is shown in Figure 72. This was done to have the end of the outer floor beams at the same elevation during laboratory testing. It was envisaged that during testing condition, the tangent to the deflected shape of the inner FB at the opposite end of the box girder would be horizontal due to fixed boundary condition. So the deflected shape of the inner FB was rotated further to make the tangent horizontal at the opposite end of the box girder and resulting deflected shape is shown in Figure 73. The distance between the tangent and tip of the inner FB at the centerline of box girder was the design lift-up, and it was measured graphically to be about 0.1 in. (2.5 mm).

3.2.2 Determination of Design Lift-up Analytically

The design lift-up was also determined analytically by taking reaction forces at the end of the inner FB obtained from GM analysis and calculating the resulting displacement by statics. Figure 74 shows the reaction forces at the ends of the inner FB obtained from the GM analysis. The inner floor beam was acted upon by a vertical reaction and a moment at the centerline of the simulated box girder web. The proportion of the wheel loads coming to the inner FB is identified as P. Value of P was determined by vertical force equilibrium and was about 26 kip (116 kN). Then the resulting deflection at the centerline of the simulated box girder web was calculated under combined action of reaction force, reaction moment and P. The resulting displacement was calculated to be about 0.1 in. (2.5 mm) upward, which verifies the graphical calculation. Hence, an upward displacement of 0.1 in. (2.5 mm) was applied at the flange of the simulated box girder web aligned with centerline of the inner FB during FEA of the specimen model and laboratory testing.

3.3 Description of the Specimen

The 3D view of the specimen (prototype deck) is shown in Figure 75. The specimen consisted of a deck plate with 3 floor beams, 5 ribs and a part of box girder web provided with bottom flange. The floor beam at the midspan is identified as the "inner FB" and two other floor beams are identified as "outer FB". The simulated box girder web, along with the bottom flange is identified as the edge girder. The ribs are numbered sequentially, starting from the edge girder side with the rib adjacent to the edge girder identified as "Rib 1". The specimen was oriented along the east-west direction of the laboratory, and the north direction is shown in the figure. The extent of the specimen in the SM is shown in Figure 76. Rib 1 essentially represents Rib 10 of GM and inner FB represents FB 14 of GM. The connection between Rib 1 and inner FB was the most fatigue critical.

The plan view of the specimen is shown in Figure 77. The specimen was 27 ft. 6 in. (8.4 m) long and 12 ft. (3.7 m) wide. The floor beams were extended 3 ft. 6 in. (1.1 m) beyond the deck plate on the north side through floor beam extensions (FB Extension in Figure 77). The floor beam extensions were spliced to the floor beams using bolts. The specimen was fabricated in two panels 15 ft. 9 in. (4.8 m) and 11 ft. 9 in. (3.6 m) in lengths, and were spliced in the laboratory with CJP weld at the deck plate and slip critical bolted connections at the ribs and the edge girder. Access holes were provided at the soffit of the ribs at the spliced section. The ribs were hermitically sealed by providing full depth $^{3}/_{8}$ in. (9.5 mm) sealing plates on both sides the access holes. At the junction with the floor beam, the edge girder was continuous. Copes were provided in the floor beams for continuing the edge girder-to-deck plate weld uninterrupted. The details of the splice connection is shown in Figure 78.

The dimensions of the prototype deck elements were according to the design drawings of the lift bridge. The sectional elevation of the specimen is shown in Figure 79. The thickness of the deck plate was ¾ in. (19 mm). The ribs were of closed trapezoidal shape with rounded bottom (U-shaped) having an overall depth of 1ft. 2 in. (356 mm). The ribs were $^{5}/_{16}$ in. (8 mm) thick and had a rounding radius of 4 in. to the inner surface of the rib wall. The ribs were spaced at 2ft. 4 in. (711 mm) center-to-center. The floor beams were of inverted T-section having ½ in. (13 mm) thick web and a 12 in. x ¾ in. (305 mm x 19 mm) thick bottom flange. The floor beams have an overall depth of 3 ft. 4 in. (1 m). The floor beams were spaced at 11 ft. 9 in. (3.6 m) center-to-center. The overall depth of the edge girder was 4 ft. 4 in. (1.3 m) and it had a 12 in. x ¾ in. (305 mm x 19 mm) bottom flange. The deck plate was extended 6 in. beyond the centerline of the edge girder towards the south side. The edge girder web was stiffened with $^{5}/_{8}$ in. (16 mm) thick transverse stiffeners aligned with the centerline of the floor beams. Longitudinal stiffeners matching the width of the bottom flange of the floor beam were also provided at the web of the edge girder. The transverse stiffeners were run continuous.

According to the client's directive, the connection details of the specimen were specified as follows: (a)rib-to-deck plate connection: 80% PJP weld with minimum of 70% DOP and a fit-up gap not exceeding 0.020 in. (0.5 mm); (b) rib-to-floor beam connection: $^{5}/_{16}$ in. (8 mm) fillet weld with fit-up gap not exceeding $^{1}/_{16}$ in. (1.5 mm). The full-size specimen was proposed to be fabricated in two panels and later being spliced in the laboratory, to simulate the field splice condition. The transverse deck splice was specified as a CJP weld at the deck plate and bolted splice at the ribs, with a tolerance of $^{1}/_{16}$ in. (1.5 mm) for vertical and horizontal misalignments. In addition, it was specified to perform the

weld using a backing bar and to remove the backing bar after welding is done, and to back gouge and back weld the root and to inspect the quality by 100% UT. Any reinforcement and local defects above $^1/_8$ in. (3 mm) were specified to be ground flush with the top surface of the deck plate. The deviation from flatness in any direction of the deck was specified as ¼ in. (6 mm) at all sections, except at either side of the splice where it was specified as $^1/_8$ in. (3 mm). The specimen was fabricated by High Steel Structures at their Lancaster facility.

3.4 Analytical Studies of the Specimen Model

3.4.1 Details of the Specimen Model

The detail description of the specimen is given in section 3.3. The FE model of the specimen replicated the specimen for laboratory testing. The deck was proposed to be fabricated in two panels to simulate the transverse field splice condition. Accordingly, the splice connection between the two deck panels was simulated in the specimen model. The bolted splice connections at the ribs and the edge girder were modelled as tie constraints with hard contact definition between the mating surfaces. However, the CJP weld at the deck plate was not modelled. All other welded connections in the specimen were modelled as $^5/_{16}$ (8 mm) fillet welds with idealized zero notch radius at the weld toes and complete penetration at the weld root. The elements of the prototype deck were modelled as an integral unit.

3.4.2 Material Properties

Widely accepted linear elastic material properties of steel were used for analysis. The modulus of elasticity and Poisson's ratio of steel were assumed as 29000 ksi (2.0×10^5

MPa) and 0.3 respectively.

3.4.3 Details of Element Type and Meshing

The specimen model was meshed with 3D continuum solid hexahedral elements, incorporating twenty node, quadratic, reduced integration and second order isoparametric formulation. In ABAQUS, this element is identified as C3D20R. The C3D20R element was used as it is known to provide accurate results for three dimensional stress analyses and is effective in capturing stress concentration effects (Dassault Systemes 2012). Each node of the element has 3 translational degrees of freedom. The specimen model consisted of 492,295 elements and 2,710,612 nodes, generating 8,191,836 solution variables or nodal degrees of freedom. The mesh of the specimen model was generated automatically by ABAQUS with an average minimum mesh size of 1 in. and an average aspect ratio of about 6. The average maximum and minimum corner angles were 82° and 98° respectively. As discussed earlier, the quality of the mesh was important to avoid singularity while inverting the Jacobian of isoparametric transformation. The quality of mesh was in accordance with the standards set by ABAQUS. Automatically generated non-uniform mesh for the model limited the freedom of propagation of spurious modes that are associated with these reduced integration elements.

3.4.4 Loading

The specimen model was analyzed for the most critical disposition of the tandem axle as determined from GM analysis and consistent with the laboratory testing. The load position in plan and elevation are shown in Figures 80 and 81 respectively. The specimen model was analyzed for load position L1T29, to produce the most critical stress state at the rib-to-floor beam connection adjacent to the box girder. The Rib 10-to-FB 14 connection

adjacent to the box girder was identified as the most fatigue critical location in the GM analysis. In the specimen model, the welded connection between Rib 1 and inner FB adjacent to the edge girder is equivalent to the Rib 10-to-FB 14 connection in the GM. The load from each wheel pair of the tandem axle was uniformly distributed over a rectangular load patch of 10 in. (254 mm) long and 20 in. (508 mm) wide as specified by AASHTO LRFD BDS. These load patches are identified as LP in Figure 80. Each pair of load patches in the transverse direction represented one axle of the tandem. Although a transverse gap of 1 in. exists in the middle of each wheel pairs, it was ignored in the idealized rectangular wheel contact for simplicity in modelling. As seen from Figure 80, the tandem axles were symmetrically placed 2 ft. (610 mm) on either side of inner FB simulating symmetric longitudinal disposition of tandem axles (longitudinal load position L1). In the transverse direction (Figure 81), the wheel pairs adjacent to the edge girder was placed centrally between ribs 1 and 2, simulating transverse load position T29. The spacing between the tandem axles in the longitudinal direction and the spacing between the load patches in the transverse direction were consistent with the latest provisions of the AASHTO LRFD BDS. The total load applied on the deck was 82.8 kip (368 kN), which is three times the AAHTO fatigue design load (0.75×HS20 + 15% impact) as specified by AASHTO for Fatigue I limit state design of orthotropic decks. This resulted in a total load of 41.4 kip (184 kN) per axle or 20.7 kip (92 kN) per wheel pair or load patch. The load was applied as a uniformly distributed pressure load of 0.1035 ksi per load patch. The loading in the specimen model were consistent with loading in the static and fatigue tests of the prototype deck and the location of load patches were consistent with the location of the load pads on the prototype deck during laboratory testing.

3.4.5 Boundary Condition

The boundary conditions applied to the specimen model are shown in an underside view of the model in Figure 82. The north end of the floor beams were assigned fixed boundary conditions where all the nodes on the surface were restrained against displacement in all three directions. To the south, the bottom flange of the edge girder aligned with the centerline of the two outer floor beams was restrained against displacement in all the three directions.

The bottom flange of the edge girder aligned with the centerline of the inner FB was given displacement boundary condition as determined from the GM and SM analyses. Displacement degrees of freedom in the horizontal plane were restrained, but an upward displacement of 0.1 inch was applied at that location. This upward displacement or design lift-up was determined from the GM and SM analyses as discussed in section 3.2. In the laboratory testing, the under-deck actuator giving the design lift-up was floor mounted and the top and bottom clevises of the actuator was arranged to allow in-plane rotation of the inner FB. To account for this, the top and bottom clevises of the under-deck actuator were modelled as solid blocks and the hydraulic jack was modelled by a “slot and cordon” connector element (Figure 83). The connector element was given a vertical displacement boundary condition of 0.1 in. and rotational degree of freedom about y-axis of the element or in-plane rotation of the inner FB. The bottom surface of the bottom clevis of the simulated actuator was restrained against displacement in all three directions to simulate the condition of under-deck actuator being fixed to the lab floor through the actuator support. The bolted connection between the bottom flange of the edge girder and the top clevis of the actuator was modelled as tie constraint in the specimen model.

3.4.6 Analysis Results

3.4.6.1 Behavior of the Deck Plate and the Ribs

The contours of the maximum principal stress on deformed configuration of the deck are shown in Figures 84 and 85. Similar to GM and SM, two way deformation of the deck was observed with high stresses and deformation of the deck plate locally under the load pads.

The variation of transverse stresses on the top and the bottom surfaces of the deck plate, and the outer and inner faces of the rib wall along a section aligned with the centerline of the east load pads are shown in Figure 86, along with the deformed configuration of the deck at that section. The transverse section was selected on the east side, because the deck showed lesser stress values on the west side due to the presence of access holes on the rib soffit at the transverse splice location. Tensile stresses are plotted on the top surface of the deck plate and the outer face of the rib wall. Tensile stresses were considered as "+ve. As is evident, the deck plate deformed like a continuous beam supported over the ribs, where it deflected in sagging curvature in between the rib walls and in hogging curvature over the rib walls. So the stresses on the top surface of the deck plate were compressive and on the bottom surface were tensile in between the ribs. Opposite trend was observed when the deck plate deflected in hogging curvature over the rib walls as is expected for continuous beam showing opposite trend over the supports. The stresses in the deck plate peaked under the load pads as it underwent maximum transverse deformation under the load pads, and the stresses were insignificant away from the load pads. It can also be seen that the stresses at the inner and the outer faces of the rib wall was localized under the load pads, confirming that the response of the orthotropic deck is localized under the wheel loads. Ribs 1 and 2

which were under the south side load pads and rib 4 which was under the north side load pads, underwent maximum deformation as the stresses on their walls were much higher as compared to other ribs. The ribs under the load pads distorted due to the framing action between the rib and the deck plate. The distortion introduced linearly distributed stresses in the rib walls. The stresses were of opposite sense on the inner and the outer faces where the rib walls underwent flexural deformation. However, the magnitude of the these stresses on the inner and the outer faces of the rib walls under the wheel loads were different due to the presence of axial stresses in the ribs. The stresses on the top and the bottom surfaces of the deck plate are also compared in Figure 87 which clearly indicates flexural deformation of the deck plate as continuous beam supported by the ribs. The stresses on the top and bottom surfaces of the deck plate were almost of similar magnitude, indicating pure bending in the transverse direction with insignificant membrane stress.

It should be noted that the stresses at the bottom surface of the deck plate and the outer surface of the rib wall near the rib-to-deck plate connection were compressive. However, due to the presence of high tensile residual stresses at the weld toe, the connection could experience a total tensile stress cycle under the action of nominal compressive stresses under the wheel loads and hence can develop fatigue cracking from the weld toe as it was observed in existing bridges in service. Hence, this connection being fatigue critical, was extensively instrumented at a section under the load pads during the laboratory testing to measure the stress ranges at the rib-to-deck plate connections. The instrumentation at the rib-to-deck plate connections is discussed later in section 4.4.

3.4.6.2 Behavior of the Floor Beams

GM and SM analyses showed that the stresses in FB 14 i.e. the floor beam around

which the loads were positioned, was significantly more than the other floor beams. Accordingly, the behavior of the floor beams in specimen model analysis has been presented here in terms of the response of the inner FB which essentially represents FB 14 of GM.

The deformed configuration of the inner floor beam is shown in Figure 88 overlaid on the undeformed configuration. The bottom flange of the edge girder aligned with the centerline of the inner FB was given upward displacement of 0.1 in. (2.5 mm). Consequently, the inner FB deformed as a propped cantilever with support displacement (vertically upward) at the edge girder side. The displacement profile of the inner FB was similar to FB 14 as was observed in GM and SM analyses.

The maximum principal stress contour on the inner FB web is shown in Figure 89. Since the inner FB was integral with the edge girder, the wheel loads were transferred to the box girder through the floor beam by shear. The transfer of wheel loads as shear to the box girder resulted in a diagonal tension field from the bottom (tension) flange to the top corner formed by the floor beam web and the edge girder web. The shear induced tensile stress in the floor beam web was interrupted by the cutouts, and the stress field deviated around the cutout. As a result, high stress concentration developed in the inner Fb web at the Rib 1-to-inner FB connection where the tension fields were approximately tangential to the cutout. The Rib 1-to-inner FB connection also contributed to the increase in stress due to the presence of weld toe notch. As such, the high stress concentration was observed at the Rib 1-to-inner FB connection (Figure 89) in specimen model analysis similar to the GM and SM analyses. Stresses were tensile at the connection towards the edge girder side and compressive on the other side. The maximum tensile principal stress in the inner FB

web was about 12.5 ksi (84 MPa).

Fatigue cracking at the weld toe is primarily attributed to crack growth from micro discontinuities subjected to the stress range normal to the weld toe. The variation of stress normal to the weld toe on inner FB web at the Rib 1-to-inner FB connection is shown in Figure 90. The magnitude of the maximum normal stress in the tension side was about 5.7 ksi and in the compression side was about 7.4 ksi. Both the maxima occurred at about 50° from the rib soffit, and hence the Rib 1-to-inner FB weld toe at 50° from the rib soffit was critical for fatigue cracking from the weld toe and thus was extensively instrumented at that location (see section 4.4).

Experimental studies of the mockup specimens (Roy and Mukherjee, 2015) showed a failure mode where crack growth was observed from the weld root subjected the maximum principal stress field in the floor beam web. The variation of maximum principal stress at the Rib 1-to-inner FB weld root is shown in Figure 91. The magnitude of the maximum principal stresses at the weld root were about 8.3 ksi and 12.4 ksi at the tension and compression sides respectively. Both the maxima occurred at about 50° from the rib soffit.

Out-of-plane bending of the inner FB was expected due to the presence of access holes on the rib soffit at the transverse splice location, which affected the flexural and torsional stiffness of the ribs. Figure 92 shows the variation of the stress normal to the weld toe on the east and west faces inner FB at Rib 1, along a path normal to the weld toe on the floor beam web. As is evident from the figure, significant out-of-plane stress was observed at the weld toe, which gradually decreased away from the weld toe and became primarily in-plane.

3.4.7 Comparison of Specimen Model Analysis with GM and SM Analyses

The specimen model was a slight modification of the modified Option 1 FE model where only the design lift-up was changed from 0.07 in. to 0.1 in. Accurate determination of the lift-up made the results very close to the GM and SM analyses. Figure 93 compares the shear force in the specimen model with the GM analysis, and it shows a very good correlation with the GM analysis. This was also verified by comparing the principal stress contour in the inner FB web with SM and is shown in Figure 94. The principal stress contour matched very well with the SM analysis results.

3.5 Design of the Test Setup

The test setup for laboratory testing was devised based on the FEA, such that the critical stress state of the full-bridge deck could be reproduced in the specimen. The north elevation of the test setup is shown in Figure 95. The floor beam extensions were fixed to the north wall using wall fixtures to simulate the fixed boundary conditions. To the south, the specimen was supported at the bottom flange of the edge girder on two support columns aligned with the centerline of two outer floor beams, which simulated the pinned boundary conditions. The details of setup and the fixtures is given in Chapter 4. The AASHTO fatigue loading was simulated by two above-deck actuators installed in the critical load position as determined from FEA. The two actuators were placed symmetrically 2 ft. (610 mm) on either side of the inner FB. In the transverse direction (Figure 96), the south load pads were placed centrally between ribs 1 and 2. An under-deck actuator was installed supporting the edge girder flange at the centerline of the inner FB for giving the global displacement boundary condition. The details of the loading and the loading protocol for the laboratory testing is discussed in Chapter 4.

4 FULL-SCALE LABORATORY STUDIES

4.1 Fabrication of the Prototype Deck

Details of the prototype deck fabrication is presented in Roy and Mukherjee (2015). A summary of the fabrication details is presented here. The prototype deck was fabricated by High Steel Structures at their Lancaster facility, using approved weld procedure specifications (WPS). The WPS for the rib-to-floor beam welds was developed on a mockup panel containing 3 ribs and 3 floor beams that was subsequently qualified by evaluating macro-etched cross sections. For the rib-to-deck plate welds, WPS was developed and qualified by fabricating several mockups with different welding parameters and in one case a different joint preparation, and subsequent evaluation of weld penetrations and weld profiles on macro-etched sections.

The prototype deck was fabricated as two panels, 15 ft. 9 in. (4.8 m) and 11 ft. 9 in. (3.6 m) long respectively, to simulate the transverse field splice condition in the fatigue testing. The two panels will be referred as the long panel and the short panel in subsequent texts. The panels were spliced in the laboratory and the splicing procedure is discussed in detail in section 3.3. The rib-to-deck plate and the rib-to-floor beam connection details used for the prototype deck are shown in Figure 97.

The short panel was fabricated prior to the long panel. Both panels were fabricated following the same sequence and welding procedures. The rib-to-deck plate welds were performed in sequence for ribs 3, 5, 2, 4 and 1 (refer Figure 75 for rib numbering), by single pass Submerged Arc Welding (SAW) process simultaneously on two sides of the rib (Figure 98). The floor beams were match cut according to as-fabricated rib profile and were fitted around the ribs using tack welds, to the specified fit-up gap not exceeding $^{1}/_{16}$ in. (2

mm) as shown in Figure 99. The floor beams were then welded to the deck plate using $^{5}/_{16}$ in. (8 mm) fillet welds on both sides of the web (Figure 100). The rib-to-floor beam fillet welds were performed in 2F position (Figure 101) by a single pass continuously around the rib using Gas Metal Arc Welding (GMAW) process with ribs standing vertically up. Subsequently, the edge girder was welded to the deck plate followed by welding of the floor beam web to the edge girder. These were two sided $^{5}/_{16}$ in. (8 mm) fillet welds. Finally the floor beam flange-to-edge girder web was connected by a CJP weld. The prototype deck panels were shipped to ATLSS by High Steel and were assembled and erected in the laboratory.

4.2 Test Setup

The north elevation of the test setup is shown in Figure 95. As discussed earlier, the prototype deck consisting of a deck plate stiffened by 5 ribs and 3 floor beams and a simulated box girder web with flange (referred as edge girder), was tested in a novel test setup with adequate fixtures which was devised based on a multi-level 3D FEA to reproduce the critical stress state of the full bridge deck in the specimen. Refer section 3.3 for description of the specimen. The fixtures for the specimen were designed to simulate the boundary conditions of the FE model (refer section 3.4.5 for the boundary conditions). The extensions of the floor beam (floor beam extensions) beyond the deck plate were fabricated separately. The specimen was oriented along the east-west direction of the laboratory as shown in Figure 95 and will be referred accordingly in subsequent texts. The floor beam extensions were spliced to the floor beams using bolts and on the other side (north side) were connected to the reaction wall using wall fixtures to simulate the fixed boundary conditions at the end of the floor beams. Wall columns B-1, C and B-2 (Figure

95) were connected to the west outer, inner and east outer floor beams respectively. The bottom flange of the edge girder was supported on support columns A and B at the south side of the specimen aligned with the centerline of the east and the west outer floor beams. The connection between the support columns and the edge girder simulated the pinned boundary condition at the south side of the specimen. The above-deck actuators were hung from an arrangement of two parallel cross beams and longitudinal loading beam as shown in Figures 95 and 96. The bottom flange of the edge girder, aligned with the centerline of the inner FB, was supported on an under-deck actuator (Figure 95) that was used for simulating the global displacement boundary condition. As shown in the sectional elevation of the test setup in Figure 102, the under-deck actuator was mounted on the laboratory floor and was connected to the edge girder bottom flange using custom fixtures. Note that the above-deck actuators were not at the inner FB location, however they are shown in Figure 102 to depict the transverse load arrangement. Details of the test fixtures are provided in Roy and Mukherjee (2015). Most of the fixtures were built by Haberle Steel Inc. of Souderton, Pennsylvania, and the rest were from the existing inventory of the ATLSS Center.

Total three hydraulic actuators, two above the deck and one under the deck, were used for applying the load to the prototype deck and for simulating the boundary condition respectively. The details of the actuators are provided in section 4.6.3. The overhead actuators were located 4 ft. (1.2 m) apart, symmetrically 2 ft. on either side of the inner FB as shown in Figure 95 according to the loading arrangement discussed in section 4.6.2. The above-deck actuators to the east and the west side will be referred as east actuator and west actuator respectively in subsequent texts. The west actuator was located directly on the

transverse splice location (Figure 95).

The above-deck loading simulated the tandem rear axle of an AASHTO fatigue truck in the most critical disposition determined from FEA and the under-deck actuator provided the global displacement boundary condition. The details of the loading and the loading protocol are discussed in section 4.6. At each above-deck actuator location, a spreader beam was installed to distribute the loads from the actuator to the deck via two rectangular loading pads placed 6 ft. (1.8 m) apart in the transverse direction. Each loading pad simulated the contact of a pair of wheels with rubber tires, at each end of an axle.

A W12x190 column was installed next to the under-deck actuator as a safety measure. This column was used for supporting the inner FB when the testing was stopped and the under-deck actuator was not hydraulically live. The safety column was anchored to the laboratory floor using the same custom fixture for the underdeck actuator.

4.3 Installation of Fixtures and Prototype Deck

The supports for the prototype deck (wall columns and the support columns) and the safety column were installed in the laboratory prior to delivery of the specimen (Figure 103). The floor beam extensions were installed on the wall columns. Bolt holes were drilled on the floor beam extensions towards the specimen side (south side) by the fabricator. On the other side, holes were drilled on the floor beam extensions using the connection plates and angles on the wall columns as templates.

The long and the short panels of the prototype deck were installed towards the east and the west side of the laboratory, and will be accordingly referred to in subsequent texts as the east panel and the west panel respectively. The specimen was installed by the erection crew of High Steel. The two deck panels were spliced in the laboratory by a CJP groove

weld at the deck plate and bolted splice at the ribs and the edge girder, simulating the field splice in the real bridge.

The deck panels were shipped to ATLSS by the fabricator on January 27, 2014. Level measurements of the deck surface was performed on the two deck panels. A string attached two small weights placed at the two ends of the deck formed a chord. This chord was used as a reference datum from where the deck levels were measured using a measuring scale (Figure 104). Significant out-of-flatness were observed in the deck panels which exceeded the specified tolerance of ¼ in. (6 mm). Consequently, the deck panels were sent back to the fabrication shop for heat treatment of the deck panels. After heat straightening, the deck panels were reshipped to ATLSS on March 3, 2014. The east panel was installed first as shown in Figure 105. The north end of the floor beams were spliced to the floor beam extensions and the bottom flange of the edge girder was bolted to support column A. The bolt holes on the floor beams and the edge girder flange were drilled with the splice plates on the floor beam extensions and the top plates on support column respectively as templates. The west panel was then installed in the similar way as the east panel and is shown in Figure 106.

During assembly of the deck panels in the laboratory, significant lack of fit was noted between the panels, primarily due to the weld heat effects on asymmetric cross section of the specimen. The heat marks on the deck specimen are shown in Figure 107. The maximum out-of-flatness in the deck plate was measured to be about $^{3}/_{4}$ in. (19 mm), which exceeded the specified tolerance of $^{1}/_{4}$ in. (6 mm). At the transverse splice, a relative out-of-flatness of the deck plates exceeding $^{5}/_{8}$ in. (16 mm) existed before welding, which also exceeded the specified tolerance of $^{1}/_{16}$ in. (2 mm) between the mating deck panels

(Figures 108 and 109). As shown in Figure 109, the out-of-flatness was reduced considerably to about $^{3}/_{16}$ in. (5mm) by jacking up the west panel (Figure 110) and tack welding the panels, although the out-of-flatness still exceed the specified tolerance. The maximum root gap at the transverse splice location (Figure 111) was about ½ in. (13 mm), which also exceeded the specified tolerance of $^{3}/_{8}$ in. (10 mm). The ribs were also misaligned at the transverse splice location (Figure 112), and the maximum misalignment was about $^{3}/_{8}$ in. (10 mm) which also exceeded the specified tolerance of $^{1}/_{16}$ in. (2 mm).

The ribs and the edge girder were spliced using slip critical bolted connections.. Copes were provided in the floor beams for continuing the edge girder-to-deck plate weld uninterrupted. The CJP weld for the deck plate splice was performed after splicing the ribs and the edge girder. The backing bar for the CJP weld was specified to be removed after welding, which was accomplished by a brass backing. Copes were provided in the ribs and in the edge girder for running the backing bar uninterrupted. Initially, a root pass with Shielded Metal Arc Welding (SMAW) process was done with the backing bar in place. In addition to the root pass, total seven passes of SAW process (Figure 113) was required to perform the CJP deck splice. The backing bar was removed after 3 passes of the SAW process. Figure 114 shows the weld root at the underside of the deck after removal of the backing bar. Visual inspection of the weld root showed multiple areas of lack of fusion (LOF), and the condition of the weld root was questionable. Subsequently, two root passes were performed in the overhead position to repair the weld root (Figures 115 and 116). Figure 117 shows the weld root after the repair. Start and stop of the repair weld can be observed at each of the rib copes (provided for running the backing bar), as those areas could not be repaired due to lack of access (Figure 118). The welded deck splice was

ultrasonically inspected (Figure 119) by KTA QA inspector using conventional Ultrasonic Testing (UT). Rejectable indications were observed at the weld start and stop over the rib copes. In addition to this, rejectable indications were also observed at 10 other locations, where the depth of indications ranged between 0.54 in. (14 mm) to 0.73 in. (18 mm); note that the deck plate thickness is ¾ in. The maximum weld reinforcement at the deck splice location was about $^{1}/_{8}$ in. (3 mm) and it was observed at two weld start and stop locations. The weld reinforcement was within the specified fabrication tolerance and hence was not grounded with deck plate surface. Laser measurements of the deck level was conducted after the specimen installation. A reference datum (red line in Figure 120) was established using a laser equipment, and deck levels were measured from that reference datum with a tape measure (Figure 120). The deck surface was plotted using the laser measurements and is shown in Figure 121. Maximum elevation difference of $^{3}/_{16}$ in. (5 mm) was observed at the transverse splice location. The maximum out-of-flatness in the deck plate was measured to be about $^{3}/_{4}$ in. (19 mm). The transverse splice being one of the loaded section (under the east actuator), it provided an opportunity of testing the splice including the influence of the deviations on the fatigue performance of the deck.

After installation of the specimen, the floor columns and the under deck actuator, crawl tests were performed. The details of crawl tests are discussed in section 4.5. After the completion of crawl tests, the loading fixtures for the static and fatigue tests were installed. The cross beams were installed connected to a wall column wall at the north end, and to a floor column at the south end (Figure 96). The above-deck actuators were connected to the loading beam and the entire assembly was hung from the cross beams at the desired longitudinal and transverse position. The spreader beams along with the loading

blocks and the loading pads were positioned on the deck plate, oriented in the transverse direction symmetrically about the actuators. The bottom clevises of the actuator was then fastened to the top flange of the spreader beams. Finally the guide angles were installed containing the loading blocks in position during fatigue testing. The final test setup is shown in Figure 122.

4.4 Instrumentation and Data Acquisition

The prototype deck was extensively instrumented to determine its global response and to measure the local stresses at the fatigue sensitive connection details. The instrumentation plan was developed based on FEA of the full-scale prototype model (refer section 3.4). Stresses were measured using surface mounted, encapsulated metallic, bonded or welded electrical resistance strain gauges. In addition, vertical displacement of the ribs, the inner FB and the deck plate were measured using linear variable differential transformers (LVDTs). The majority of the strain gauges were installed at the Rib 1-to-inner FB connection, on the inner FB web and the north and south walls of Rib 1. Strain gauges were also installed on the top and the bottom surfaces of the deck plate and the inner and the outer surfaces of rib wall of ribs 1, 2, 4 and 5. The strain gauges on the top and the bottom surfaces of the deck plate were concentrated near the deck splice and at the rib-to-deck plate connections. These two transverse sections are identified as X-X and Z-Z, which are at 2 ft. (610 mm) west and east of inner FB, respectively. Sections X-X and Z-Z coincided with the west and the east above-deck actuators, respectively. Gauges on the top surface of the deck plate were also installed at the centerline of inner FB identified as section Y-Y. The gauges on the inner and the outer surfaces of the rib wall were installed at section Z-Z abutting the rib-to-deck plate welds on either side of the ribs. Other strain

gauges were installed at: the soffit of Rib 1; the rib wall and sealing plate at the rib-to-sealing plate connection; the inner FB flange and the edge girder web near the edge girder-to-inner FB connection; the bottom flange of inner FB at section Y-Y; the splice plates and the stiffeners to the edge girder.

During the initial static tests, 106 uniaxial gauges of ¼ in. (6 mm) gauge length, 75 uniaxial gauges of 1 mm gauge length, 18 rosettes and 7 LVDTs were installed on the prototype deck, involving a total of 242 data channels. In addition, the load and the displacement outputs from the three actuator load cells were recorded in 6 data channels. During subsequent fatigue testing, the LVDTs were disconnected.

In this document, each channel associated with the instruments is identified by a number for reporting purposes. The channel number is denoted by the Arabic numeral such as 1, 2, 3, etc. Each element of the rosette is identified by a unique number.

4.4.1 Details of Sensors

Strain gauges of uni-axial and rosette configurations having different resistances and applicable temperatures were used. Gauges had either 1 mm or ¼ in (6 mm) gauge lengths. On the deck plate, both weldable and bondable uni-axial gauges were used. The strain gauges used on the inner FB web and the ribs were bondable and weldable uniaxial gauges and rosettes. The different types of strain gauges used were:

1. Vishay Micro Measurements LWK-06-W250B-350 uniaxial weldable gauges having 350Ω resistance and ¼ in. (6 mm) gauge length;
2. Texas Measurements FLA-1-11-1L uniaxial bondable gauges having 120Ω resistance and 1 mm gauge length; and
3. Texas Measurements FRA-1-11-1L stacked rosette (also called rectangular rosette)

bondable gauges having 120Ω resistance and 1 mm gauge length.

Prior to installation of strain gauges, the surface of the specimen was ground to bare steel at the strain gauge locations. The strain gauges were installed in accordance with the guidelines provided by the strain gauge manufacturers.

The LVDTs were Macro Sensors DC 750-1000, having a nominal displacement range of ±1 in. (±25 mm).

4.4.2 Instrumentation on Deck Plate

Forty five weldable uni-axial gauges of ¼ in. (6 mm) gauge length and 8 bondable uni-axial gauges of 1 mm gauge length were installed on the top and bottom surfaces of the deck plate (channels 163 to 215).

The strain gauges on the deck plate were installed primarily at the rib-to-deck plate connection, at section Z-Z (channels 163 to 180 and 191 to 207). The strain gauges were provided at ribs 1, 2, 4 and 5, both at the north and the south intersection of the rib walls with the deck plate, and were oriented in the transverse direction of the deck as detailed in Figure 123. The strain gauges were intended to capture the local out-of-plane bending at the rib-to-deck plate connection under wheel loads. At each intersection with the rib wall, two back-to-back strain gauges were provided on the top and the bottom surfaces of the deck plate adjacent to the rib-to-deck plate weld toe, outside the rib, to capture bending stress in the deck plate. Gauges on the bottom of the deck plate were of 1 mm gauge length to capture the peak localized strain due to steep stress gradient observed in FEA at the weld toe notch. These gauges were installed at a distance 0.5t or $^3/_8$ in. (9.5 mm) from the weld toe on the deck plate, where "t" is the thickness of the deck plate. Another uniaxial gauge of ¼ in. (6 mm) gauge length was installed on the bottom surface of the deck plate at 1.5t

or 1 1/8 in. (28.6 mm) from the weld toe on the deck plate. The rationale behind having gauges at 0.5t and 1.5t was to extrapolate the stress values from these two measurements to the weld toe as per the AASHTO recommendations. A uniaxial strain of ¼ in. (6 mm) gauge length was also provided on the top of the deck plate, within the projection of the rib, close to the root of the rib-to-deck plate weld. Due to the limitations posed by the fabrication of the requirements of closed rib orthotropic decks, the strain gauge at the bottom of the deck plate aligned with this gauge on the top surface could not be installed. The layout of the gauges on the deck at the intersection with a typical north wall of a rib is shown as Detail A in Figure 123. The layout of the gauges on the deck plate at the intersection with the south wall of a rib is similar to Detail A but handed. The gauges on the top of the deck plate were covered with mastic to protect it from getting damaged from the pounding effect of the load pads, as most of the gauges at the rib-to-deck plate connection were under the load pads. At each intersection with the rib, a pair of back to back strain gauges was also installed on the rib walls, abutting the rib-to-deck plate weld toe on the rib. These gauges were provided to capture the bending of the rib wall and are discussed in section 4.4.3 along with the instrumentation on ribs.

Uniaxial gauges of ¼ in. (6 mm) gauge length were installed in back-to-back configuration on the top and the bottom surfaces of deck plate on either side of the transverse CJP deck plate splice at section X-X, abutting the weld toes as shown in Figure 124 (channels 181 to 188 and 208 to 215). These gauges were oriented in the longitudinal direction of the deck plate, along the centerline of the south-west and the north-west load pads and were installed in the 1 in. (25 mm) gap between the load pads. On each side of the splice, the gauges were installed at a distance of 0.5t or 3/8 in. (9.5 mm) and 1.5t or 1

1/8 in. (28.6 mm) from the weld toes on the deck plate. The rationale behind having gauges at 0.5 t and 1.5 t has already been discussed earlier. The purpose of these gauges was to measure the high tensile and compressive stresses observed from FEA at the bottom and the top surfaces of the deck plate locally under the load pads due to longitudinal bending of the deck. The arrangement of the gauges in back-to-back configuration also allowed to determine the membrane stresses in the deck plate if any. The gauges on the top of the deck plate were covered with mastic to protect it from getting damaged from the pounding effect of the load pads

Three LVDTs were installed under the deck plate at section Z-Z, for measuring the vertical displacement of the deck (Figure 125). The LVDTs were attached to the soffit of the deck plate: between ribs 1 and 2 (channel 8); between ribs 3 and 4 (channel 10); and between ribs 4 and 5 (channel 12). Additional LVDTs were also installed at the same section on the soffit of the ribs, which are discussed in the following section along with instrumentation on ribs. The relative displacements between the LVDTs provided an assessment of deformation of deck plate with respect to the rib. Two uniaxial gauges (channels 189 and 190) of ¼ in. (6 mm) gauge length were installed on the top surface of the deck plate at section Y-Y, orientated along the transverse direction of the deck. These gauges were intended to capture the global transverse bending stress in the deck. Aligned with these gauges, uniaxial gauges were installed on the bottom surface of the inner FB flange, which will be discussed in section 4.4.4.

4.4.3 Instrumentation on Ribs

Thirty one uni-axial gauges of ¼ in. (6 mm) gauge length, 34 uni-axial gauges of 1 mm gauge length and 10 rosettes were installed on the rib walls (channels 68 to 162). Apart

from the gauges at the rib-to-floor beam and rib-to-deck plate connection, gauges were also installed on the inner surface of the rib walls at the connection with the sealing plates provided inside the ribs near the transverse deck splice.

3D FEA of the full bridge deck identified the rib 1-to-inner FB connection as the most fatigue critical. All the gauges on the Rib 1 wall at the junction with the inner FB were installed on the north and south walls symmetric with respect to the centerline of Rib 1, both to the east and the west sides of the rib (channels 68 to 137 in Figure 126). The figure shows the north wall of Rib 1. The channel numbers of the gauges installed on the south wall of Rib 1 are shown in parenthesis. Fatigue cracking at the weld toe is primarily attributed to the crack growth from the micro discontinuities at the weld toe subject to the stress range normal to the weld toe. FEA results showed that the maximum stress in the Rib 1 wall normal to the rib-to-floor beam weld toe occurred at a section of the rib wall at about 50° from the centerline of the rib soffit. So the weld toe at 50° was identified as the potential zone for fatigue cracking and it was decided to install gauges extensively at that location. Accordingly, a bondable rectangular rosette gauge of 1 mm gauge length was installed abutting the rib-to-floor beam weld toe on the rib wall at a distance of 0.4t or $^{1}/_{8}$ in. (3.2 mm) from the weld toe, to capture the complex stress distribution at that location and to determine the magnitude and direction of principal stresses at that location. One of the arms of the rosette was aligned normal to the weld toe. Due to the presence of steep stress gradient close to the weld toe, it was needed to capture the peak localized strains to have the correct stress distribution normal to the weld toe along the 50° radial line. Accordingly, a uniaxial gauge of 1 mm gauge length was installed on the rib wall next to the rosette, at t or $^{5}/_{16}$ in. (8 mm) from the weld toe measured normal to the weld toe on the

rib. The uniaxial gauge was oriented normal to the weld toe. The rationale behind having gauges at 0.4t and t was to extrapolate the stress values from these two measurements to the weld toe. In order to get the complete distribution of stress normal to weld toe along the 50° radial line, three more uniaxial gauges of ¼ in. (6 mm) gauge length were installed at a distances of 1 in. (25 mm), 2 ½ in. (63 mm) and 4 in. (102 mm) respectively, oriented normal to the weld toe on the rib. The stress obtained from the gauge measurements at 4 in. (102 mm) from the weld toe was essentially the nominal stress on the rib wall due to global longitudinal bending of the rib, free from the notch effect of the weld toe. Gauges were also installed in identical pattern along the 25° radial line and also at the soffit of Rib 1. Though 50° was the location of highest stresses normal to the weld toe, weld root at 25° was identified from FEA as the location of maximum principal stress. Maximum principal stress is critical for crack growth from volumetric discontinuities as was observed from the fatigue tests of small-size mockups (NJDOT Project Report, 2015). However, it is not possible to measure the stress at weld root with the available technology. So, gauges were installed along 25° radial lines and also at the rib soffit to capture the entire stress distribution at the weld toe near the rounding of Rib 1 wall at the junction with inner FB.

As discussed in the previous section and shown in Figure 123, strain gauges were installed on the deck plate and the rib wall at the rib-to-deck plate welds of ribs 1, 2, 4 and 5, at the transverse section Z-Z. The strain gauges (channels 138 to 141 and 146 to 158) were installed on both inner and outer faces of the rib wall in back-to-back configuration and were oriented along the inclined depth of the rib wall. The inside strain gauges were installed at $^{13}/_{32}$ in. (10 mm) from the weld root. High temperature resistant weldable strain gauges of ¼ in. (6 mm) gauge length were installed on the inner face of the rib wall to

avoid damage to the strain gauges from the high heat produced during welding of the rib to the deck plate. However, all the gauges on the inner surface of the rib walls were damaged during the rib-to-deck weld fabrication. On the outer surface of the rib wall, uniaxial gauges of 1 mm gauge length were installed at distances of at 0.5t or $^{5}/_{32}$ in. (4 mm) and 1.5t or $^{15}/_{32}$ in. (12 mm) from the weld toe on the deck plate. The rationale behind having gauges at 0.5 t and 1.5 t has already been discussed earlier. The purpose of the strain gauges on the ribs walls was to measure the out-of-plane bending of the rib wall under wheel loads and the high compressive stress which was observed from FEA at the weld toe on the ribs due to localized bending of the rib-to-deck plate connection under the wheel loads.

Gauges were installed on the inner surface of north and south walls of ribs 1 and 5, adjacent to the rib-to-sealing plate connection (channels 142 to 145 and 159 to 162 in Figure 127). Gauges were installed only for the sealing plate towards the inner FB. These gauges were installed at High Steel facility (Figure 128). It was observed from FEA that the stress normal to the weld toe was maximum at 60° from the rib soffit. So, uniaxial gauges of 1 mm gauge length were installed at distances of 0.5t or $^{5}/_{32}$ in. (4 mm) and 1.5t or $^{15}/_{32}$ in. (12 mm) from the weld toes on the ribs, along 60° radial lines. These gauges were oriented along the longitudinal direction of the deck.

Three LVDTs were installed on the soffit of the ribs 1, 2 and 4 at section Z-Z. The LVDTs were identified as: channel 7 on Rib 1; channel 9 on Rib 2; and channel 11 on Rib 4.

4.4.4 Instrumentation on Floor Beam

Among the three floor beams, only the inner FB around which the loads were

positioned, was instrumented with strain gauges. In total, 7 uni-axial gauges of ¼ in. (6 mm) gauge length, 23 uni-axial gauges of 1 mm gauge length and 8 rosettes were installed on the inner FB (channels 14 to 67). Strain gauges on the inner FB were primarily installed at the connection with Rib 1, symmetrically on the north and south sides of the rib as shown in Figure 129. The strain gauges were installed in back-to-back configuration on the east and the west faces of the floor beam web to measure the in-plane membrane and out-of-plane bending stress components. Figure 129 shows the east face of the floor beam, and the channel numbers of the gauges installed on the west face are shown in parenthesis. Additional strain gauges were installed on the top and bottom faces of the inner FB bottom flange at the connection with edge girder and on the bottom face of the bottom flange at section Y-Y.

FEA of the full bridge deck showed that a diagonal tension field developed from the bottom flange of the of the floor beam to the top corner formed by the floor beam web and the edge girder. As the stress field deviated around the cutout in the floor beam web, high stress concentration was observed at the Rib 1-to-inner FB weld toe, which was further elevated by the weld toe notch. As such, the Rib 1-to-inner FB weld toe around the rib rounding was identified as the most critical for fatigue cracking. Fatigue cracking at the weld toe is primarily attributed to the crack growth from the micro discontinuities at the weld toe subject to the stress range normal to the weld toe. Similar to Rib 1, FEA results showed that the maximum stresses in the inner FB web normal to the rib-to-floor beam weld toe on the floor beam web occurred at a section at about 50° from the centerline of the rib soffit. So, the weld toe at 50° was identified as the potential zone for fatigue cracking and it was decided to install gauges extensively at that location. A bondable rosette gauge

of 1 mm gauge length was installed abutting the rib-to-floor beam weld toe on the floor beam web at a distance of 0.4t or $^1/_5$ in. (5 mm) from the weld toe, to capture the complex stress distribution at that location and to determine the magnitude and direction of principal stress at that location. One of the arms of the rosette was aligned normal to the weld toe. Due to the presence of steep stress gradient close to the weld toe, it was needed to capture the peak localized strains to have the correct stress distribution normal to the weld toe along the 50° radial line. So, a uniaxial gauge of 1 mm gauge length was installed on the floor beam web next to the rosette, at t or $^1/_2$ in. (13 mm) from the weld toe measured normal to the weld toe on the floor beam, where "t" is the thickness of the floor beam web. The uniaxial gauge was oriented normal to the weld toe. The rationale behind having gauges at 0.4t and t was to extrapolate the stress values from these two measurements to the weld toe. In order to get the complete distribution of stress normal to weld toe along the 50° radial line, another uniaxial gauge of 1 mm gauge length was installed at a distance of 1.5t or ¾ in. (19mm) from the weld toe, oriented normal to the weld toe on the floor beam. Gauges were also installed in the identical pattern along the 25° radial line. Though 50° was the location of highest stresses normal to weld toe at the rib 1-to-inner FB connection, weld root at 25° was identified from FEA as the location of maximum principal stress. Maximum principal stress is critical for crack growth from volumetric discontinuities as was observed in the fatigue tests of small-size mockups. However, it is not possible to measure the stress at weld root with the available technology. Accordingly, gauges were installed along the 25° radial lines to capture the entire stress distribution on the floor beam web along the rounding of Rib 1-to-inner FB connection. Uniaxial gauge of 1 mm gauge length was installed on the east and west faces of the floor beam web at the rib soffit,

oriented along the tangent to the weld toe at a distance of 0.4t or $^1/_5$ in. (5 mm) from the weld toe. The stress normal to the weld toe was almost zero at the soffit of the rib as observed from FEA, so gauge was oriented along tangent to measure the circumferential stress at that location.

Uniaxial gauges were also installed on the inner FB flange at the connection with the edge girder web and are shown in Figures 130 and 131 (channels 56 to 65). Gauges were installed on the top and the bottom surfaces of the floor beam flange. On the top surface, gauges were installed at two sections, 1 in. (25.4 mm) on either side of the centerline of the inner FB web. Gauges on the bottom surface were installed at three sections, one section at the centerline of the inner FB web and other two sections at 1 in. on either side of the centerline of the inner FB web. Gauges were oriented along the transverse direction of the deck. At all the sections, a uniaxial gauge of 1 mm gauge length was installed at a distance of 0.5t or $^3/_8$ in. (9.5 mm) from the weld toe on the flange, where "t" is the thickness of the inner FB flange. Another uniaxial gauge of ¼ in. (6 mm) gauge length was installed next to the 1 mm gauge at a distance of 1.5t or 1 $^1/_8$ in. (29 mm) from the weld toe on the flange.

Additional uniaxial gauges of ¼ in. (6 mm) gauge length were installed on the bottom flange of the inner FB at section Y-Y. The gauges are shown in Figure 132 (channels 66 and 67). The gauges were oriented along the transverse direction of the deck and were installed at two sections, one section centrally between ribs 1 and 2 and the other section centrally between ribs 4 and 5. These gauges were aligned with gauges on the top of the deck plate. The purpose of these two gauges was to measure the bending stress in the floor beam flange due to global transverse bending of the deck. A LVDT (channel 13) was also

installed at the bottom of the floor beam flange aligned with the centerline of Rib 3, to measure the vertical displacement of the inner FB.

4.4.5 Instrumentation on Edge Girder

Two uniaxial gauges of ¼ in. (6 mm) gauge length were installed on the north face of edge girder web aligned with the centerline of the inner FB. The gauges shown in Figure 131 (channels 230 and 231) were oriented along the depth of the web. High stress concentration was observed in FEA at the weld toe on the edge girder web at the edge girder web-to-edge girder bottom flange connection due to the applied upward displacement by the under-deck actuator. Accordingly, gauges were installed at distances of 0.5t or $^{9}/_{32}$ in. (7 mm) and 1.5t or $^{27}/_{32}$ in. (21 mm) from the weld toe on the web, so that the stress at the weld toe can be obtained by extrapolating from these two measurements following AASHTO recommendations.

4.4.6 Other Instrumentation

4.4.6.1 Instrumentation on Splice Plates

Uniaxial gauges of ¼ in. (6 mm) gauge length were installed on the north and the south side splice plates of ribs 1, 2 and 4 at section X-X and are shown in Figure 133 (channels 216 to 221). The gauges were oriented along the longitudinal direction of the deck.

Uniaxial gauges of ¼ in. (6 mm) gauge length were also installed on the north and south side web splice plates of the edge girder web at section X-X (channels 232 to 235 in Figure 133). The figure shows the south side splice plate; the channel numbers of the gauges installed on the north side splice plate are shown in parenthesis. Another uniaxial

gauge of ¼ in. (6 mm) gauge length was also installed at the surface of the bottom splice plate of the edge girder flange at section X-X (channel 236 in Figure 133). The gauges were oriented along the longitudinal direction of the deck

The purpose of these gauges was to capture the pure bending stress at the transverse splice section due to the longitudinal bending of the deck.

4.4.6.2 Instrumentation on Sealing Plates

As discussed in section 4.4.3, the maximum stress normal to the weld toe of the rib-to-sealing plate connection was observed at 60° from the rib soffit and on the sealing plate towards the inner FB. So, a uniaxial gauge of 1 mm gauge length was installed on the surface of the sealing plate towards the splice at ribs 1 and 5, at a distance of 0.5t or $^{3}/_{16}$ in. (5 mm) from the weld toe both at the north and the south walls of the ribs. Another uniaxial gauge of ¼ in. (6 mm) gauge length was installed next to the 1 mm gauge at a distance of 1.5t or $^{9}/_{16}$ in. (14 mm). The rationale of having gauges at 0.5t and 1.5t has already been discussed earlier. All these gauges were oriented along the 60° radial line normal to the weld toe on the sealing plate. The gauges are shown in Figure 127 (channels 222 to 229). These gauges were installed at High Steel facility.

4.4.6.3 Instrumentation on Transverse Stiffener to the Edge Girder

Uniaxial gauges were installed on the east and the west faces of the transverse stiffener provided at the south face of the edge girder web at the edge girder-to-inner FB connection. The gauges are shown in Figure 131 (channels 237 to 246). These gauges were installed near the longitudinal stiffener-to-transverse stiffener weld toe and the transverse stiffener-to-edge girder flange weld toe on the transverse stiffener. The gauges were oriented along the depth of edge girder web. At each weld toe, a uniaxial gauge of 1 mm

gauge length was installed at 0.5t or $^{5}/_{16}$ in. (8 mm) from the weld toes, where "t" is the thickness of the transverse stiffener. Another uniaxial gauge of ¼ in. gauge length was installed next to the 1 mm gauge at 1.5t or $^{15}/_{16}$ in. (24 mm) from the weld toes. The reason behind having gauges at 0.5t and 1.5t has already been explained earlier.

4.4.7 Data Acquisition

Data were collected using programmable digital data loggers manufactured by Campbell Scientific Inc. (CSI). The data loggers were provided with analog input cards (CR 9050 and CR 9051), which processed the output signal from the instruments. The processed signals were then stored in a removable memory card and could be downloaded to a permanent storage. Each analog card could accommodate 126 data channels, where each data channel was a quarter Wheatstone Bridge circuit. For the crawl tests and the initial static tests, two model CR9000 data loggers (identified as NJ_DAQ_1 and NJ_DAQ_2), and one model CR5000 data logger (identified as NJ_DAQ_3) were used. For the subsequent static and fatigue tests, only two CR9000 data loggers (NJ_DAQ_1 and NJ_DAQ_2) were retained, as the LVDTs connected to NJ_DAQ_3 were disconnected. A model CR1000 data logger was also used during the fatigue test which recorded the load outputs from the above-deck actuator load cells and the trigger from the actuator controller (see section 4.6.4). The data output from this logger was used to send automated email to the research team in case the load level in the above-deck actuators was below 3 kip or the test was shut down (trigger voltage was below 2.5 mV).

The inline load cells of the actuators (see section 4.6.3) were also connected to the data logger.

For the crawl tests and the static tests, data was sampled at a frequency of 10 Hz

and averaged over one second (i.e. 10 samples) before recording on the memory card. For the fatigue test, the data was collected at a frequency of 10 Hz without averaging. The analog cards did not have any real time filtering capabilities. To reduce noise and spurious signal in collected data, the settling time was set at 100 μsecs and the integration time was set at 670 μsecs. The settling time is the time taken for the input channel to settle to its new value when switched between the channels and a change in signal occurs. The integration time is the time over which the input signal is averaged to reduce the noise caused due to random fluctuations in the signal.

4.5 Crawl Tests

Three types of tests were performed on the prototype deck: crawl tests, static tests and fatigue test. The crawl tests involved rolling a bogie (test truck) representing the AASHTO tandem axle, as shown in Figure 134, across the deck at a very slow speed to determine the response of the deck elements under a moving load. The crawl tests were conducted for three transverse positions to assess the response of the deck under different disposition of the wheel loads. During the subsequent static tests, however, it was realized that the west support column was not fully fastened to the laboratory floor, and the resulting flexibility affected the global deformation of the specimen and invalidated the crawl test results. Since, the overhead loading fixtures were already installed for the static and the fatigue tests, repeating the crawl tests would have required disassembling the overhead loading fixtures for providing access for the crawl truck. To avoid delay and additional efforts, it was decided to proceed with the static and fatigue. The crawl tests were repeated after completion of the fatigue test. .

4.5.1 Test Truck

The test truck (Figure 134) represented the rear axles of a tractor-trailer in tandem configuration according to the fatigue loading for orthotropic decks provided in the AASHTO LRFD BDS, 6th edition. The truck consisted of two axles attached to a 12 ft. (4.4 m) long and 3 ft. 5 in. (1.0 m) wide steel frame made of beam sections for supporting steel billets (weight). In the longitudinal or the rolling direction, the axles were spaced at 4 ft. (1.2 m.). A pair of wheels was attached at each end of each axle. In the transverse direction, the center-to-center distance between the wheel pairs at the ends of each axle was 6 ft. (1.8 m.) Each wheel was fitted with retreaded truck tires pressurized to about 90 psi (620.5 kPa). The truck was loaded with four steel billets. The combined weight of the truck and the four billets was 53.7 kip (238.9 kN), which was about 2.2 times the rear axle load of 24 kip (106.8 kN) for the AASHTO notional fatigue truck. For verification of infinite life, however, the fatigue testing of the deck was performed under a gross tandem axle weight of 82.8 kip (368.3 kN), which was 3.45 times the AASHTO notional fatigue truck. Thus, the crawl test loading was about 65% of the fatigue limit state loading.

4.5.2 Test Positions

The crawl tests were conducted for three transverse positions as shown in Figures 135 to 137. The transverse positions were chosen to simulate different shear spans of the floor beam, at the floor beam-to-box girder connection, creating different stress concentration at the rib-to-floor beam connection. In addition, the transverse load positions also covered the critical response of the deck components in the transverse direction. The truck was positioned such that either one wheel or both wheels of the left wheel pair was located symmetrically between the ribs, on a rib wall, or over a rib. These placements of

the left wheel pair also resulted in dispositions of the right wheel pair, where the deck plate over the ribs or between the ribs was loaded in different configurations. As a result, the deck plate and the ribs, whose responses are driven by local effects of individual wheels, were subjected to several different load conditions, where the wheels (tire contacts) were positioned partially or fully between the rib walls, or on the rib walls. These load positions several critical stress states in the deck plate, the rib walls and rib-to-deck plate connections.

4.5.3 Test Procedure

The test truck was pulled by a manually operated hydraulic winch and cable system that was reacted against the deck. A guide truss (Figure 138) along the length of the deck was used underneath the test truck to guide the truck in a straight line on a transverse position. The top and bottom chords of this guide truss employed 6x6x$^{3}/_{4}$ angles and the diagonal members used 2 x 2 x $^{3}/_{8}$ in. (51 x 51 x 10 mm) angles. Brackets were provided at the ends of the guide truss, which were used to clamp the truss to the deck and also to support the hydraulic winch on the west end and a pulley on the east end (Figure 138). The test truck was rolled in the east to west (i.e. forward) and west to east (i.e. reverse) directions for each position. For the forward roll, the cable was connected to the truck and hydraulic winch via the pulley. For the reverse roll the cable was directly connected to the truck and hydraulic winch.

The following procedure was adopted for crawl tests in each transverse position. The guide truss was positioned on the deck at the desired position. The south end of the inner FB was displaced upward by 0.045 in. (1 mm) by using the under-deck actuator. This value of displacement was determined from FEA of GM and SM. The test truck was lifted

on the deck using the overhead crane and aligned with the guide truss at the east end of the deck. The steel billets were lifted and placed on the truck one at a time in the sequence as shown in Figure 134. The steel rope from the winch was pulled along the truss and through the pulley on the north end and hooked onto the underside of the truck. The truck was pulled across the deck for a fixed distance of 18 ft. 9 in. (5.7 m), which was the maximum available distance for the truck to roll. The roll distance was not equal on either side of the inner FB due to space restrictions for accommodating the truck at the ends of the deck. The roll distances were 10 ft. 9 in. (3.3 m) and 8 ft. (2.4 m) to the east and the west of inner FB respectively. During the roll of the truck, the displacement given by the under-deck actuator was varied along the length of the roll. The displacements for different positions of the truck was determined from the FEA of GM and SM. The displacement profile was identical for all the transverse positions and is shown in Figure 139. The time taken by the truck to cover the distance was noted using a stop watch. The steel rope was hooked to the truck directly for the reverse roll. The truck was reverse rolled the same distance and the time taken for the reverse roll was measured using the stop watch. The average speed maintained for the crawl test in every transverse position was about 0.08 mph (1.2 km/h). Once the reverse roll was completed, the truck was disconnected from the winch, the billets were unloaded one by one, and the truck was taken off the deck. The under deck actuators were returned to zero position, and the procedure was repeated for the next transverse position.

As explained in section 4.4.7, the crawl test data was sampled at a frequency of 10 Hz and averaged over one second (i.e. 10 samples) before recording on the memory card. For each transverse position, the strain gauges and the LVDTs were zeroed before placing the truck and billets on the truss and giving initial displacement. The sensors were zeroed

to remove any offsets caused due to the electrical characteristics of the system. Data collection was started as soon as the sensors were zeroed. The collection of the data was stopped after the crawl test was completed, the truck was lifted off the deck, and the under deck actuator was returned to zero position.

4.6 Static and Fatigue Tests

4.6.1 Loading

The rib-to-floor beam connection detail of the proposed deck design needed to be verified for infinite fatigue life or Fatigue I Limit State according to AASHTO LRFD BDS, 6th edition. Thus the above-deck actuators, each representing one axle of the rear tandem, was cycled between a minimum of 5 kip (22.2 kN) and maximum of 46.4 kip (206.4 kN), resulting in a load range of 41.4 (184.2 kN) or a total load of 82.4 kip (368.4 kN) at the two actuators. The under-deck actuator was displaced upward synchronously with the above-deck actuators, between 0.0121 in. (0.3 mm) and 0.1121 in. (2.8 mm), corresponding to the minimum and the maximum loads respectively, resulting in a displacement range of 0.1 in. (2.5 mm). The minimum load was maintained to simulate dead load effects and to avoid loss of contact between the loading pads and the deck during tests.

4.6.2 Loading Arrangement

The above-deck actuators were installed on the deck (Figure 140) to simulate the most critical disposition of the tandem axle as determined from the FEA of the GM. The two above-deck actuators were placed symmetrically 2 ft. on either side of the inner FB (Figure 95) to simulate the symmetric load position, resulting in a 4 ft. spacing between the two actuators following the AASHTO specifications. As discussed earlier, the load

from each actuator was distributed through a spreader beam into two rectangular load pads (simulating the wheel contact with the deck plate) 10 in. long (254 mm) and 20 in. (508 mm) wide, spaced 6 ft. (1.8 m) apart in transverse direction (according to AASHTO LRFD BDS). In the transverse direction, the south side load pads were placed centrally between ribs 1 and 2 adjacent to the edge girder to simulate the most critical transverse disposition of the tandem axle.

The under-deck actuator, which was used to simulate the global displacement boundary condition, was floor mounted and aligned with the centerline of the inner FB at the south end of the deck.

4.6.3 Hydraulic Actuator

The above-deck actuators were Hannon 5110 with a maximum load rating of 110 kip (490 kN). These actuators were double acting fatigue rated and had a total stroke of 10 in. (254 mm).

The under-deck actuator was Lynair H-B1003, which had a maximum load rating of 220 kip (980 kN). The actuator had 10 in. (254 mm) diameter rod with a 6 in. (152 mm) stroke.

Hannon 5110 actuators had inbuilt LVDTs with a measuring range of ± 10 in (254 mm) and for Lynair H-B1003 actuator, external LVDT with a measuring range of ±3 in. (76 mm) was used to measure the displacement of the actuator.

The load applied by the above-deck actuators were measured using Lebow 3129-112 fatigue rated load cells whose maximum load rating is 150 kip (668 kN). The load feedback in the under-deck actuator was measured by Lebow 3129-112 load cell with a maximum load rating of 220 kip (979 kN).

All the actuators were fitted with Vickers SM-440 servo hydraulic valves, which regulated the flow of hydraulic oil in and out of the actuator. To regulate the flow between the pump and the actuators two hydraulic service manifolds (HSM) were used. The above-deck actuators were assigned to one HSM and the under-deck actuator was assigned to the second HSM.

4.6.4 Actuator Controller

The actuators were controlled by a MTS Flextest 100 digital controller. The controller had a capability of controlling nine actuators (channels) and two hydraulic service manifolds (HSM) simultaneously. The above-deck actuators were operated under load control. The displacements of these actuators were monitored. The under-deck actuator was operated under displacement control, with the load monitored. A haversine wave-form was used as command for all actuators.

4.6.5 Loading Protocol

The loading protocol was defined as follows. Initially, the two above-deck actuators applied a minimum load of 5 kip (22.2 kN). Subsequently, the above-deck actuators cycled between the minimum load and a maximum load of 46.4 kip (206.4 kN). In each loading step, the under-deck actuator applied a displacement corresponding to the global vertical displacement boundary condition. In the initial load step the under-deck actuator was displaced upward by 0.0121 in. (0.3 mm). Subsequently, the under-deck actuator was cycled between this minimum and maximum upward displacement of 0.1121 in. (2.8 mm).

4.6.6 Test Procedure

Static tests were performed prior to initiating the fatigue test and intermittently

during the fatigue test. These so called “static tests” followed the same sequence as the fatigue test, but was conducted at a slow (or almost static) loading rate. The loading and displacement protocols for static tests is shown in Figures 141 and 142 respectively for the above-deck and the under-deck actuators. During the static tests the load at each actuator was changed between the minimum and the maximum value in 5 seconds and the loads were held at load step 1 for 10 seconds. The first static test was conducted prior to initiating the fatigue test to determine the base sate of the structure. Subsequent static tests were conducted at regular time interval to determine the change in state of the deck in terms of the measured stresses at the strain gauges. The static test results are discussed in detail in Chapter 6.

The fatigue testing of the prototype deck was performed by repeated application of the loading sequence as discussed under the loading protocol. The loading and displacement protocols for the fatigue test is shown in Figures 143 and 144 respectively for the above-deck and the under-deck actuators. Initially, the fatigue test was run at 1 Hz frequency for about 400,000 cycles. Subsequently the test frequency was increased to 2 Hz, when stability of the test could be ensured. The test was conducted uninterrupted 24 hours a day and seven days a week, except for interruptions due to routine checks, maintenance or significant events. To verify infinite life fatigue performance, the prototype deck was tested for 8 million load cycles without any fatigue cracking. The fatigue test results are discussed in Chapter 6.

4.6.7 Inspection Regimen

The specimen was inspected for possible fatigue cracking regularly at an interval of 4 hour with the exception during night time when the last inspection for a day was at

10:30 PM while the first inspection for the next day was at 7:00 A.M. The inspections were aided with 10X magnifying glass. The inspection plan is shown in Figure 145. The critical areas of the deck: Rib 1-to-inner FB connection; rib-to-deck welds at the loaded section; CJP deck splice at the loaded section and the edge girder-to-inner FB weld were inspected at every four hour interval. The complete prototype deck was inspected once every day during fatigue testing. After 5 million cycles, the guide truss for the load pads was removed, the area on the deck plate in the loaded area was cleaned, and the deck plate underneath the load pads was inspected for any fatigue cracking. Subsequent to this inspection, deck plate underneath the load pads was inspected at every 1 million cycle till the termination of the test at 8 million cycles.

5 POST-TEST DESTRUCTIVE EVALUATION

Subsequent to fatigue testing, a few representative rib-to-floor beam and deck plate splice details were destructively evaluated to determine the as-fabricated condition, and any evidence of fatigue cracking that could not be detected by visual inspection. The rib-to-floor beam details were extracted from the Rib 1-to-inner FB welded connection. The splice details were extracted from the transverse CJP deck splice: (a) over the rib wall; (b) under south-west load pads between ribs 1 and 2; and (c) under north-west load pads inside Rib 4. The location of the sections are discussed in the following sections.

5.1 Rib-to-Floor Beam Weld

Multiple macro-etched cross sections of Rib 1-to-inner FB connection were prepared at discreet locations, and detailed measurements of the welds were made at each section to compare the fabricated conditions with the specified connection detail. Statistical estimates of the as-fabricated weld geometry were determined from these measurements.

The rib-to-floor beam sections are identified by the specimen identification (FS for full-scale prototype) suffixed by the side of the connection (e.g., N for North and S for South) and then suffixed by the location of the section measured in degree from the rib soffit at the centerline (e.g., 25 and 50). For identification of the sections at the intersection with rib-to-deck plate weld, section location is replaced by “C” which is abbreviation for corner. Total 6 cross sections were prepared with 3 sections on each side of the connection. The sections are shown in Figure 146.

The rib-to-floor beam weld sections were etched with 5% Nital. The macro-etched sections were then digitally photographed. The dimensional parameters of the rib-to-floor beam weld were measured from the digital photographs of the macro-etched sections as

described in the following. The photographs were imported into AutoCAD 2014 (Autodesk, Inc.). The nominal floor beam thickness was considered as the basis for the measurement. A scaling factor was computed as the ratio of the nominal floor beam thickness to the floor beam thickness measured from the digital photographs in AutoCAD. The other measured dimensional parameters were multiplied with this scaling factor to obtain the respective sizes. The dimensional parameters are shown in Figure 147. The measured dimensional parameters were: (a) the lack of fusion of the weld, *LOF* and (b) the root opening or fit-up gap between the rib and the floor beam, *R*.

The macro-etched sections of the rib-to-floor beam welds are shown in Figures 148 to 153. The destructive weld measurements on the macro-etched sections are tabulated in Table 1. The value of R ranged between 0.012 in. and 0.18 in. (~$^{3}/_{16}$ in.), with a mean of 0.068 in. (~$^{1}/_{16}$ in.) and a large COV of 94.5%. Such large COV can be expected considering the small magnitude of R. Out of 6 sections, the R value in 4 sections were less than the specified maximum of $^{1}/_{16}$ in. (2 mm). Large values of R were noted at sections FS_N_C and FS_S_C. These sections were at the intersection with the rib-to-deck plate weld. The LOF showed a much lesser variance (COV of 18.8%), with a mean of 0.374 in. (10 mm), or mean fusion of about 25%. Such small fusion or large LOF is typical of fillet welded connections. The weld profiles were typical of manual fillet welds with large LOF. At the rib-to-deck plate and the rib-to-floor beam intersections, however, the weld profiles were questionable.

5.2 Transverse CJP Weld at Deck Splice

As discussed earlier in section 4.4, rejectable indications were noted during UT of the CJP deck plate splice weld. This CJP weld was non-destructively evaluated after the

fatigue test using Phased Array Ultrasonic Testing (PAUT). The purpose of the PAUT was: to evaluate the quality of the weld; to compare with the UT results; and to check the efficacy of a PAUT protocol developed by the author (Mukherjee 2015) in determining flaws in the CJP deck weld. After PAUT multiple macro-etched cross sections of the connection detail were prepared at discrete locations and compared with the non-destructive evaluations.

5.2.1 PAUT Evaluations

Continuous scanning capability of PAUT was utilized in evaluating the CJP deck weld. The total 12 ft. (3.7 m) length of the weld was divided into 12 segments of 1 ft. (305 mm) each, and each segment was scanned continuously as shown in Figure 154. The scanning was started from the south edge of the specimen and continued towards the north edge.

The schematic of the scanning setup is shown in Figure 155. The scanning assembly consisted of an Olympus 10L32-A1 (10 Hz frequency) probe mounted on a SA1-N60S shear wave wedge. The probe had 32 elements, however only 16 elements could be used at a time due to the limitation of the scanning equipment. An encoder was also connected to the probe-wedge assembly for recording the scan position along the scanning direction.

The scan setup in the laboratory is shown in Figure 156. The probe was mounted normally on the wedge and wedge was placed on the deck plate. The attached encoder was rolled in the scanning direction, along an angle guide clamped on the deck. The probe-wedge assembly was placed as close to the weld toe as possible, which resulted in a distance of $2\ ^{19}/_{32}$ in. (66 mm) from the center of the weld to the back of the wedge. A guide was placed at the back of the wedge so that the wedge remained at the fixed distance during the scanning. The probe-wedge assembly and the encoder were connected to Olympus

MX1 equipment which was used for performing the scan and recording the data.

The parameters used for scanning are listed in Table 2. Sectorial scans were performed to obtain the full coverage of the weld, and the sound beam was swept through a range of angles from 45° to 75° with an angle step of 0.2°. The scan resolution was 0.05 in. (1.3 mm) i.e. data was collected at every 0.05 in. (1.3 mm) distance.

The wedge was slid along the deck plate in the scanning direction (parallel to the weld) and the encoder rolled along the vertical leg of the angle recording the distance of travel. Tension was maintained in the encoder wire during the scanning for proper functioning of the encoder, by pressing the probe-wedge assembly against the deck plate while performing the scan. Scanning was performed for a 60 dB gain.

5.2.2 Comparison between UT and PAUT Evaluations

Figure 157 shows the flaw zones (identified as red rectangles) for both UT and PAUT. The vertical scale is exaggerated compared to the horizontal scale to make the CJP weld wider. The two results showed good correlation, except PAUT detected more flaw zones than UT. PAUT being a more advanced technique than UT, it is expected for PAUT to detect more flaw zones as compared to UT. As it can be seen, the flaw zones were distributed over the entire length of the weld, suggesting that the quality of the CJP weld was questionable.

Figure 158 shows the extent and depth of the flaws inside the weld for both PAUT and UT. As is evident, the PAUT and the UT results showed good correlation, however PAUT detected more flaw zones. At certain locations, the extent of the flaws were comparable between UT and PAUT, but their depths were different. PAUT has much finer resolution than UT and it is expected for PAUT to detect very small difference in depths.

5.2.3 Destructive Evaluation

Seven cross sections of the CJP deck weld were produced, polished and etched to destructively evaluate the quality of the weld and to measure the depth of the flaws and compare with the non-destructive evaluations. The cross-sections were identified by an Arabic numeral from north to south starting at 1 (Figure 159). Sections 1 and 2 were over the south and north walls of Rib 1 respectively. Sections 3, 4 and 5 were under the south-west load pads between ribs 1 and 2. Section 6 was over the north wall of Rib 3 and section 7 was under north-west load pads inside Rib 4. The weld sections were etched at with 5% Nital and were then digitally photographed.

5.2.4 Comparison of Destructive and Non-Destructive Evaluations

The comparison between the destructive and non-destructive measurements are tabulated in Table 3 in terms of the depth of the flaws from the deck plate surface. The PAUT results matched the destructive measurements very well, further verifying the efficacy of PAUT over conventional UT.

The macro-etched section 1 is shown in Figure 160. No lack of fusion (LOF) was observed in the cross section of the weld. However, an undercut was created on the deck plate at the splice root face while performing the overhead repair weld. This undercut appeared as an indication during PAUT (Figure 161).

The macro-etched section 2 is shown in Figure 162. A lack of fusion was observed in the cross section of the weld that existed in the original submerged arc welding process, and was not fully fused by the overhead repair weld pass. The LOF showed a strong indication during PAUT scanning (Figure 163).

Similar to section 2, multiple LOF were observed in sections 3, 4, and 5 (Figures 164, 166, and 168 respectively), which appeared as strong indications during PAUT (Figures 165, 167, and 169 respectively).

Similar to section 1, undercuts were noted in sections 6 and 7 (Figures 170 and 173 respectively). The notch like undercut can be clearly seen at the weld root in Figures 171 and 174 respectively, which appeared as strong indications during the PAUT (Figures 172 and 175 respectively).

5.2.5 Assessment of Results

The developed PAUT protocol successfully detected the weld flaws and proved its efficacy over conventional UT. Although an AASHTO detail category is compromised from C to D while leaving the backing bar in place, still it should be adopted following the existing practices in United States, considering the ease of fabrication and for reducing the probability of these flaws at the weld root. Despite the flaws, the CJP deck plate weld splice in the prototype deck, however didn't exhibit any fatigue cracking after 8 million cycles of testing,. It should be noted that the prototype deck is a single data point for this type of CJP deck weld fabrication, and should not considered as a general representation of the performance of this connection.

6 EVALUATION OF TEST RESULTS

6.1 Results of Static Tests

At the onset, a static test was performed before initiating fatigue testing on the deck specimen. Three static test trials were conducted for the shakedown of residual stresses and for ensuring repeatability of the test results. The results of only the final trial are presented here. During fatigue testing, intermittent static tests were performed at about every million load cycles, or following any significant event, to evaluate the change in state of the structure.

During the initial static tests, 106 uniaxial gauges of ¼ in. (6 mm) gauge length, 75 uniaxial gauges of 1 mm gauge length, 18 rosette gauges of 1 mm gauge length and 7 LVDTs were installed on the prototype deck, involving a total of 242 data channels (as discussed in section 4.4). In addition, the load and displacement outputs from the three actuators were recorded in six other data channels. Subsequently, the LVDTs were disconnected during the fatigue testing and intermittent static tests. All other gauges were retained, except gauges on the top of the deck plate got damaged during the course of the fatigue testing. All measurements were conducted within the nominal elastic range of the material. The strains measured at the uniaxial gauges were converted to stresses by multiplying with the accepted modulus of elasticity for steel of 29,000 ksi ($2x10^5$ MPa). For the rosettes, the strains measured at the rosette arms were used to determine the principal and the directional stresses at the rosette locations. The relevant static test results are discussed in this chapter. For further details, please refer to Roy and Mukherjee (2015).

6.1.1 Global Response of Prototype Deck

The global response of the prototype deck is discussed in this section in terms of the measurements at the sensors on the deck at sections Y-Y and Z-Z. Uniaxial strain gauges, oriented along the transvers direction of the deck, were installed on the top surface of deck plate and at the bottom of inner FB at section Y-Y. An LVDT was also installed at the soffit of the inner FB at section Y-Y. At section Z-Z, LVDTs were installed on the soffit of the ribs and at the underside of the deck plate in between the ribs. Uniaxial strain gauges, oriented along the transverse direction of the deck were also installed on the top and the bottom surfaces of the deck plate at section Z-Z.

The static test results are presented as plots of strain gauge and/or LVDT measurements along sections Y-Y and Z-Z, against the distance measured from the south end of the deck. The measured quantities (stresses or displacements) are presented on the Y-axis or the ordinate, and the distance from the south end along the section on the X-axis or the abscissa. Also shown on the plots are: the plan of the deck with the section identified; the increasing direction of abscissa; and the pertaining transverse section of the deck with the instrument location and critical load position shown. It may be noted that the transverse disposition of the wheel loads are indicated on the transverse section Y-Y, although the section did not cut through the load pads. The downward displacements measured at the LVDTs are presented as –ve, and the tensile stresses measured at the strain gauges are presented as +ve.

6.1.1.1 Response of Deck Plate and Ribs

Figure 176 shows the displacements recorded by the LVDTs at section Z-Z during the static test at the maximum load, along with the FEA results. The LVDTs were installed

at the soffit of the ribs 1, 2 and 4 and on the underside of the deck plate in between the ribs 1 and 2, ribs 3 and 4, and ribs 4 and 5. The displacement pattern indicated reverse bending of the deck plate associated with the distortion of the rib cross section across the transverse section. The south wheel load was spread across parts of ribs 1 and 2 and the deck plate in between the ribs, which caused relatively larger local displacements of Rib 2 and the deck plate between ribs 1 and 2. The displacement of Rib 1, however, was less due to its proximity to edge girder which was displaced upward by the under-deck actuator. The larger displacements of Rib 4 and the deck plate between ribs 4 and 5 were due to the global transverse deformation of the deck under wheel loads. In fact, the maximum displacement over the transverse section was recorded at the soffit of the deck plate between ribs 4 and 5. The decrease in vertical displacement of the deck between ribs 2 and 4 (channel 9) indicated hogging flexural deformation of the deck in the transverse direction in between ribs 2 and 4. The displacements recorded by the LVDTs matched with the FEA results, verifying the accuracy of the FE model.

Figure 177 shows the stress ranges measured at the uniaxial gauges installed on the top and bottom surfaces of the deck plate at section Z-Z. FEA results are also shown in the figure. It can be seen that the deck deformed as a continuous beam in the transverse direction supported by the ribs, with the stresses peaking under the load pads and gradually decreasing away from it. The deck deformed in a sagging curvature under the load pads between ribs 1 and 2 and over Rib 4, and in hogging curvature over the rib walls. As a result stresses on the top of the deck plate were compressive, and on the bottom of the deck plate were tensile in between the rib walls. Opposite trend was observed over the rib walls with tensile stress on the top of the deck plate and compressive stress on the bottom of the

deck plate. The measurements at the gauges matched very well with the FEA results, further verifying the accuracy of the FE model. The stresses were almost of equal magnitude on the top and the bottom surfaces of the deck plate indicating pure bending of the deck plate with insignificant membrane stresses. The distribution of transverse stresses on the deck plate were symmetrical with respect to the centerline of the simulated tandem axle, with similar stresses at the south-east and north-east load pads. The maximum measured compressive and tensile stress ranges were about 10 ksi (69 MPa).

6.1.1.2 Response of Inner FB

Uniaxial strain gauges of ¼ in. (6 mm) gauge length were installed on the soffit (underside of the bottom flange) of the inner FB at section Y-Y, centrally between ribs 1 and 2 and ribs 4 and 5. These strain gauges (channels 66 and 67) were oriented transversely, and was aligned with similar strain gauges on the top of the deck plate (channels 189 and 190). An LVDT (channel 13) was also installed on the soffit of the inner FB at section Y-Y, aligned with the centerline of Rib 3.

The measurements at these gauges are shown in Figure 178 along with the FEA results. The measurements matched well with the FEA results, verifying the accuracy of the FE model. The measured stress ranges at channels 66 and 67 were 2.9 ksi (20 MPa) and 4.6 ksi (32 MPa) respectively. The measured stress ranges at channels 189 and 190 were -0.3 ksi (2 MPa) and -0.5 ksi (4 MPa) respectively. As expected, the inner FB and the deck plate experienced global compressive and tensile stresses at the top of deck plate and bottom of inner FB due to flexural deformation of the deck in the transverse direction. Because of the composite action with the deck plate with the ribs, the compressive stresses were significantly smaller than the tensile stresses. Tensile stress at bottom flange was more

at channel 67 (between ribs 4 and 5), which was expected as the recorded displacement (Figure 176) was maximum at the LVDT there (channel 12 between ribs 4 and 5). Since the load pads were significantly away from the gauges on the deck plate under the static test load configuration, the gauges did not experience any local deformation. The maximum displacement measured by the LVDT was 0.016 in. (0.4 mm).

6.1.2 Response of Rib-to-Deck Plate Connection

Response of the rib-to-deck plate connection is presented in terms of stresses measured at the uniaxial gauges installed in back-to-back configuration on the deck plate and rib walls at section Z-Z coinciding with the east above-deck actuator (section 4.5). On the deck plate, the strain gauges were installed on the top and the bottom surfaces, oriented in the transverse direction, normal to the rib-to-deck plate weld. On the rib walls, strain gauges were installed on both surfaces, oriented along inclined depth of the rib wall, normal to the rib-to-deck weld. However, the gauges on the inner face of the rib walls got damaged while welding the ribs to the deck plate. The results are presented for the ribs under the load pads i.e. north wall of Rib 1 and south wall of Rib 2 under south-east load pads and walls of Rib 4 under north-east load pads

Measured stress ranges at the rib-to-deck plate connections under the south-east load pads are shown in Figure 179. The stresses on the bottom surface of the deck plate and on the outer surface of rib wall was compressive near the rib-to-deck plate connection as the connection underwent local out-of-plane deformation under the wheel loads. However, presence of high tensile residual stress at the weld toe would cause localized tensile stress field and could cause fatigue cracking of the connection. The maximum compressive stress ranges were measured at the rib-to-deck plate connection for north wall

of Rib 1 (channels 140 and 193) and were about 12.5 ksi (86 MPa) and 6 ksi (41 MPa) near the weld toe on rib and deck plate respectively. The compressive stress ranges at the rib-to-deck plate connection for south wall of Rib 2 (channels 146 and 196) were lower. The compressive stress range at the gauge closer to rib-to-deck weld toe was higher due to weld toe notch and the stress range decreased at the next gauge. Stresses were tensile on the top surface the deck plate near the welded connection. The stresses under the load pads away from the weld were compressive and tensile on the top and bottom surfaces of the deck plate respectively (channels 167 and 195), indicating sagging global flexural deformation of the deck plate under the load pads in the transverse direction.

Figures 180 and 181 compare the measurements at the rib-to-deck plate connections under the south-east load pads with the FEA results. Tensile stresses are plotted on the outer face of the rib wall and the top of deck plate. Figure 180 shows the stresses on the top of deck plate and the outer face of rib wall. The measurements showed similar trend as the FEA. The compressive stress ranges at the gauges on the rib walls were slightly higher than the FEA results. Since the response of orthotropic decks is manifested locally under wheel loads, it is possible that a small transverse shift in the load position could cause a significant change in the bending stress and rapidly changing local stress. The stresses on the outer surface of the south wall of Rib 1 showed opposite trend of flexural deformation to that of north wall with tensile stresses at the rib-to-deck plate connection, indicating distortional deformation of Rib 1. Figure 181 shows the stresses on the bottom face of the deck plate and inner face of the rib wall. As observed from FEA, the stresses on the inner face of rib wall were tensile near the connection as opposed to compressive on the outer face of the rib wall due to large out-of-plane bending of the rib wall. However, their magnitudes were

not same due to presence of axial stress in the rib wall. This phenomenon could not be verified by the measurements as the gauges on the inner face of the rib wall was damaged during welding the ribs to the deck plate. The gauges on the bottom surface of deck plate showed similar trend as FEA. The stresses on the bottom surface of deck plate were almost of similar magnitude to that on the top of deck plate, indicating transverse bending of deck plate with insignificant membrane stress.

Measured stress ranges at the rib-to-deck plate connections under the north-east load pads are shown in Figure 182. Similar to the rib-to-deck plate connection under the south-east load pads, the stresses on the bottom surface of the deck plate and on the outer face of rib wall was compressive near the rib-to-deck plate connection as the connection underwent local out-of-plane deformation under the wheel loads, however, the stress ranges were lower. The maximum compressive stress ranges were measured at the rib-to-deck plate connection for north wall of Rib 4 (channels 152 and 202) and were about 3 ksi (21 MPa) and 7 ksi (48 MPa) near the weld toe on the rib and the deck plate respectively. The compressive stress ranges at the rib-to-deck plate connection for south wall of Rib 4 (channels 150 and 200) was lower than the north wall. The compressive stress range at the gauge closer to rib-to-deck weld toe was higher due to weld toe notch and the stress range decreased at the second gauge. Stresses on the top surface of the deck plate were tensile near the welded connection. The stress under the load pads away from the weld were compressive on the top surface of the deck plate (channel 174), indicating sagging global flexural deformation of the deck plate under the load pads in the transverse direction.

6.1.3 Response of Rib-to-Floor Beam Connection

The response of the rib-to-floor beam connection is presented in terms of the

stresses measured at the gauges on the inner FB web and Rib 1 at the rib-to-floor beam connection. As determined from FEA of the global model, Rib 1-to-inner FB connection adjacent to the edge girder was the most critical and hence the connection was extensively instrumented. All the gauges on the floor beam web at the Rib 1-to-inner FB connection were installed symmetrically on the north and south sides of the rib, and on each side the gauges were installed back-to-back on the east and west faces of the floor beam web to measure the in-plane and the out of plane stress components. The gauges on the Rib 1 wall were installed symmetrically on the north and the south walls as well as to the east and the west sides.

Fatigue testing of mockup specimens, the results of which are presented by Roy and Mukherjee (2015), identified a failure mode of the rib-to-floor beam connection by crack growth from the LOF at the weld root, normal to the maximum principal stress field. Rosette gauges of 1 mm length were installed in back-to-back configuration on the inner FB web adjacent to the weld toe to capture the complex stress distribution of stresses near the weld toe and to determine the magnitude and direction of principal stresses at those locations. The principal stresses measured from the back-to-back rosettes on the south side of Rib 1 (tension side of the connection towards edge girder) are tabulated in Tables 1 to 4. The layout of the rosette gauges and the direction of the principal stresses are also shown in the respective tables. Tensile stresses are defined as +ve. The direction of principal stresses is presented for the principal stress of the larger magnitude, with respect to the vertical. This angle is defined +ve in counter-clockwise direction. The floor beam web to the south of Rib 1 (towards edge girder) experienced tensile stresses. The measured maxima of principal stresses at the rosette gauges on the inner FB web are also shown in

Figure 183.The measured maxima of principal stresses were about 9.8 ksi (68 MPa) on the south side of the rib and -13.7 ksi (95 MPa) on the north side of the rib, at 25 degree from the rib soffit. The principal stresses on the west faces were less, indicating presence of some out-of-plane bending of the floor beam web and/or twisting of Rib 1. The stresses on the west face was probably low due to the presence access holes at the rib soffits on the west side of the floor beam, affecting the flexural and torsional stiffness of the ribs. However, the direction of the principal stresses on the east and west faces were comparable.

It should be noted that fatigue damage at welded connections is caused by stress range and not maxima of stresses. The measured principal stress ranges at the rosette gauges on the inner FB web are shown in Figure 184, along with the FEA results. The measured maximum principal stress ranges at the rosette gauges on the floor beam web were about 9.0 ksi (62 MPa) on the south side of the rib and -12.5 ksi (86 MPa) on the north side of the rib, at 25 degree from the rib soffit. The measured stress ranges were lower than FEA results. The FE model had a perfect weld toe notch with zero notch radius, however, the physical weld toe in the specimen would have a finite radius. Hence, the principal stresses in real structure would be lower than the FEA results. The distribution of principal stresses on the south side of inner FB web are presented graphically in Figure 185. The orientation of maximum principal stress was almost tangential to the rib-to-floor beam connection, and was similar to the FEA results. The distribution of principal stresses was consistent with the transfer of simulated wheel loads from the deck plate to the edge girder by shear in the floor beam web. Shear force developed between the distributed loads and the nearest support (in this case the edge girder). In this shear span, a diagonal tension field developed in the inner FB web from the bottom (tension) flange to the top corner

formed by the edge girder, deck plate and floor beam. The diagonal tensile field deviated around the cutout near the round bottom rib due to discontinuity in the floor beam web causing stress concentration at the rib-to-floor beam connection around the rib rounding. The diagonal tension field being tangential to the connection, the maximum principal stress was about tangential to the rib-to-floor beam connection. As stated earlier and as also seen in Figure 184, the principal stress ranges on the west face of the inner FB were less than that on the east face indicating presence of some out-of-plane bending of the floor beam web and/or twisting of Rib 1.

Fatigue cracking at the weld toe mostly initiates from the weld toe micro discontinuities subject to the stress range normal to the weld toe. The measured principal stresses and their orientation were used to calculate the stresses along the rosette arms, one of which was aligned normal to the rib-to-floor beam weld toe. Figures 186 and 187 show the measured stresses and stress ranges on the inner FB web normal to the weld toe as obtained from the gauge measurements. The maxima of the normal stress were about 3.9 ksi (27 MPa) and -6.9 ksi (-48 MPa) on the south and the north sides of the rib respectively, at 50° from the rib soffit. The maximum stress ranges were about 3.6 ksi (25 MPa) and -6.3 ksi (-46 MPa) on the south and the north sides of the rib respectively, at 50° from the rib soffit. Among the three gauges along each radial lines, the largest (magnitude) of the stress was observed at the first gauge or gauge closest to the weld toe (the arm of the rosette aligned normal to the weld toe). It can also be seen pictorially form Figures 188 to 195, where stress ranges measured at gauges installed along radial lines on the inner FB web are plotted along with the FEA results. The measurements showed similar trend as the FEA results. The measured stress ranges on the Rib 1 wall normal to the weld toe are shown in

Figures 196 to 205 along with the FEA results. The gauge measurements showed similar trend as FEA, with the largest (magnitude) of the stress at the gauge closest to the weld toe. Similar to FEA, reverse bending of the rib wall was observed from the static test results at about 1 in. from the weld toe. However, the measured stress values did not match well with FEA close to the weld toe. Due to the steep stress gradient close to the weld toe, a slight shift in the gauge location from its intended position could have caused the difference in stress values.

6.1.4 Response of CJP Deck Splice

Figure 206 shows the stress ranges measured at the uniaxial gauges, installed on the top and the bottom surfaces of the deck plate adjacent to the transverse deck splice under the south-west load pads. The FEA results are also shown in the figure. These strain gauges (channels 181 to 184, and channels 208 to 211) were oriented along the longitudinal direction of the deck. The measurements at the gauges under the north-west load pads are not shown as the stresses were similar to the gauges under the south-west load pads. Similar to the FEA results, the measured stresses were tensile at the bottom of the deck plate due to global longitudinal bending of the deck. The maximum stress range recorded at the bottom of deck plate was about 7 ksi (48.3 MPa). The stresses measured at the bottom of the deck plate matched well with the FEA results. Two of the gauges (channels 182 and 183) on the top of the deck plate under the south-west load pads got damaged during the crawl test. Gauges on the top of the deck plate under the north-west load pads also got damaged during the crawl tests. Stresses on the top of the deck plate were compressive, however their magnitude was less than the stresses on the bottom of the deck plate, indicating presence of tensile membrane stress in the longitudinal direction of the deck. In

addition, stresses recorded by the gauges on the top of the deck plate deviated significantly from the FEA results. The top deck gauges were directly on the wheel path of the crawl tests, which could have damaged the gauges. In that case, the stresses recorded by these gauges are questionable.

6.2 Results of Fatigue Test

Static tests were conducted prior to fatigue test. The initial static tests provided the baseline condition of the deck. Initially, the test was run at 1 Hz frequency for about 400,000 cycles shifted to 2 Hz frequency when the stability of the fatigue test was ensured. The test was conducted uninterrupted 24 hours a day and seven days a week, except for interruptions due to routine checks, maintenance or significant events. The specimen was inspected for possible fatigue cracking regularly at an interval of 4 hour with the exception during night time when the last inspection for a day was at 10:30 PM while the first inspection for the next day was at 7:00 A.M. The inspections were aided with 10X magnifying glass. All the data collected for each day of testing was also checked regularly for any spike or irregularity in the data. Any unusual incident was flagged and immediate course of actions were taken to sort out the problem. Intermittent static tests were carried out at about every million cycles interval, when the testing was interrupted for routine maintenance and conducting the static tests.

The fatigue testing was continued up to 8 million cycles, which is the upper bound of AASHTO Category C design curve at the Constant Amplitude Fatigue Threshold (CAFT). No fatigue cracking was detected in the deck. The results would indicate infinite life performance, as long as the site specific overloads did not exceed the test load more than 1 in 10000 occurrences. The test results also demonstrated that the large deviation from

the specified fabrication tolerances and the rejected welding procedures, which were noted during the specimen fabrication and installation, did not affect the fatigue performance of the deck. This suggests that the specified fabrication tolerances are arbitrary. A static test was performed after the fatigue test in order to acquire information on any changes in behavior of the specimen in comparison to the baseline condition when the fatigue test was initiated. The static test measurements at the strain gauges, including at the gauges local to the rib-to-deck plate and rib-to-floor beam connections, didn't show any significant variation, implying that the deck was essentially undamaged.

6.2.1 Evaluation of Intermittent Static Test Results

As discussed earlier, intermittent static tests were carried out at about every million cycles interval, when the testing was interrupted for routine maintenance and conducting the static tests. Theses static tests permitted collection of longer duration of data at higher sampling rate that produced stable data with reduced noise and allowed assessment of the changes in the state of the deck by comparing stresses at the critical gauges with the prior static tests. Figures 207 to 212 show the change in stresses at some of the critical gauges, measured during the intermittent static tests. The abscissa of these plots (the lower horizontal axis) shows the number of stress cycles on a linear scale. The dates of the static tests are marked sequentially on the upper horizontal axis of the plots, matching with the corresponding number of fatigue stress cycles.

Figures 207 and 208 show the history of maximum tensile principal stress ranges and maximum compressive principal stress ranges measured at the 1 mm rosette gauges on the inner FB web at the connection with Rib 1. Figure 209 shows the history of maximum tensile principal stress ranges measured at the 1 mm rosette gauges on the Rib 1 south wall

at the connection with inner FB. It can be seen from these figures, the principal stress ranges at the rosettes dropped initially, by about 0.5 ksi, but later remained stable. This can be due to the wide fluctuation of ambient temperature happening during that time of the year. However, the drop was insignificant. These stress history plots confirm that the stress ranges were stable during the fatigue test and there was no fatigue damage of the connection after 8 million cycles, which was also confirmed by regular visual inspection.

Figure 210 shows the history of stress ranges measured at the uniaxial gauges on the Rib 1 north wall aligned normal to the Rib1-to-deck plate weld, and abutting the weld toe. These gauges were located at the loaded section Z-Z to the east of the floor beam under the south loading pad. The stress history plot shows a drop in the stress range of about 1 ksi (6.9 MPa) after 4 million cycles, however no fatigue cracking was detected at this connection by visual inspection. Figure 211 shows the history of stress ranges measured at the uniaxial gauges on the deck plate at the same section The stress ranges observed at the back-to-back (top and bottom) gauges (channels 167 and 195) showed that the deck plate was in pure bending with negligible membrane stresses. The stress ranges at both the gauges decreased by about 1.5 ksi (10.4 MPa) after 5 million cycles and remained stable till the completion of the test. However, no cracks were observed by visual inspection. Gauges identified by channel numbers 165 and 166 were located directly under the south load pad and were damaged after 1 million and 6 million cycles of fatigue testing, respectively. The stress history plots of the undamaged gauges located at the Rib 1-to-deck plate connection suggested that the rib-to-deck plate connection directly under the load pad was undamaged. This was also confirmed by visual inspection of the connection.

Figure 212 shows the history of stress ranges measured at the uniaxial gauges,

installed back-to-back on the top and bottom surfaces of the deck plate adjacent to the transverse deck splice, and under the south-west load pads. Results from only two gauges are shown, as the other gauges on the top of the deck got damaged during the course of testing. The stress ranges observed at the gauges showed that the deck plate was in pure bending with negligible membrane stresses. However, the stress range at the top gauge decreased by about 3 ksi (20.7 MPa) after 5 million cycle, but remained stable till the completion of the test. The top gauges were replaced after 5 million cycles as they got damaged while lifting the load pads for inspecting the deck splice. However, no fatigue cracking could be detected visually. The stress gradient adjacent to the load pad being very high, an insignificant shift in the location of the gauge could cause significant change in the stress value.

Therefore, no significant change was noted in the stress ranges at the critical gauges during the intermittent static tests, confirming that the deck specimen essentially remained undamaged after 8 million cycles of fatigue testing.

6.2.2 Assessment of Fatigue Performance

6.2.2.1 Performance of Rib-to-FB connection

The fatigue performance of rib-to-floor beam connection was evaluated against cracking from weld toe and weld root, although no cracking was observed at the connection. The FEA results showed high stress concentration and stress gradient at the Rib 1-to-inner FB connection. Consequently, this connection was identified as the most critical and was extensively instrumented. Fatigue cracking at the weld toe is primarily attributed to the crack growth from the micro discontinuities subject to the stress range normal to the weld toe. The stress range normal to the weld toe was determined by local

stress approach as recommended in AASHTO LRFD BDS. According to AASHTO, the local structural stress range at the weld toe was to be determined by linearly extrapolating up to the weld toe the measured stresses at two reference points, at 0.5 t and 1.5 t from the weld toe, where t is the thickness of the floor beam web. However, the gauges were installed on the inner FB web at 0.4 t, t and 1.5 t from the Rib 1-to-FB weld toe. The FEA showed that linearly extrapolating the stress values from 0.4 t and 1.5 t to the weld toe caused insignificant change to the stress at the weld toe as the stress values at 0.4 t, 0.5 t and 1.5 t were essentially along a straight line (Figure 213). Accordingly, the two reference points were taken at 0.4 t and 1.5 t for calculating local structural stress range at the weld toe. Calculation of the local structural stress range at the tension side of the connection at the point of maximum normal stress is shown in Figure 214. In addition, the fatigue performance of the connection was also evaluated against cracking from the weld root using principal stress range at weld root as obtained from the FEA, as this failure mode was observed in fatigue testing of mockup specimens (Roy and Mukherjee, 2015). .

Fatigue performance of the connection against cracking from the weld toe is evaluated in Figure 215, where the local stress range normal to the weld toe versus the life at the termination of the fatigue test is plotted along with AASHTO design S-N curve. For better accuracy, the plotted stress ranges were computed from the results of initial static tests performed at the beginning of the fatigue test. The maximum value of the local stress ranges at the tension and the compression side of the connection were about 5.2 ksi (36 MPa) and 8.8 ksi (61 MPa) respectively. As is evident, the estimated local stress ranges from the measurements matched well with the FEA results. Based on nominal stress ranges, the fatigue resistance of welded connections against fatigue crack growth from the weld

toe is defined by AASHTO Category C, having a CAFT of 10 ksi (69 MPa). The estimated local stress ranges were below the CAFT. As is well known, the local stress range estimated as per the linear extrapolation presented here is not applicable to assessment of fatigue performance in the infinite life regime (Roy et al. 2012b). Considering the Category C design curve extended below the CAFT, the lower bound life (95% confidence on 95% probability of survival life) is about 31 million cycles for the tension side, which way exceeds the anticipated occurrence of fatigue limit state stress cycles within the 75 years design life of the deck. Therefore, the rib-to-floor beam connection detail is expected to exhibit infinite fatigue life. It was also experimentally verified that there was no fatigue damage after 8 million cycles. It can also be seen from Figures 207 to 209, no significant change in the measured stresses adjacent to the connection was noted during the course of fatigue testing up to 8 million cycles. For the compression side, the lower bound life is 6.5 million cycles. However, being a nominally compressive zone, the crack will not propagate when it comes out of the residual tensile stress zone.

Fatigue performance of the connection against cracking from the weld root is evaluated in Figure 216, where the local principal stress range at the weld root as determined from FEA versus total life is plotted along with AASHTO design S-N curve, which is based on nominal stress range. The principal stress ranges at the weld root were about 11.5 ksi (79 MPa) and 12.3 ksi (85 MPa) at the tension and the compression sides of the connection respectively. As it can be seen from Figure 216, the performance of this connection exceeded the lower bound or 95% confidence on 95% probability of survival life for Category B details, which is close to the upper bound or 95% confidence on the 95% probability of failure of Category B' details. The limited test data suggests the

performance of the connection to be better than AASHTO Category B'. In view of the limited test data and the expected scatter in the performance of the connections due to the inherent variability in welded connections, the test result was inadequate to evaluate this scatter and draw any statistically significant conclusion against cracking from weld root. In that respect the fatigue test results from this study should be considered as indicative.

6.2.2.2 Performance of Rib-to-Deck Plate Connection

The fatigue testing was conducted for the disposition of the tandem axle for creating the most critical stress state at the rib-to-floor beam connection. This load disposition did not produce the most critical stress demand at the rib-to-deck plate connection. Nevertheless, the fatigue performance of rib-to-deck plate connection is evaluated in Figure 217 against the measured stress range, where the local stress range normal to the weld toe versus the life at the test termination is plotted along with AASHTO design S-N curve. The stress ranges are plotted for the north wall of Rib 1, as maximum stress ranges were observed at that connection. For better accuracy, the plotted stress ranges were computed from the results of initial static tests performed at the beginning of the fatigue test.

The local stress range at the weld toe were obtained by linearly extrapolating from measured stress values at 0.5t and 1.5t ahead of the weld toe; channels 193 and 194 for weld toe on deck plate and channels 140 and 141 for weld toe on Rib 1. The extrapolated stress ranges at the weld toe were about 8 ksi (55 MPa) and 12.5 ksi (86 MPa), respectively on deck plate and rib. Stress ranges were also determined from FEA in a similar manner and they were about 8 ksi (55 MPa) and 9.5 ksi (66 MPa), respectively at the weld toe on deck plate and the rib. The local structural stress ranges were compressive at the

connection. However, the presence of tensile residual stresses at the weld toe could result in the local tensile stress range leading to fatigue cracking from the weld toe. As is evident, the estimated local stress ranges from the measurements matched well with the FEA results. Based on nominal stress ranges, the fatigue resistance of welded connections against fatigue crack growth from the weld toe is defined by AASHTO Category C, having a CAFT of 10 ksi (69 MPa). The estimated local stress ranges were below the CAFT except for the experimental result for weld toe on rib. As discussed earlier, the local stress range estimated as per the linear extrapolation presented here is not applicable to assessment of fatigue performance in the infinite life regime (Roy et al. 2012b). Considering the Category C design curve extended below the CAFT, the lower bound life (95% confidence on 95% probability of survival life) is about 2.2 million cycles and 8 million cycles for weld toe on rib and deck plate respectively. However no fatigue cracking was observed after 8 million cycles from both weld toe on rib and deck plate. Also it can be seen from Figures 210 and 211, that no significant change in the measured stresses adjacent to the connection was noted during the course of fatigue testing up to 8 million cycles.

It should be noted that the AASHTO fatigue design curves were developed based on fatigue test results on full scale beam specimens under constant amplitude loading and represent 95% confidence on 95% probability of survival fatigue life. Due to inherent variability, welded connections are expected to exhibit scatter in their performance. The limited test data of the subject deck was inadequate to evaluate this scatter and draw any statistically significant conclusion. The difference between the estimated design life and the test result corresponding to the cracking mode at the weld toe could be attributed to this inherent variability.

6.2.2.3 Performance of Transverse Deck Splice

The fatigue performance of the CJP groove welded deck plate splice is evaluated in Figure 218, where the local stress range normal to the weld toe versus total life is plotted along with AASHTO design S-N curve. Evaluating the performance of this detail is of special interest as significant deviations were observed at the deck splice from the specified fabrication tolerances during specimen installation and the CJP deck plate weld included number of rejectable indications (volumetric defects). The stress ranges are plotted for the deck splice under the south-west load pads, where the larger stresses were measured.

Similar to the other details, the local structural stress ranges at weld toe were determined by extrapolating from measurements at 0.5t and 1.5t ahead of the weld toe; channels 181 and 182 for weld toe on the top of the deck plate and channels 208 and 209 for weld toe on the bottom of the deck plate. The extrapolated stress ranges at the weld toe were about 7 ksi (48 MPa) on the top and bottom surfaces of the deck plate. Stress ranges were also determined from FEA in a similar manner and they were about 6 (38 MPa) and 7 ksi (51 MPa), respectively on the top and bottom surfaces of the deck plate. As is evident, the estimated local stress ranges from the measurements matched well with the FEA results. Stress ranges on the top of the deck plate were compressive. However, the presence of tensile residual stresses at the weld toe could result in the local tensile stress range at the weld toe on the top of the deck plate leading to fatigue cracking from the weld toe. According to the AASHTO specifications a groove welded deck plate splice with backing bar left in place is a Category D detail. For the subject deck, the backing bar was removed and the weld reinforcement was not ground smooth. The detail is equivalent to a transverse butt splice between two plates done by a CJP weld, with weld reinforcement in place, which

is defined as AASHTO Category C against fatigue crack growth from the weld toe, having a CAFT of 10 ksi (69 MPa). Considering the Category C design curve extended below the CAFT, the lower bound life (95% confidence on 95% probability of survival life) is about 13 million cycles for the tension side. It was also experimentally verified that there was no fatigue damage after 8 million cycles. It can also be seen from Figure 212, no significant change in the measured stresses adjacent to the connection during the course of fatigue testing up to 8 million cycles. The test results showed that the CJP deck splice exhibited no cracking after the upper bound fatigue cycles for AASHTO Category C detail at CAFT, even with significant deviations from the fabrication tolerances. It can be concluded that the commonly specified fabrication tolerances for orthotropic decks are too stringent and arbitrary at best, and further research is required to find out rational fabrication tolerances for economic fabrication of the deck with lesser efforts.

6.3 Results of Crawl Tests

Crawl tests were performed to characterize the response of the deck under moving load in different positions. As discussed earlier, the initial crawl tests were discarded due to some fixture issue. Accordingly, the crawl tests were repeated after the fatigue test was completed. The LVDTs were reconnected to the deck for the crawl test.

The crawl test results are presented as plots of strain gauge and/or LVDT measurements along with the FEA results against the travel of the test truck. Considering the symmetry of the prototype deck with respect to inner FB, the travel of the test truck is presented as the distance of the truck centerline from inner FB on the X-axis or the abscissa. The measured quantities (stresses or displacements) along with the FEA results are presented on the Y-axis or the ordinate. The start and end points of travel for the crawl test

truck was 10 ft. in (3 m) to the west side and 8 ft. 9 in. (2.7 m) to the east side of the inner FB respectively. Thus, the total distance travelled by the test truck in each crawl test position was 18 ft. 9 in. (5.7 m). Identifying the centerline of inner FB as the origin, the distance of the test truck to the west of inner FB is presented as negative and the distance to the east of inner FB is presented as positive. Tensile stresses are presented as +ve. Downward displacements are presented as –ve. The plots also include the elevation of the deck with the gauge section and the crawl truck distance identified.

It may be noted that the combined weight of the truck and the four billets was 53.7 kip (238.9 kN), which was about 2.2 times the tandem rear axle load of 24 kip (106.8 kN) for the AASHTO notional fatigue truck. For verification of infinite life, however, the fatigue testing of the deck was performed under a gross tandem axle weight of 82.8 kip (368.3 kN), which was 3.45 times the AASHTO notional fatigue truck. Thus, the crawl test loading was about 65% of the fatigue limit state loading.

6.3.1 Global Response of Prototype Deck

The global response of the prototype deck is discussed in this section in terms of the measurements at the sensors on the deck at sections Y-Y and Z-Z. Uniaxial strain gauges, oriented along the transvers direction of the deck, were installed on the top surface of deck plate and at the bottom of inner FB at section Y-Y. A LVDT was also installed at the soffit of the inner FB at section Y-Y. At section Z-Z, LVDTs were installed on the soffit of the ribs and at the underside of the deck plate in between the ribs.

6.3.1.1 Response of Ribs and Deck Plate

Plots of vertical displacements at section Z-Z are shown in Figures 219 and 220. The plots show the variation of displacements as the test truck rolled along the deck. The

section of the respective sensor is shown in the longitudinal section of the deck, where the displacements are plotted.

The response at a sensor changed with the longitudinal position of the test truck. The maximum response occurred when the centerline of the crawl truck was over inner FB, or in other words one of the axle was over the section of the gauge. In Figure 219 the vertical displacement of the Rib 1 measured at the LVDT channel 7 is plotted and in Figure 220 the vertical displacement of the deck plate between ribs 1 and 2 measured at the LVDT channel 8 is plotted.

The displacement profiles for the LVDTs under the deck plate and the ribs generally exhibited a single peak displacement with a peak at the maxima. At the LVDTs, the maximum peak response occurred when the rear axle of the crawl truck crossed the transverse section Z-Z (for a roll from east to west, or forward roll). For the reverse roll, the maximum peak response occurred when the front axle of the crawl truck crossed the transverse section Z-Z (for a roll from west to east, or reverse roll). The crawl test results showed similar trend as of FEA. The crawl test results for the three transverse positions were similar because of the fact that same displacement profile was used for the under-deck actuator for all the three crawl test positions.

6.3.1.2 Response of Inner FB

Plots of the vertical displacement and the normal stress in transverse direction recorded at the soffit of inner FB at section Y-Y by the LVDT (channel 13) and the uni-axial strain gauge (channel 66) are shown in Figures 221 and 222 respectively. The plots show the variation of displacements and stresses as the test truck rolled along the deck. The section of the respective sensor is shown in the longitudinal section of the deck, where the

results are plotted. The sensors exhibited a single modal response as the truck rolled along the deck, with the maximum response occurring in each transverse position when the truck centerline was around inner FB. For transverse positions T30 and T28, the response didn't peaked exactly when the truck centerline was at inner FB. This is because of the fact that a constant roll speed could not be maintained during the crawl test. Nevertheless, the centerline was close to the centerline of the inner FB. The maximum vertical displacement occurred in transverse load position T29. The maximum vertical displacements reduced as the truck position moved away from the center of the deck. The vertical displacement recorded for the other transverse positions were also close. Similar to the response of the LVDT, the response of the strain gauge under inner FB exhibited a single modal response as the truck rolled along the deck, with the maximum response occurring in each transverse position when the truck centerline was at inner FB. The measured stresses showed similar trend as of FEA, and were tensile in nature as the floor beam deflected in sagging curvature. In addition, the response of the inner FB was maximum for the symmetric disposition of the tandem axle or longitudinal load position L1 as was determined from FEA. It may be inferred that the global response of the inner FB did not get affected much by changes in transverse load positions and it peaked when centerline of truck was at inner FB i.e. for symmetric disposition of the tandem axle in the longitudinal direction.

6.3.2 Response of Rib-to-Deck Plate Connection

Response of the rib-to-deck plate connection is presented in terms of stresses measured at the uniaxial gauges installed in back-to-back configuration on the deck plate and rib walls at section Z-Z coinciding with the east above-deck actuator. On the deck plate, the strain gauges were installed on the top and the bottom surfaces, oriented in the

transverse direction, normal to the rib-to-deck plate weld. On the rib walls, strain gauges were installed on both surfaces, oriented along inclined depth the rib wall, normal to the rib-to-deck weld. However, the gauges on the inner face of the rib walls got damaged while welding the ribs to the deck plate.

Figure 223 shows the normal stress measured at the gauge (channel 140) on the outer surface of Rib 1 north wall at the rib-to-deck plate connection. Figure 224 shows the normal stress measured at the gauge (channel 147) on the outer surface of Rib 2 south wall at the rib-to-deck plate connection. The stresses were insignificant until the test truck crossed the inner FB and approached the gauged section. Bimodal responses, manifesting the effects of each axle of the tandem, were noted when the axles were close to the gauged transverse section. This indicated that the transverse stresses and the deck response were highly localized under the wheel. The stresses measured from the gauges on the outer surface of the rib walls were compressive as connection underwent local out-of-plane deformation under the wheel loads. The stresses measured from the crawl tests were comparable with the FEA results. The maximum stresses occurred for transverse load position T29 when the south side wheel pair was placed centrally between the ribs causing out of plane bending of the rib-to-deck plate connections. However, for the transverse position T-30, the south side wheel moved away from the channel 140 (at north wall of Rib 1) and caused symmetric bending of rib-to-deck plate connection for Rib 2 south wall (channel 147). Consequently, stress peaks were reduced, further signifying the localized effect of wheel loads on the rib-to-deck plate connections.

Figure 225 shows the normal stress measured at the gauge (channel 169) on the top of deck plate to the south of Rib 2 at the rib-to-deck plate connection. Figures 226 and 227

show the normal stress measured at the gauges (channels 175 and 202) on the top and bottom surfaces of the deck plate respectively, to the north of Rib 4 at the rib-to-deck plate connection. Similar to the gauges on the rib wall, the stresses were insignificant until the test truck crossed the inner FB and approached the gauged section. Bimodal responses, manifesting the effects of each axle of the tandem, were noted when the axles were close to the gauged transverse section. The stresses were tensile on the top surface and compressive on the bottom surface as the deck plate deformed locally in hogging curvature over the rib wall at the rib-to-deck plate connection. The results were comparable to FEA. The maximum stress values for the different transverse load positions were different indicating the localized effect of wheel loads on the rib-to-deck plate connections.

It should be noted that the response of the gauges at the rib-to-deck plate connections were not exactly of the same magnitude under both the axles. This was due to non-uniform tire contact and local transverse shift in wheel positions, and the sensitivity of the deck response to the transverse position of the wheel loads.

6.3.3 Response of Rib-to-Floor Beam Connection

The response of the rib-to-floor beam connection is presented in terms of the stresses measured at the gauges on the inner FB web at the Rib 1-to-inner FB connection. As determined from FEA of the global model, Rib 1-to-inner FB connection adjacent to the edge girder was the most critical and hence the connection was extensively instrumented. All the gauges on the floor beam web at the Rib 1-to-inner FB connection were installed symmetrically on the north and south sides of the rib, and on each side the gauges were installed back-to-back on the east and west faces of the floor beam web to measure the in-plane and the out of plane stress components.

The principal stresses on the east face of the inner FB to the south of Rib 1, measured at the rosette gauges at 25° and 50° from the rib soffit, are shown in Figures 228 and 229 respectively. The section of the respective sensor is shown in the longitudinal section of the deck, where the results are plotted. The stresses showed similar trend of FEA with tensile stress at the south side of the connection and maximum value of principal stress occurring at the 25° location. These plots show that for a single passage of the test truck, the rib-to-floor beam connection experienced only one stress cycle due to the resultant effect of the tandem axles. The stresses were highest when the center of the truck was at or close to the centerline of inner FB. Figure 230 show the principal stresses on the east face of the inner FB to the north of Rib 1, measured at the rosette gauge at 50° from the rib soffit. The stresses showed similar trend of FEA with compressive stress at the north side of the connection, and showed only one stress cycle per passage of the test truck. Similar to the south side, the stresses were highest when the center of the truck was at or close to the centerline of inner FB.

The stresses normal to the weld toe on the east face of the inner FB to the south and the north sides of Rib 1, measured at the rosette gauges 50° from the rib soffit, are shown in Figures 231 and 232 respectively. The section of the respective sensor is shown longitudinal section of the deck, where the results are plotted. The results showed similar trend of FEA, and showed one stress cycle per passage of test truck

It should be noted that for some cases, the peak response of the connection was not observed exactly when centerline of the truck was at the centerline of the inner FB. This is because of the fact that a constant roll speed could not be maintained during the crawl test. Nevertheless, the centerline was close to the centerline of the inner FB. The response of

the connection was maximum under symmetric disposition of the axles and confirmed the validity of the FEA results of GM.

6.3.4 Response of CJP Deck Splice

The longitudinal stresses at the gauges on the top and the bottom of the deck plate around the transverse deck splice are shown in Figures 233 to 235. The section of the respective sensor is shown in the longitudinal section of the deck, where the results are plotted. Figures 233 and 234 show the longitudinal stresses on the top of the deck plate under the south-west (channel 184) and the north-west (channel 185) wheel pair respectively. Bimodal responses, manifesting the effects of each axle of the tandem, were noted when the axles were close to the gauged transverse section. The stresses showed similar trend as FEA with compressive stresses on the top of the deck plate, however, the stresses were much lower than the FEA results. As discussed earlier, the gauges on the top of the deck plate around the deck plate splice was replaced after 5 million load cycles. In a location with high stress gradient, a little shift from its intended location of installation could have caused this deviation. Figure 235 shows the longitudinal stresses on the bottom of the deck plate under the south-west (channel 208) wheel pair. Similar to the top gauges, bimodal responses manifesting the effects of each axle of the tandem were noted when the axles were close to the gauged transverse section. The stresses showed similar trend as FEA with tensile stress on the bottom of the deck plate, however, the stresses were much lower than the FEA results. The CJP deck splice was inspected thoroughly for fatigue cracking, however, no crack was detected. The reason for this deviation from the FEA results for the bottom gauges cannot be ascertained. It is evident that the maximum stresses at the subject gauges were due to the global longitudinal bending of the deck.

7 CONCLUSIONS AND RECOMMENDATIONS

7.1 Conclusions

The study evaluated the rib-to-floor beam connection detail of the proposed orthotropic deck for a replacement lift bridge for infinite fatigue life, i.e., no in-service fatigue cracking during the design life of the bridge. Contrary to the conventional design of modern orthotropic decks having $^{5}/_{8}$ in. (16 mm) deck plates, trapezoidal ribs and additional cutouts in the floor beams under the rib soffit, the proposed design incorporated a $^{3}/_{4}$ in. (19 mm) deck plate stiffened by rounded bottom ribs (U-shaped) passing continuously through matching cutouts in the floor beams without any extended cut-out under the rib soffit.

The study objectives were accomplished by conducting 3D FEA of the bridge deck, fatigue testing of a full-scale prototype deck, and post-test evaluation of the welded connections. Based on the FEA, a full-scale prototype of the part bridge deck comprising 5 ribs and 3 floor beams, and a test setup that would adequately replicate the boundary conditions were decided for assessing the in-service fatigue performance of the proposed deck detail by testing in the laboratory under simulated conditions. The rib-to-floor beam detail that was considered for evaluation in the prototype deck employed $^{5}/_{16}$ in. (8 mm) fillet weld with fit-up gap not exceeding $^{1}/_{16}$ in. (1.5 mm). The prototype deck was fabricated in two panels to simulate a transverse field splice, which was specified as a CJP weld deposited with a backing bar, with the backing bar to be removed after welding, the weld root back gouged, and rewelded.

Multi-levels of 3D linear elastic FEA of the proposed bridge deck identified the rib-to-floor beam connection adjacent to an integral box girder or a primary load carrying

member as the most critically stressed region of the deck, when the rear tandem axle of the AASHTO fatigue design truck was symmetric with respect to the floor beam, and the rib was located in the shear span of the floor beam with the wheels nearest to the box girder placed centrally between the adjacent pair of ribs. The response of the orthotropic deck in general was characterized by typical global longitudinal and transverse flexure of the entire deck, and significant local deformations under the wheel loads. The stress concentration in the floor beam developed at the rib connection as the diagonal principal stress field in the shear span was interrupted by the rib opening. Stress concentrations were also noted in the rib wall around the round bottom due to out-of-plane deformation resulting from the connection involving round geometry.

The fatigue testing of the prototype deck, performed under the simulated rear tandem axles of the AASHTO fatigue truck for orthotropic deck design and subjected to the Fatigue I limit state load range of the AASHTO LRFD BDS 6th edition, was run out at 8 million cycles, without any detectable fatigue cracking in the deck. The measured stress ranges at all critical connections were less than the CAFT of their respective detail categories. The test results suggested infinite life performance of rib-to-floor beam connection detail of the proposed deck design, as long as the site specific overloads do not exceed the AASHTO Fatigue I limit state load more than 1 in 10000 occurrences.

The prototype deck fabricated in two panels to simulate a transverse field splice showed that the lack of fit between the panels at the splice due to the distortion from welding heat effects can significantly exceed the specified tolerances of $^{1}/_{16}$ in. (1.5 mm). The residual out-of-flatness between the mating deck plates even after force fitting the deck plate at the welded splice can be as large as $^{3}/_{16}$ in. (9.5 mm). In addition, the study

demonstrated that due to limited access it was practically impossible to perform the transverse splice of the deck plate as specified, i.e., depositing the CJP weld from the top with a backing bar underneath the deck plate, removing the backing bar, back gouging the weld root and re-welding in an overhead position. Use of a brass backing bar for easy removal resulted in significant LOF at the weld root, which could not be effectively repaired due to the access restrictions. Despite the rejectable volumetric welding flaws, no fatigue crack growth was detected in this connection, which was subjected to a maximum local stress range of about 7 ksi (49 MPa) under the wheel pads for the fatigue limit state loading. According to AASHTO specifications, the groove welded connections that may exhibit crack growth from volumetric defects that have not been repaired are classified as fatigue Category D. The groove welded connections with backing bar left in place is also classified as Category D, due to possible crack growth from any volumetric defects. Consistent with the existing practices for orthotropic decks in the United States, therefore the most effective way of performing the CJP weld at the transverse deck splice is to use a left-in-place steel backing bar and a wider root opening, which can ensure good fusion at the weld root.

The study also demonstrated that the large deviation from the specified fabrication tolerances and the rejected welding procedures, which were noted during the specimen fabrication and installation, did not affect the fatigue resistance of the connection details. This suggests that the commonly specified fabrication tolerances for orthotropic decks are arbitrary.

7.2 Recommendations

The rib-to-floor beam connection detail employing: (a) round bottom rib with fitted

floor beam, fit up gap not exceeding $^{1}/_{16}$ in. (2 mm); and (b) welded all around using two sided $^{5}/_{16}$ in. (8 mm) fillet weld, may be used for infinite life fatigue performance of the proposed orthotropic deck design. For ensuring the specified fit-up gap, the floor beam must be match cut against the as-fabricated ribs after welding to the deck plate. The rib-to-floor beam connection may be performed in down hand position with the ribs inverted on the deck plate, and the floor beam vertical. Performing the weld continuously in a horizontal position with the ribs standing vertical on the edges is not necessary.

The tolerances specified for fabrication and erection of orthotropic decks can be relaxed without any noticeable effect on the fatigue performance of the deck. The out-of-flatness of the orthotropic deck panel can be as large as $^{3}/_{4}$ in. (19 mm). The lack-of-fit between the adjacent panels at the deck plate welded splice can be as large as $^{3}/_{16}$ in. (5 mm mm). Force fitting of the deck plate for tack welding can be permitted and a lack-of-fit as large as $^{3}/_{16}$ in. (5 mm mm).can be tolerated after the tack welding.

The CJP groove welded transverse splice at the deck plate must be performed with a steel backing bar left in place. For ensuring adequate fusion at the weld root, at least a ½ in. (13 mm) root opening must be used. Attempts to remove the backing bar, or use of a brass or copper backing bar, and back gouging and rewilding in an overhead position must be avoided to ensure acceptable quality of this weld.

Although this research verified the infinite life fatigue performance of proposed rib-to-floor beam connection design, the effect of different geometric parameters of an orthotropic deck on the fatigue performance of the connection needs to be investigated. Research is needed related to automated fabrication of the rib-to-floor beam connection including match cutting, fitting, and robotic welding that could increase the cost-

effectiveness of this deck form. Future research is also needed for establishing rational tolerances orthotropic deck fabrication and erection, and also for investigating alternative cost-effective rib-to-floor beam connections that would promote domestic fabrication of this efficient deck system by reducing the initial cost of fabrication.

Table 1 Measured dimensional parameters of Rib 1-to-inner FB weld in full-size specimen

		Destructive Measurements by Lehigh	
SL. No.	ID[a]	LOF[b] (in.)	R[b] (in.)
1	FS_N_25	0.379	0.030
2	FS_N_50	0.478	0.022
3	FS_N_C	0.357	0.107
4	FS_S_25	0.302	0.058
5	FS_S_50	0.429	0.012
6	FS_S_C	0.300	0.180
	Maximum	0.478	0.180
	Minimum	0.300	0.012
	Mean	0.374	0.068
	Std. Dev.	0.070	0.065
	COV (%)	18.8	94.5

a. Refer to Figure 146 for identification of sections.

b. Refer Figure 147 for identification of weld parameters.

Table 2 PAUT Scan Parameters for the CJP Deck Weld

Parameter	Value
Probe	Olympus 10L32-A1
Wedge	Olympus SA1-N60S
Part material	Steel, mild
Ultrasound wave type	Shear wave (SW)
Probe Frequency	10 MHz
Available elements	32
Active elements	16
First element	1
Last element	16
Scan type used	Sectorial (S-Scan)
Minimum sector angle (Bottom boundary)	45 degree
Maximum sector angle (Top boundary)	75 degree
Angle step (S-Scan resolution)	0.2 degree
Focus depth	0.75 inches (true depth focusing)
Measurement readings:	A% (Peak amplitude detected in gate A)
	DA^ (True depth distance)
	PA^ (Horizontal distance from wedge)
	U(m-r) (Vertical cursor distance)
Scan resolution	0.05 in. (1 mm)

Table 3 Comparison between UT, PAUT and Destructive Measurements of the Transverse CJP Deck Weld

Section ID	Distance from South End (in.)	Description of the Section	UT Results		PAUT Results		Destructive Measurements (in.)
			dB	Depth (in.)	dB	Depth (in.)	
1	13.5	South Wall of Rib 1	47	0.59	41	0.60	0.65
2	27	North Wall of Rib 1	47	0.65	151.5	0.62	0.63
3	28	Under South-West LP	47	0.65	65.8	0.65	0.64
4	31	Under South-West LP	47	0.65	36.8	0.67	0.66
5	33	Under South-West LP	47	0.65	55.2	0.70	0.70
6	82.5	North Wall of Rib 3	41	0.65	200	0.68	0.68
7	99	Under North-West LP	49	0.73	77.5	0.69	0.70

Table 4 Measured Maxima of Stresses in Inner FB Web to the South of Rib 1 at 50 degree

	Measurements		Computed Principal Stresses[a] and Directions			
Face	Channel ID	Stress (ksi[b])	Maximum σp (ksi[b])	Maximum σq (ksi[b])	Direction[c] ϕ (degrees)	Illustration[d]
East	14	7.22	8.0	3.2	63.3	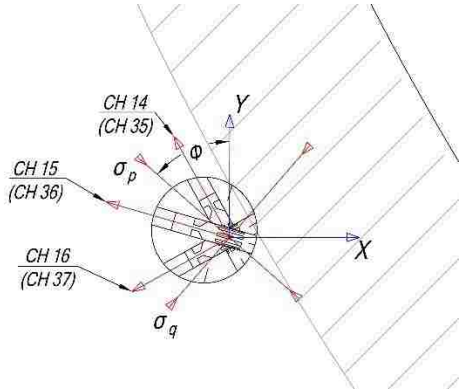
	15	3.84				
	16	3.93				
West	35	5.24	6.2	-0.9	61.5	
	36	0.26				
	37	0.09				

Notes:
[a] Tensile stresses are positive.
[b] 1 ksi = 6.91 MPa.
[c] Counter clockwise angles are positive, measured from the vertical axis (Y) passing through the center of rosette.
[d] Illustration drawn on east face. West face gauge channels are shown in parenthesis.

Table 5 Measured Maxima of Stresses in Inner FB Web to the South of Rib 1 at 25 degree

	Measurements		Computed Principal Stresses[a] and Directions			
Face	Channel ID	Stress (ksi[b])	Maximum σp (ksi[b])	Maximum σq (ksi[b])	Direction[c] ϕ (degrees)	Illustration[d]
East	19	5.59	9.8	-3.7	98.7	
	20	-3.22				
	21	0.43				
West	40	5.64	8.2	-4.6	91.6	
	41	-3.31				
	42	-2.01				

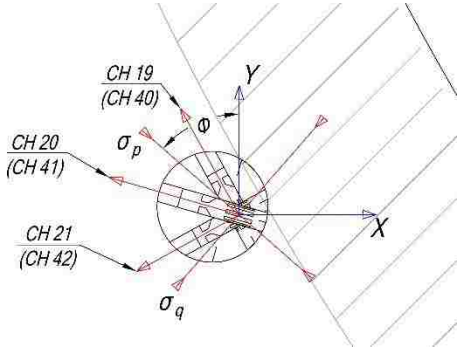

Notes:
[a] Tensile stresses are positive.
[b] 1 ksi = 6.91 MPa.
[c] Counter clockwise angles are positive, measured from the vertical axis (Y) passing through the center of rosette.
[d] Illustration drawn on east face. West face gauge channels are shown in parenthesis.

Table 6 Measured Stress Ranges in Inner FB Web to the South of Rib 1 at 50 degree

	Measurements		Computed Principal Stresses[a] and Directions			
Face	Channel ID	Stress (ksi[b])	Maximum σp (ksi[b])	Maximum σq (ksi[b])	Direction[c] ϕ (degrees)	Illustration[d]
East	14	6.63	7.3	2.9	63.3	
	15	3.55				
	16	3.60				
West	35	4.84	5.7	-0.7	61.5	
	36	0.29				
	37	0.13				

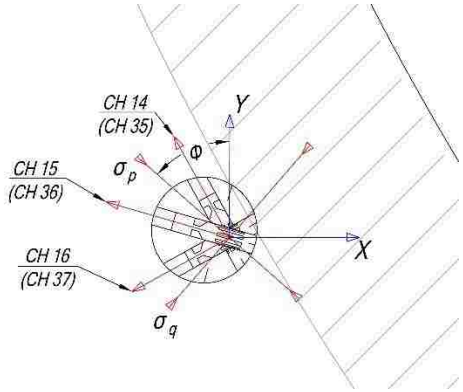

Notes:
[a] Tensile stresses are positive.
[b] 1 ksi = 6.91 MPa.
[c] Counter clockwise angles are positive, measured from the vertical axis (Y) passing through the center of rosette.
[d] Illustration drawn on east face. West face gauge channels are shown in parenthesis.

Table 7 Measured Stress Ranges in Inner FB Web to the South of Rib 1 at 25 degree

	Measurements		Computed Principal Stresses[a] and Directions			
Face	Channel ID	Stress (ksi[b])	Maximum σp (ksi[b])	Maximum σq (ksi[b])	Direction[c] ϕ (degrees)	Illustration[d]
East	19	5.18	9.0	-3.4	98.7	
	20	-2.93				
	21	0.39				
West	40	5.21	7.6	-4.2	91.6	
	41	-3.01				
	42	-1.82				

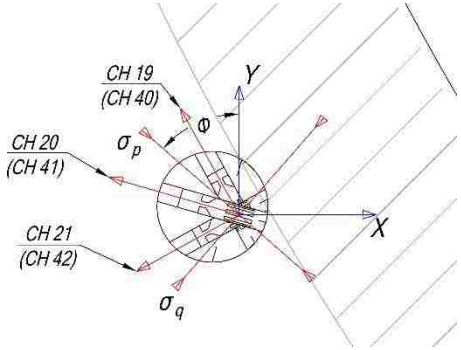

Notes:
[a] Tensile stresses are positive.
[b] 1 ksi = 6.91 MPa.
[c] Counter clockwise angles are positive, measured from the vertical axis (Y) passing through the center of rosette.
[d] Illustration drawn on east face. West face gauge channels are shown in parenthesis.

FIGURES

Figure 1 The lift bridge

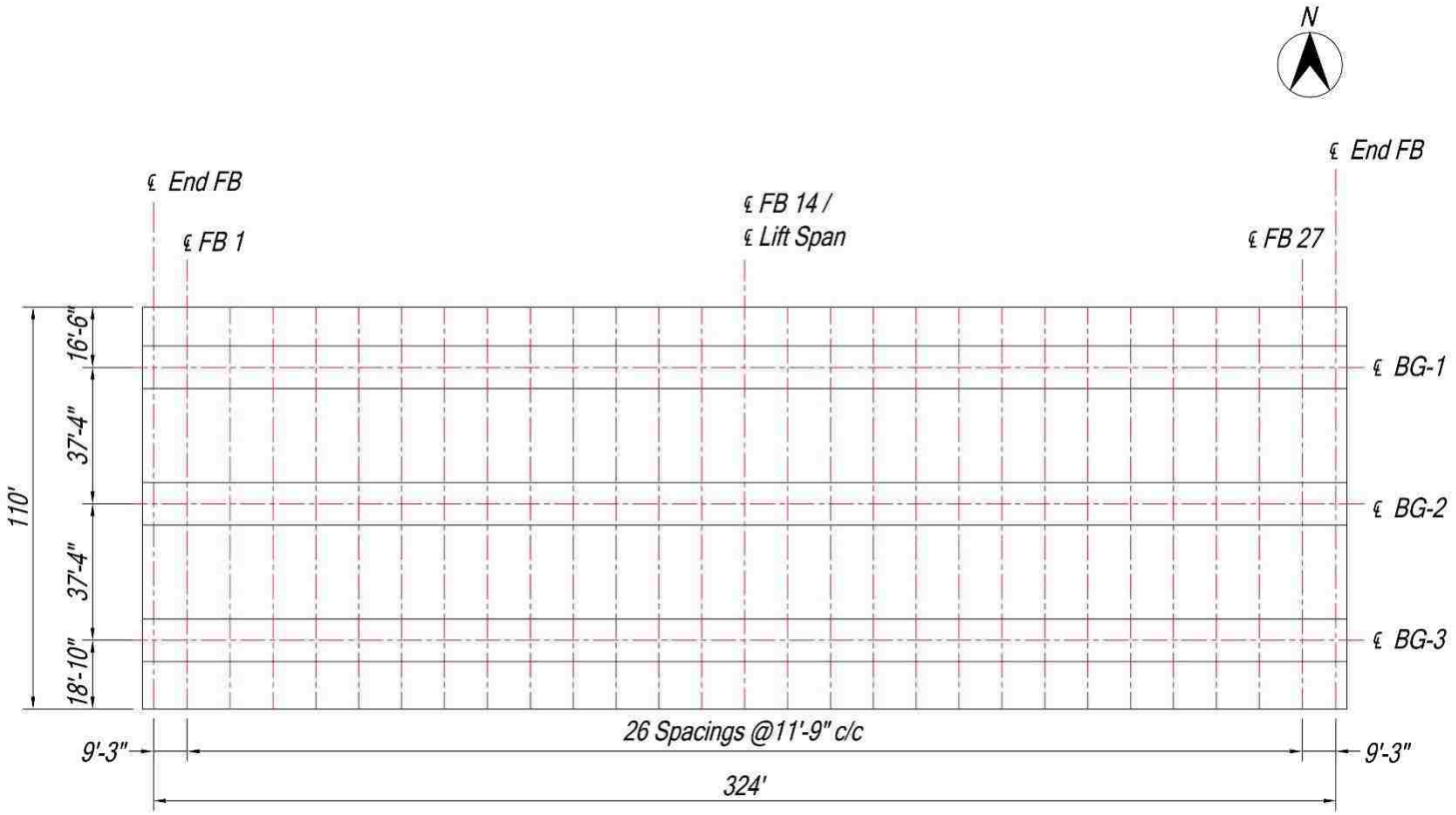

Figure 2 Framing plan of the bridge deck

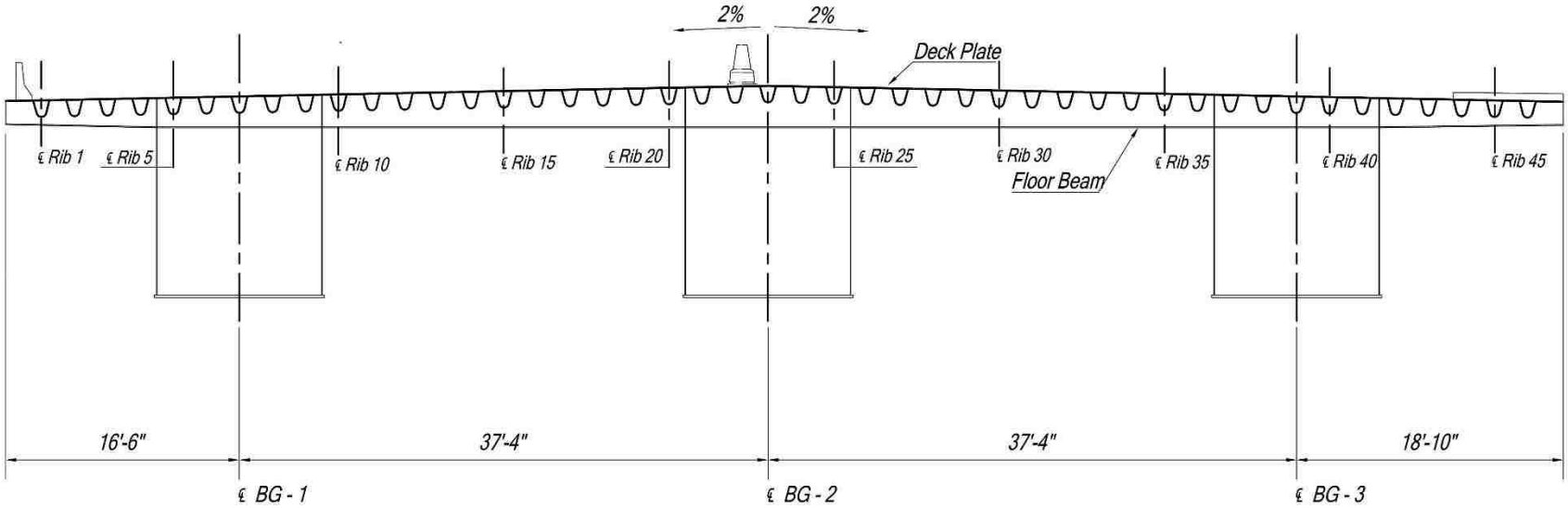

Figure 3 Cross section of the deck at floor beam

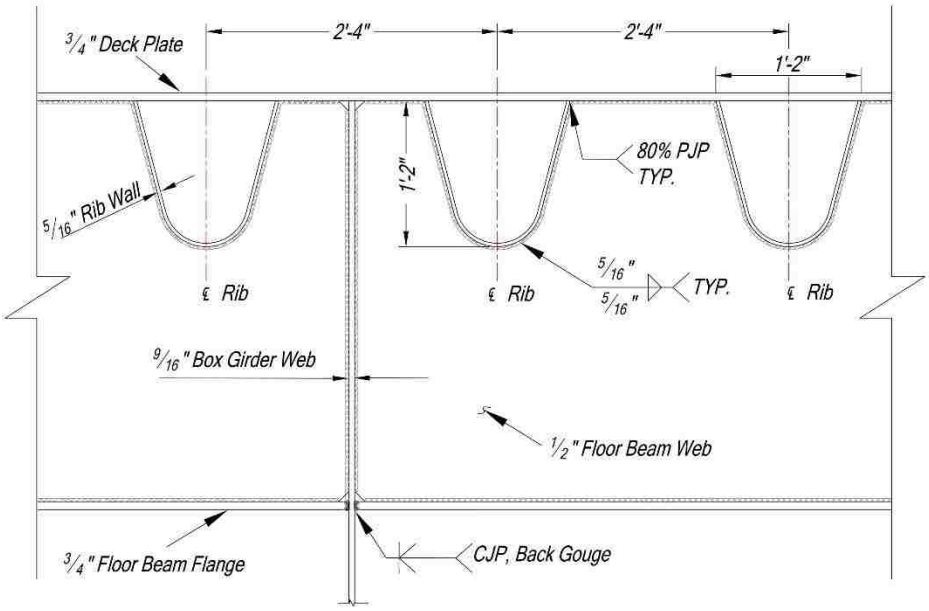

Figure 4 Design deck details

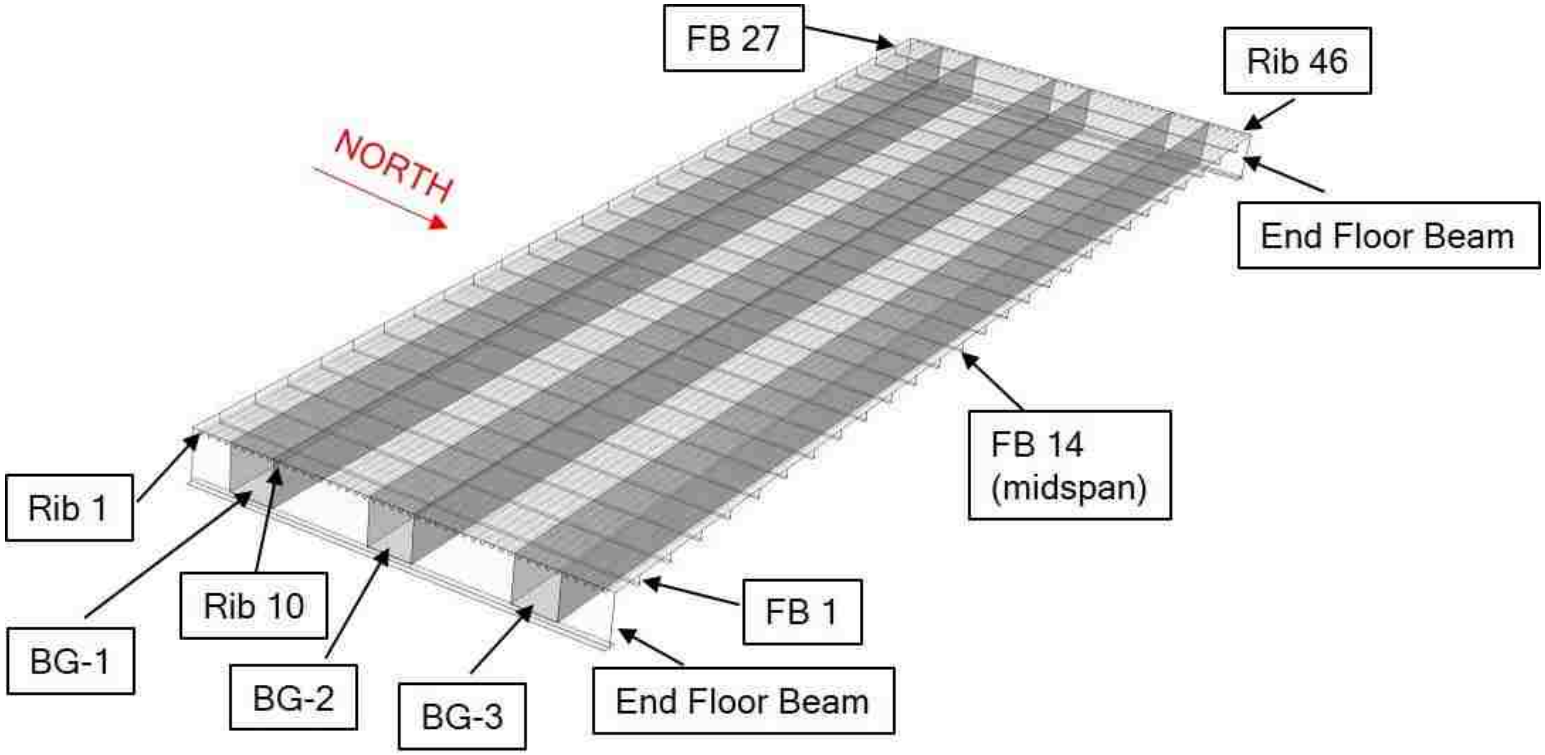

Figure 5 Global model - top view

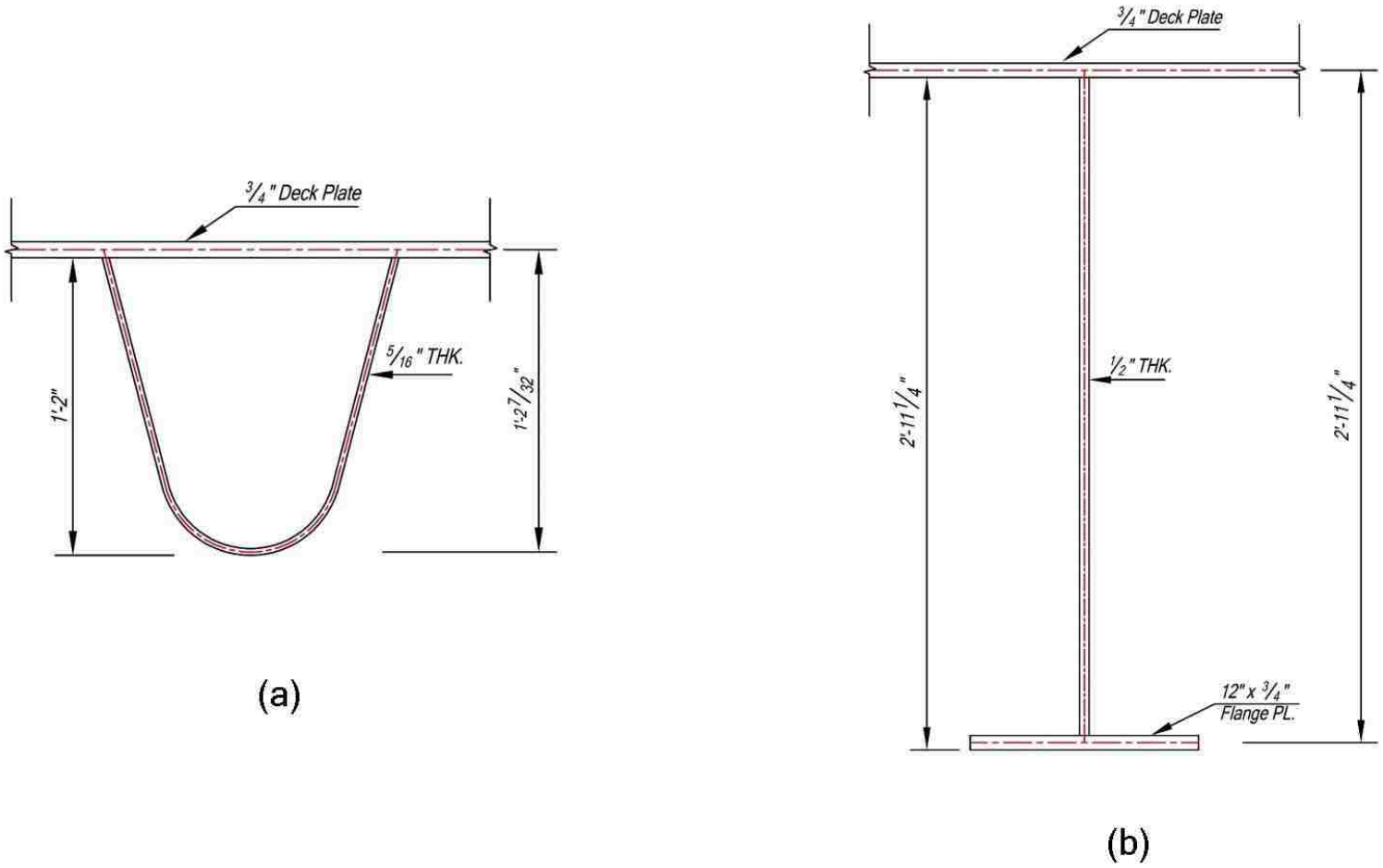

Figure 6 Details of global model: (a) rib; (b) floor beam

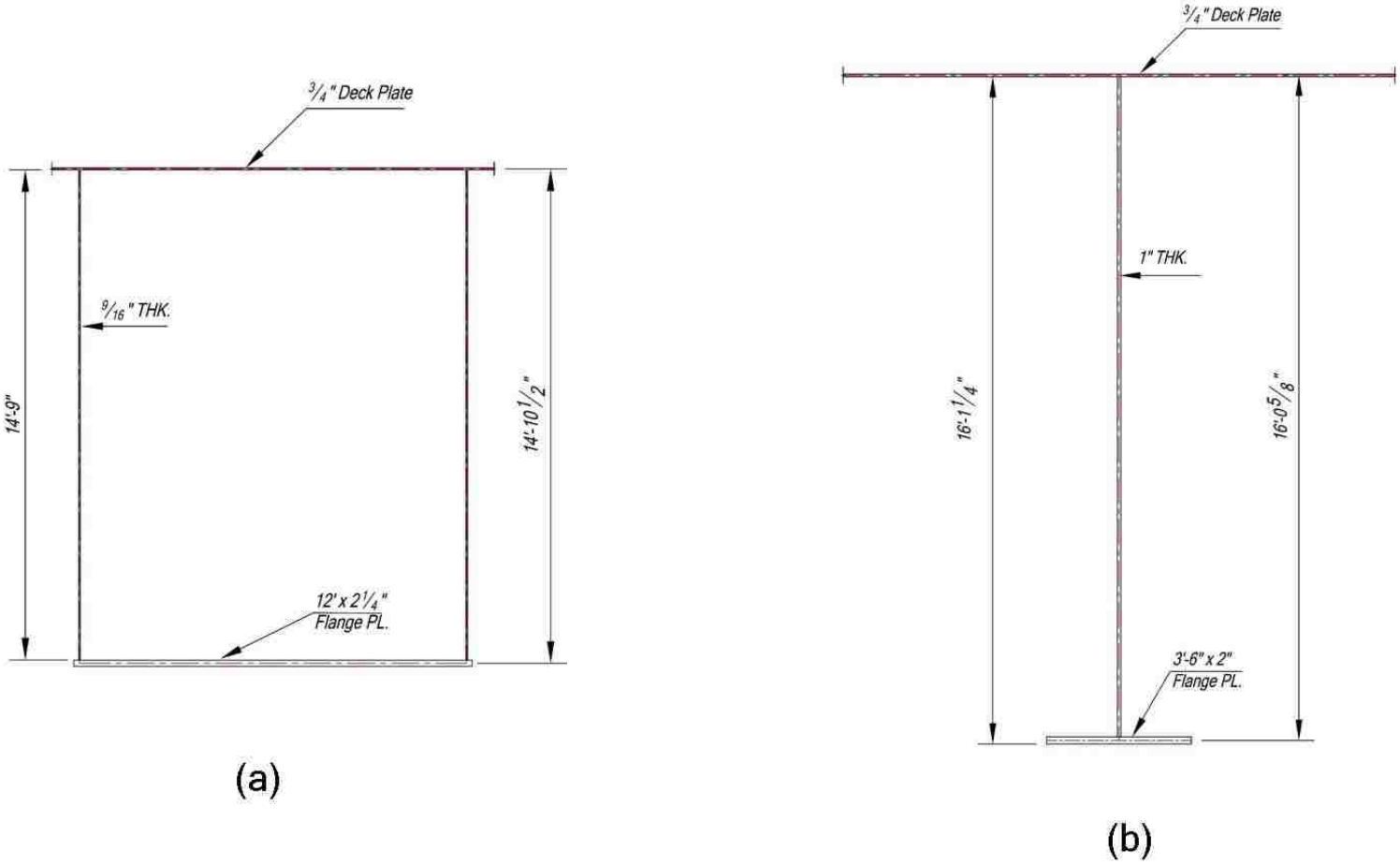

Figure 7 Cross section of: (a) box girder; (b) end floor beam

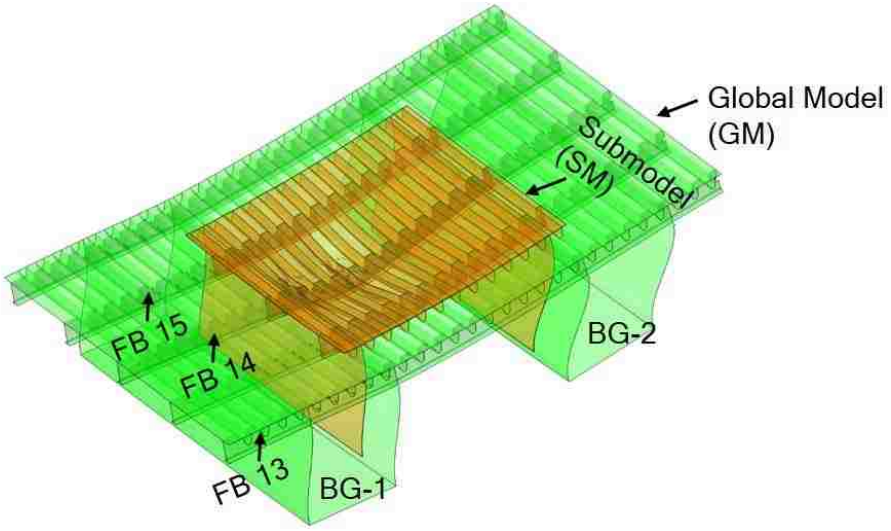

Figure 8 Top view of part GM showing extent of SM

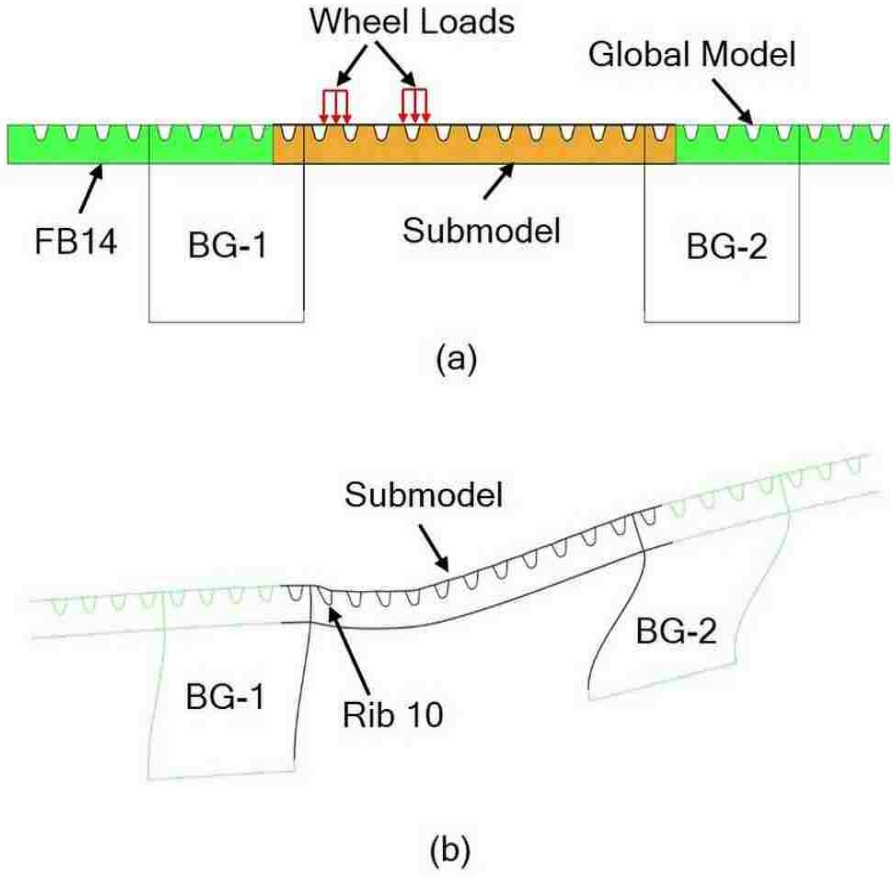

Figure 9 **Part cross sections of undeformed and deformed GMs with the extent of SM identified: (a) undeformed; (b) deformed**

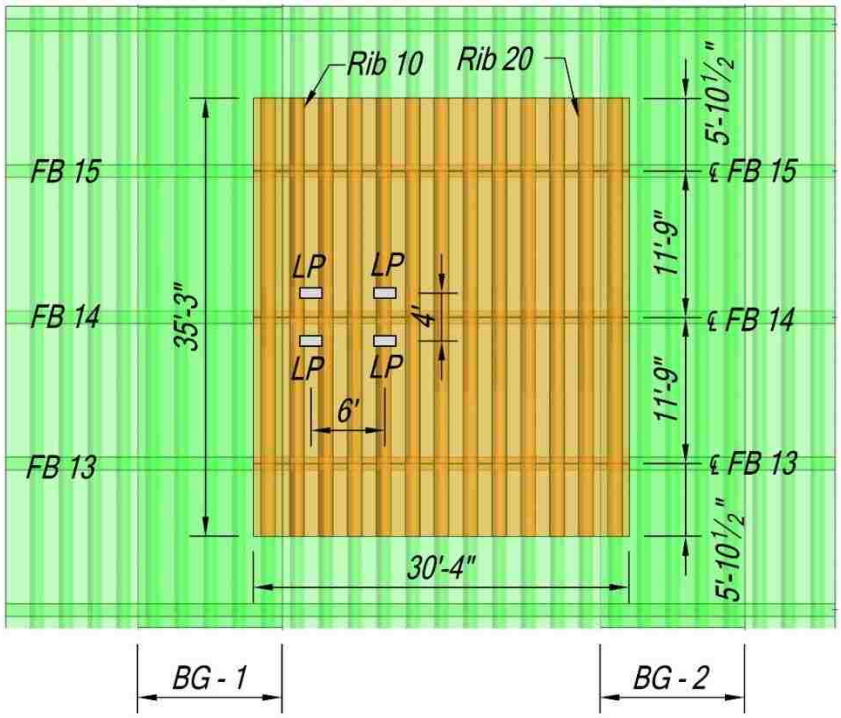

Figure 10 **Underside view of part GM showing the extent and dimensions of the SM (load positions also marked)**

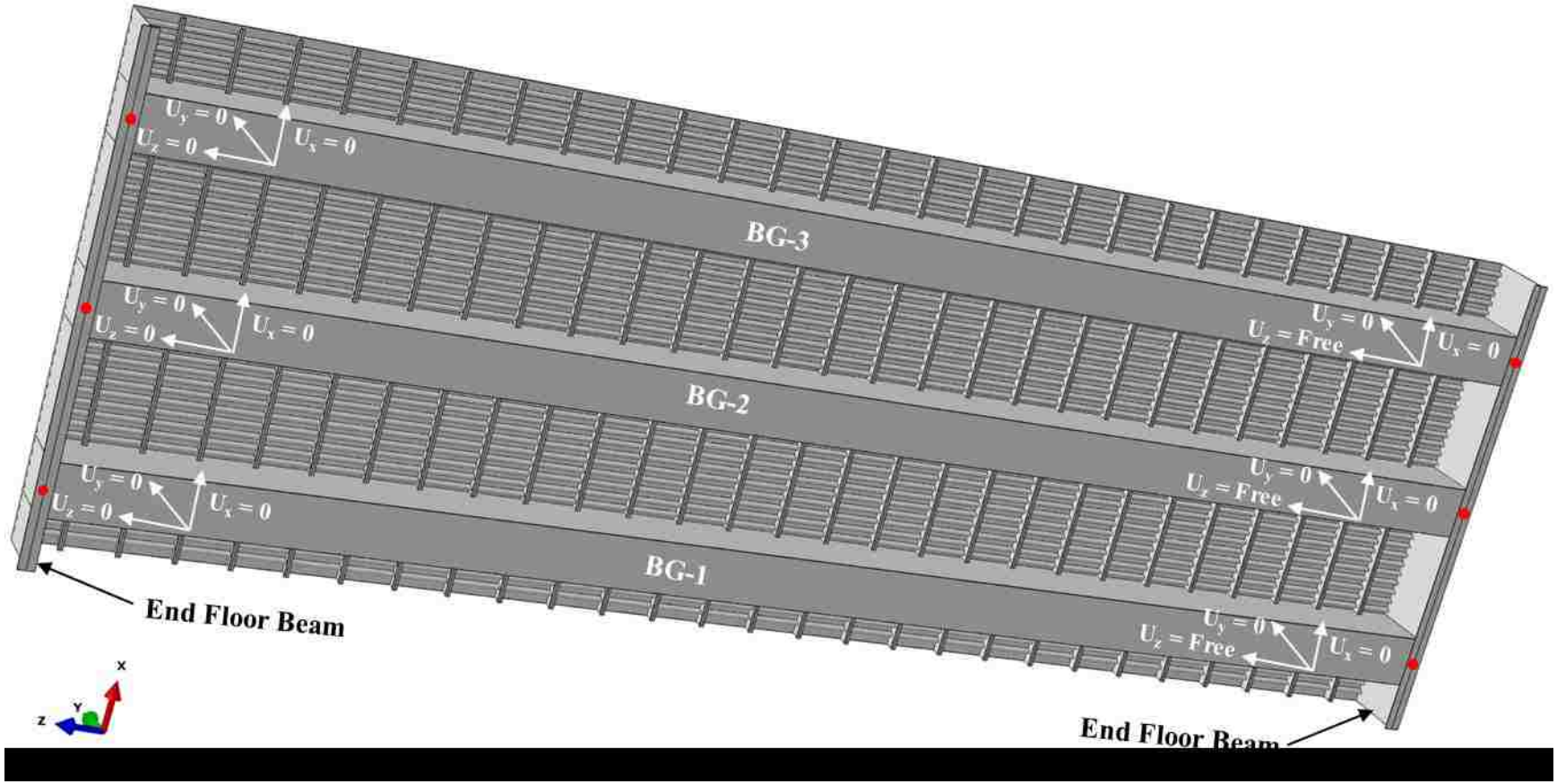

Figure 11 **3D FE model of the bridge deck – underside view showing the boundary conditions specified at the soffit of the end floor beams at locations identified as dots.**

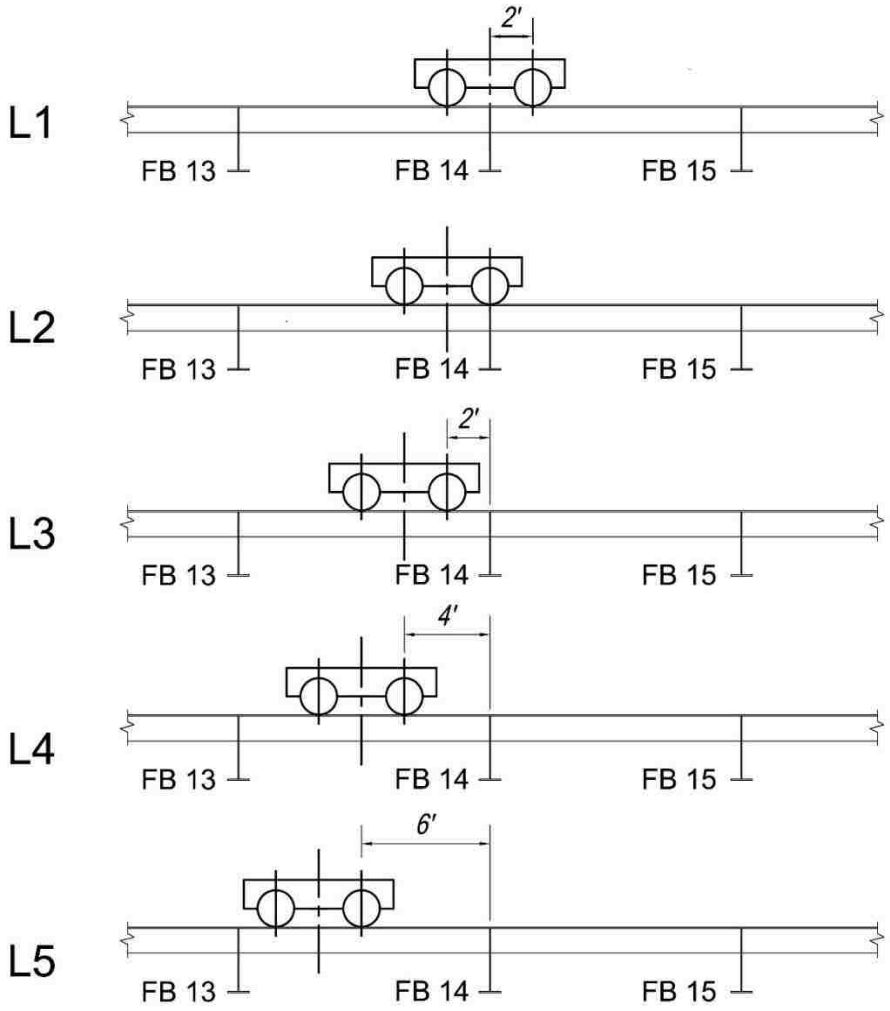

Figure 12 Longitudinal disposition of AASHTO tandem axles considered for FEA of bridge deck

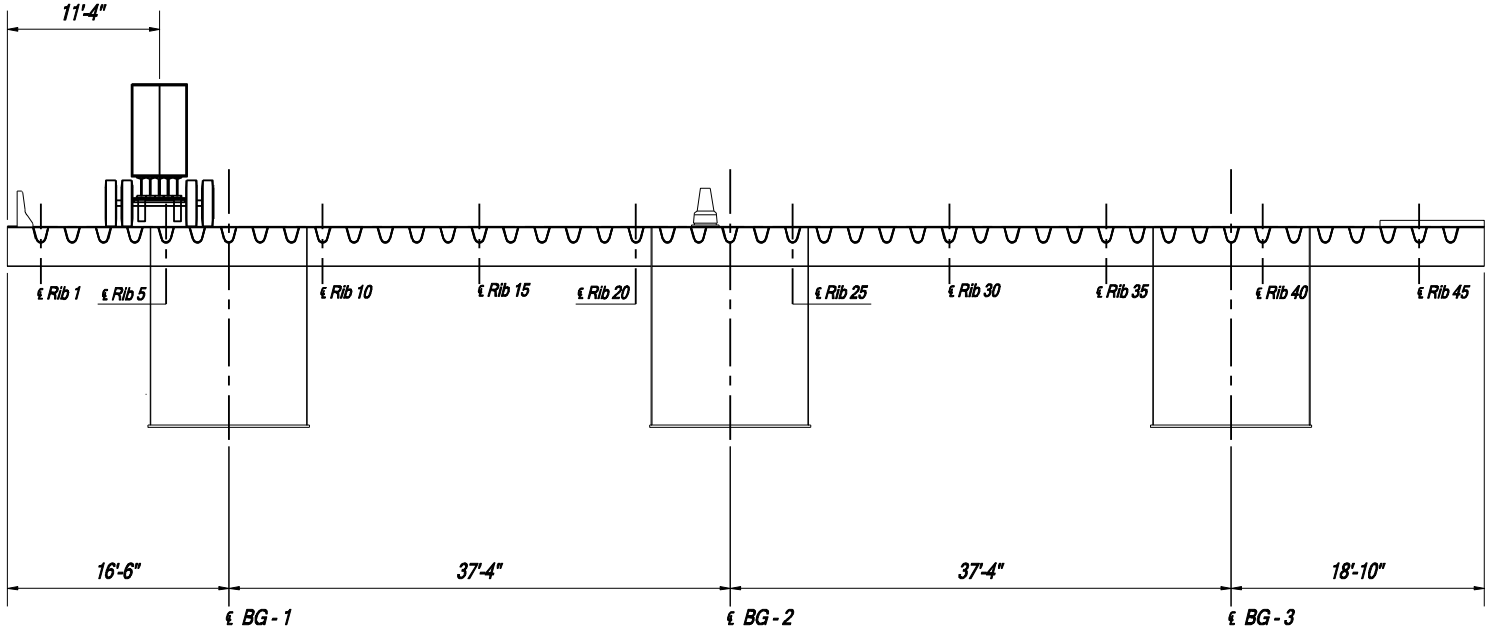

Figure 13 Transverse load position T1 considered for FEA of bridge deck

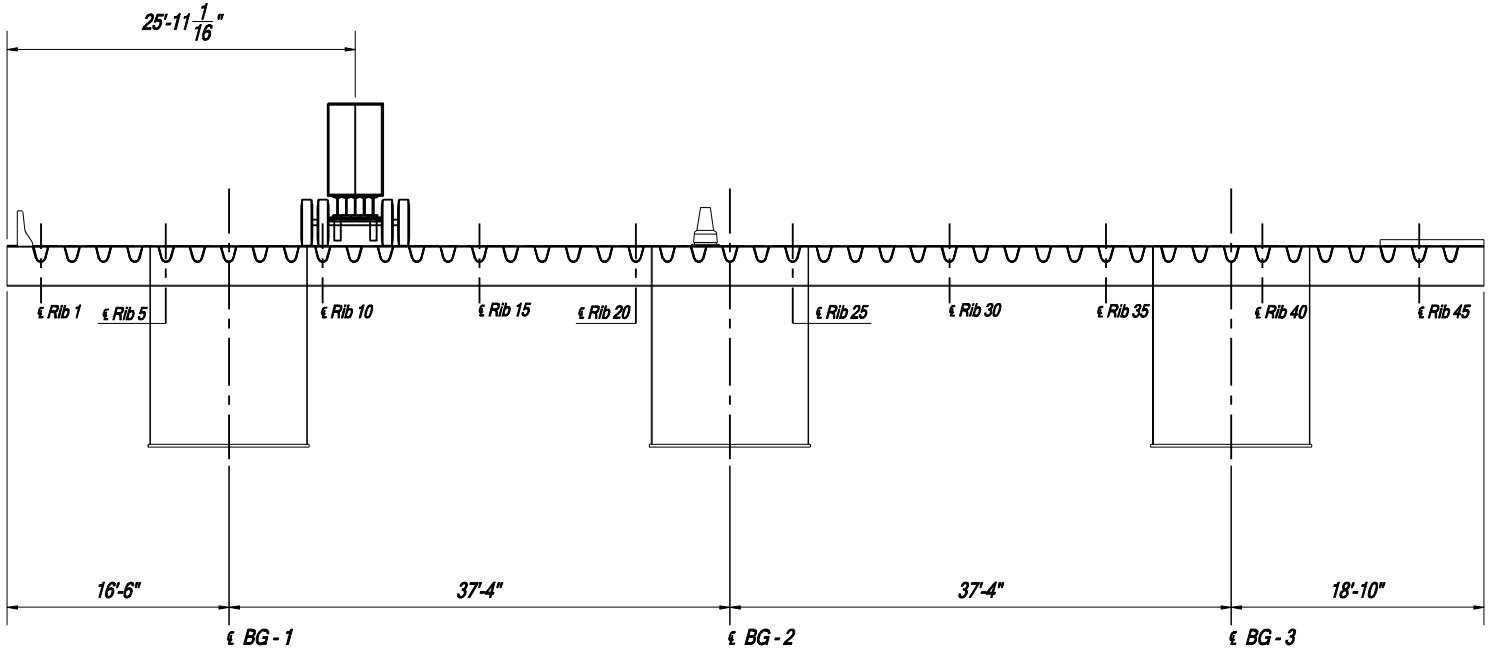

Figure 14 Transverse load position T26 considered for FEA of bridge deck

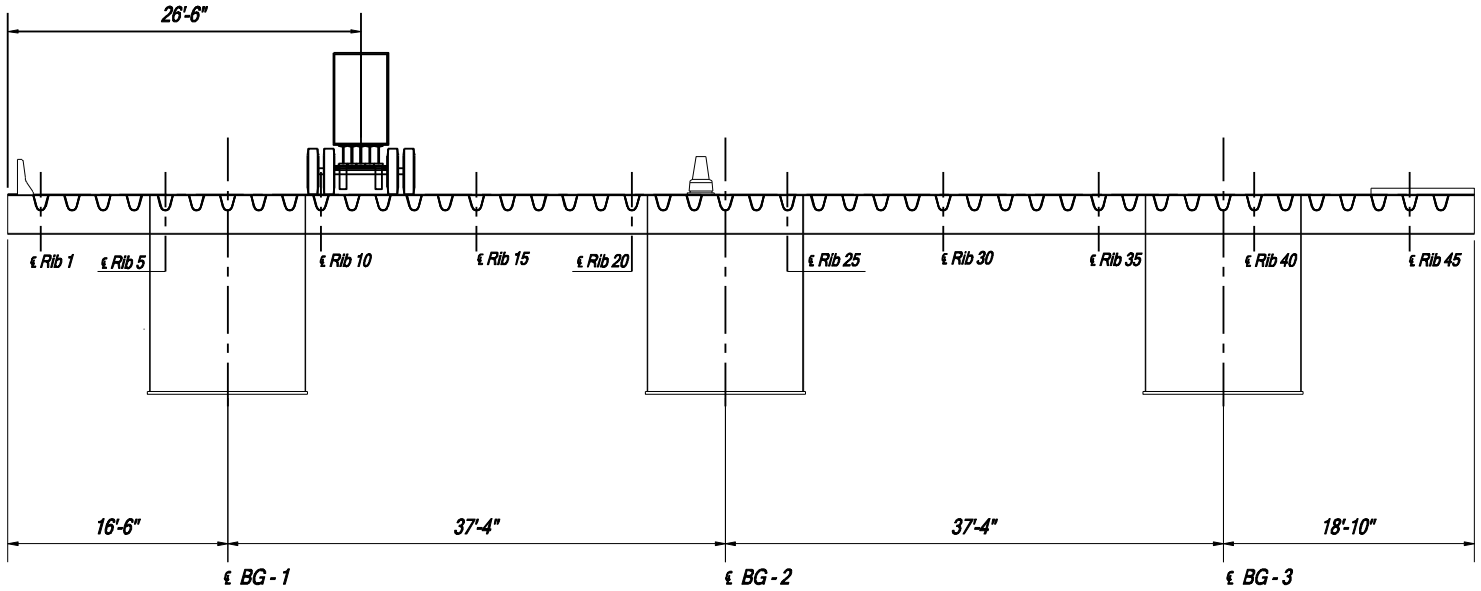

Figure 15 Transverse load position T27 considered for FEA of bridge deck

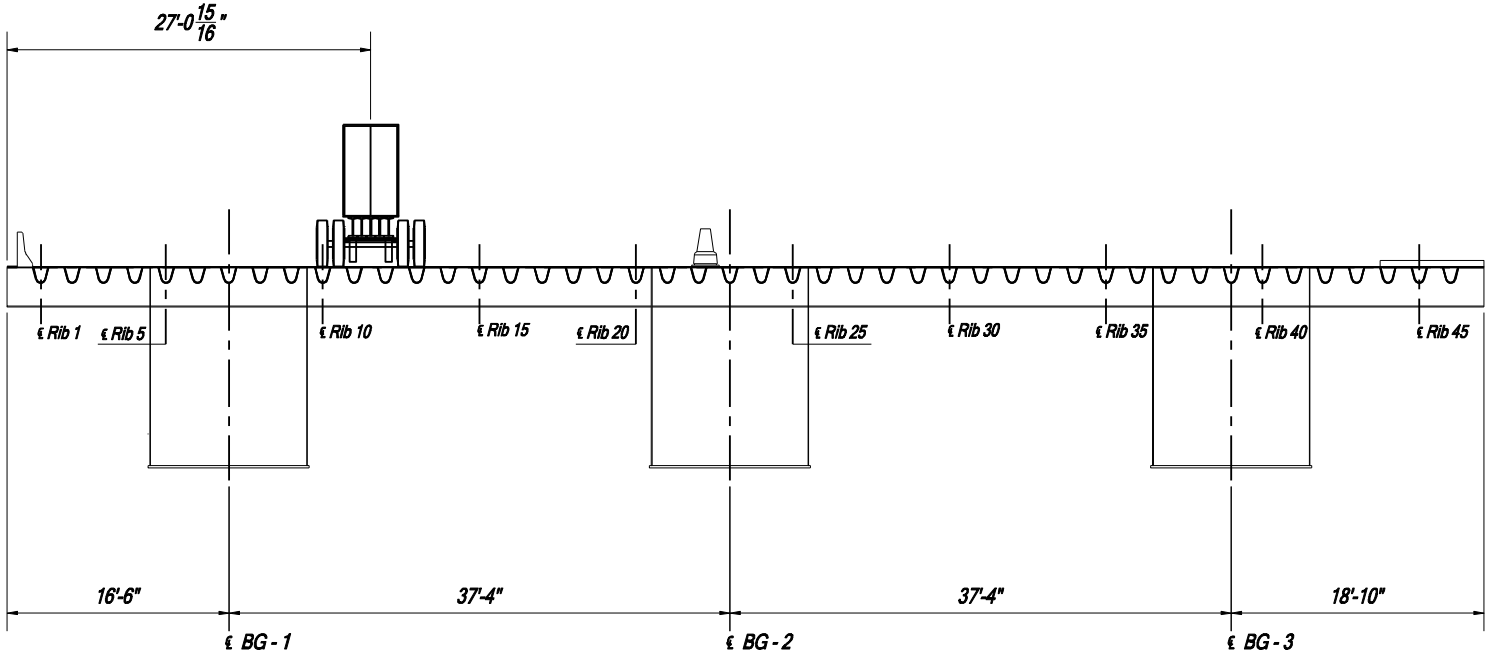

Figure 16 Transverse load position T28 considered for FEA of bridge deck

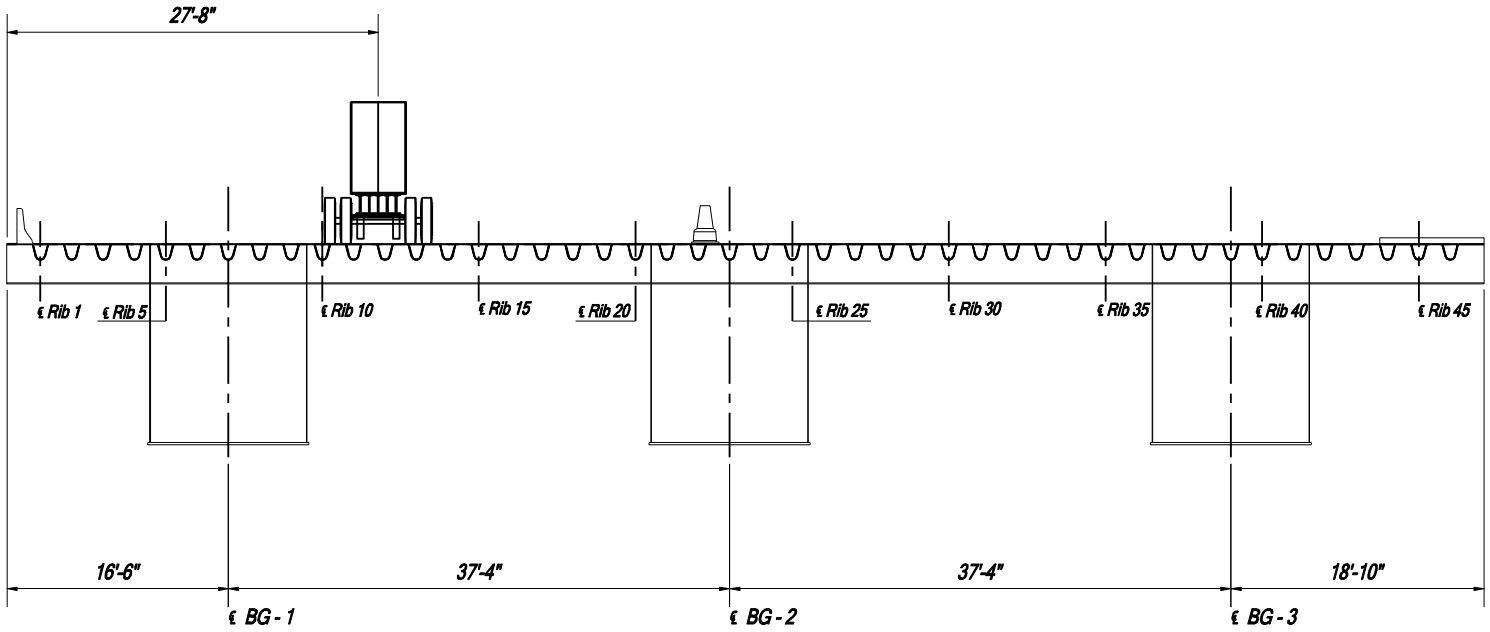

Figure 17 Transverse load position T29 considered for FEA of bridge deck

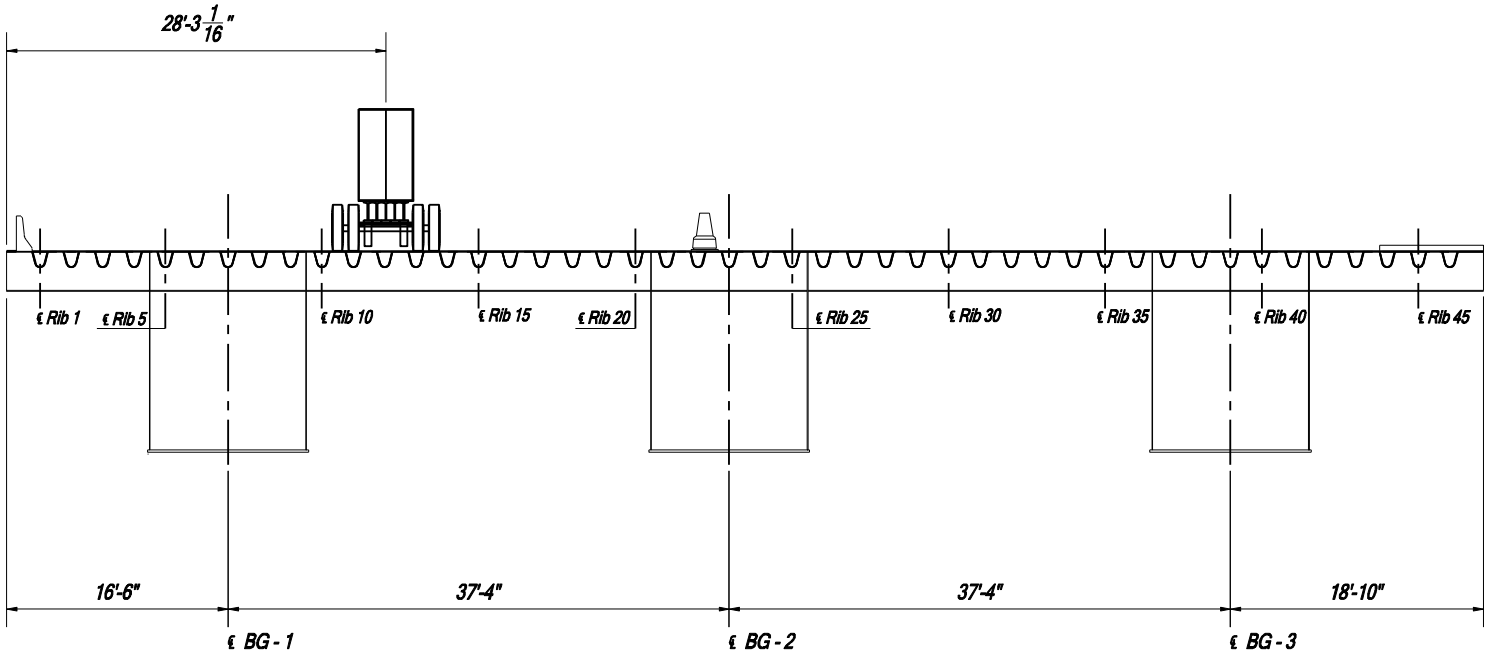

Figure 18 Transverse load position T30 considered for FEA of bridge deck

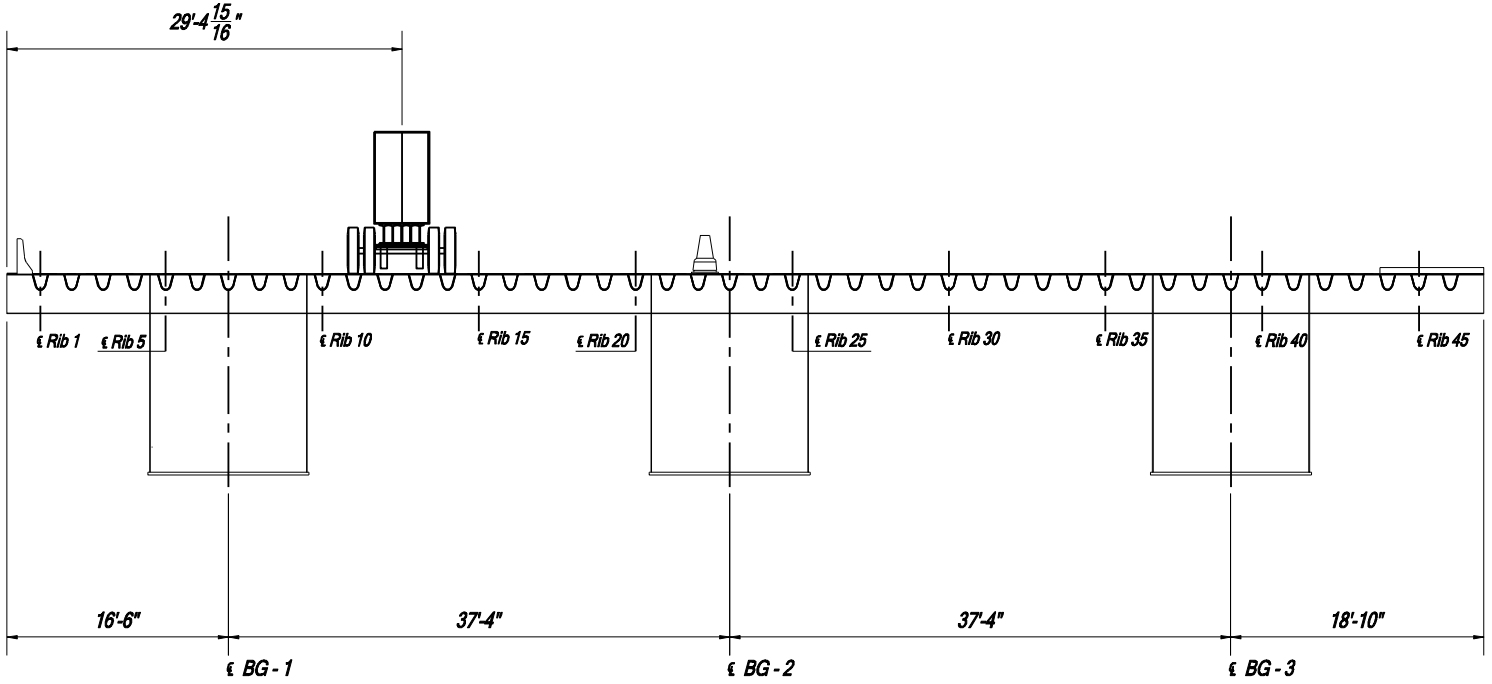

Figure 19 Transverse load position T33 considered for FEA of bridge deck

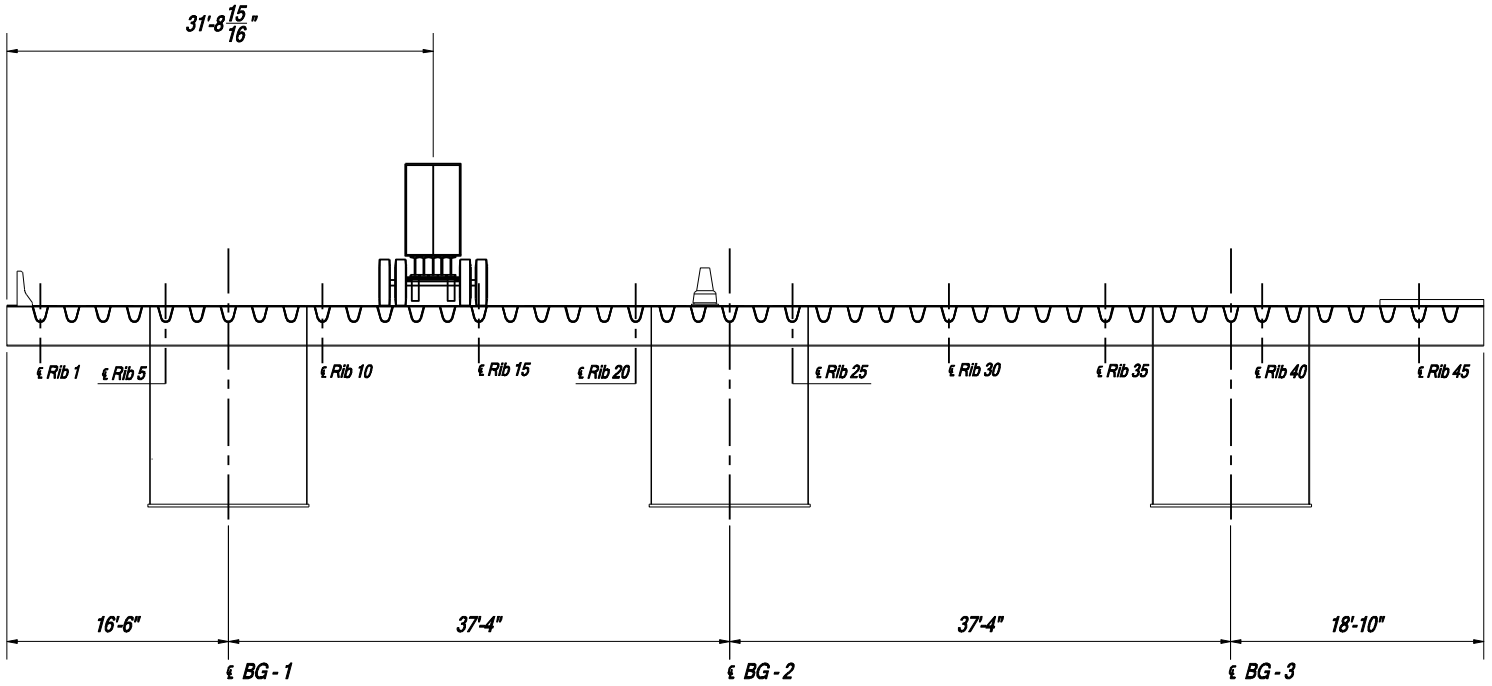

Figure 20 Transverse load position T34 considered for FEA of bridge deck

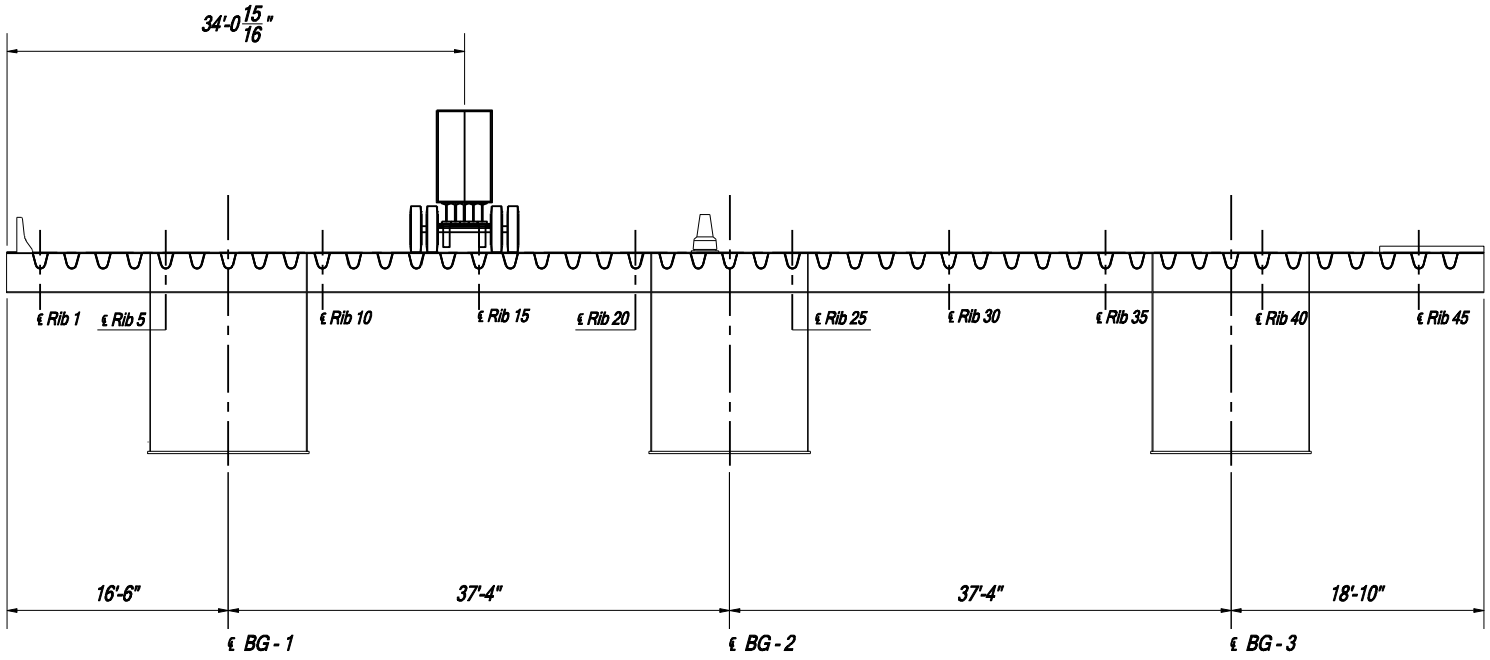

Figure 21 Transverse load position T35 considered for FEA of bridge deck

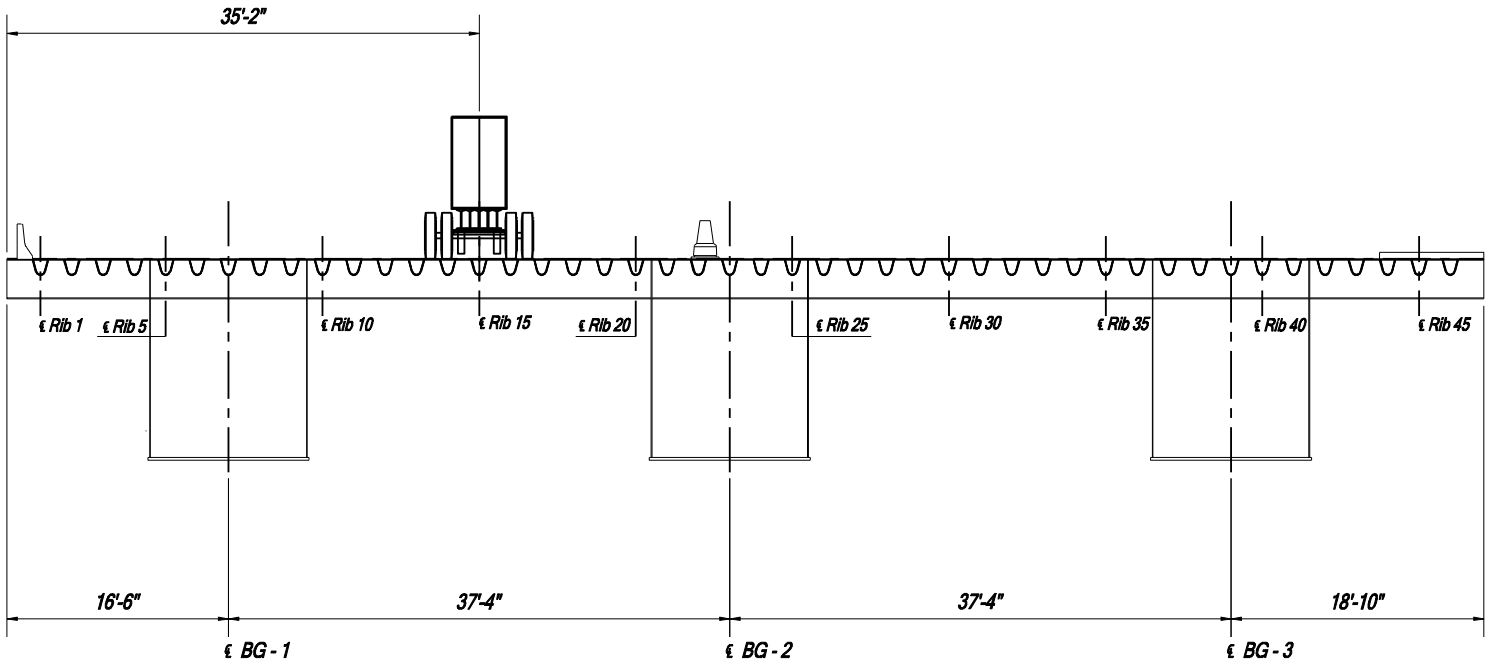

Figure 22 Transverse load position T36 considered for FEA of bridge deck

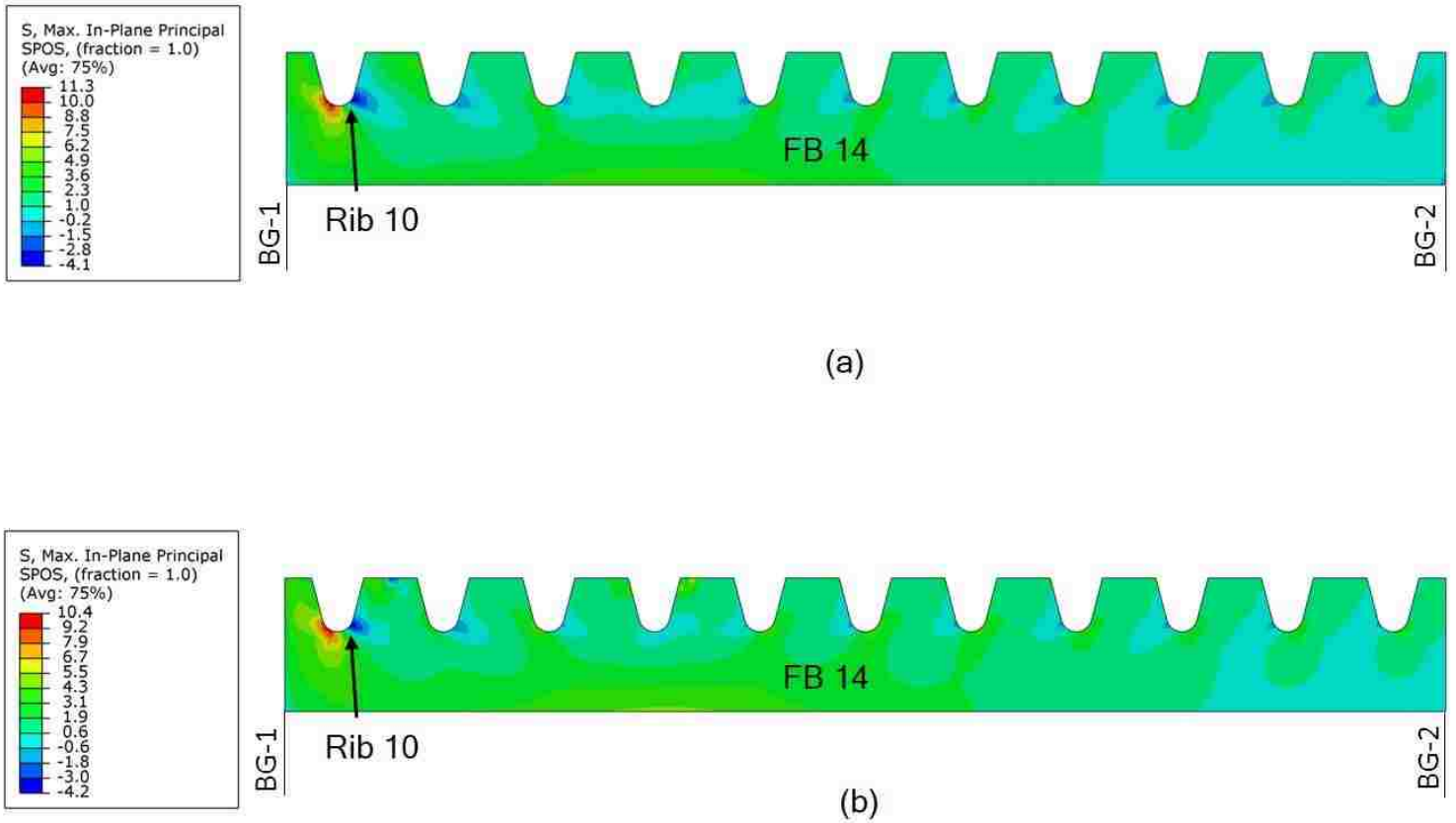

Figure 23 Maximum in-plane principal stress in FB 14 (between BG-1 and BG-2) for: (a) L1T29; (b) L2T29

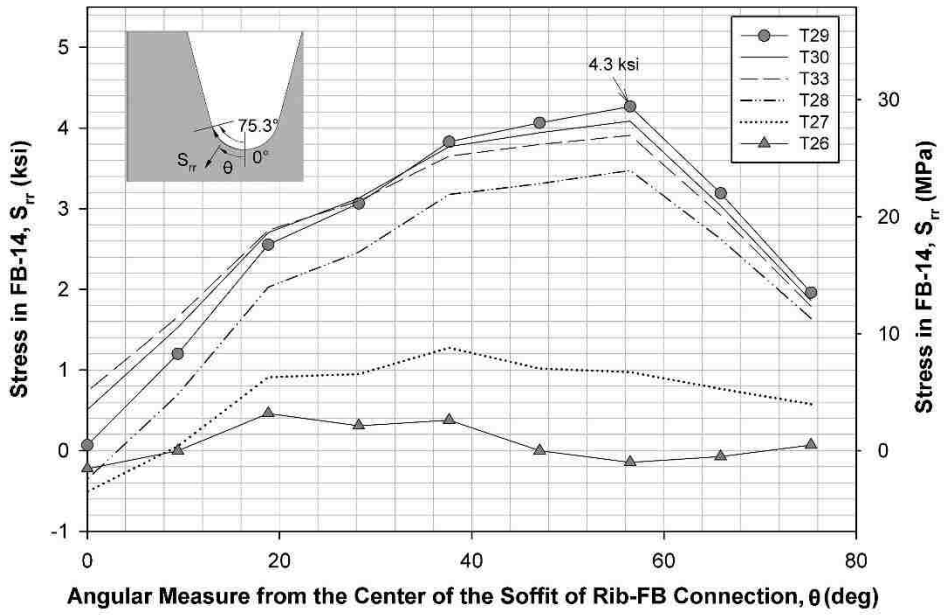

Figure 24 Comparison of tensile stress normal to rib-to-floor beam connection in floor beam web for different transverse load cases corresponding to L1

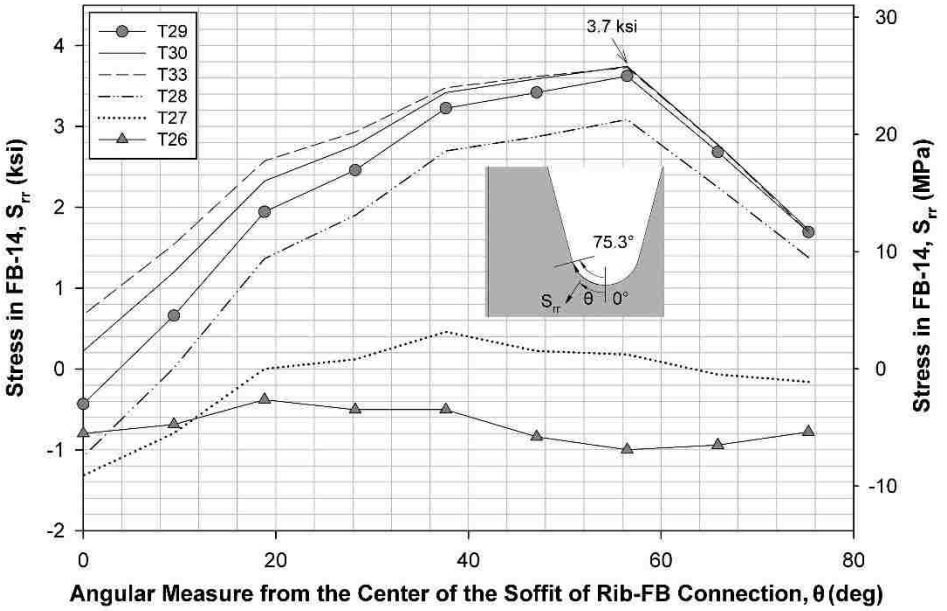

Figure 25 Comparison of tensile stress normal to rib-to-floor beam connection in floor beam web for different transverse load cases corresponding to L2

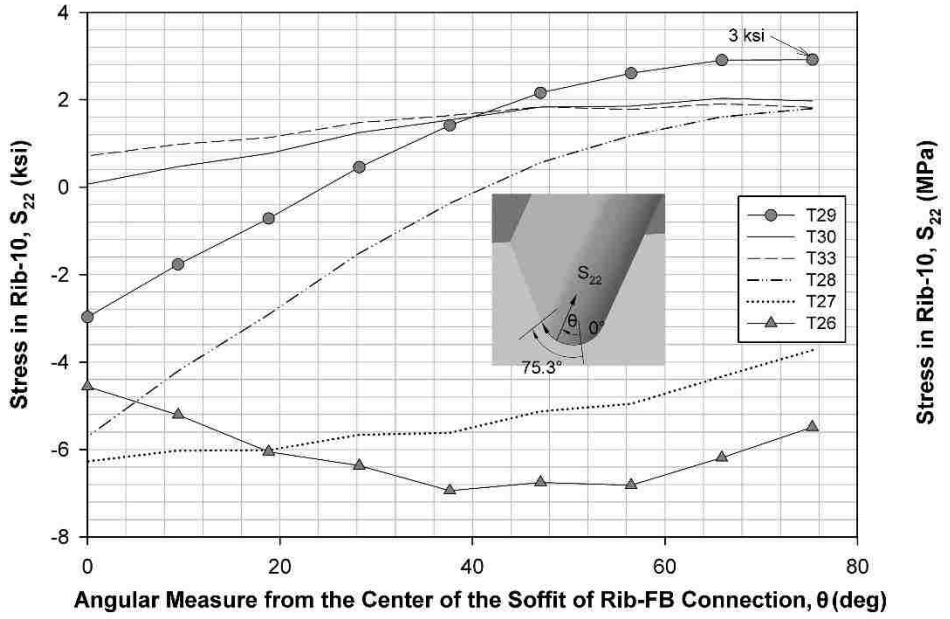

Figure 26 Comparison of tensile stress normal to rib-to-floor beam connection in rib wall for different transverse load cases corresponding to L1

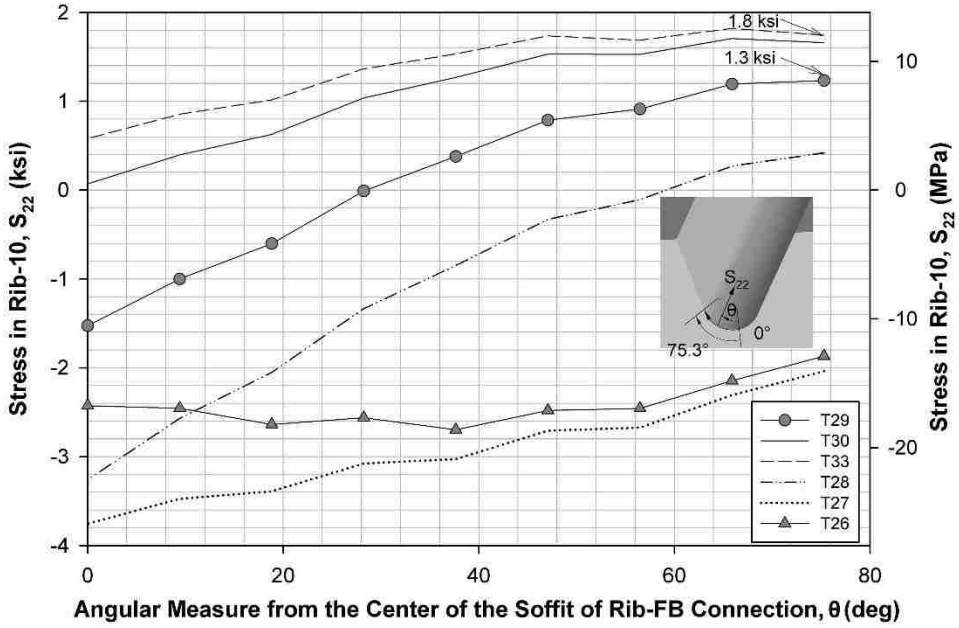

Figure 27 Comparison of tensile stress normal to rib-to-floor beam connection in rib wall for different transverse load cases corresponding to L2

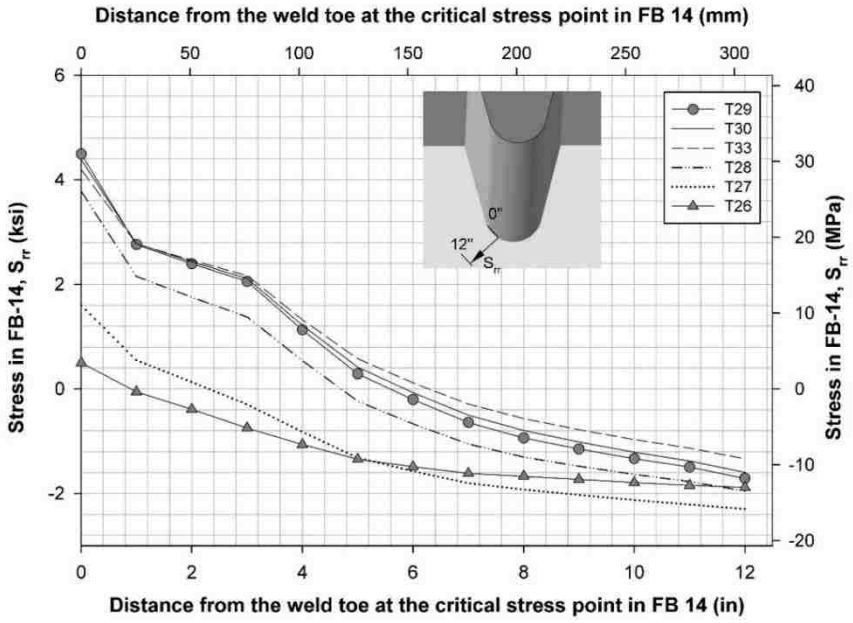

Figure 28 Variation of tensile stress normal to rib-to-floor beam connection in floor beam web along a radial path starting from the point of maximum tensile stress for L1

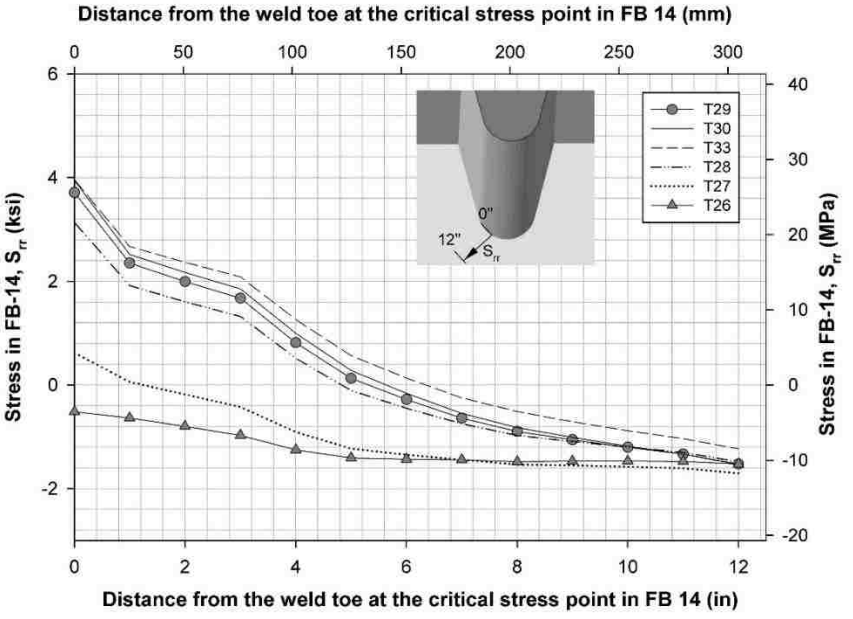

Figure 29 Variation of tensile stress normal to rib-to-floor beam connection in floor beam web along a radial path starting from the point of maximum tensile stress for L2

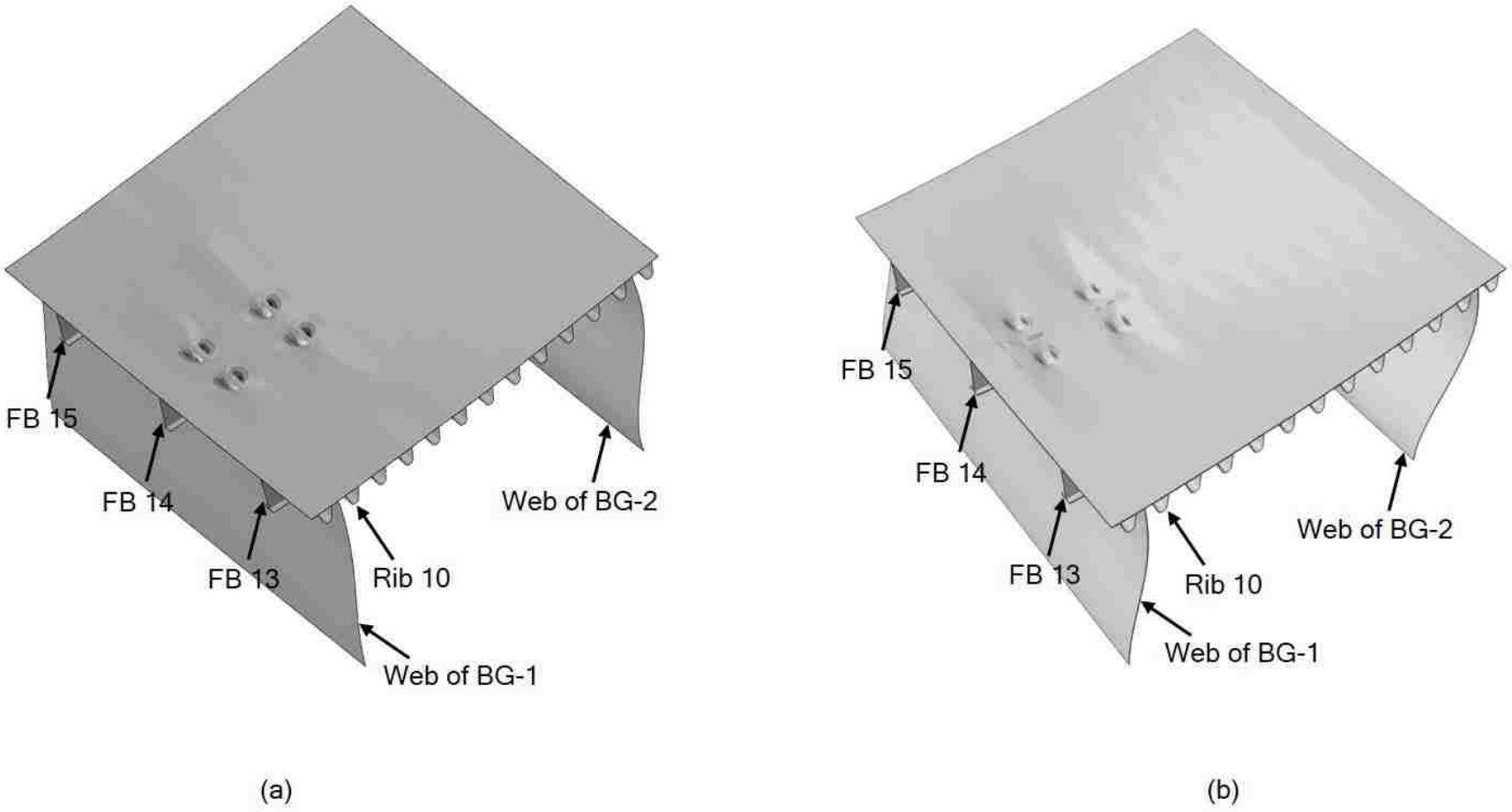

Figure 30 Principal stress contour on deformed configuration (350x) of: (a) global model; (b) submodel

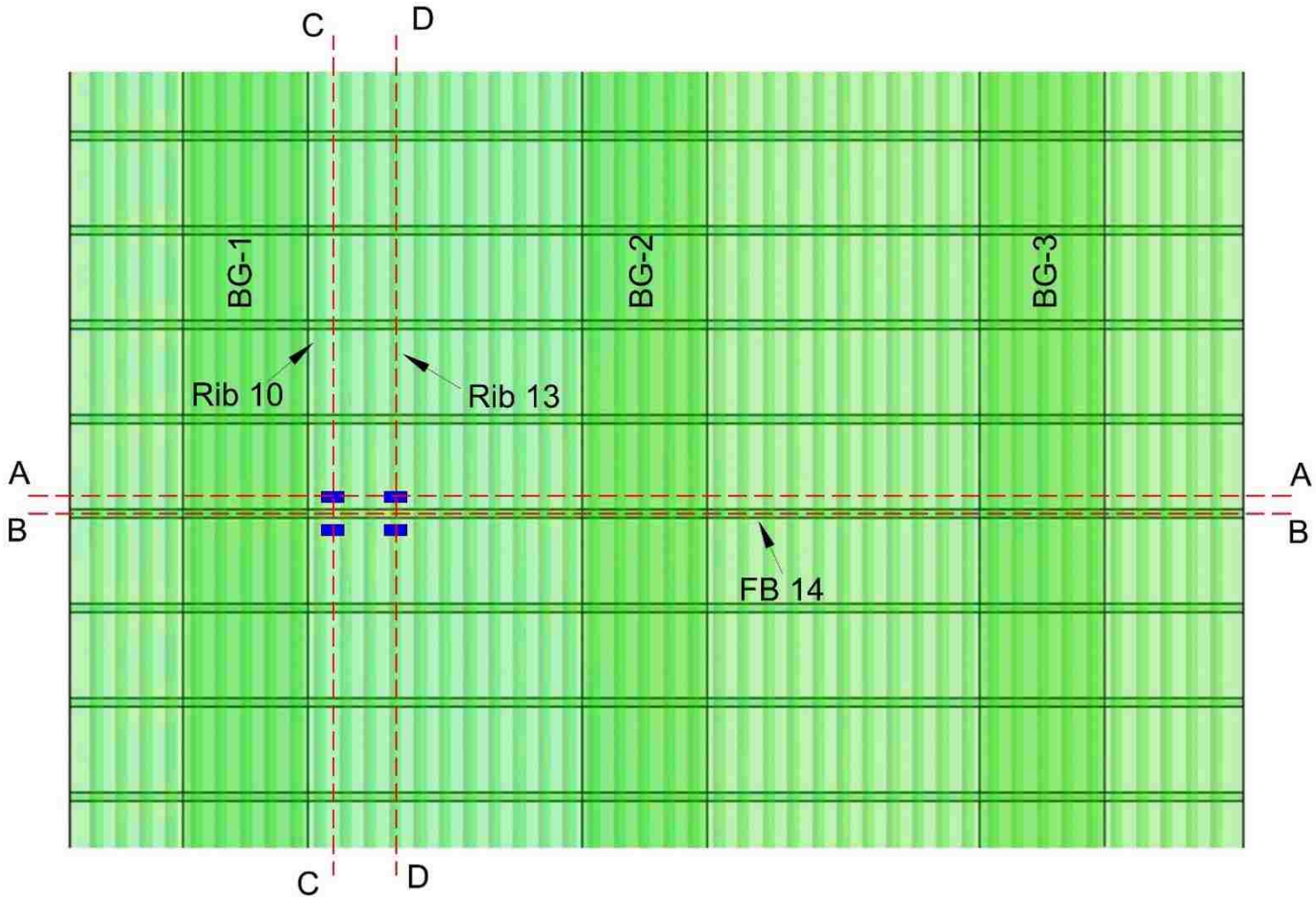

Figure 31 **Plan view of part global model showing the sections at which response of deck plate and ribs are discussed**

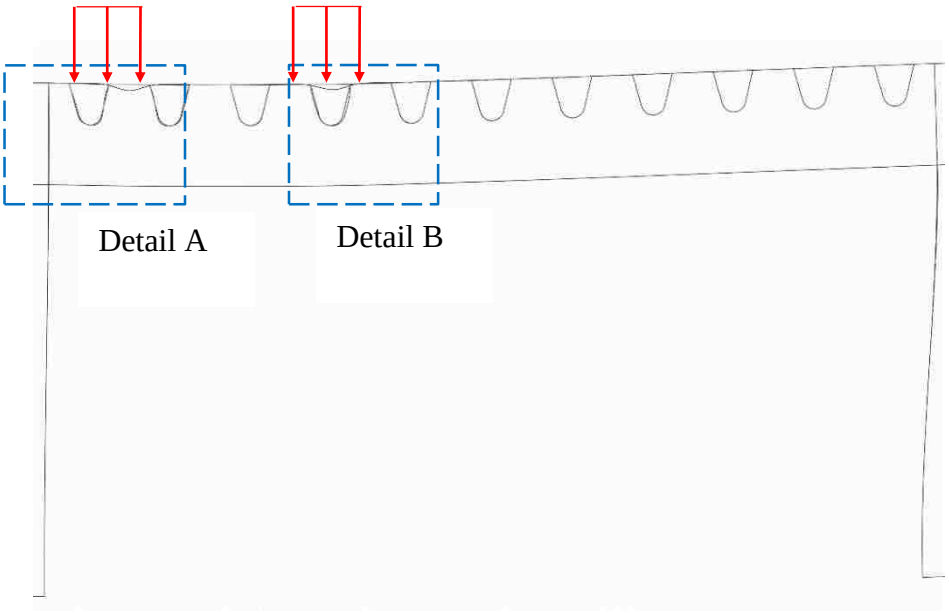

Figure 32 Overlay plot of deck comparing local transverse bending at sections A-A and B-B (50x)

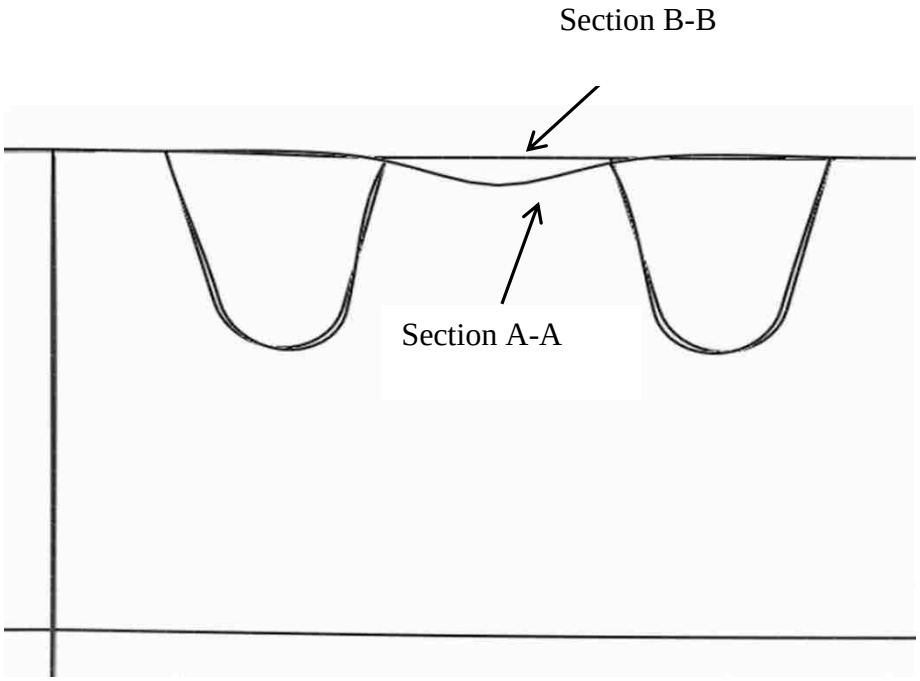

Figure 33 Detail A of Figure 32

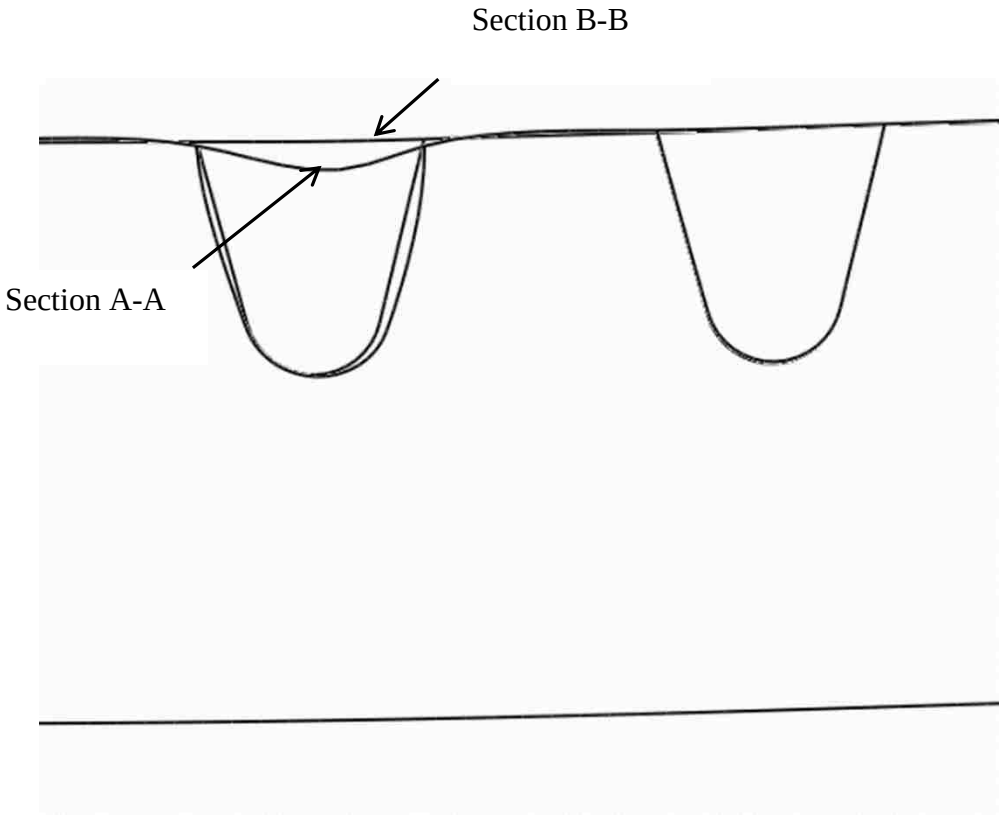

Figure 34 Detail B of Figure 32

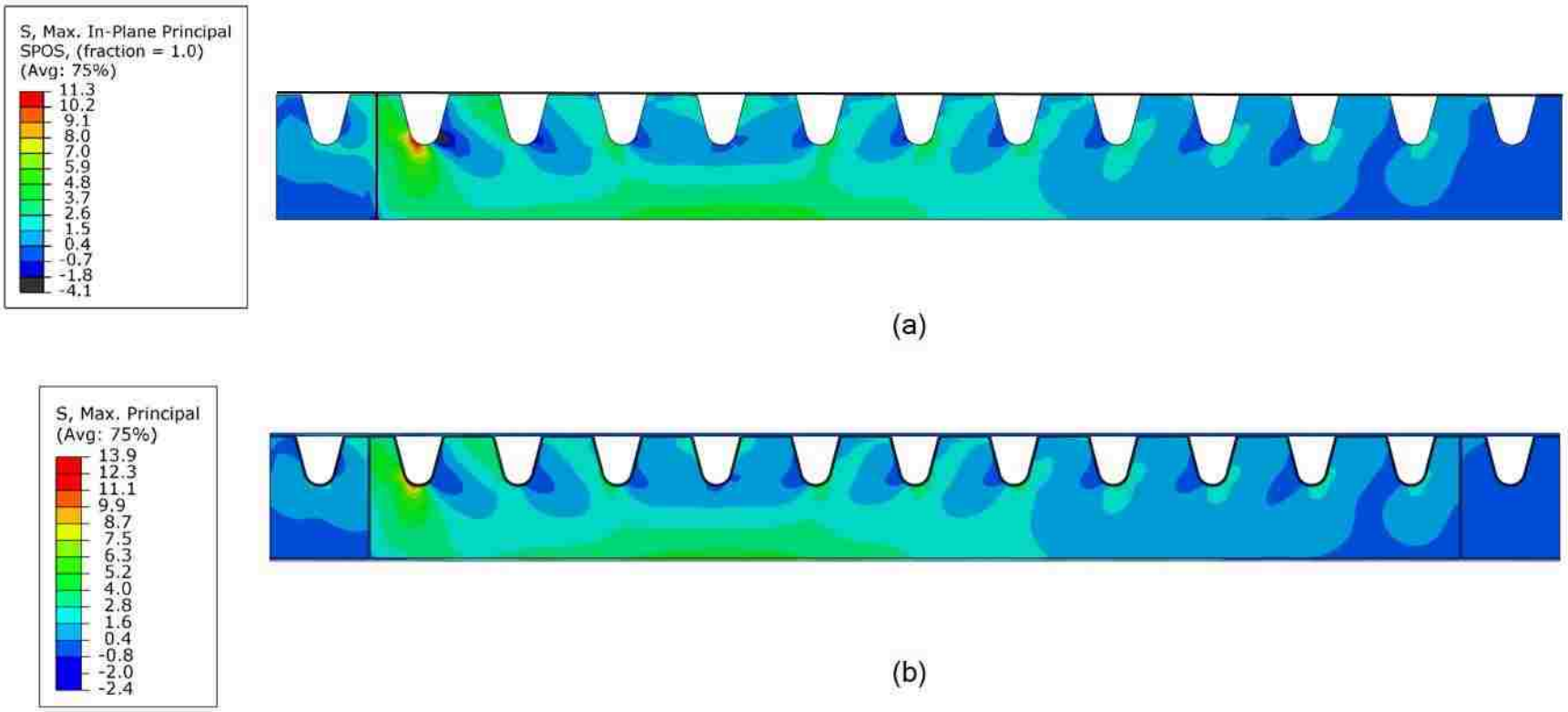

Figure 35 Principal stress contour in FB 14: (a) global model; (b) submodel

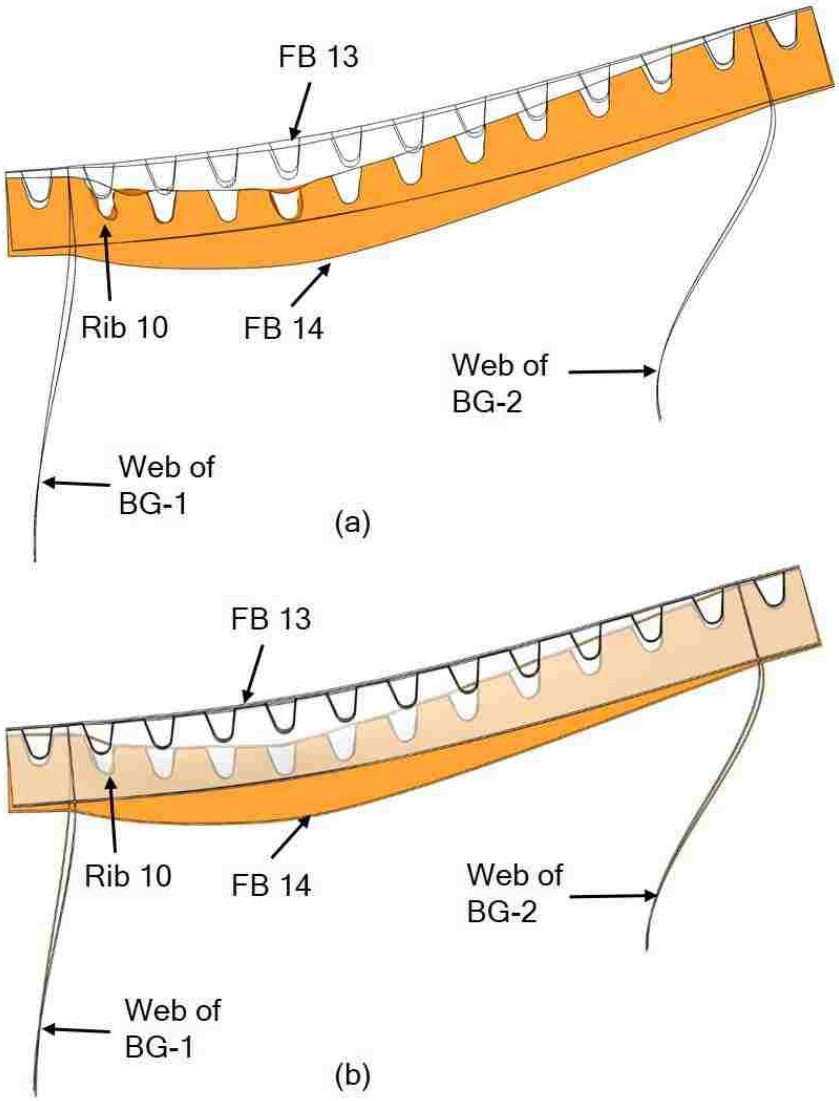

Figure 36 Maximum deformation of FB 13 and FB 14 (500x); (a) global model; (b) submodel

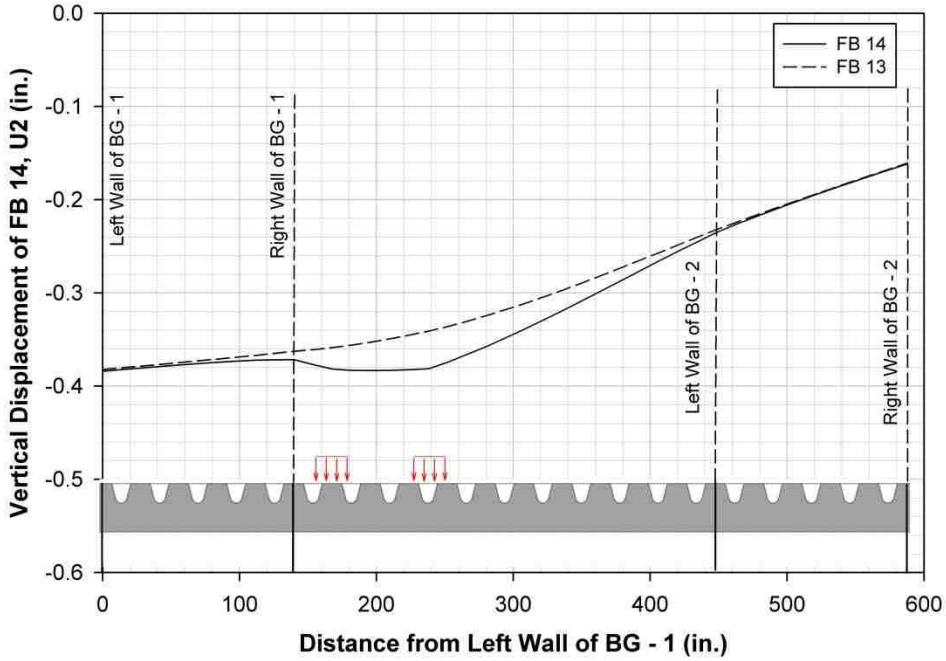

Figure 37 Comparison of vertical displacement of FB 13 and FB 14 for load case L1T29

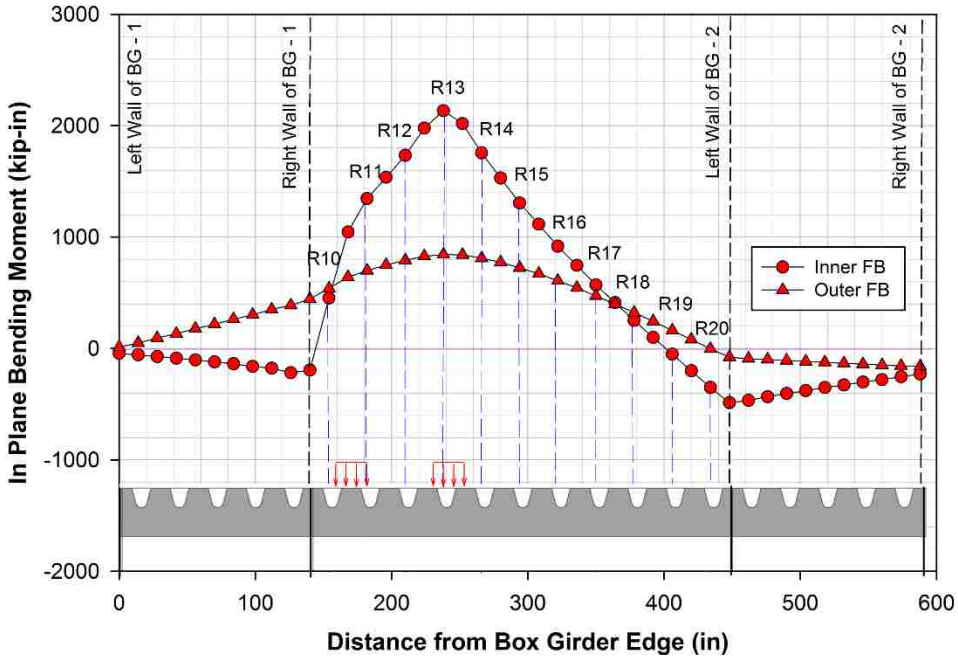

Figure 38 Variation of in-plane bending moment in FB 14 and FB 13 for GM

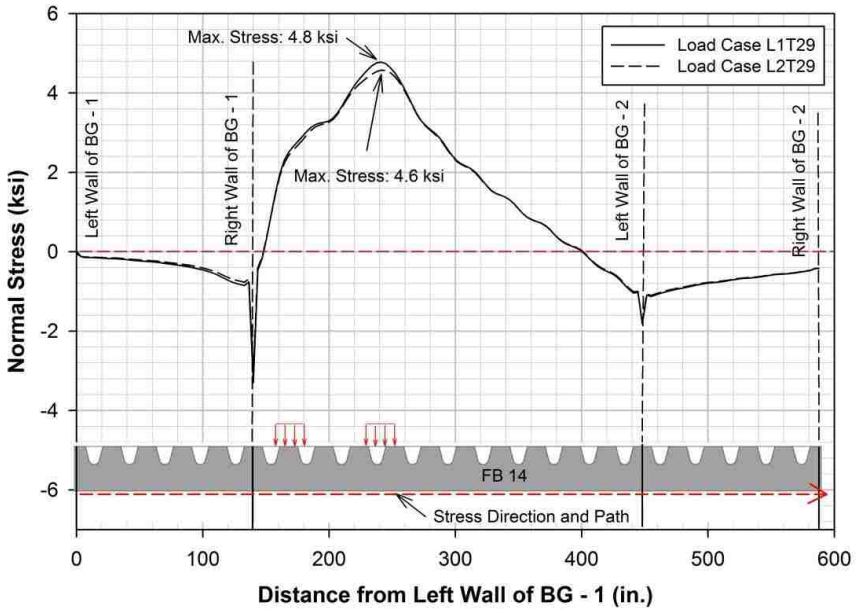

Figure 39 Distribution of transverse direction stress at the bottom of FB 14 for load cases L1T29 and L2T29

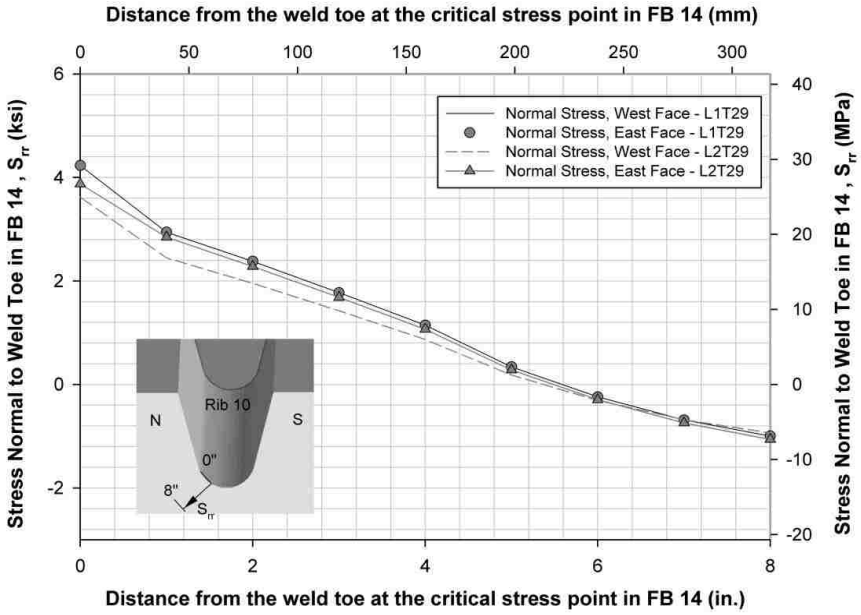

Figure 40 Comparison of normal stresses on the east and west faces of FB 14 showing out-of-plane bending

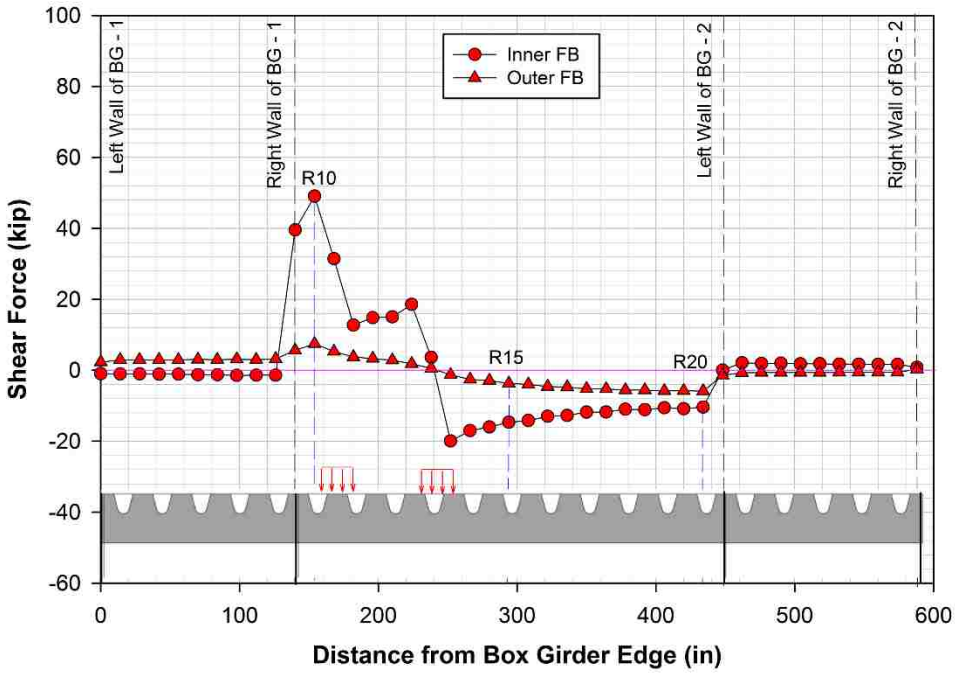

Figure 41 Variation of shear in floor beams

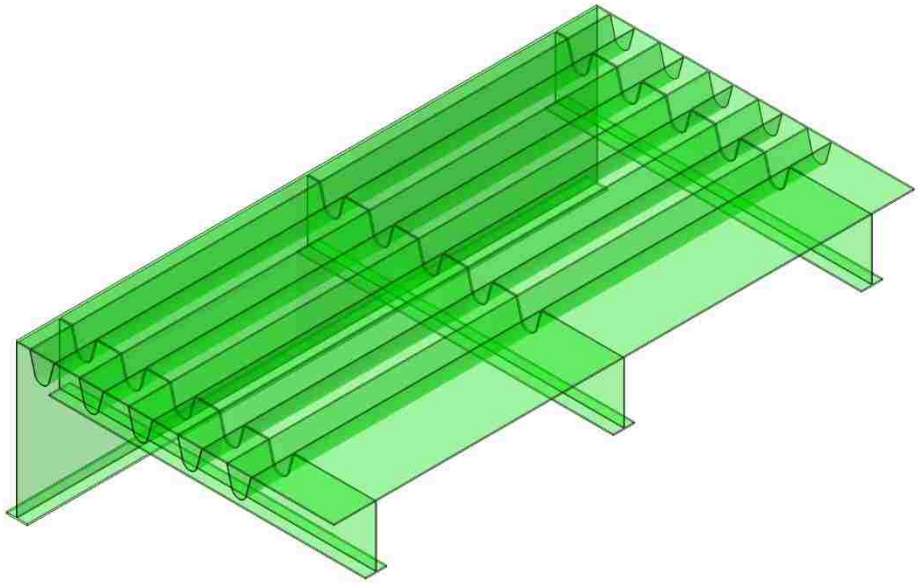

Figure 42 3D view of the first trial FE model

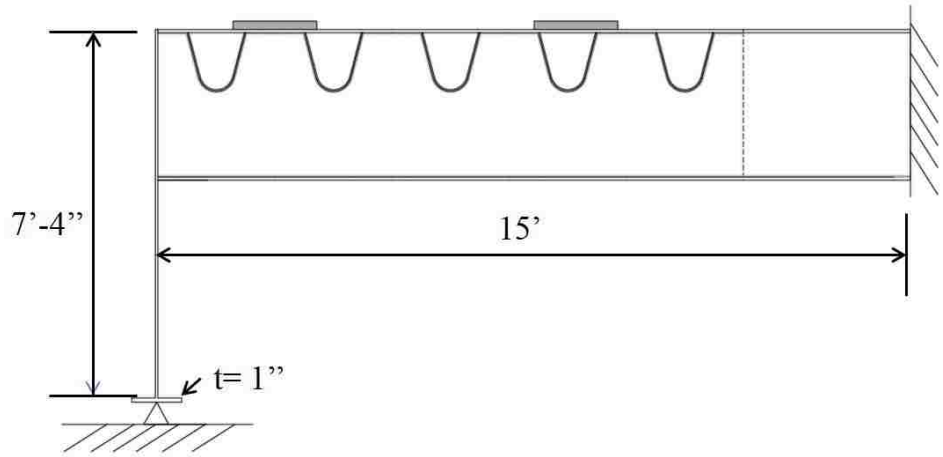

Figure 43 Sectional elevation of first trial FE model

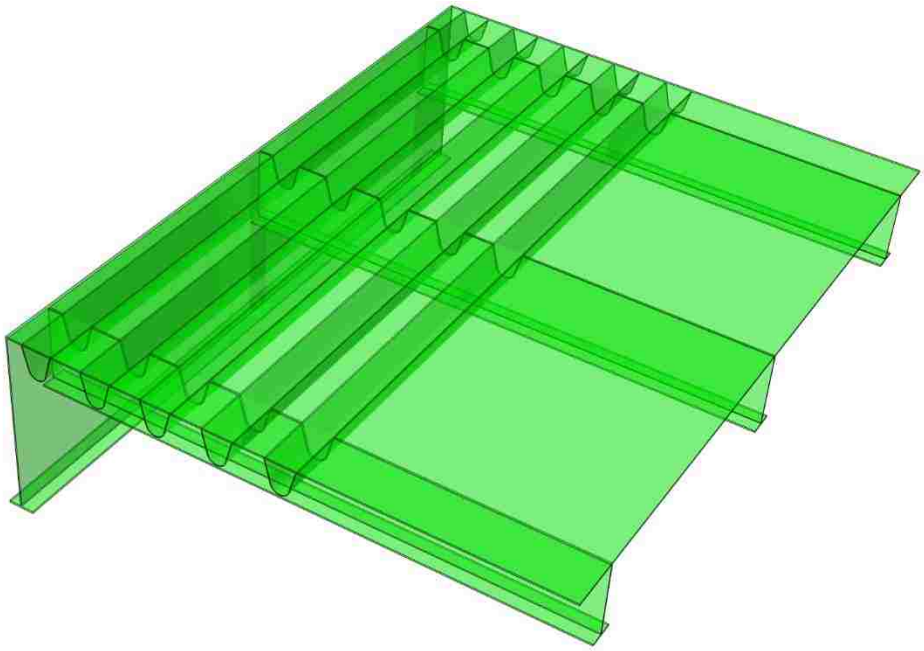

Figure 44 3D view of the second trial FE model

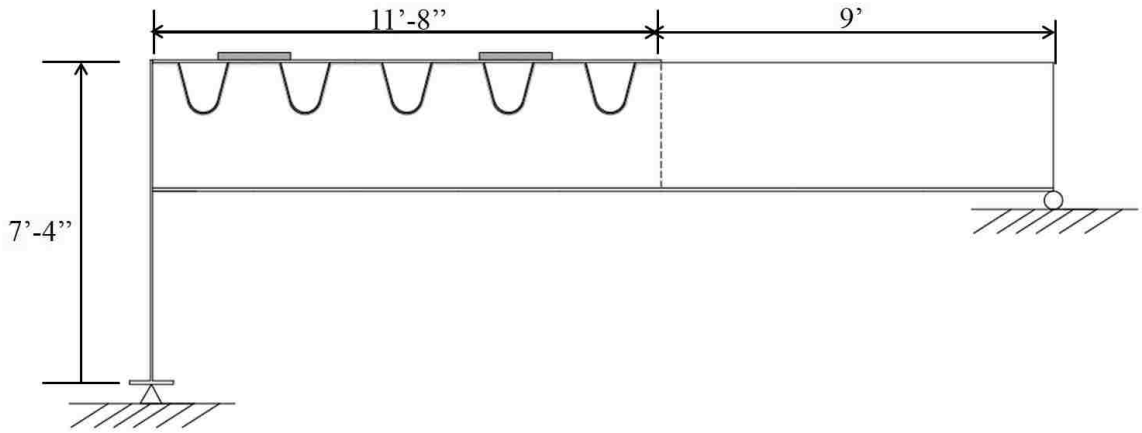

Figure 45 Sectional elevation of second trial FE model

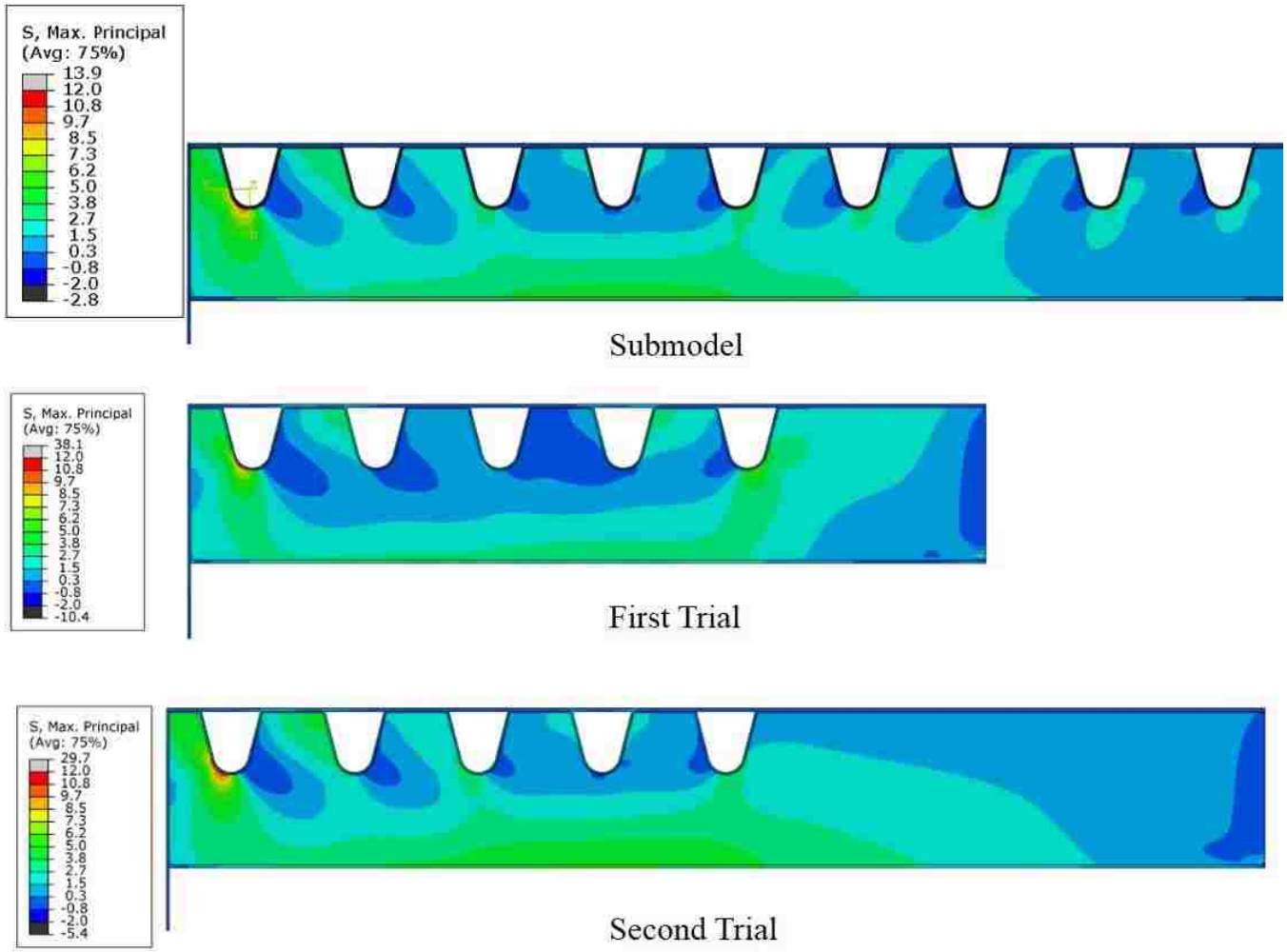

Figure 46 Principal stress comparison for first and second trial FE models

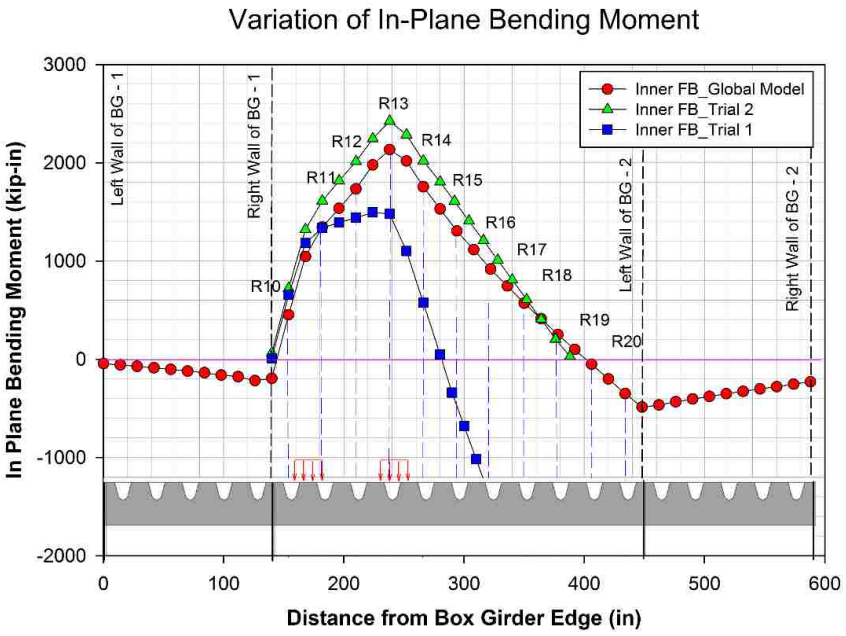

Figure 47 Comparison of in-plane bending moment of inner FB of first and second trial FE analyses with GM

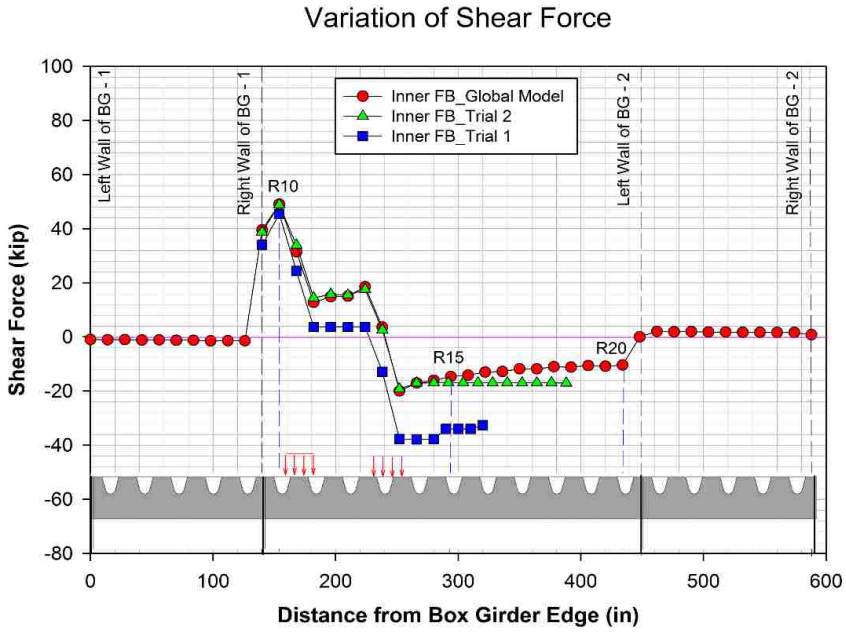

Figure 48 Comparison of shear force in inner FB of first and second trial FE analyses with GM

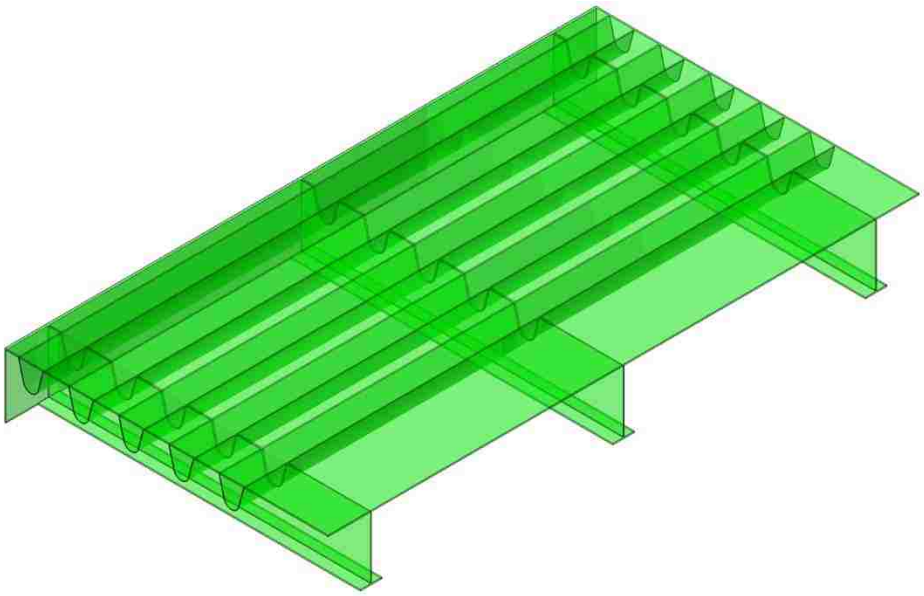

Figure 49 3D view of the third trial FE model

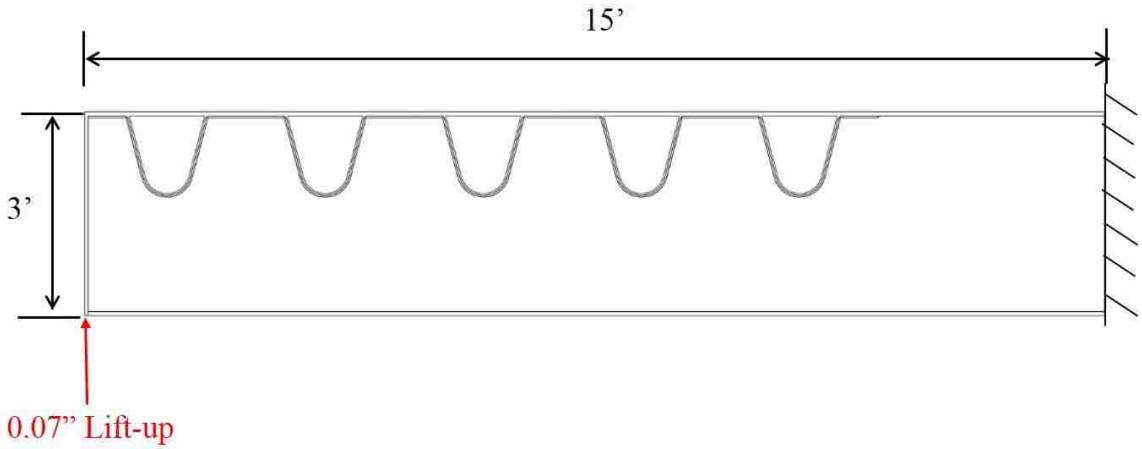

Figure 50 Sectional elevation of third trial FE model

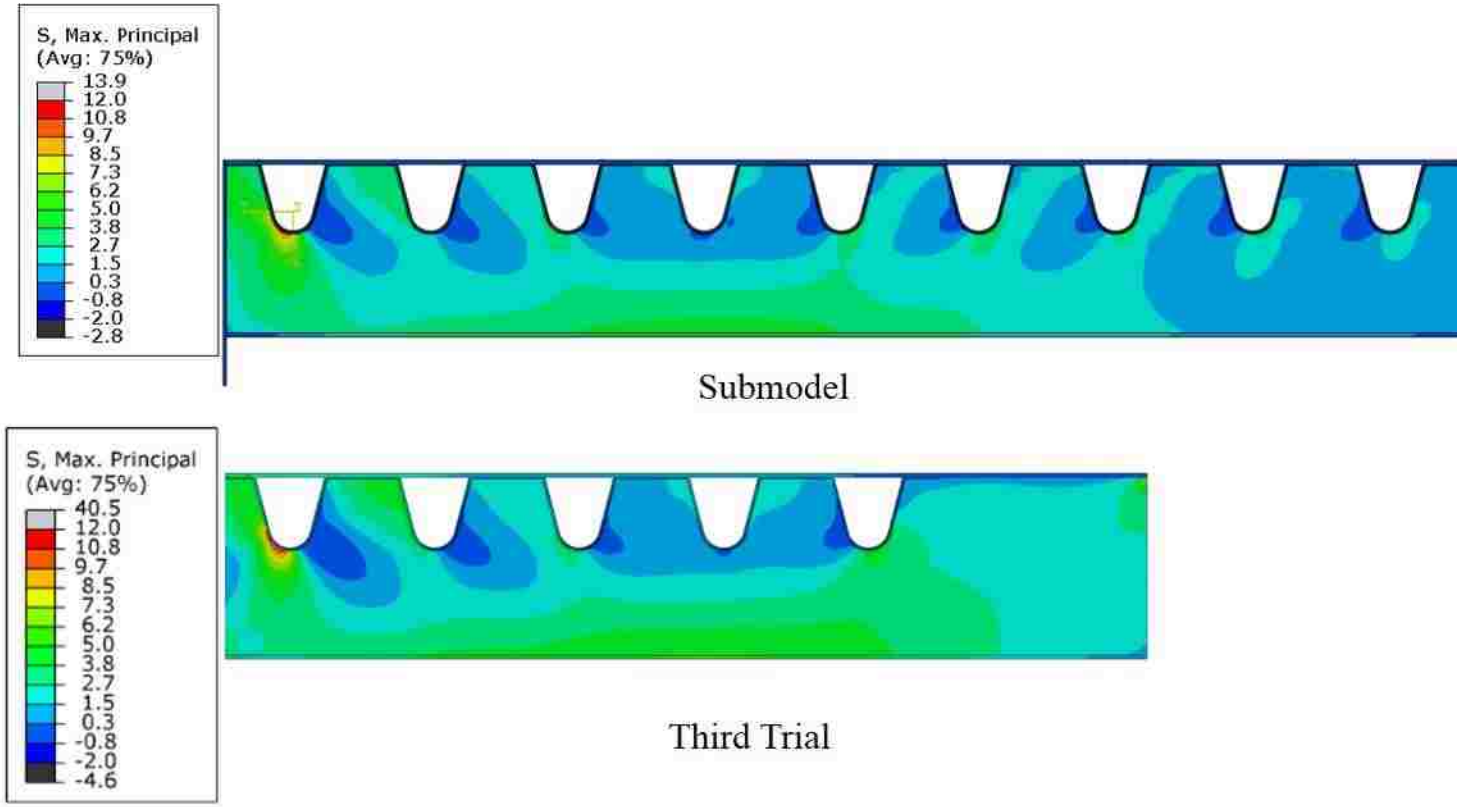

Figure 51 Principal stress comparison for third trial FE model

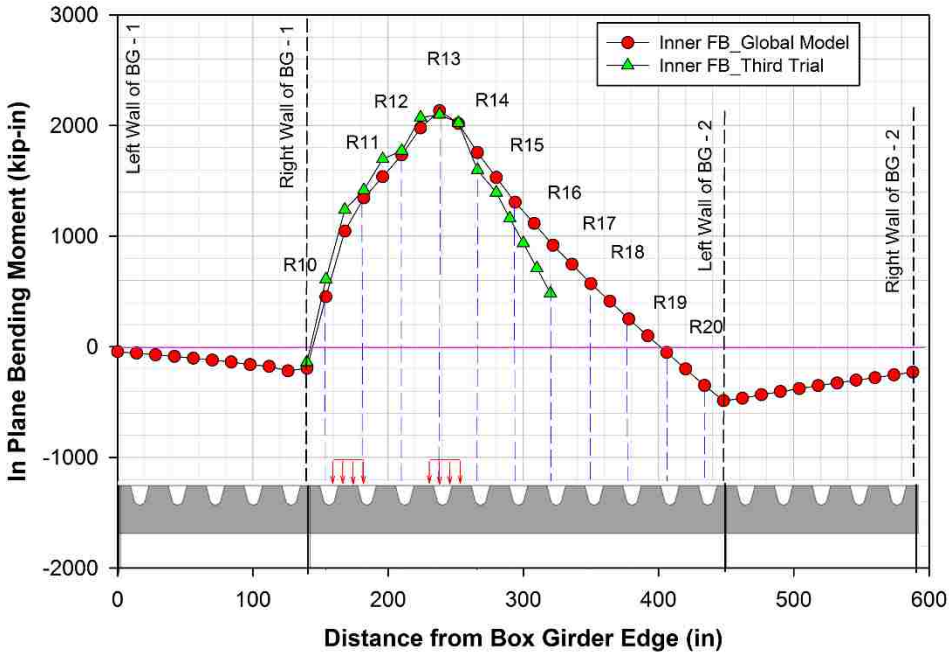

Figure 52 Comparison of in-plane bending moment of inner FB of third trial FE analysis with GM

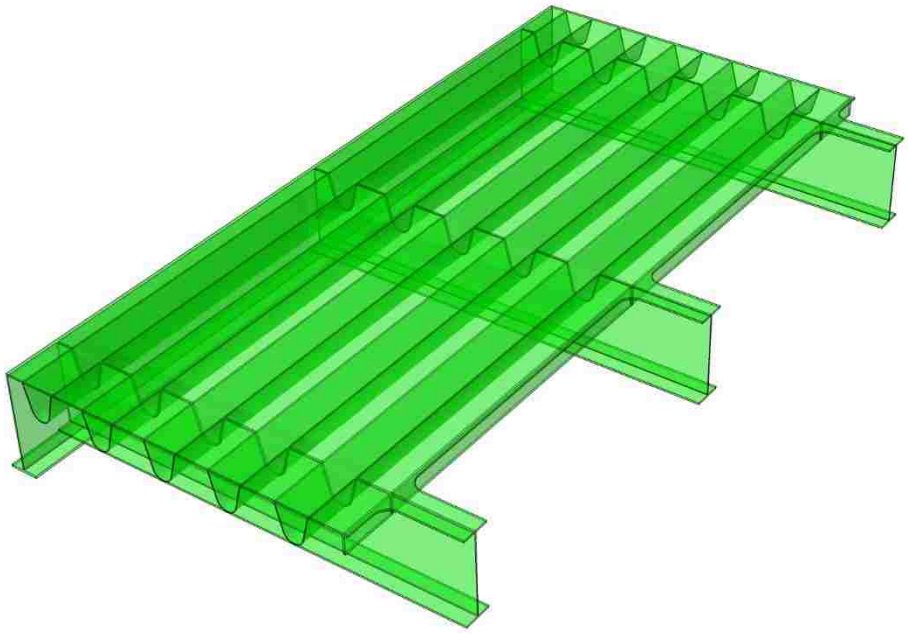

Figure 53 3D view of the fourth trial FE model

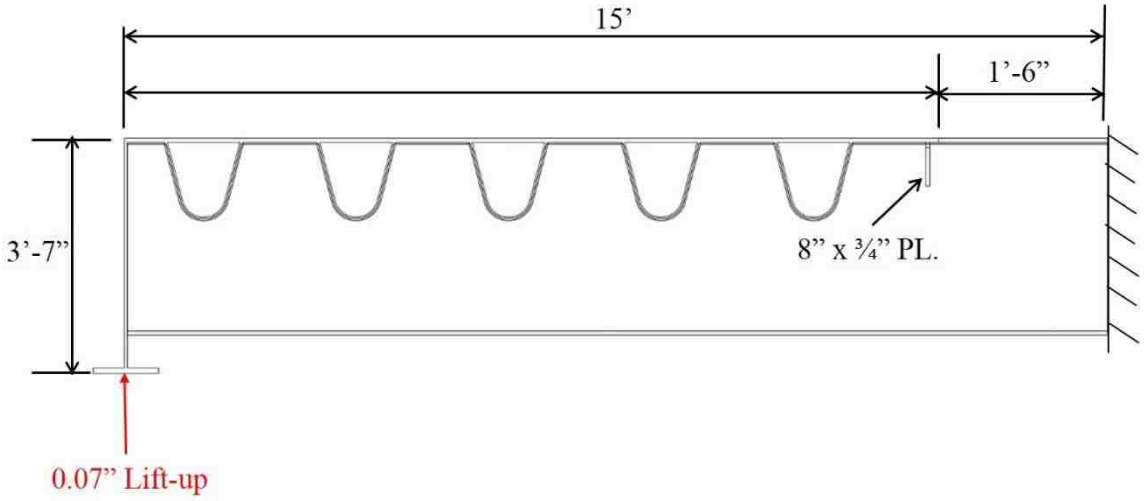

Figure 54 Sectional elevation of fourth trial FE model

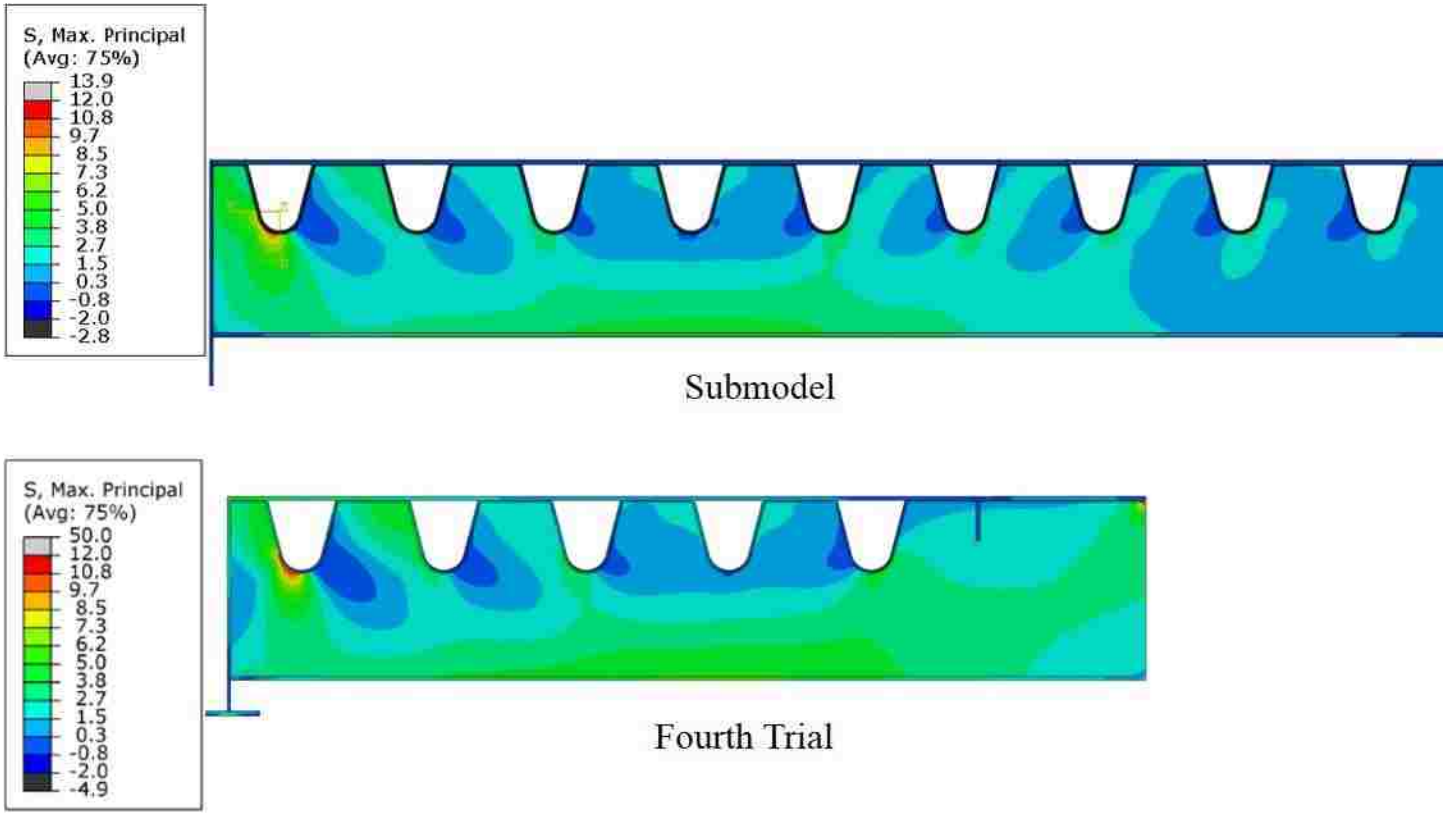

Figure 55 Principal stress comparison for fourth trial FE model

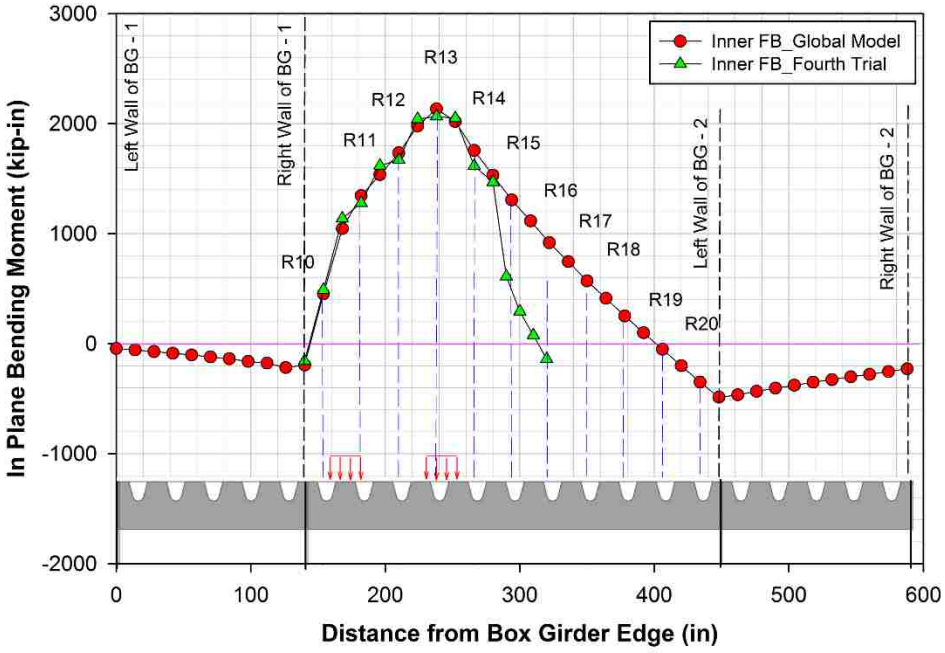

Figure 56 Comparison of in-plane bending moment of inner FB of fourth trial FE analysis with GM

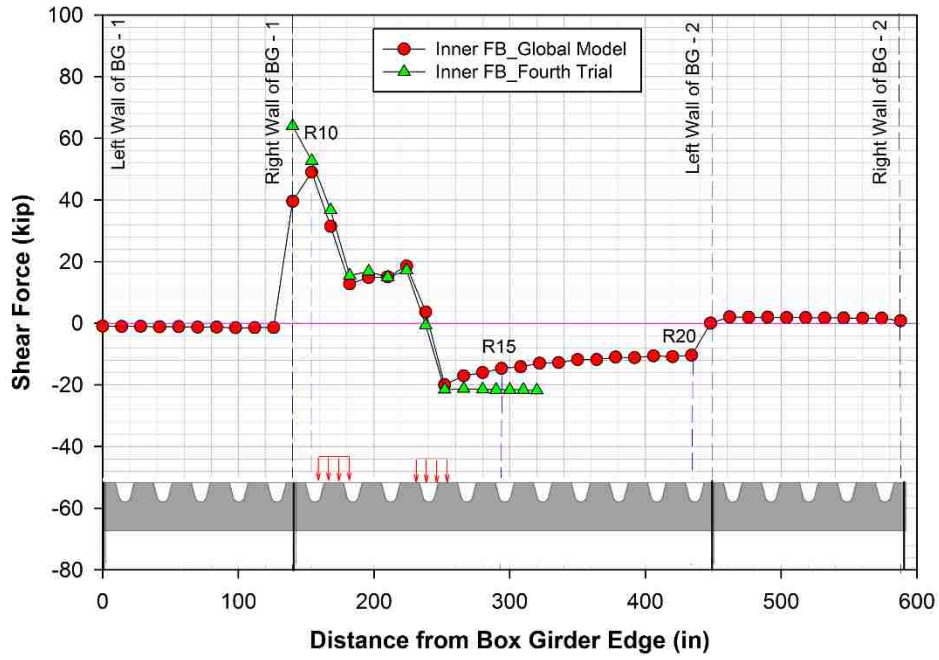

Figure 57 Comparison of shear force in inner FB of fourth trial FE analysis with GM

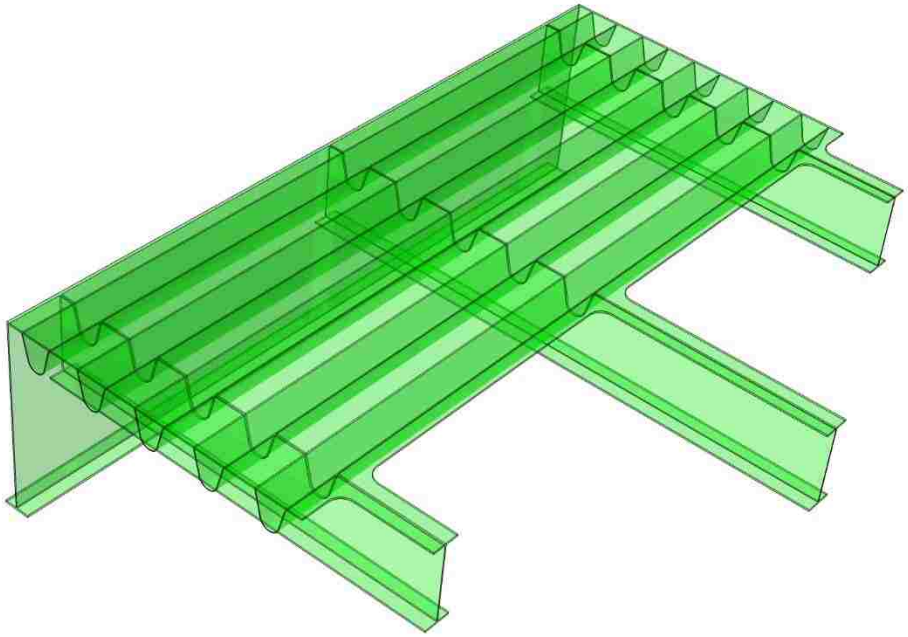

Figure 58 3D view of the fifth trial FE model

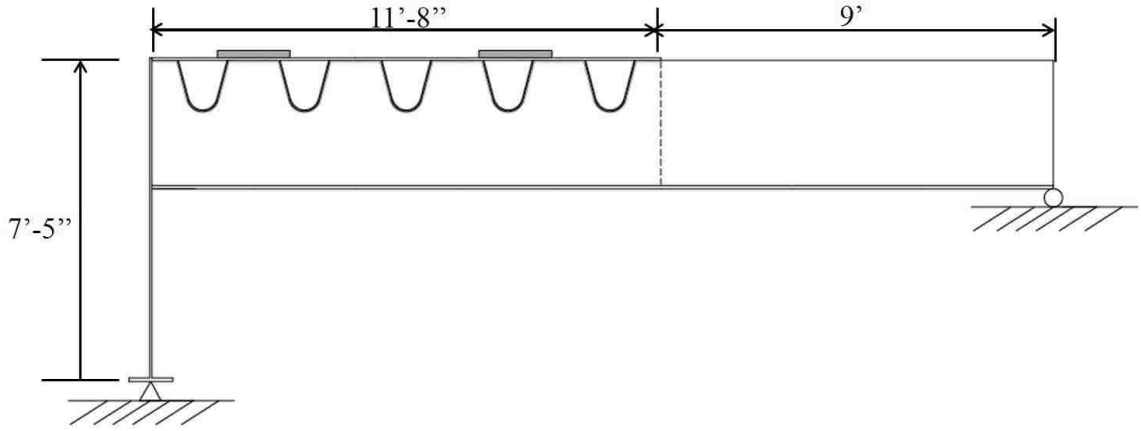

Figure 59 Sectional elevation of fifth trial FE model

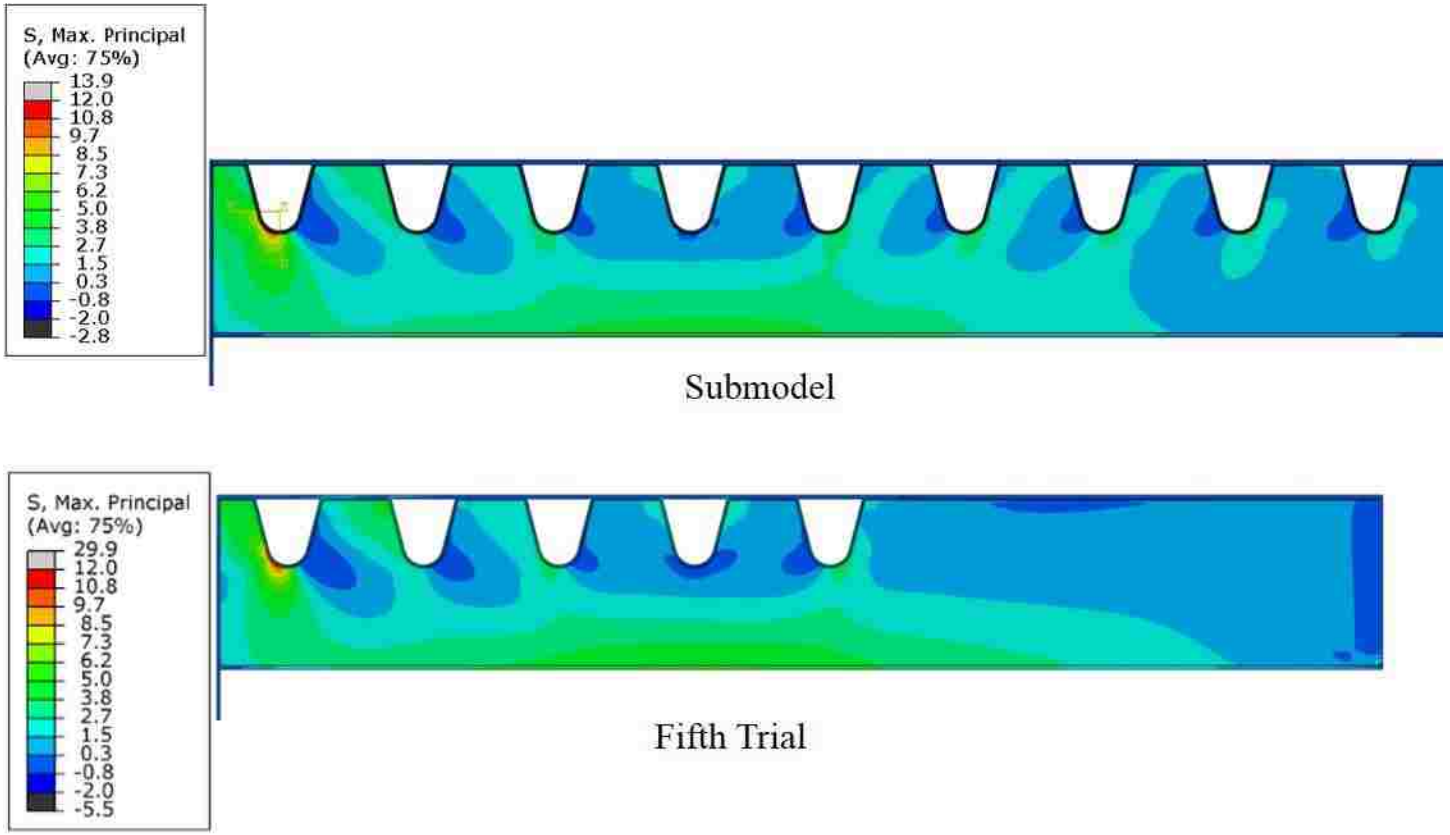

Figure 60 Principal stress comparison for fifth trial FE model

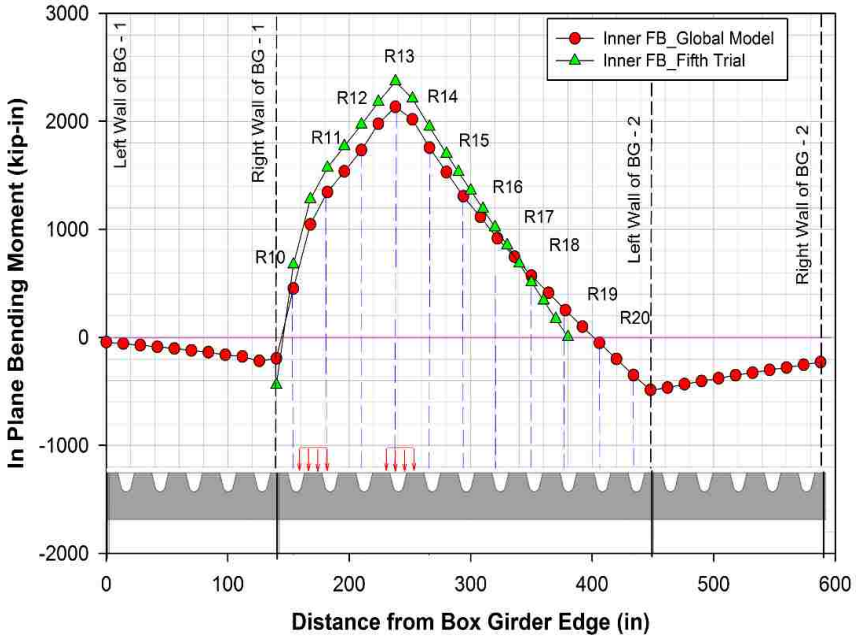

Figure 61 Comparison of in-plane bending moment of inner FB of fifth trial FE analysis with GM

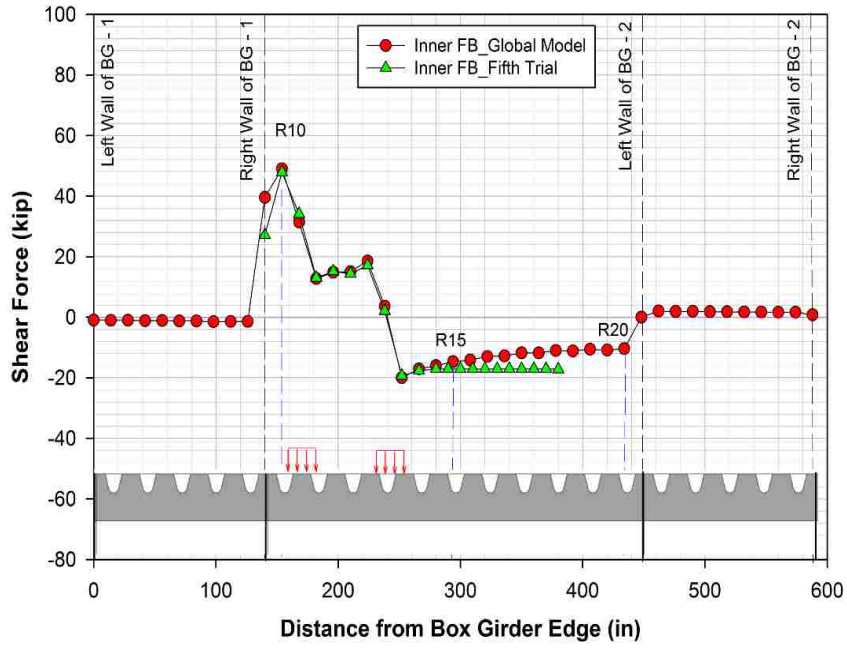

Figure 62 Comparison of shear in inner FB of fifth trial FE analysis with GM

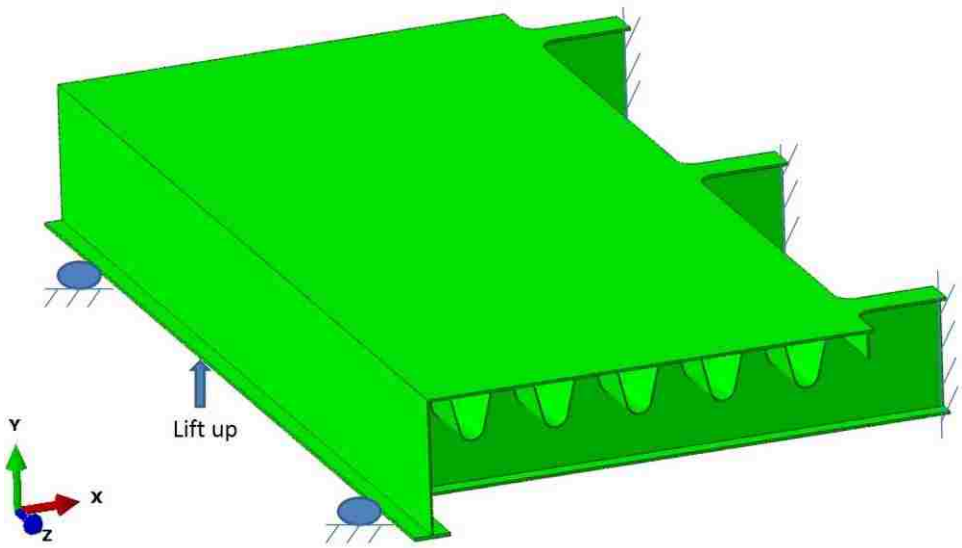

Figure 63 3D view of Option 1 (fourth trial FE model)

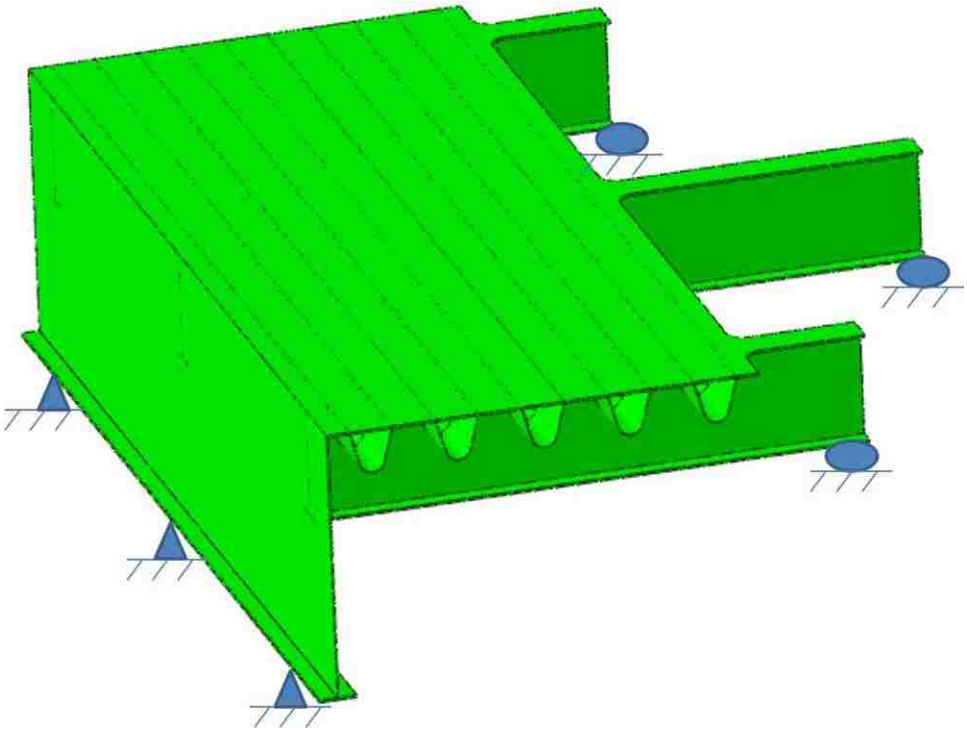

Figure 64 3D view of Option 2 (fifth trial FE model)

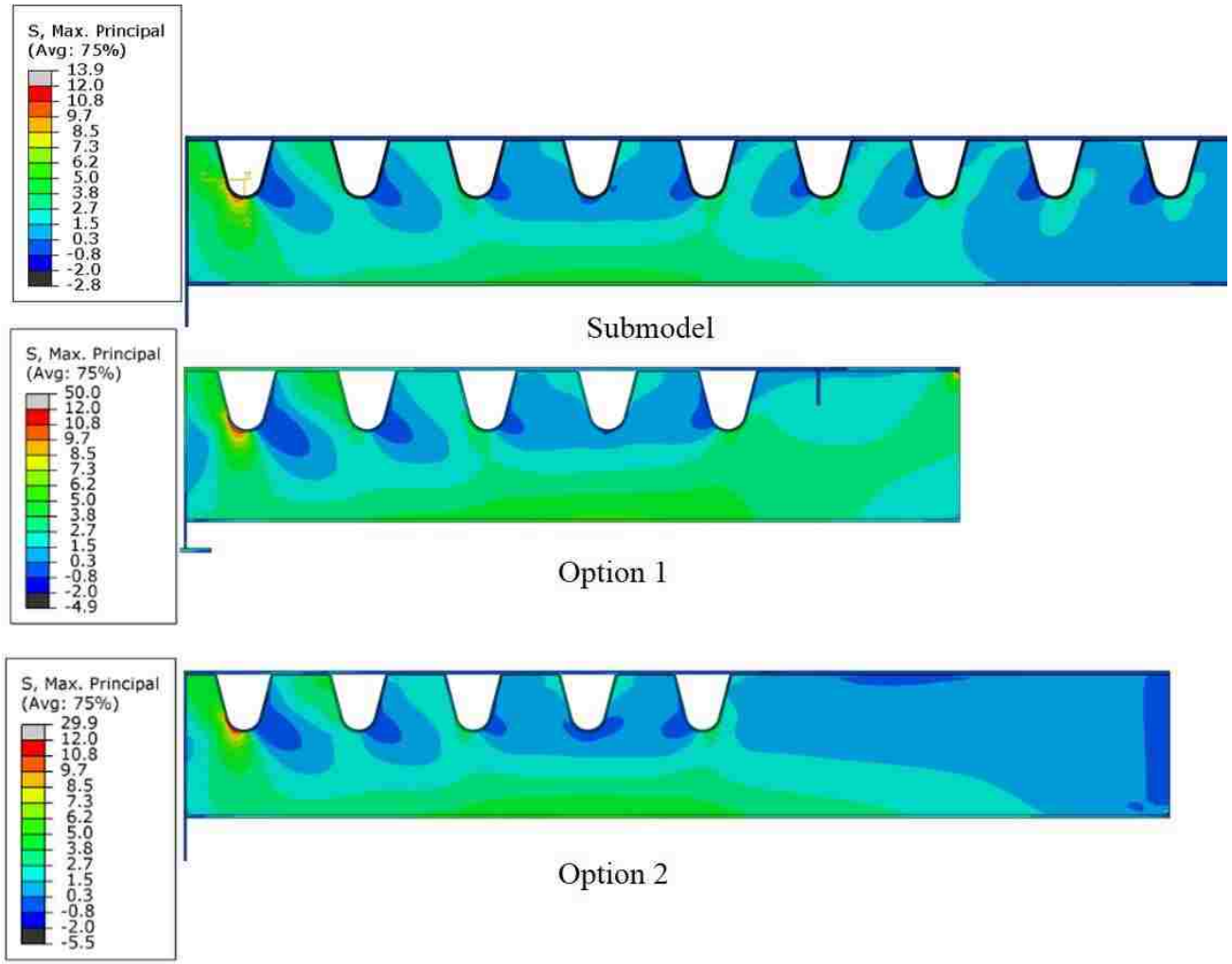

Figure 65 Principal stress comparison for Option 1 and Option 2

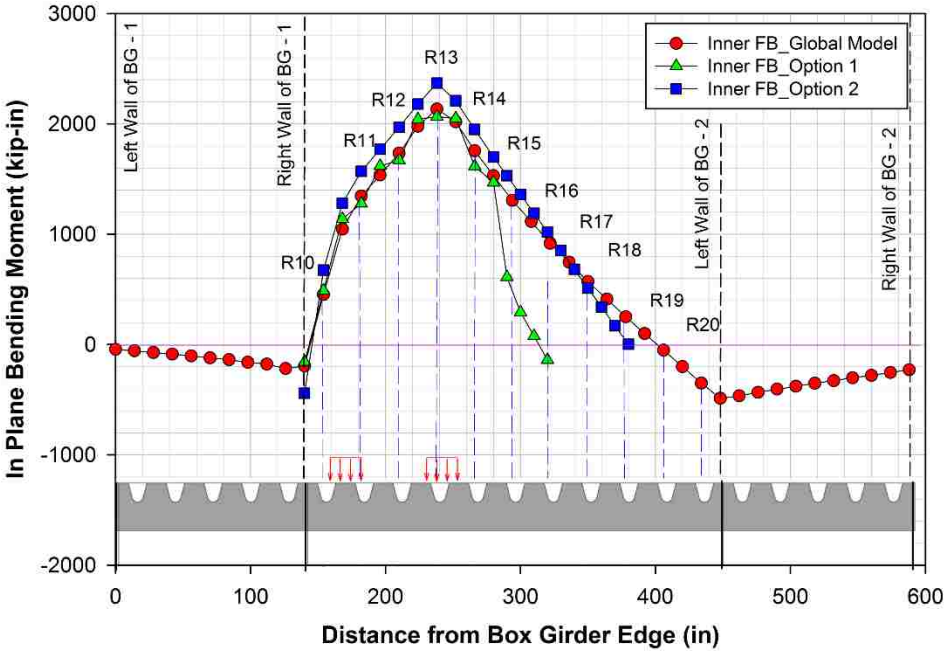

Figure 66 Comparison of in-plane bending moment of inner FB in Option 1 and Option 2 with GM

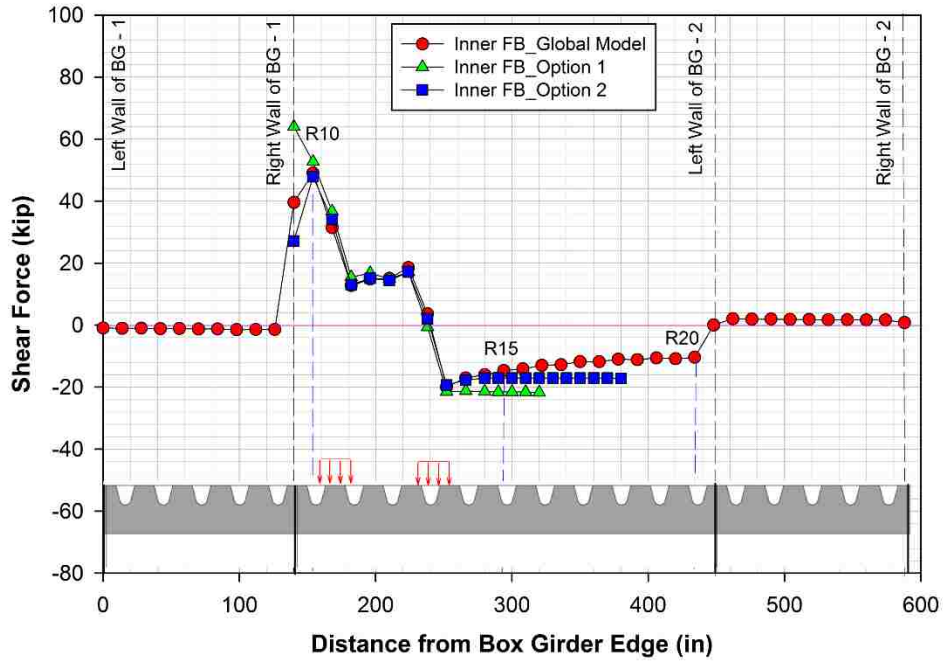

Figure 67 Comparison of shear in inner FB in Option 1 and Option 2 with GM

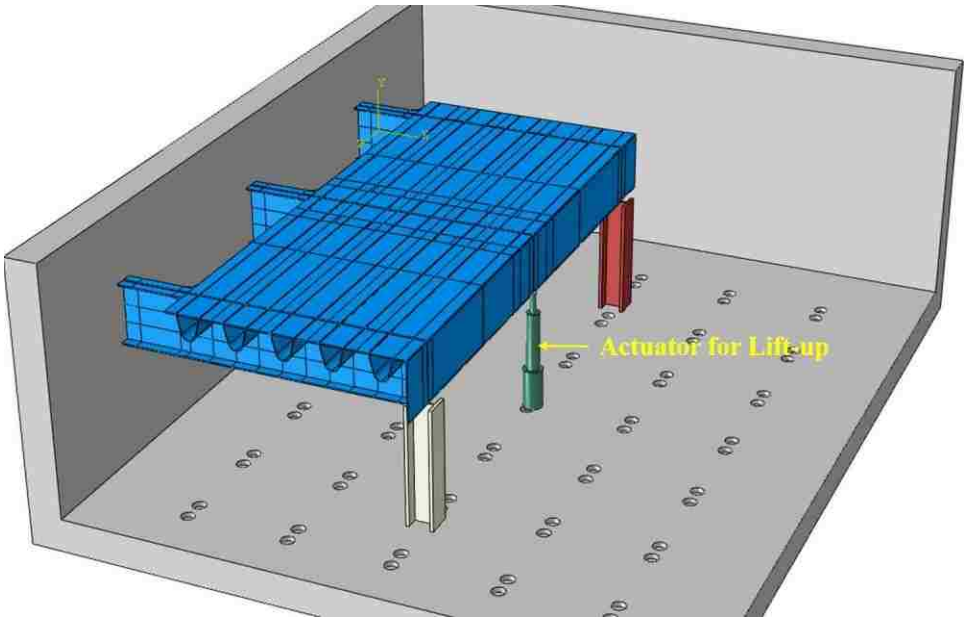

Figure 68 **Conceptual figure showing installation of Option 1 in the laboratory**

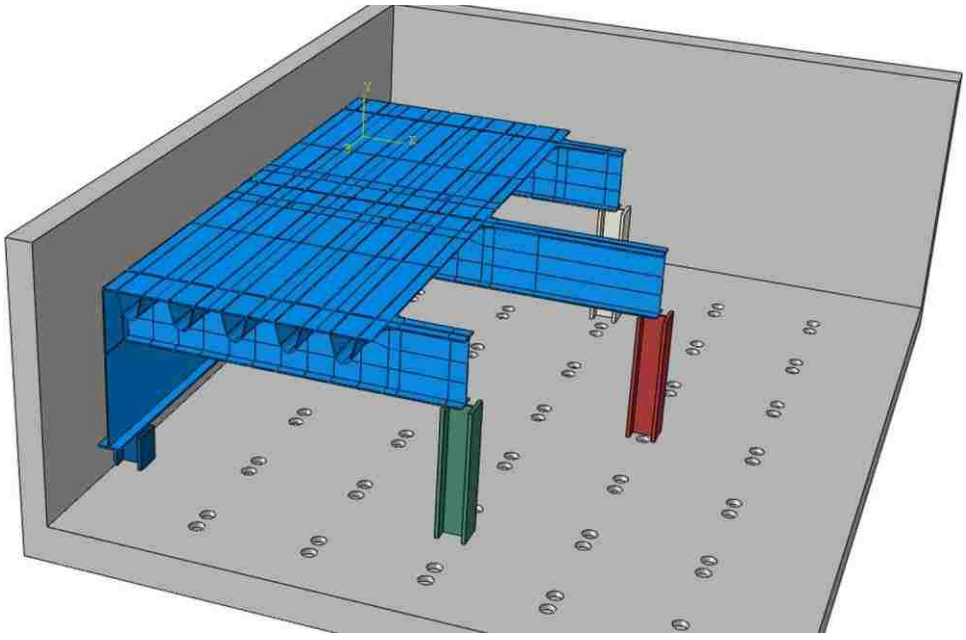

Figure 69 **Conceptual figure showing installation of Option 2 in the laboratory**

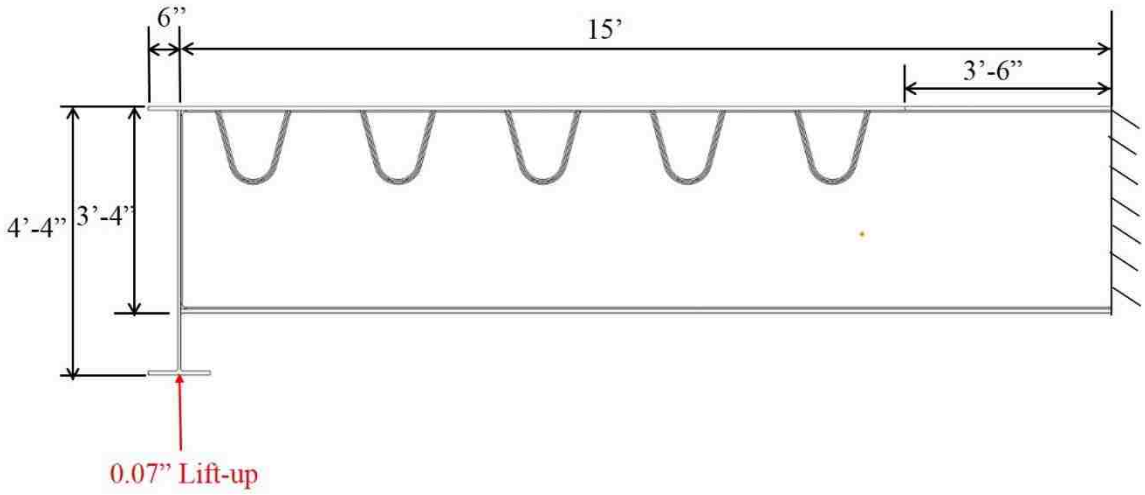

Figure 70 Sectional elevation of modified Option 1

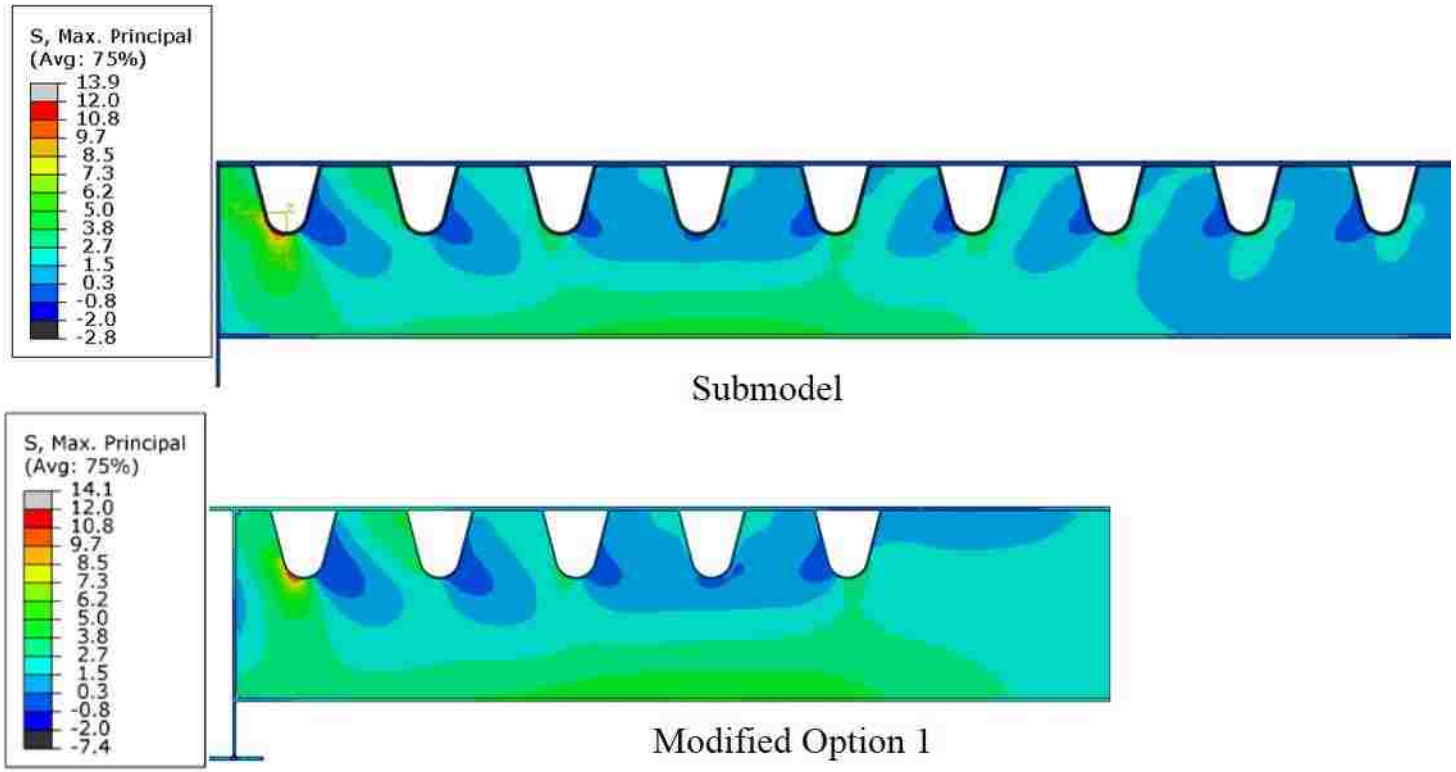

Figure 71 Principal stress comparison for Modified Option 1

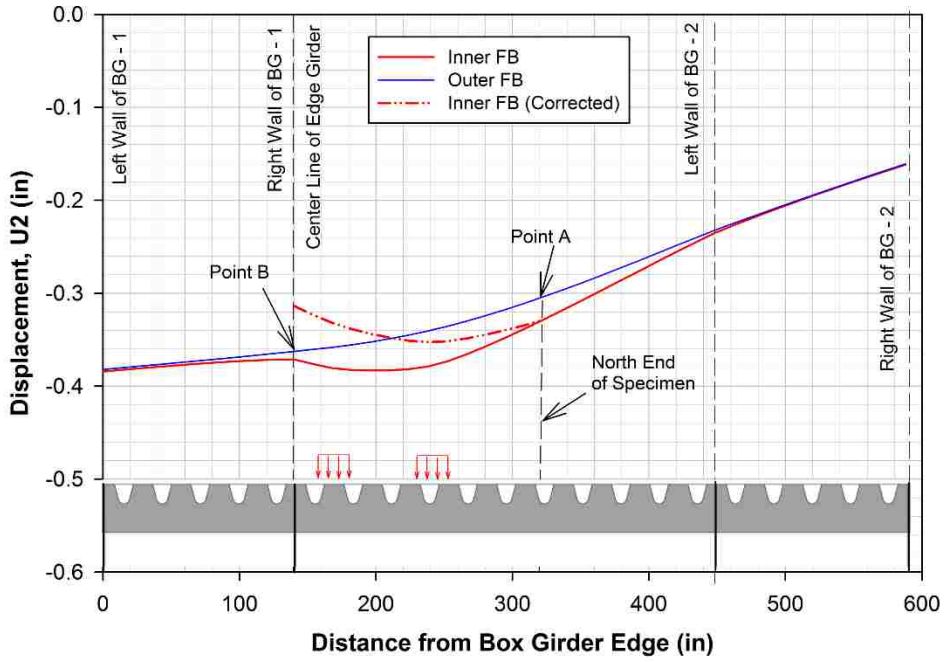

Figure 72 Deflected shape of inner floor beam before and after correction for rigid body rotation

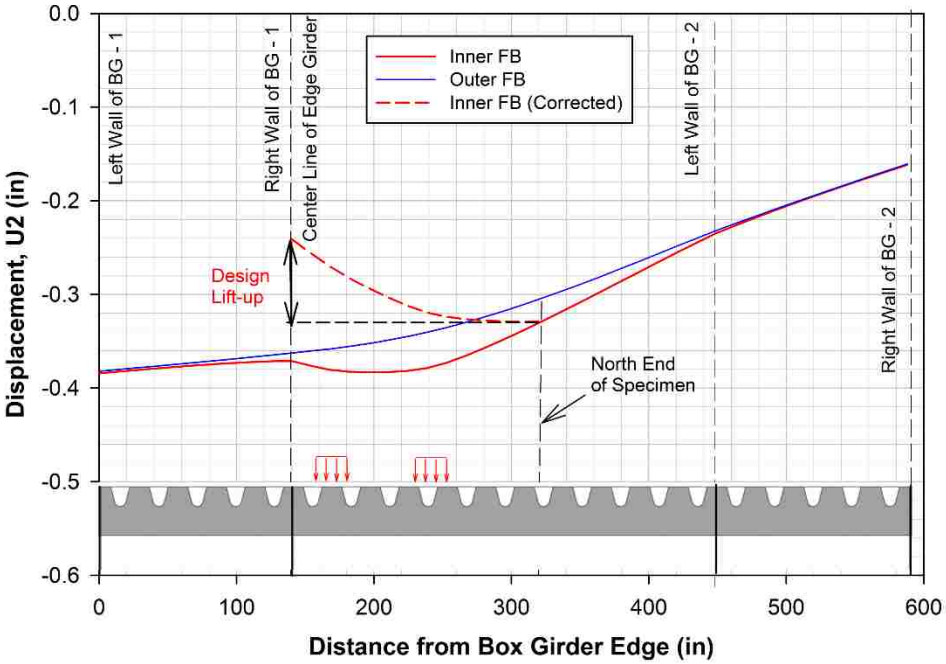

Figure 73 Calculation of design lift-up

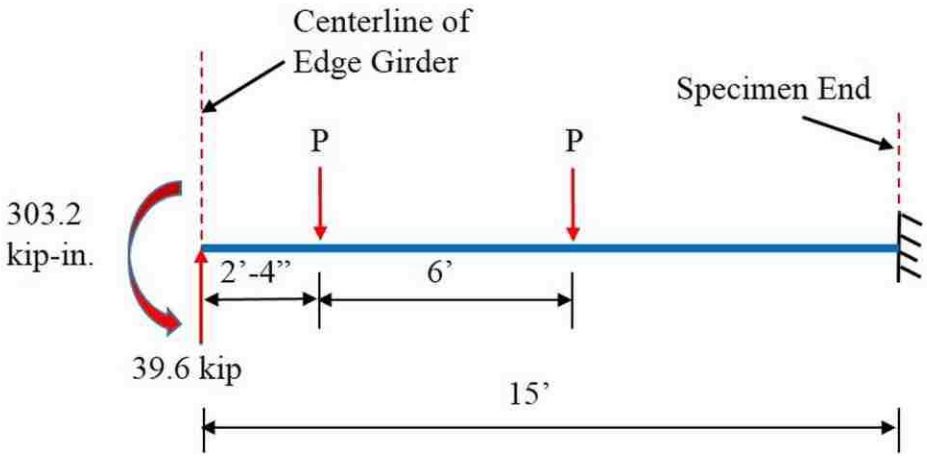

Figure 74 Calculation of lift-up from the reactions obtained from GM

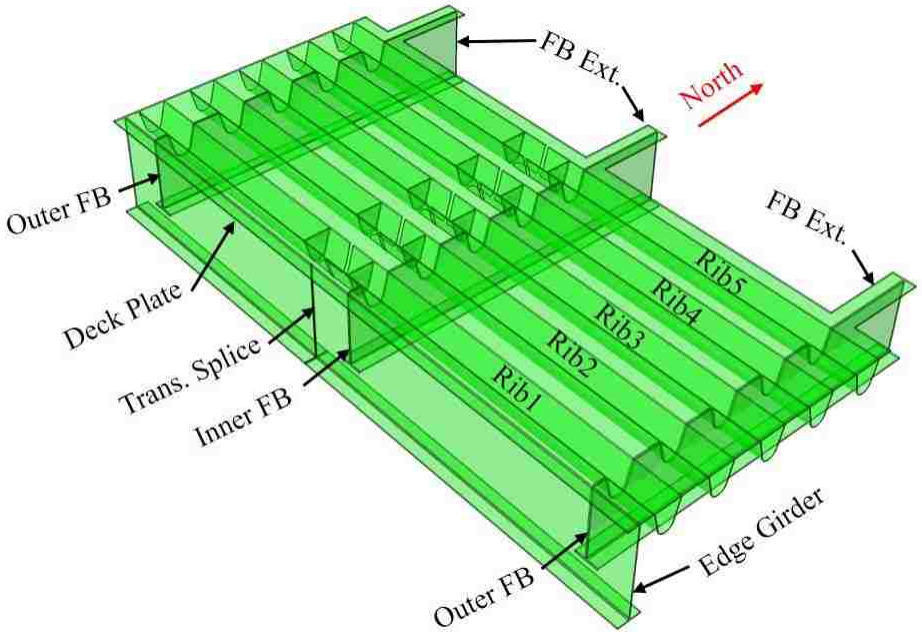

Figure 75 3D View of the specimen

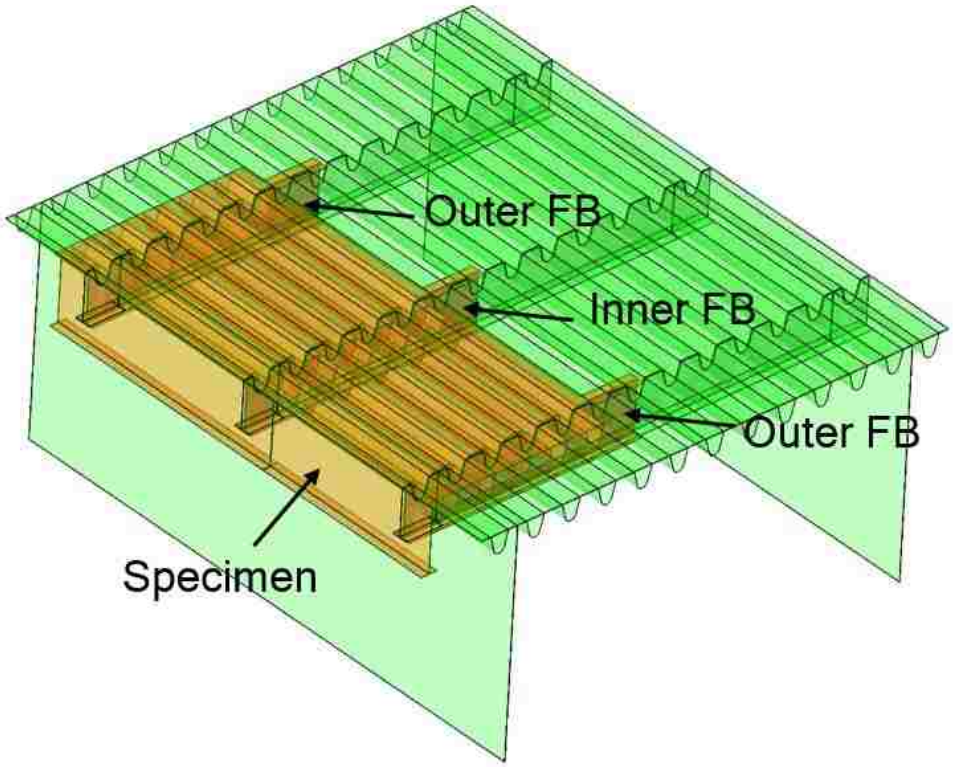

Figure 76 Top view of SM showing extent of specimen model

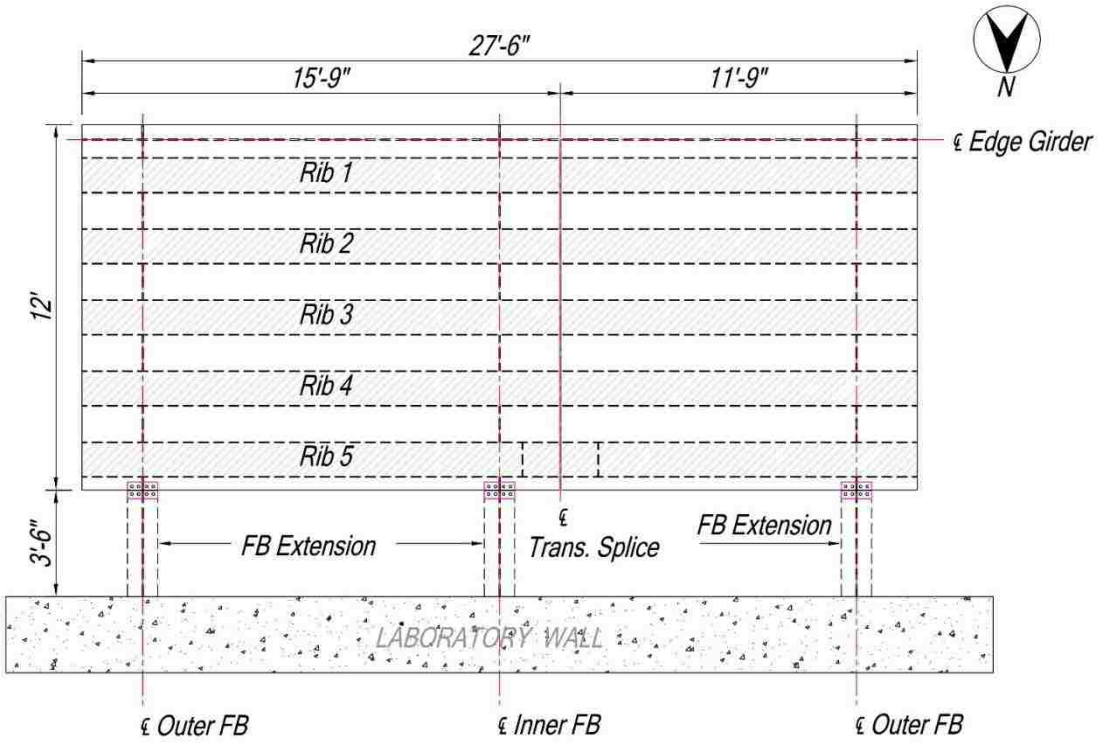

Figure 77 Plan view of the specimen

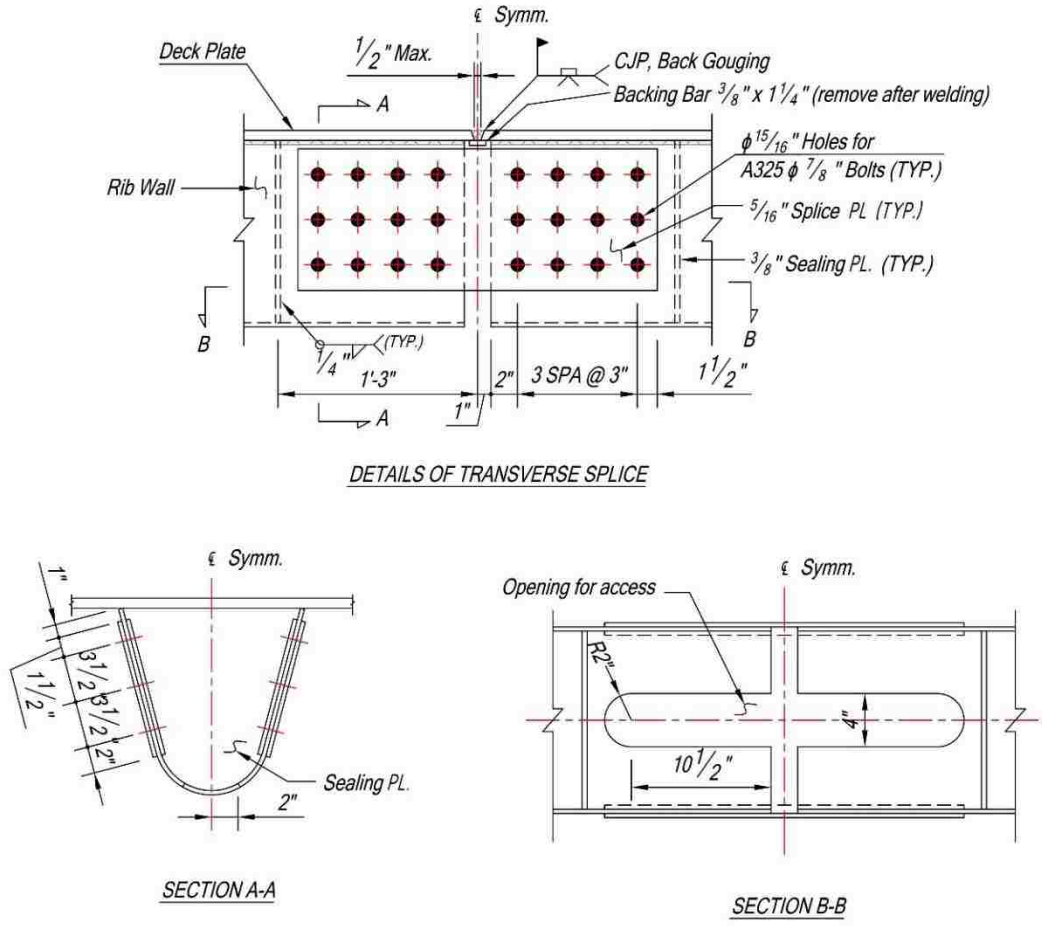

Figure 78 Details of transverse deck splice

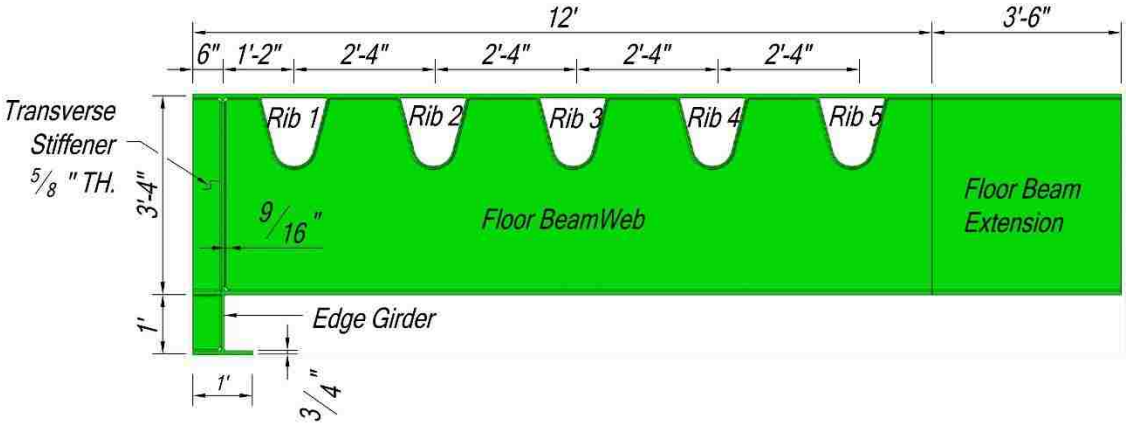

Figure 79 Sectional elevation of the specimen

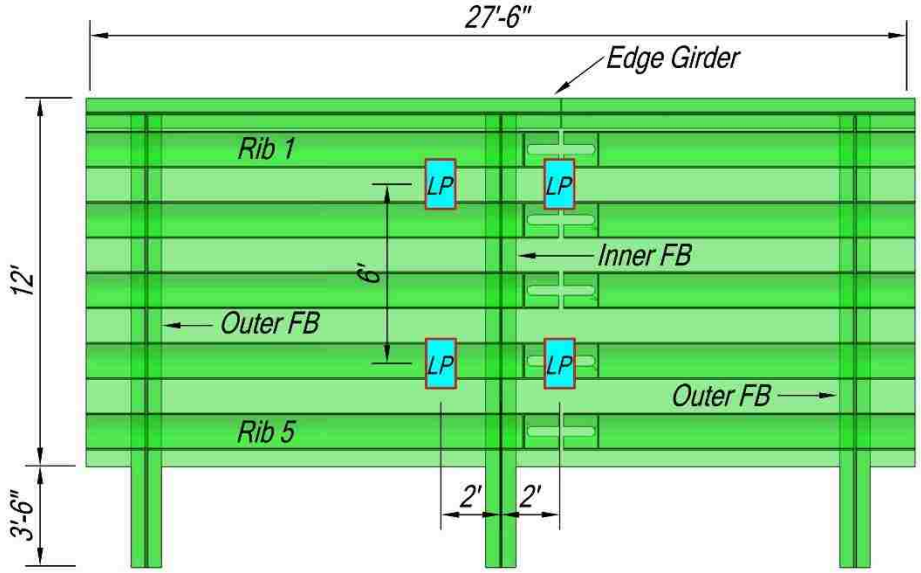

Figure 80 Top view of the specimen model with load positions shown (identified as LP)

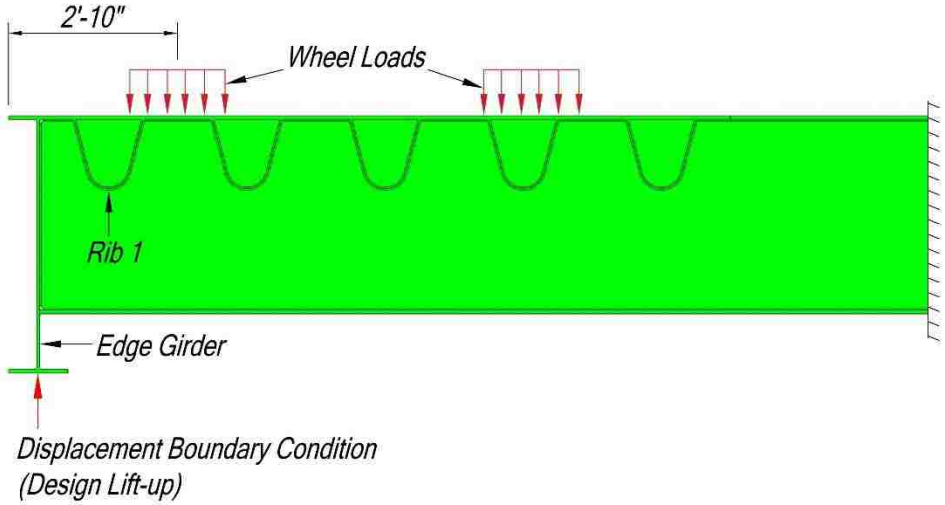

Figure 81 Sectional elevation of the specimen model showing the load position

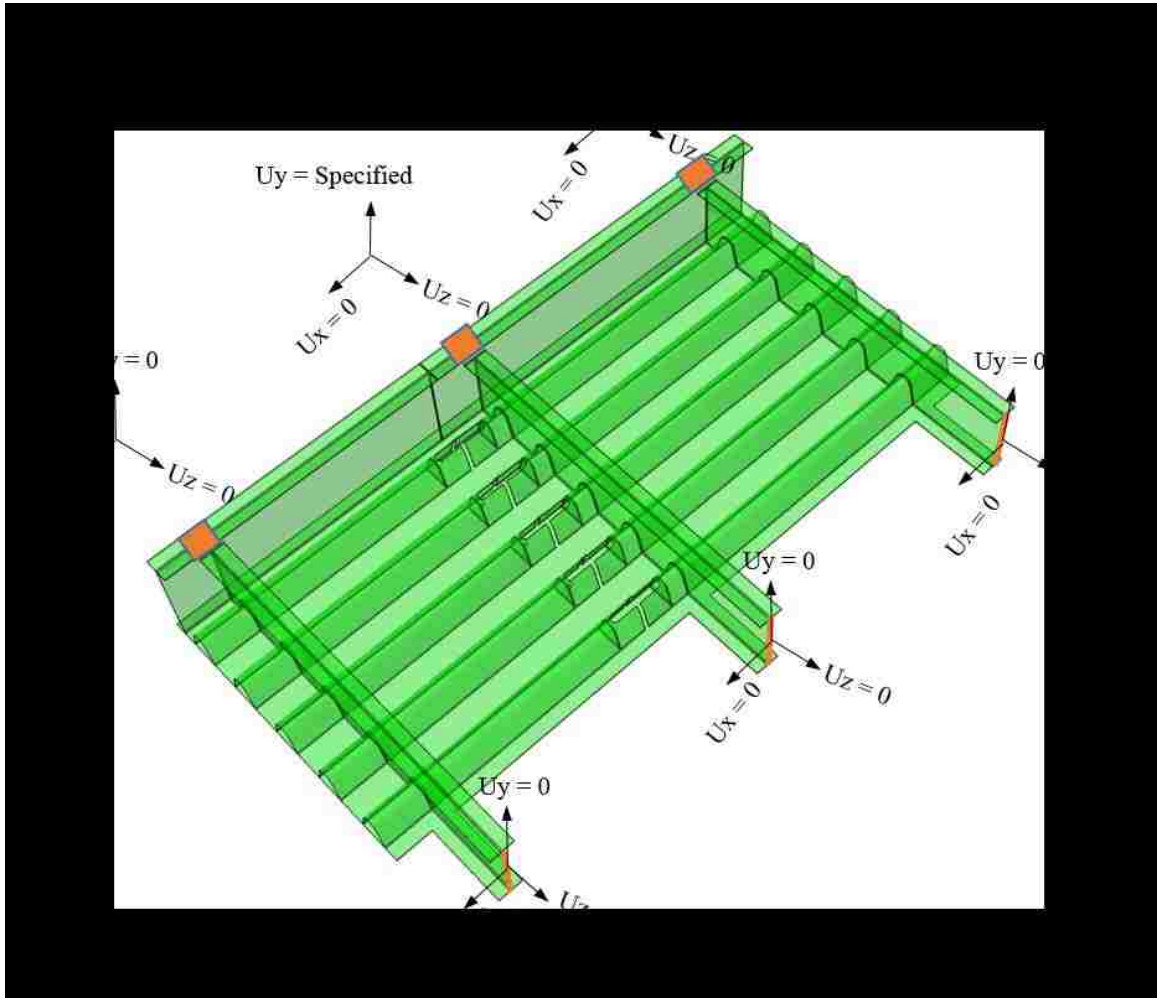

Figure 82 Underside view of the specimen model showing the applied boundary conditions

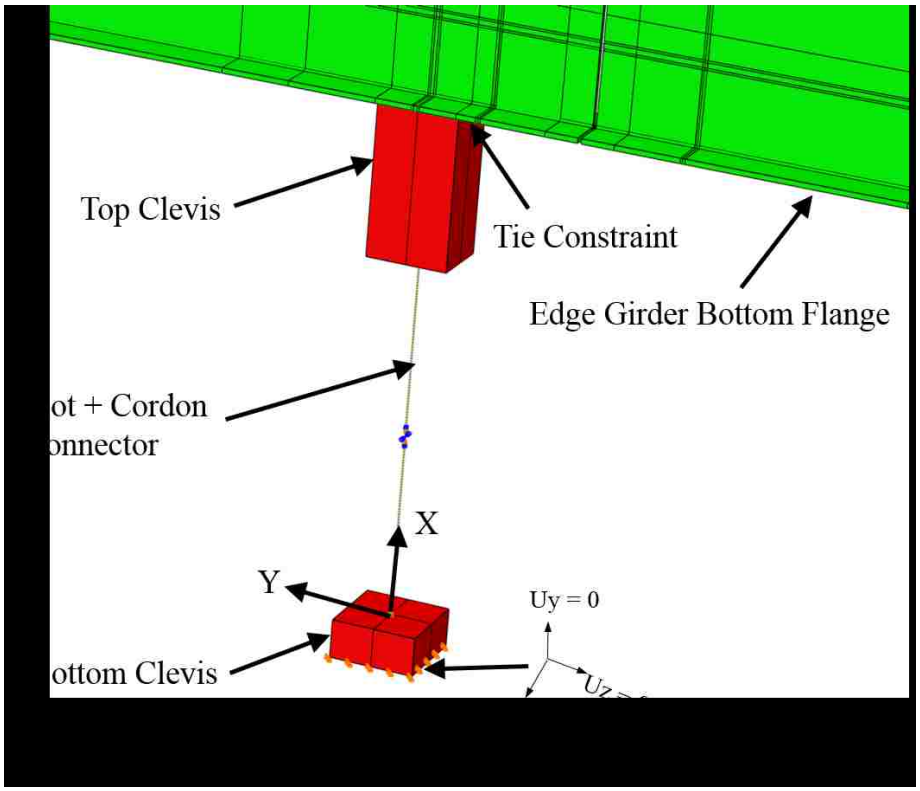

Figure 83 Under-deck actuator arrangement in specimen model

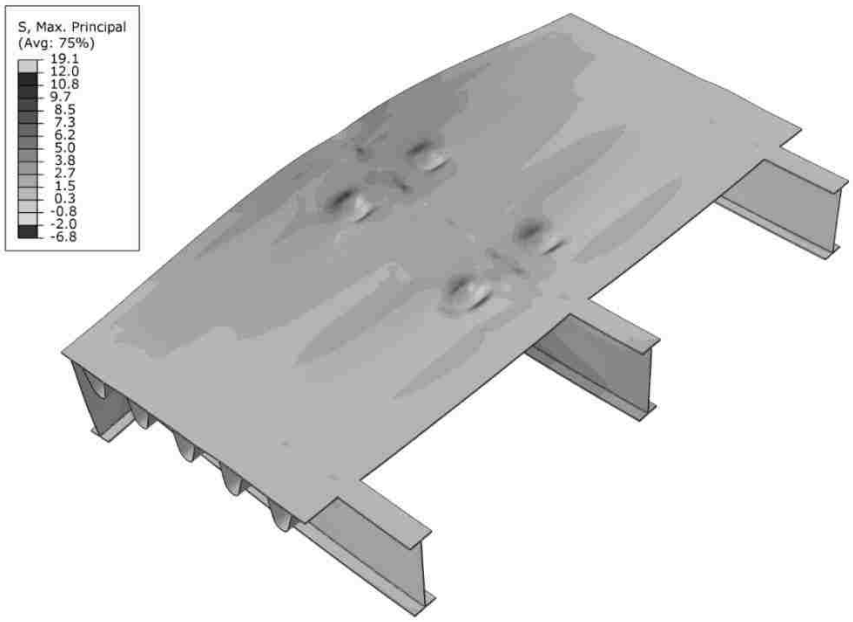

Figure 84 3D top view of the specimen showing the principal stress contour

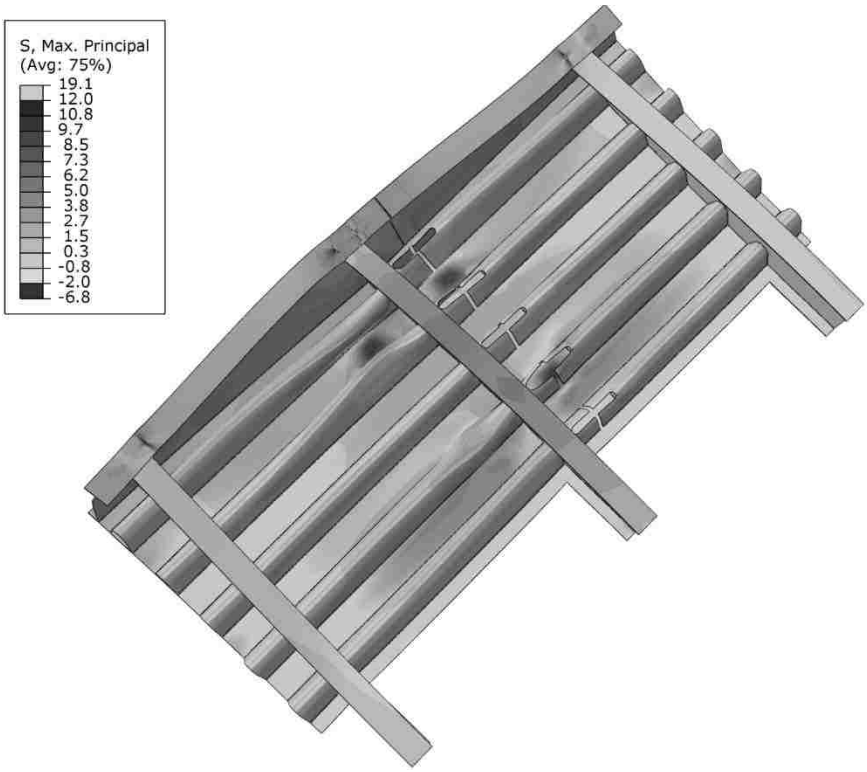

Figure 85 3D underside view showing principal stress contour

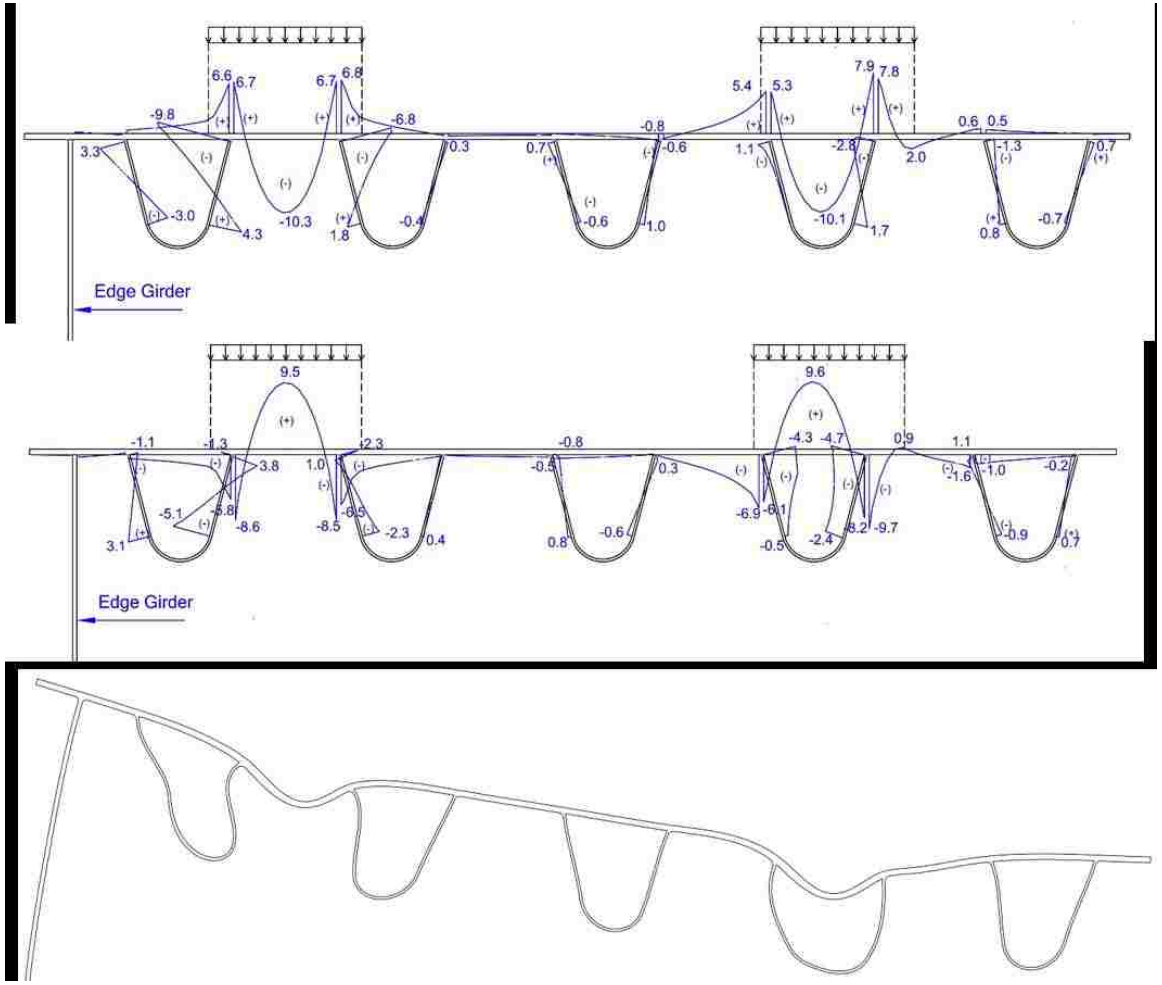

Figure 86 Transverse stresses and deformation of deck at a section through the load patches

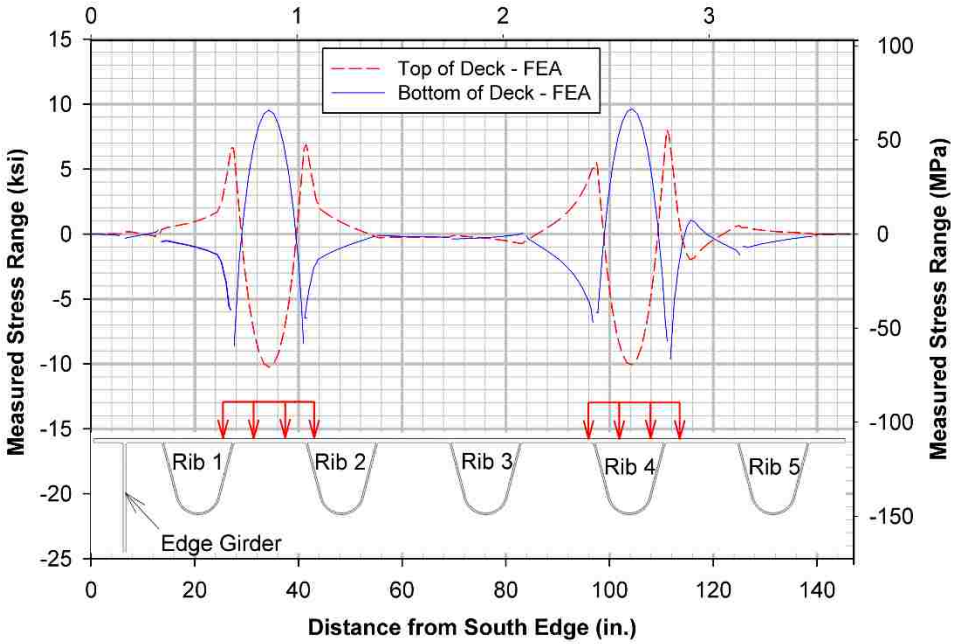

Figure 87 **Transverse stress distribution of deck plate at a section through the load pads**

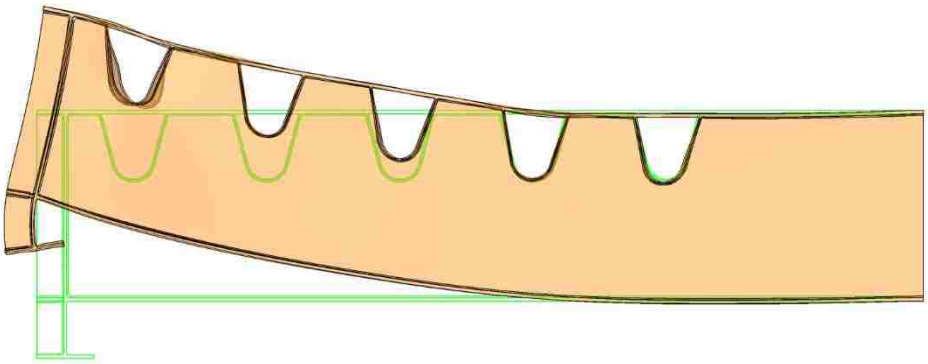

Figure 88 **Deformed configuration of inner floor beam overlaid on undeformed configuration**

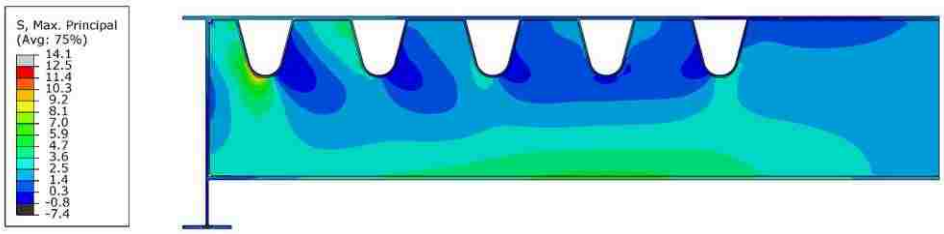

Figure 89 Maximum principal stress contour on floor beam web

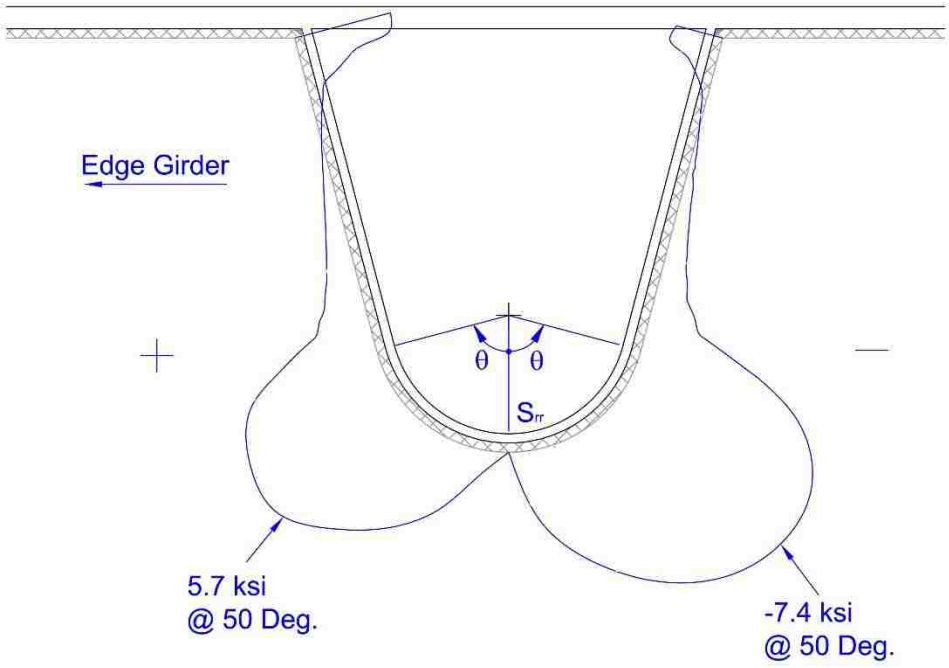

Figure 90 Variation of stress normal to weld toe on inner FB web

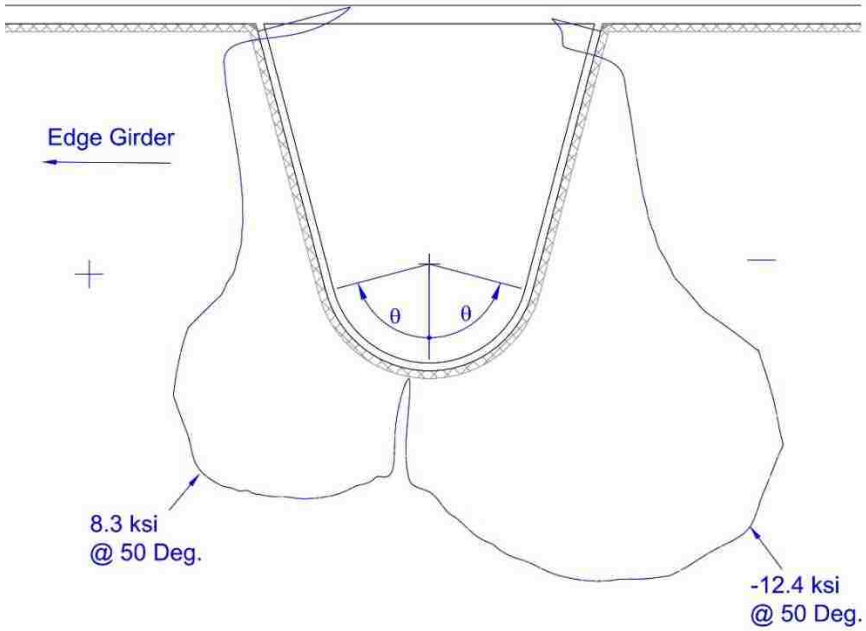

Figure 91 Variation of maximum principal stress at weld root

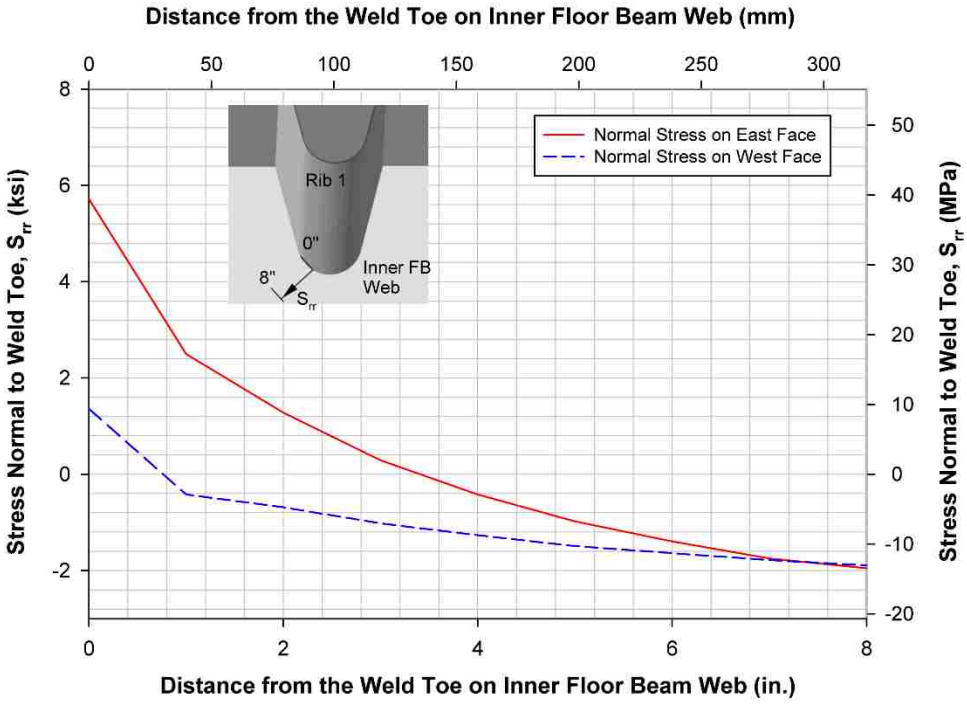

Figure 92 Out-of-plane bending of inner FB web

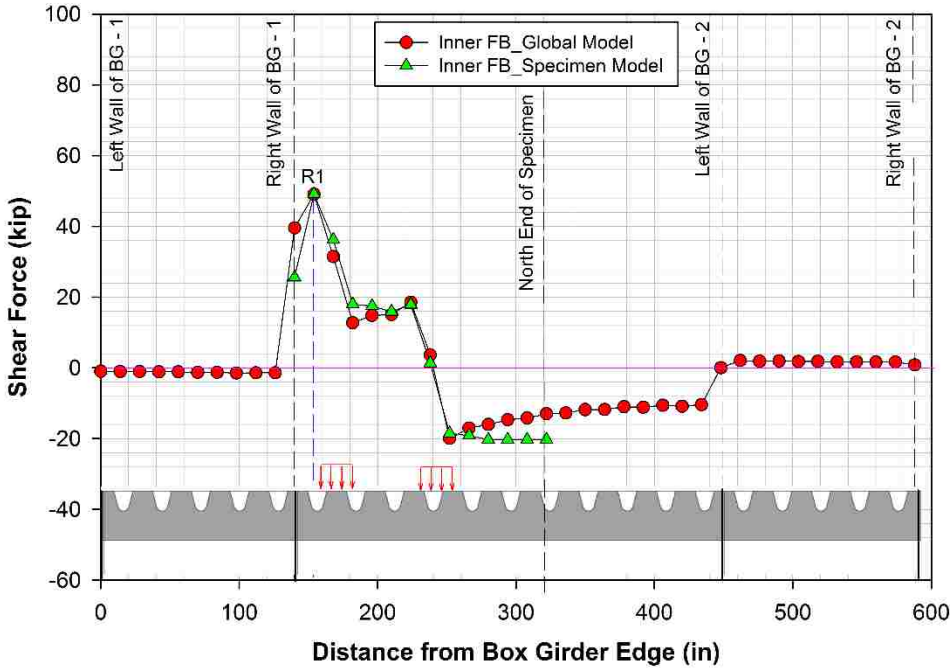

Figure 93 Comparison of shear force in GM and specimen model

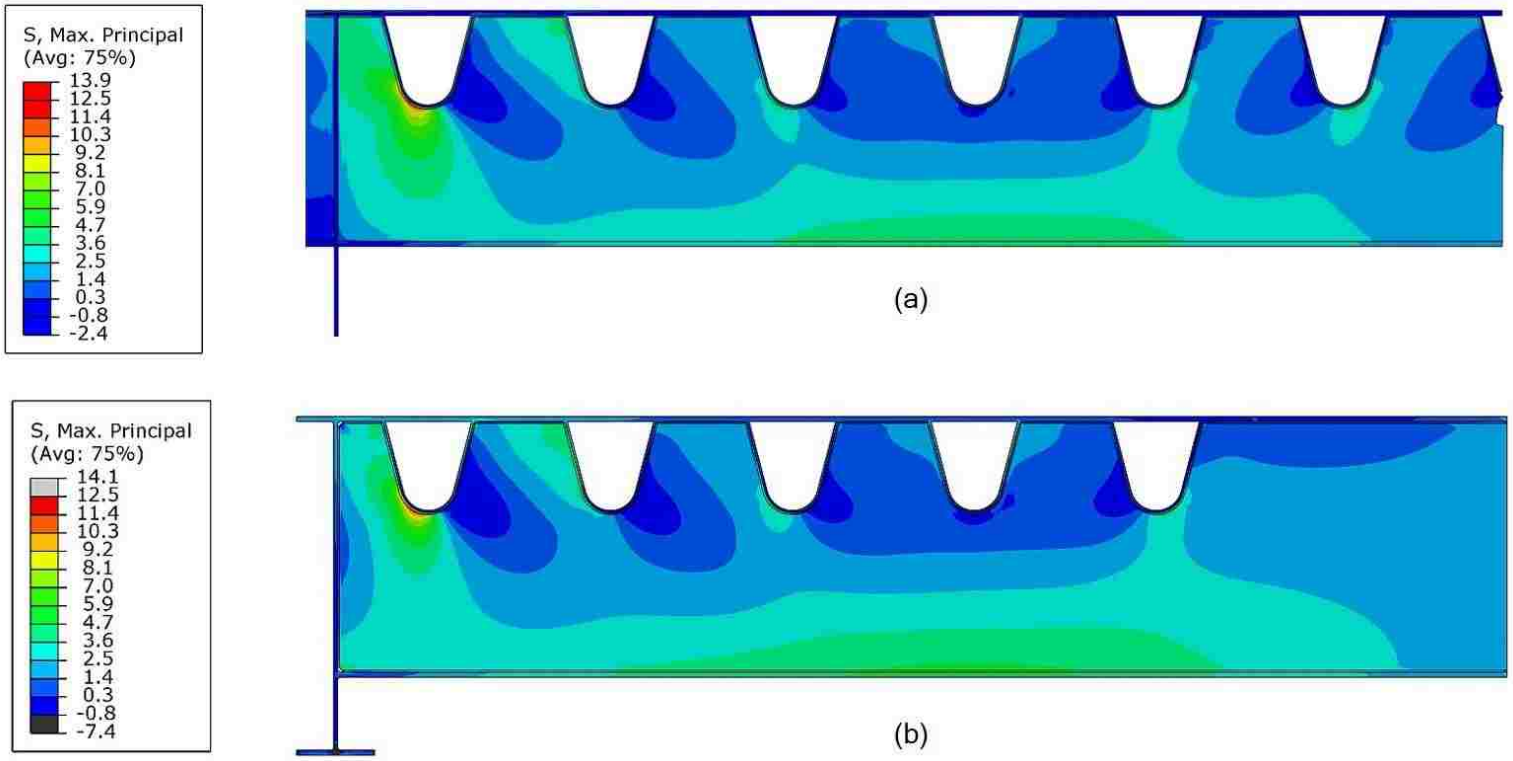

Figure 94 Principal stress contour in inner FB web: (a) SM; (b) specimen model

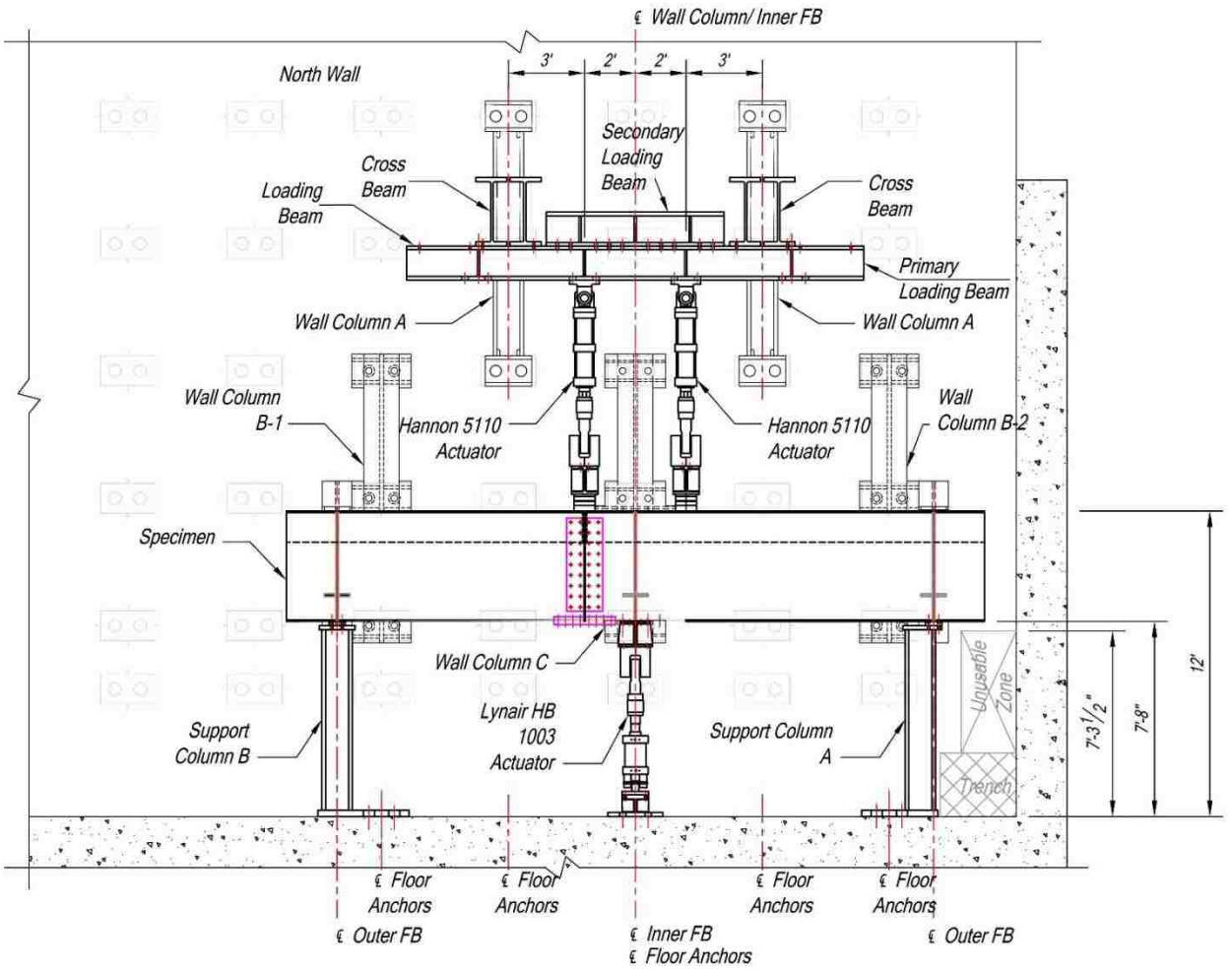

Figure 95 North elevation of the test setup

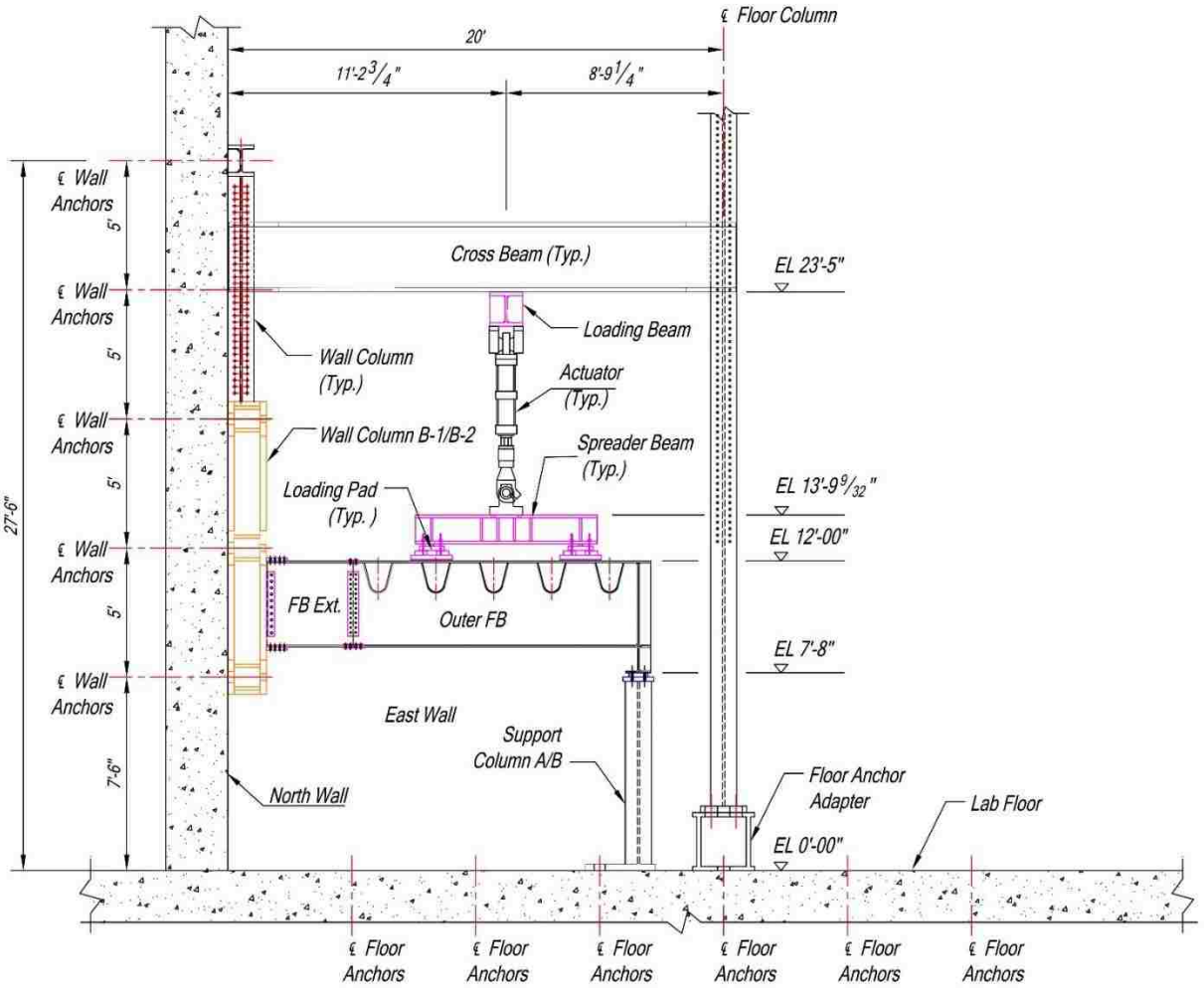

Figure 96 Side elevation of the test setup (looking east)

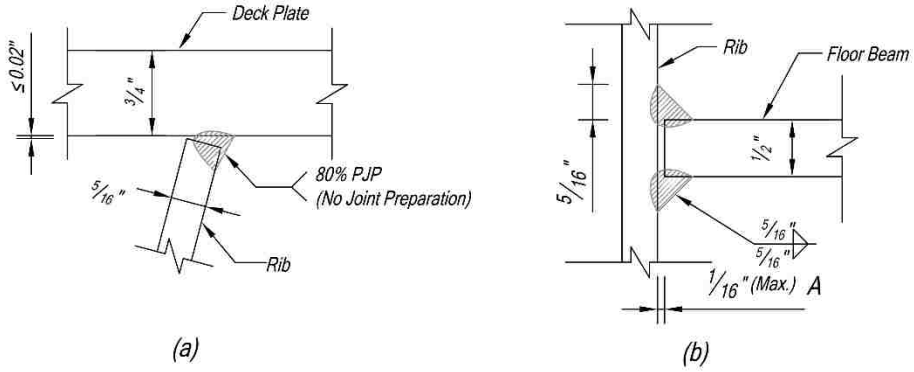

Figure 97 Connection details for full-scale prototype: (a) rib-to-deck plate connection; (b) rib-to-floor beam connection

Figure 98 Rib-to-deck plate welding procedure (not showing prototype deck fabrication)

Figure 99 Match-cutting of floor beam for rib-to-floor beam weld

Figure 100 Floor beam-to-deck plate welding

Figure 101 Rib-to-floor beam welding in 2F position

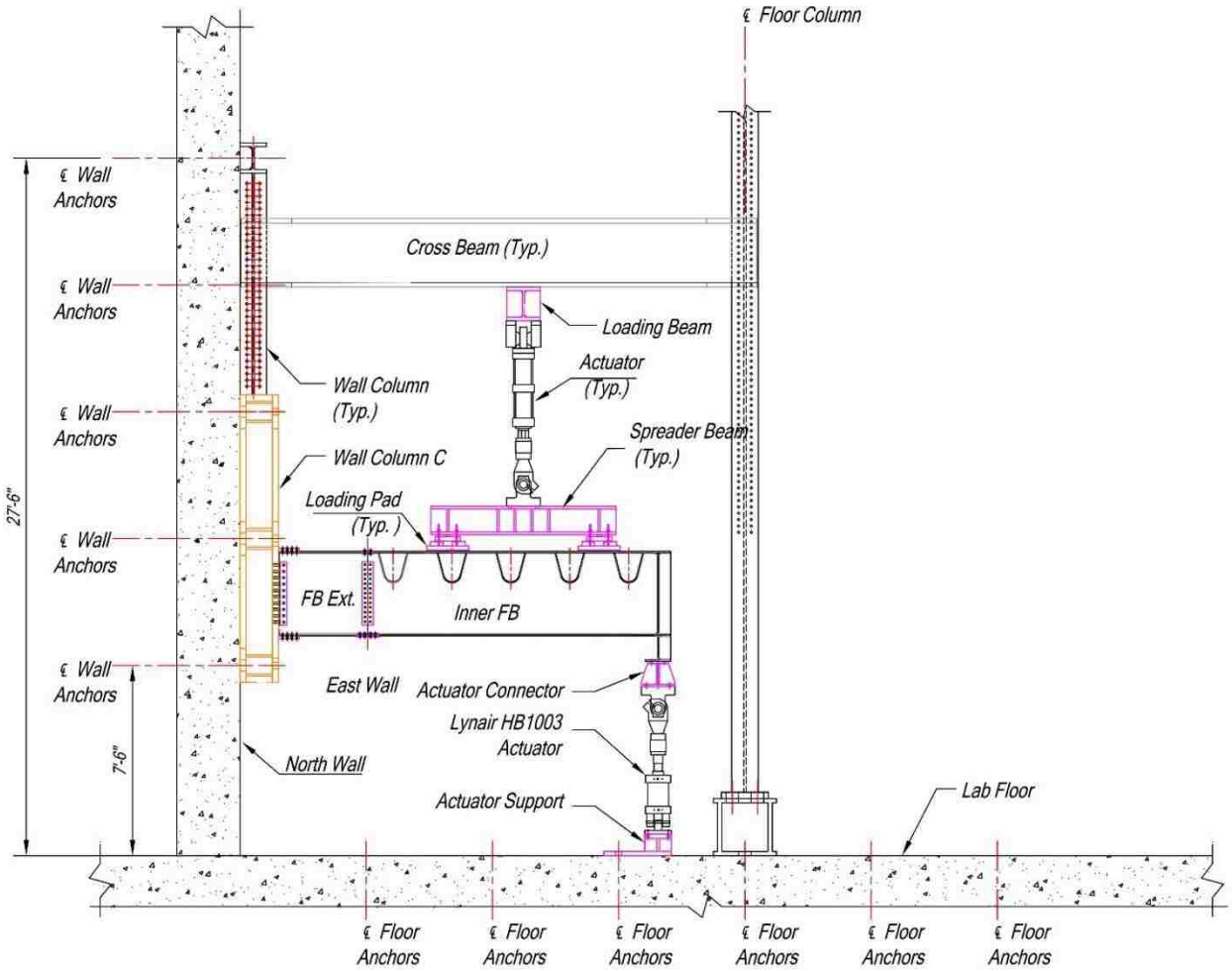

Figure 102 Sectional elevation of the test setup at the inner FB (looking east)

Figure 103 Fixtures for the prototype deck

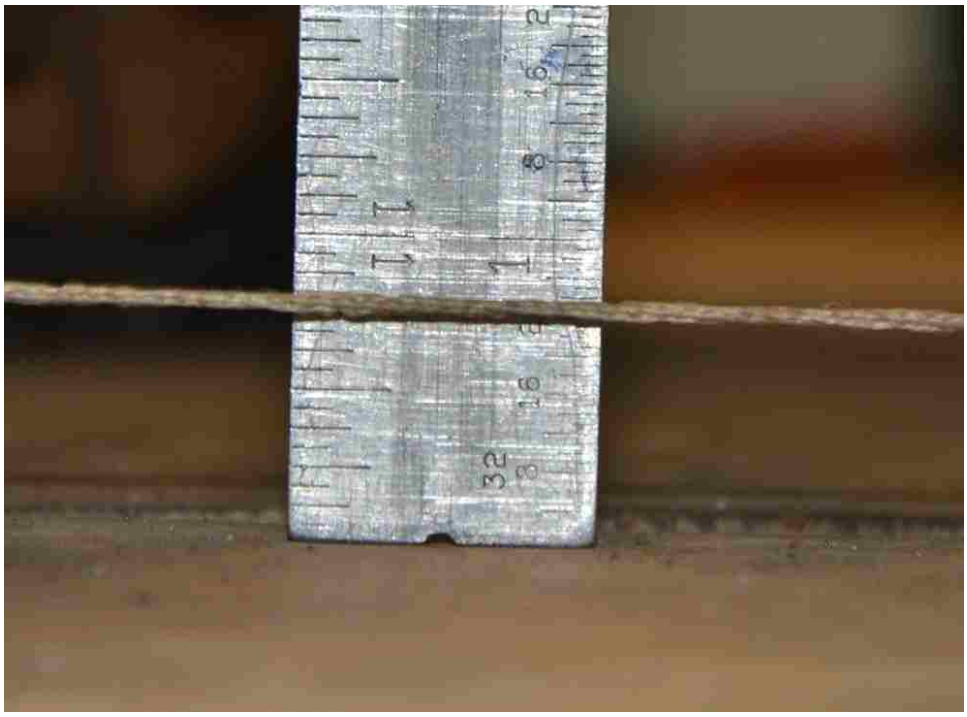

Figure 104 Measurement of deck level

Figure 105 Installation of the east panel

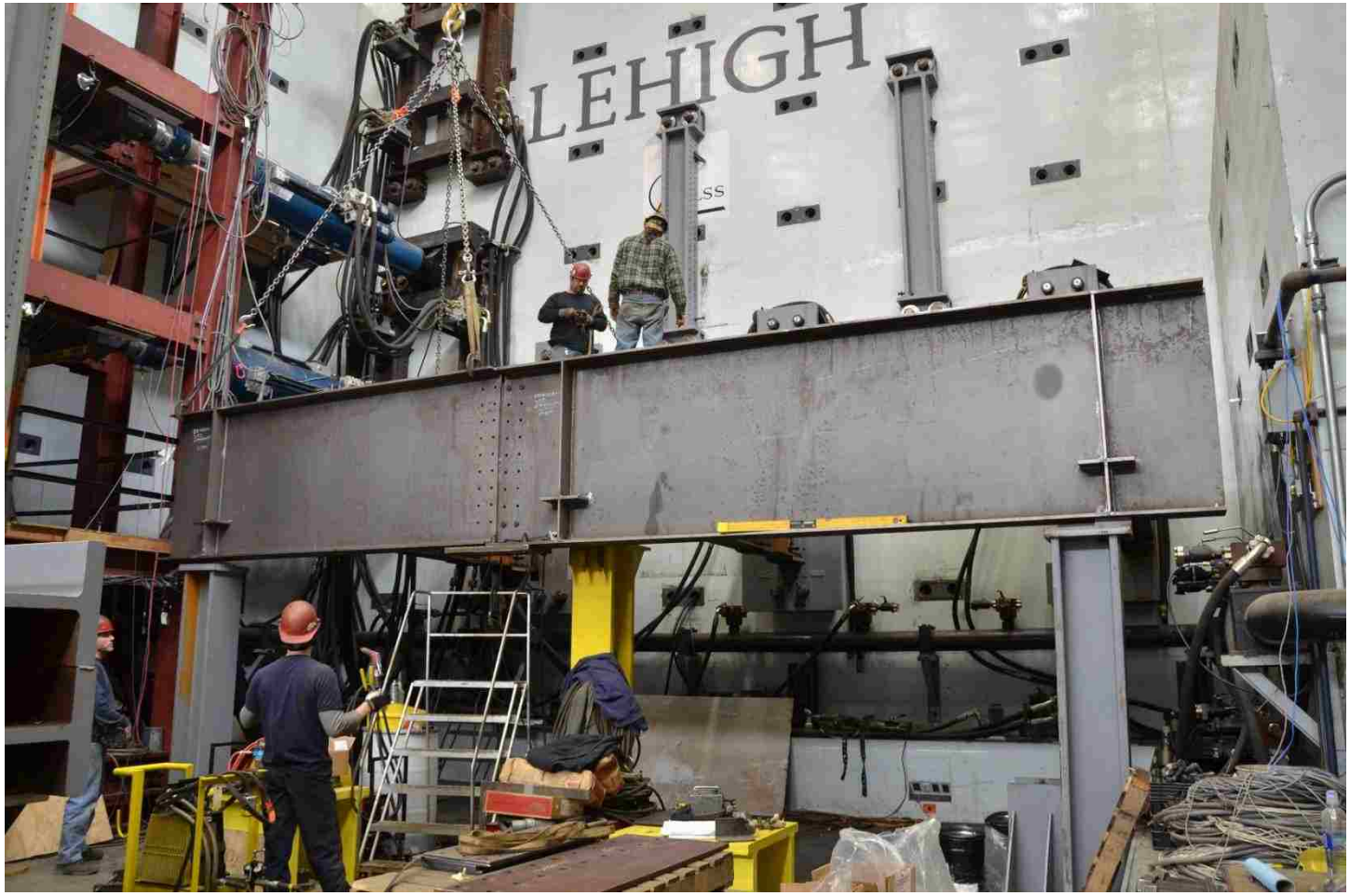

Figure 106 Installation of the west panel

Figure 107 Heat marks on the deck after heat treatment

Figure 108 Elevation difference at splice location before tacking

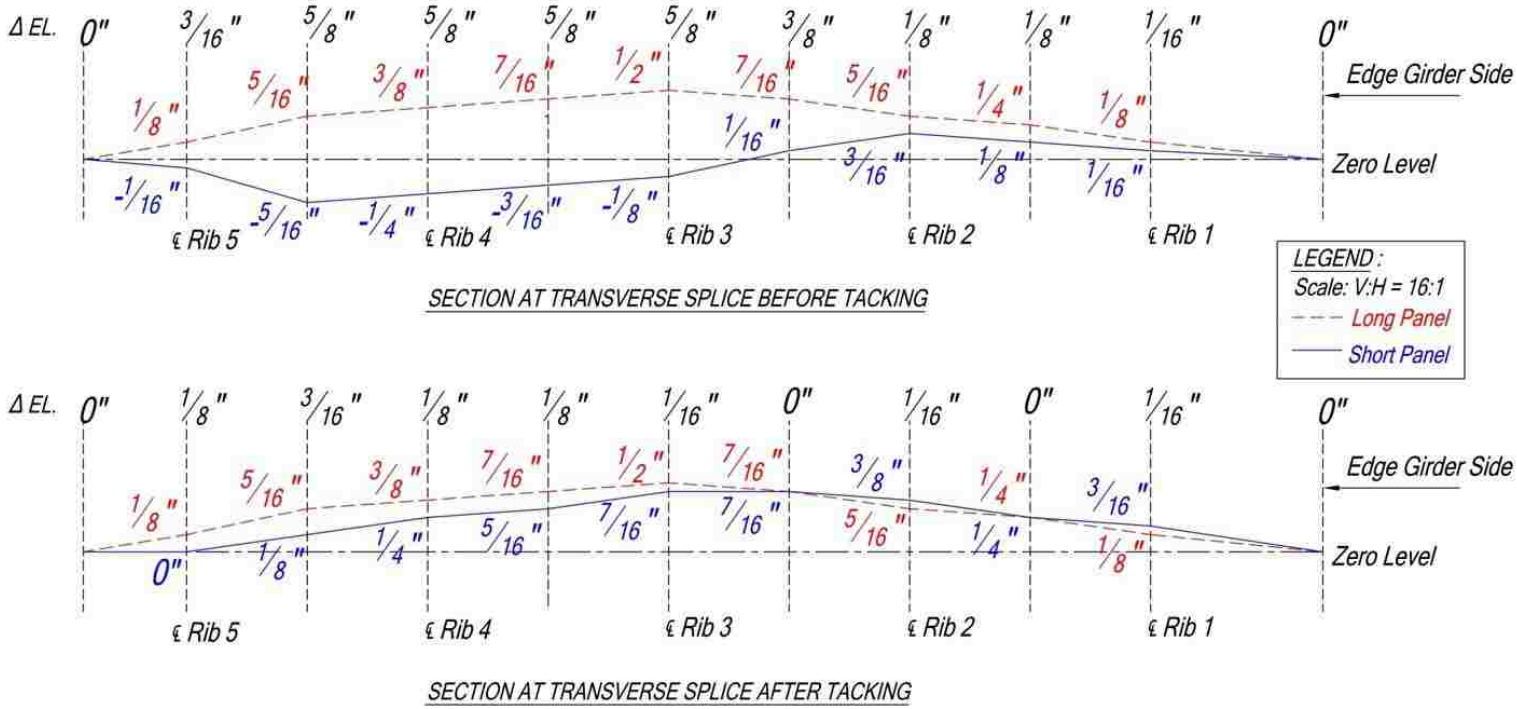

Figure 109 Comparison of elevation difference at transverse splice location before and after tacking

Figure 110 Jacking of west panel

Figure 111 Maximum root gap of ½ in.

Figure 112 Lack of alignment of the ribs

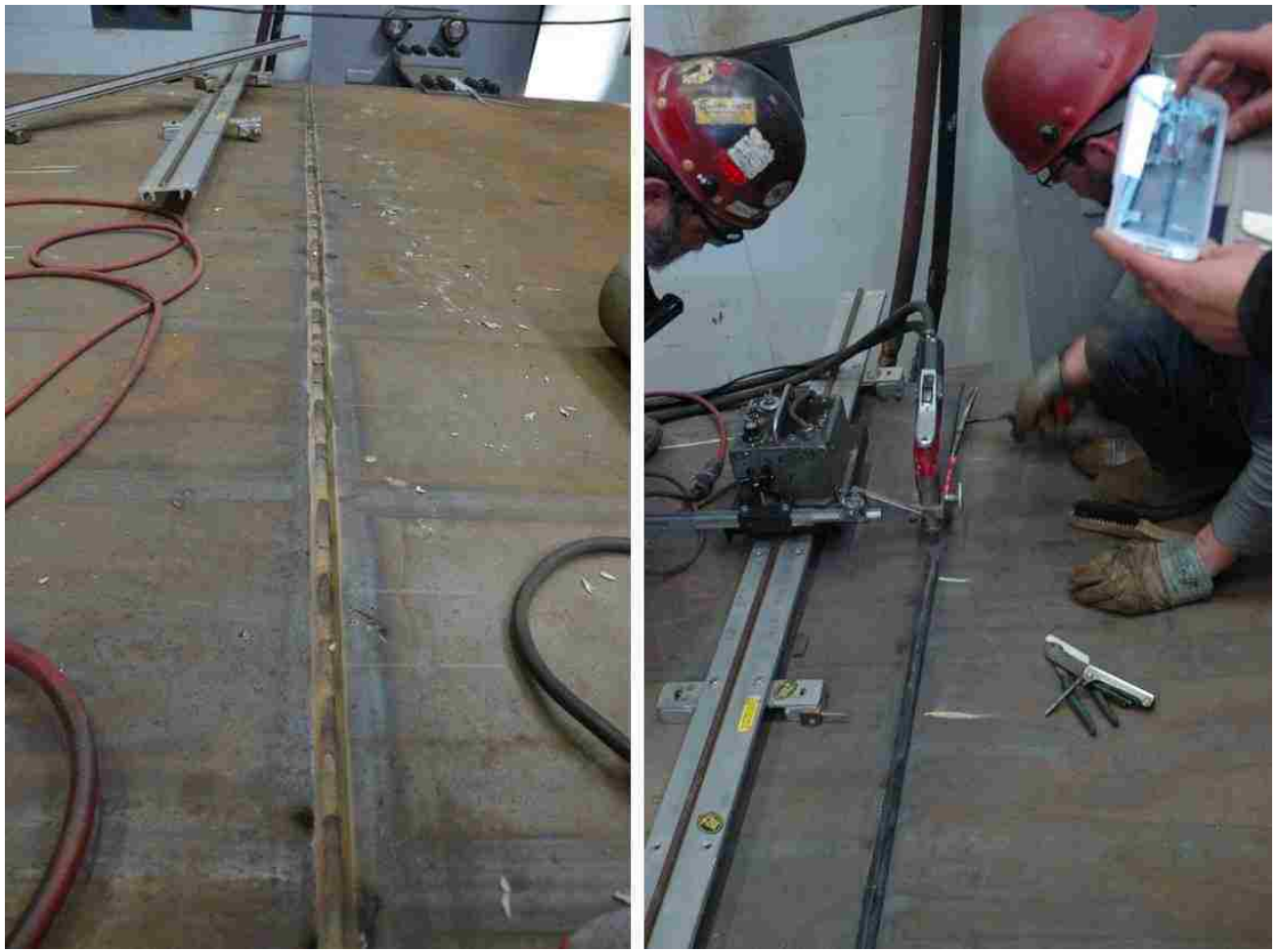

Figure 113 Root pass and fill pass for the CJP weld at the transverse deck splice at deck plate

Figure 114 Weld root after removing of backing bar

Figure 115 Back gouge and re-welding in between the ribs

Figure 116 Extensive efforts for back gouge and re-welding inside the rib

Figure 117 Weld root after re-welding

Figure 118 Lack of access over the rib wall for re-welding

Figure 119 UT of CJP Deck Splice

Figure 120 Deck level measurements using laser

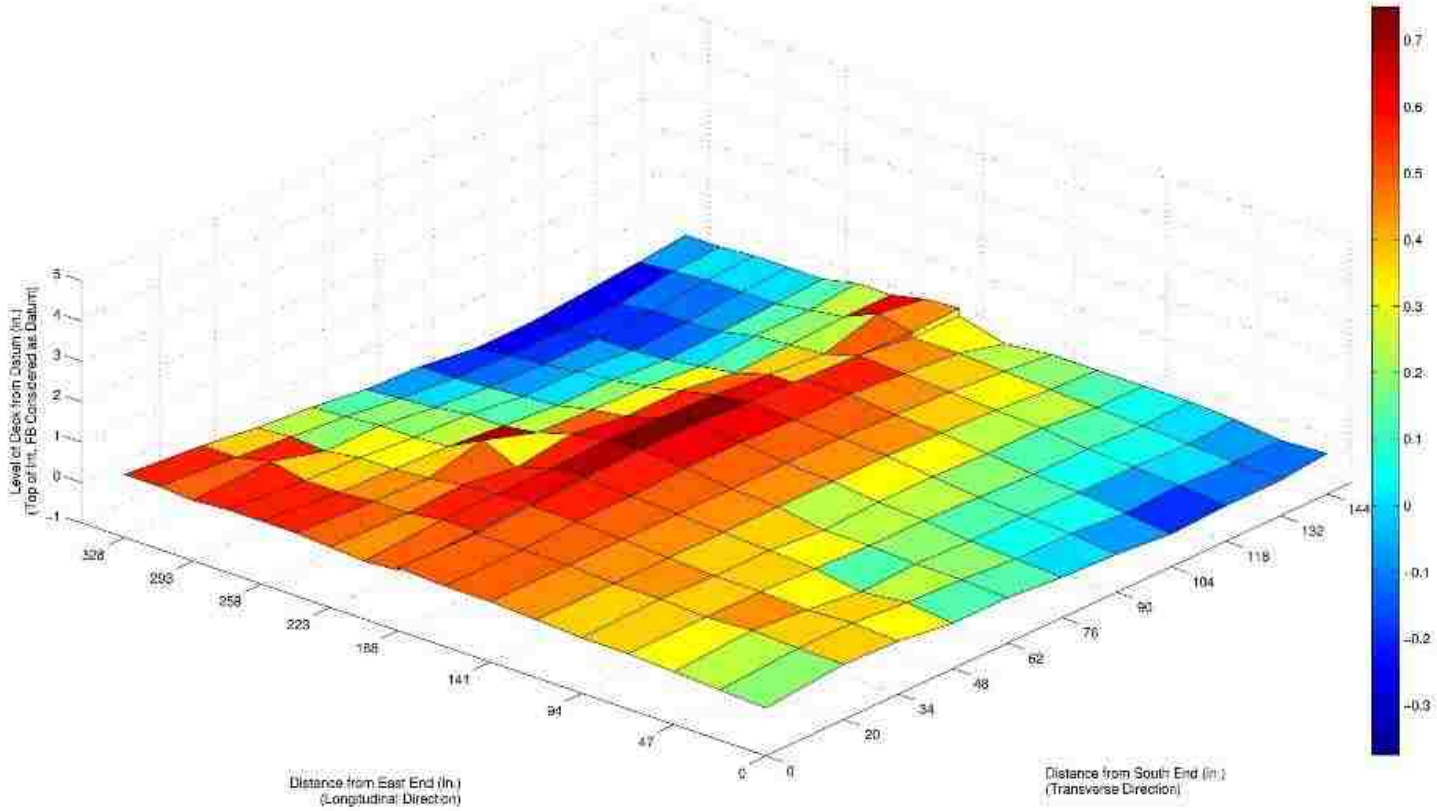

Figure 121 Laser measurements of deck level after installation

Figure 122 Test setup

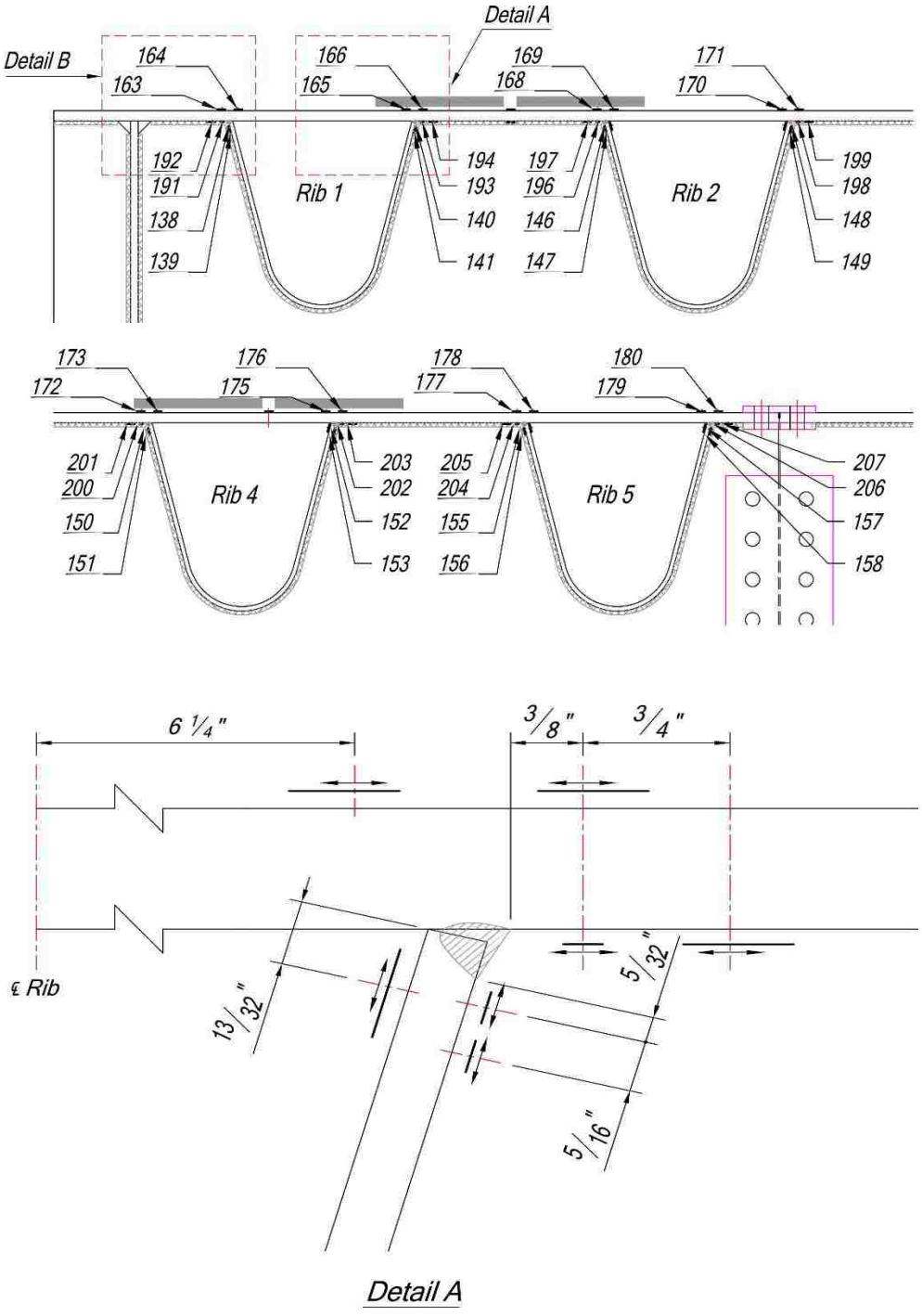

Figure 123 Gauges on deck plate at section Z-Z (Detail B is similar to Detail A but handed)

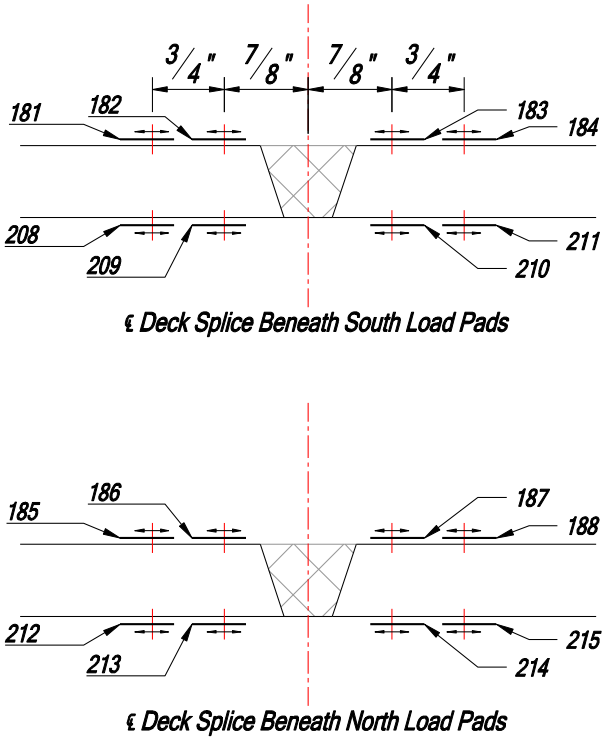

Figure 124 Gauges on deck plate around deck splice at section X-X

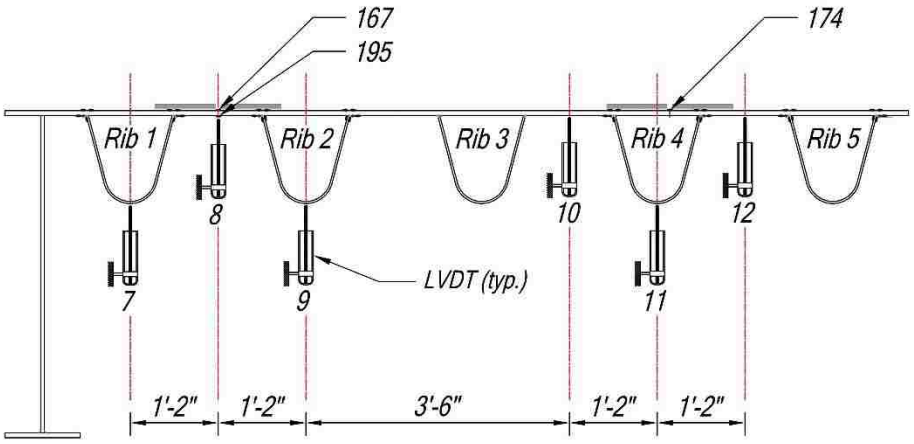

Figure 125 LVDTs at section Z-Z

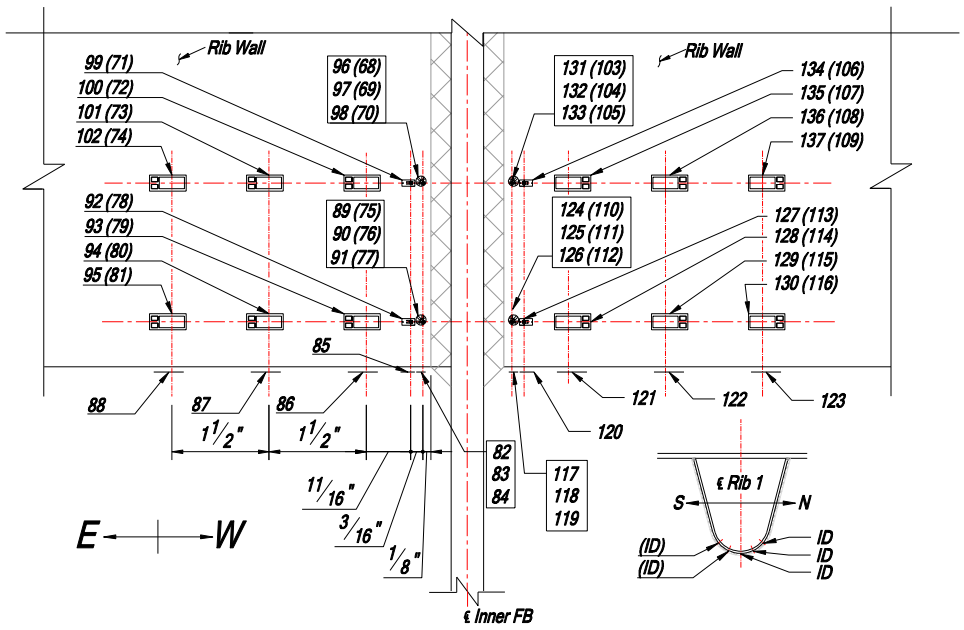

Figure 126 Gauges on north wall of Rib 1 wall at inner FB (gauges on south wall are shown in parenthesis)

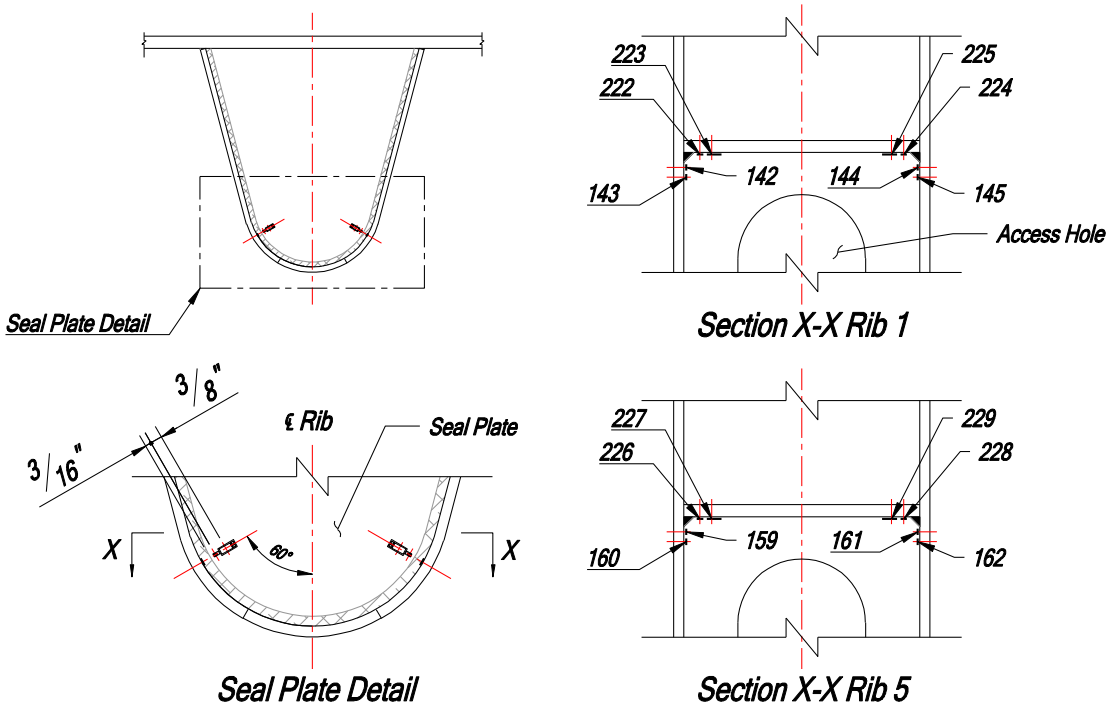

Figure 127 Gauges at rib-to-sealing plate connection

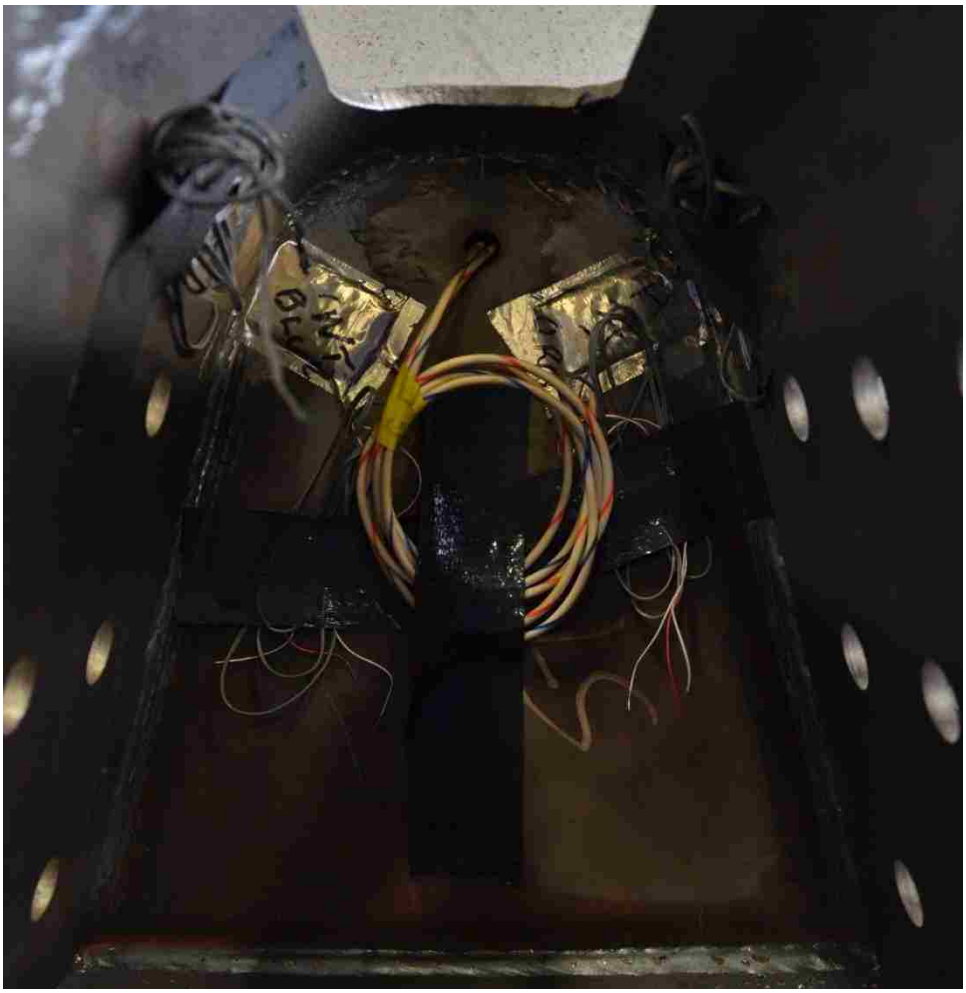

Figure 128 Installation of gauges on rib wall and sealing plate at rib-to-sealing plate connection at HIS facility

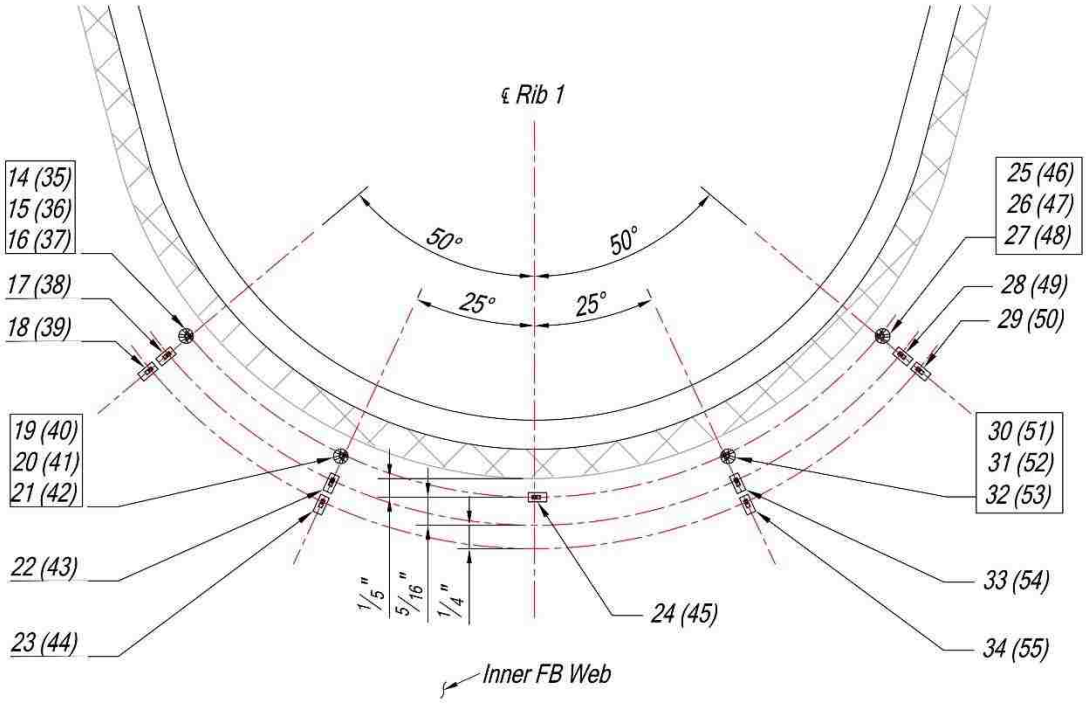

Figure 129 Gauges on east face of inner FB web at Rib 1 (gauges on the west face are shown in parenthesis)

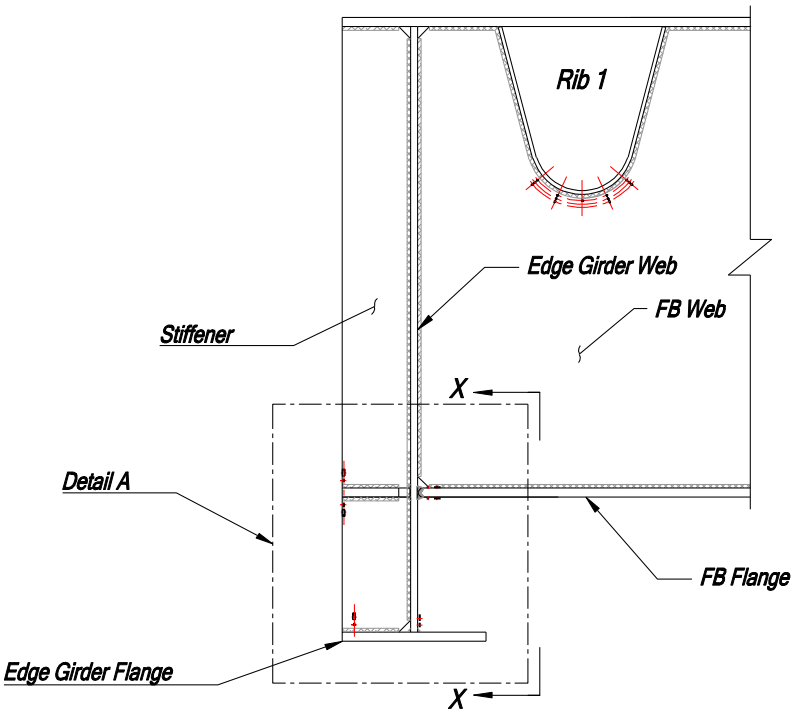

Figure 130 Gauges at inner FB-to-edge girder connection

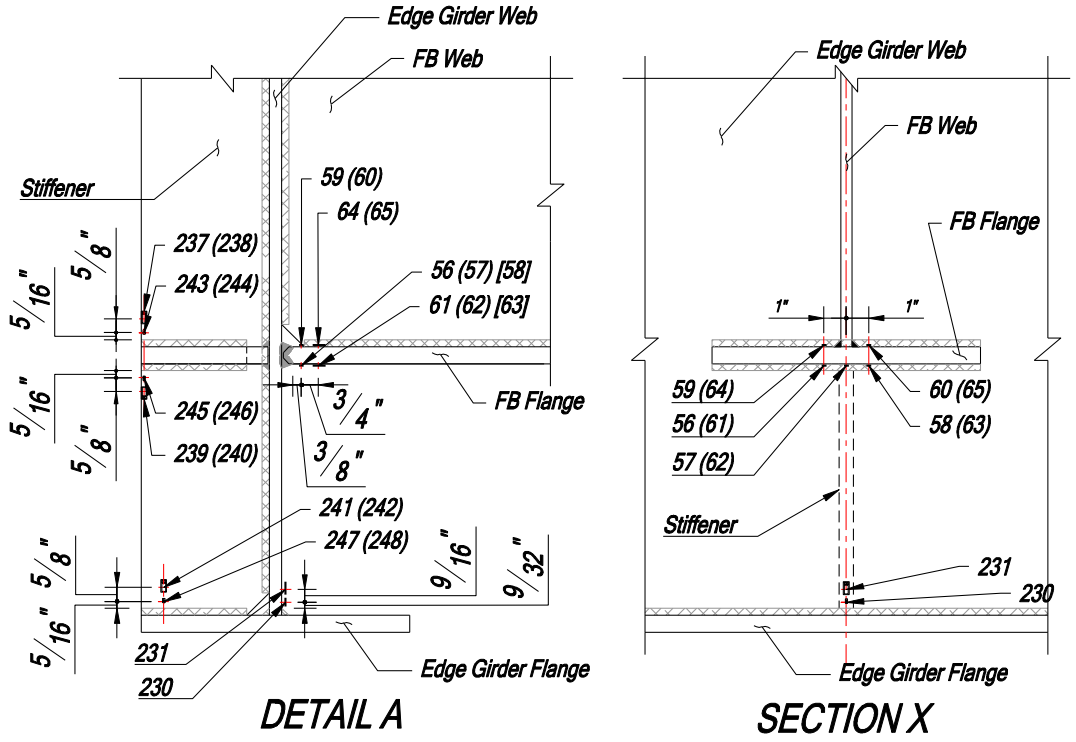

Figure 131 Gauges at inner FB-to-edge girder connection (refer Figure 130 for detail and section markings)

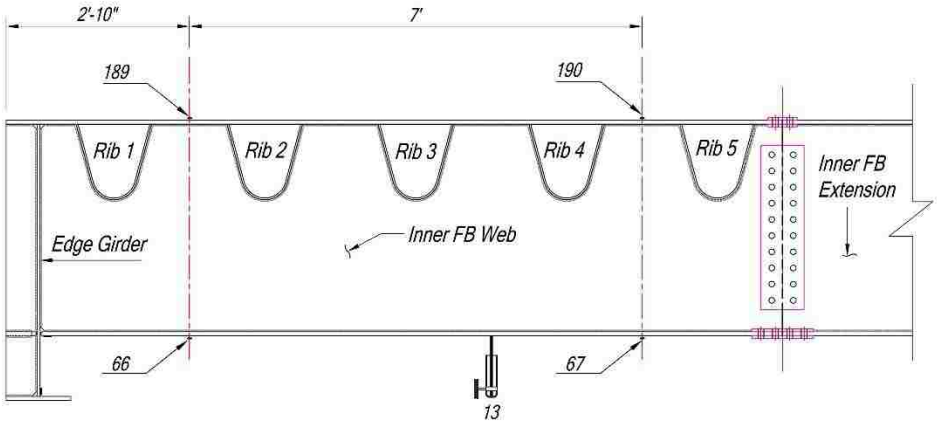

Figure 132 Gauges on inner FB at section Y-Y

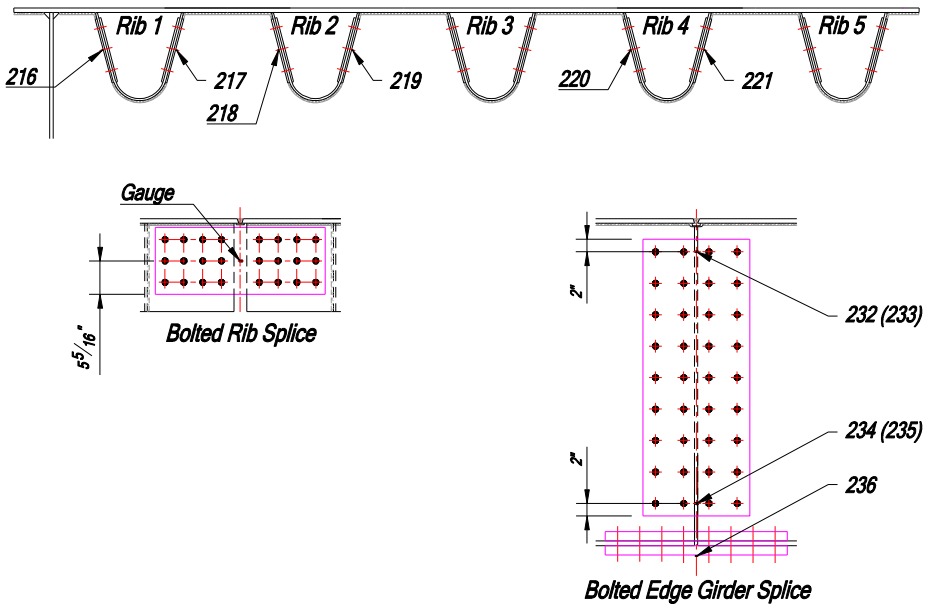

Figure 133 Gauges on the splice plates

Figure 134 Crawl truck

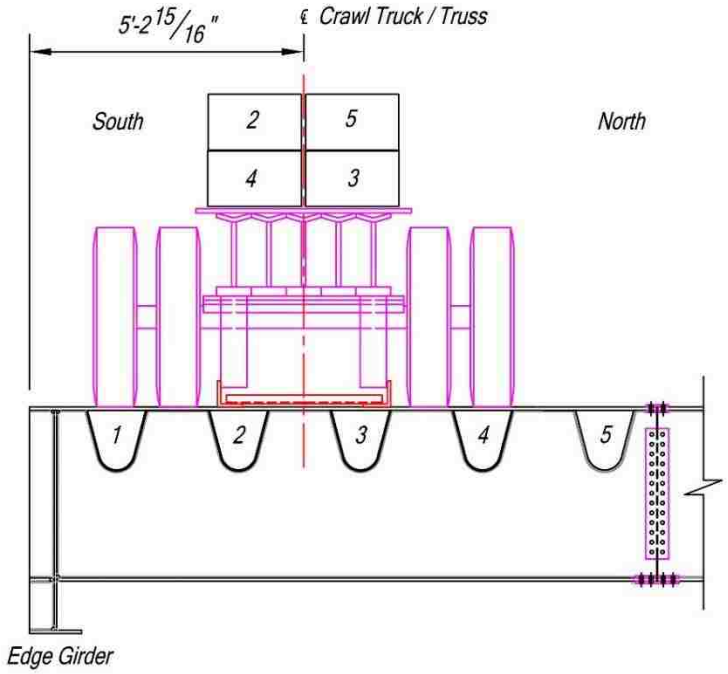

Figure 135 Crawl test position 28

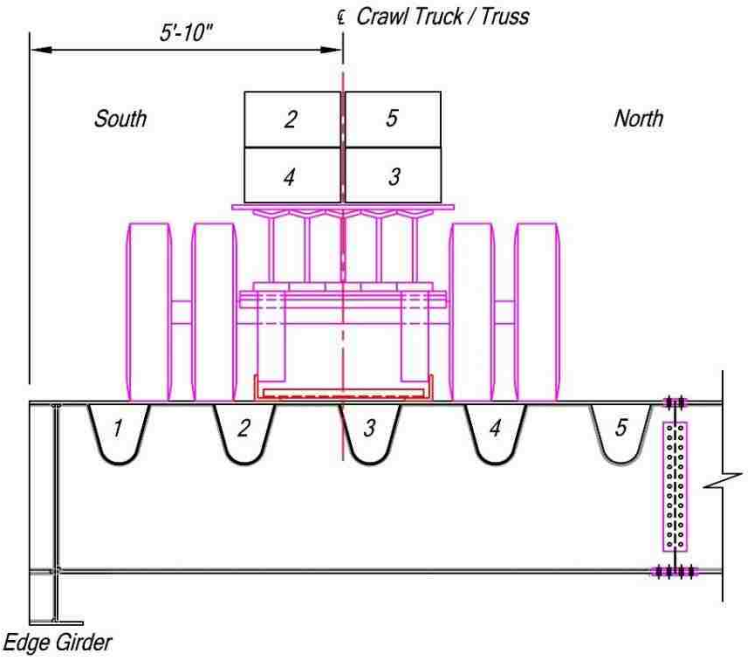

Figure 136 Crawl test position 29

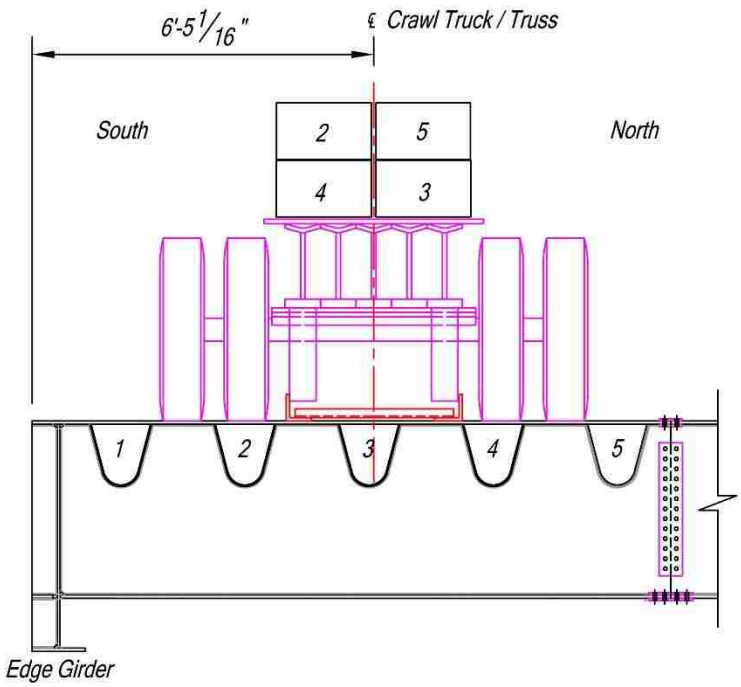

Figure 137 Crawl test position 30

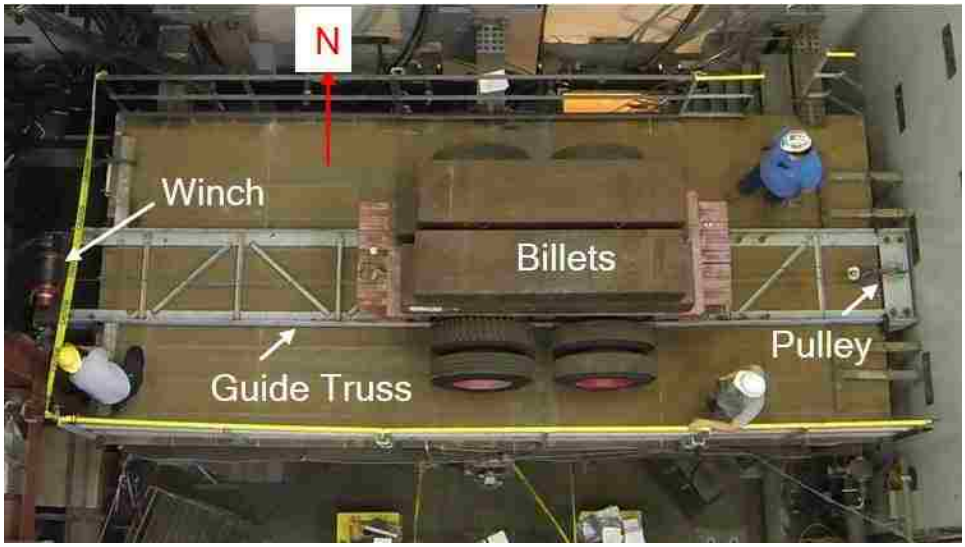

Figure 138 Crawl test setup

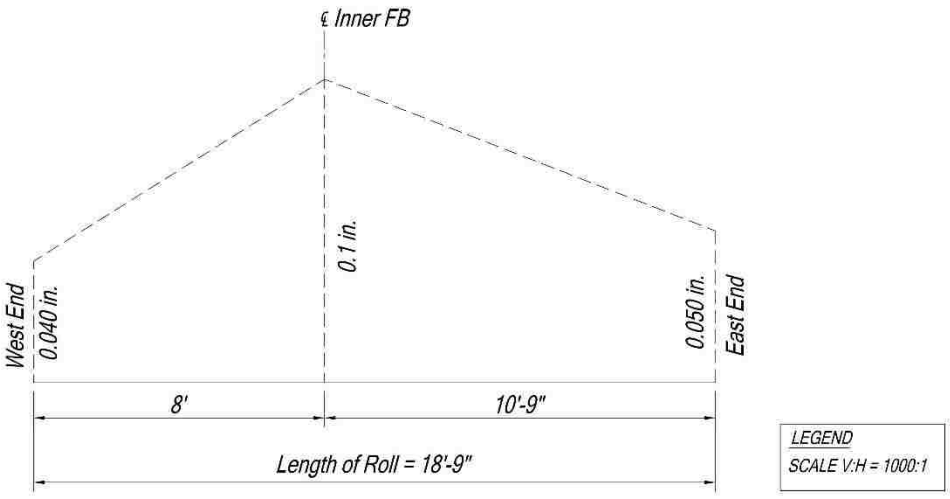

Figure 139 Displacement profile for crawl test

Figure 140 Arrangement of above-deck actuators

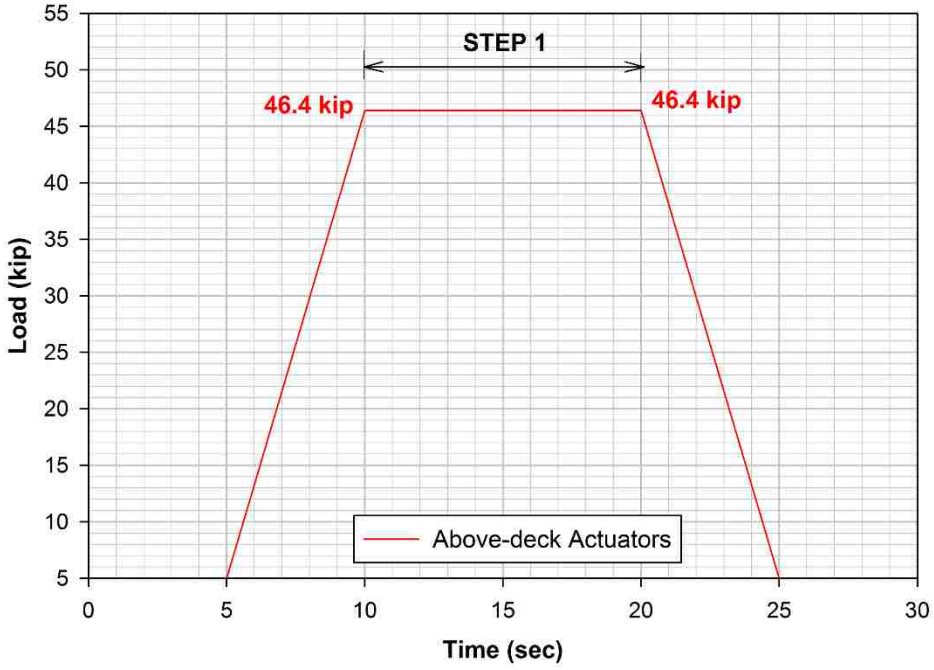

Figure 141 Loading profile for static test

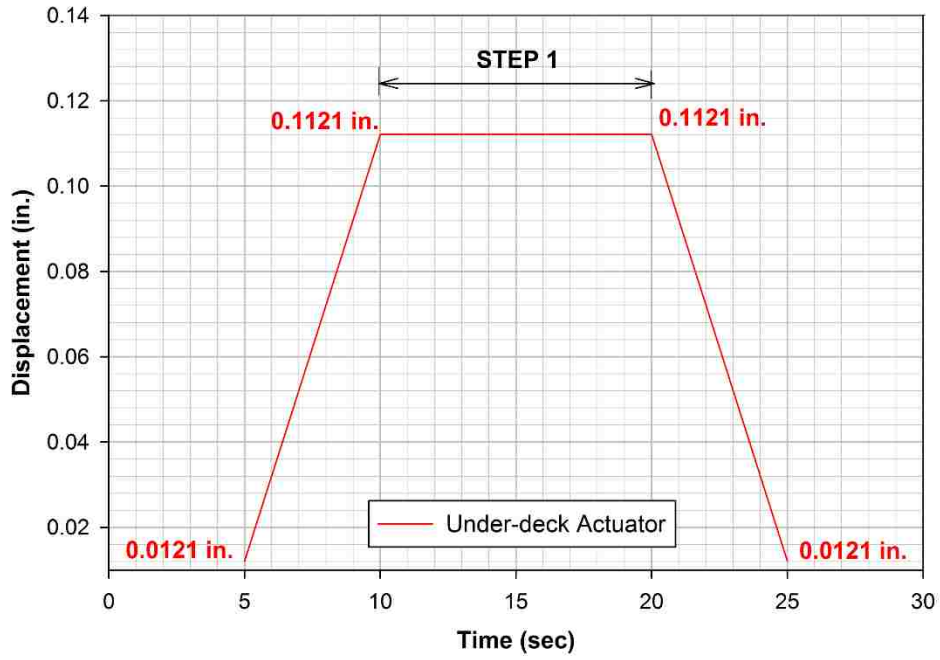

Figure 142 Displacement profile for static test

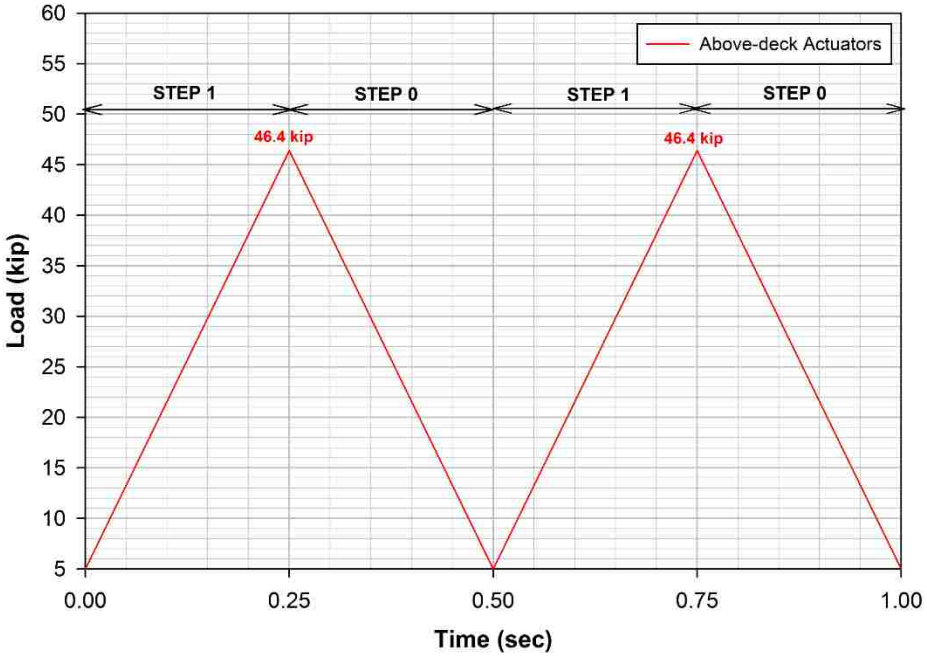

Figure 143 Loading profile for the fatigue test

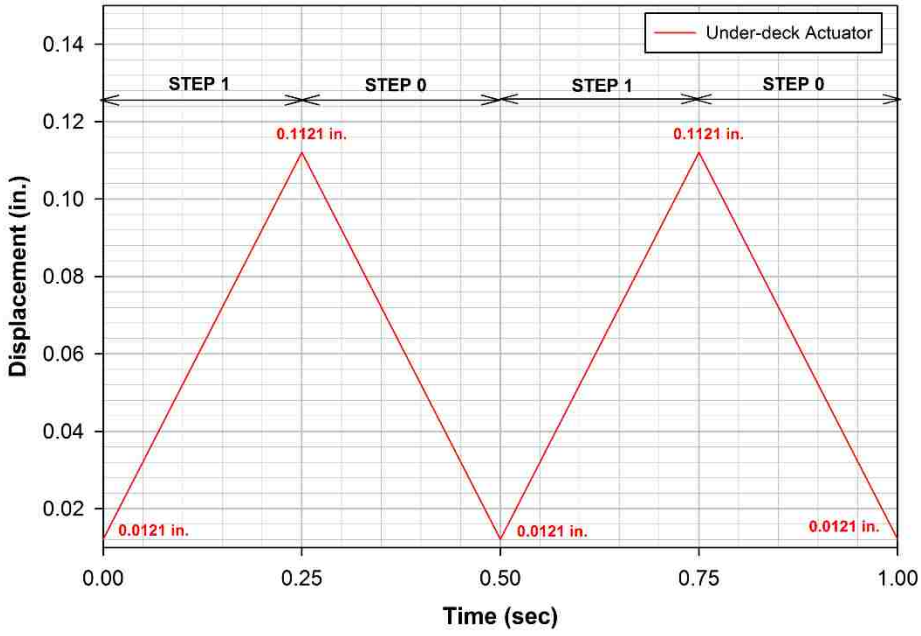

Figure 144 Displacement profile for the fatigue test

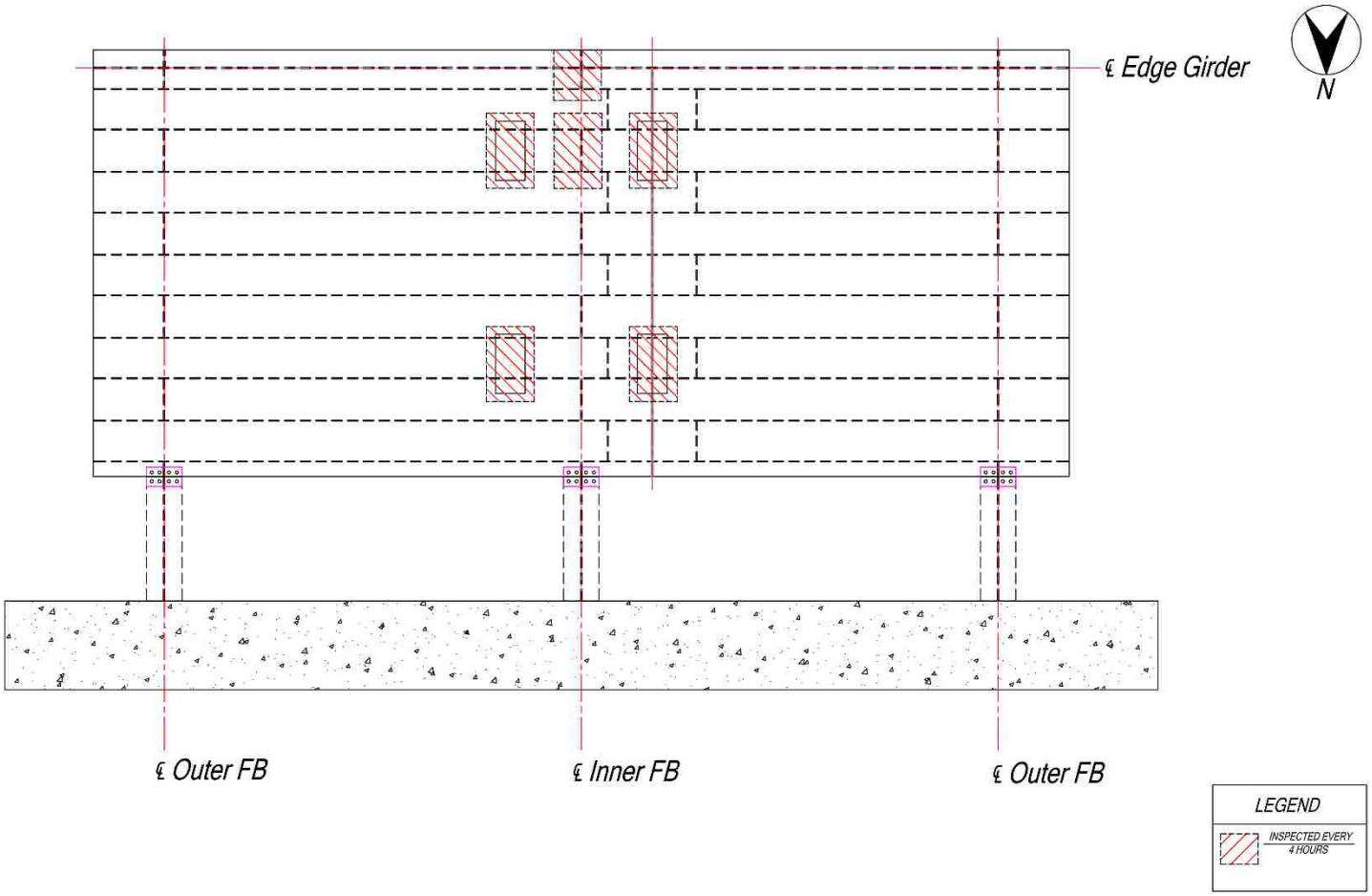

Figure 145 Inspection plan for fatigue testing

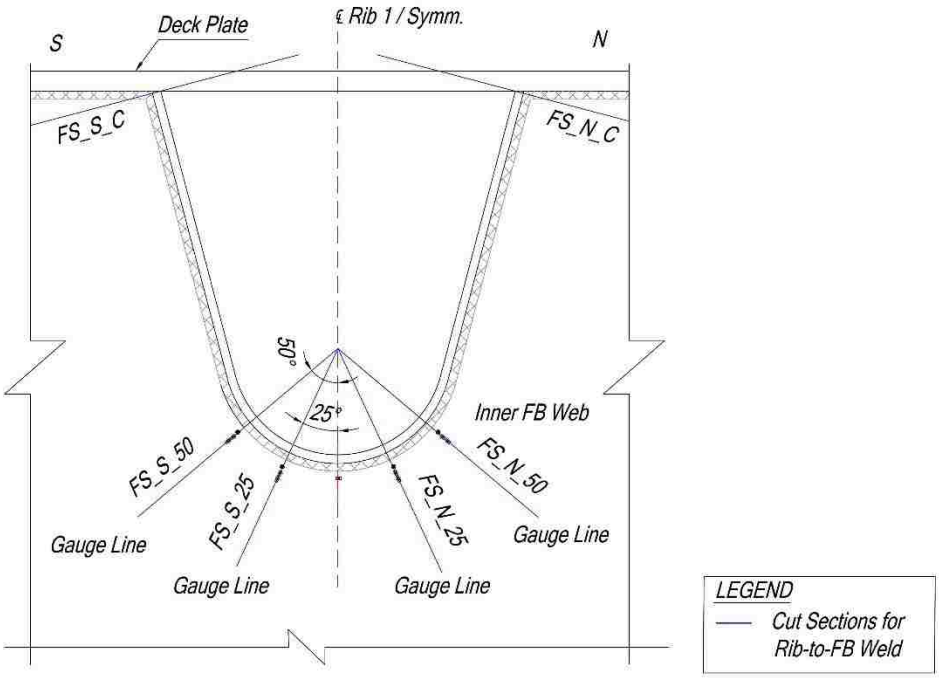

Figure 146 Section identification of Rib 1-to-inner FB weld

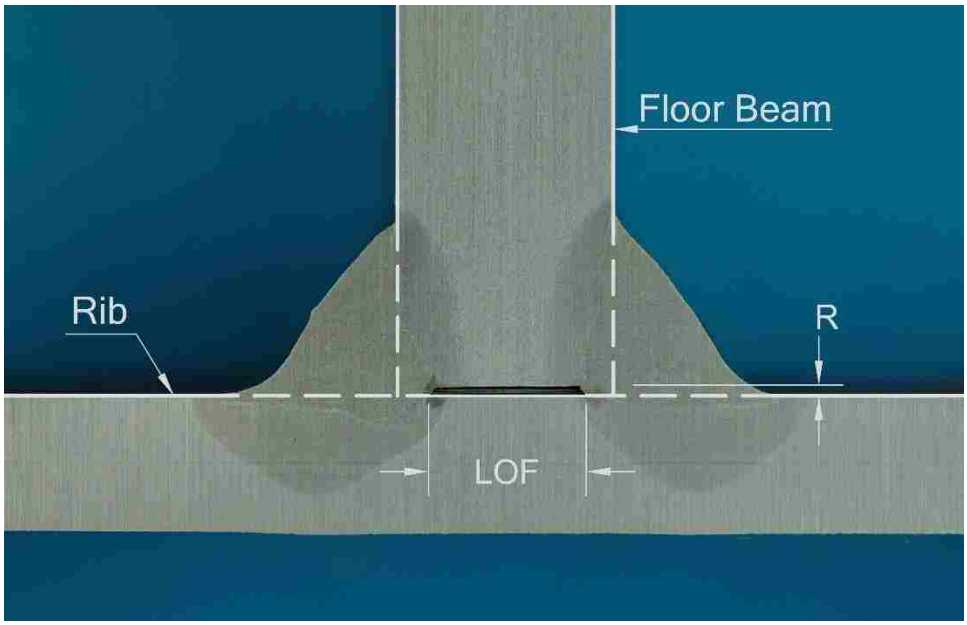

Figure 147 Schematic of rib-to-floor beam weld

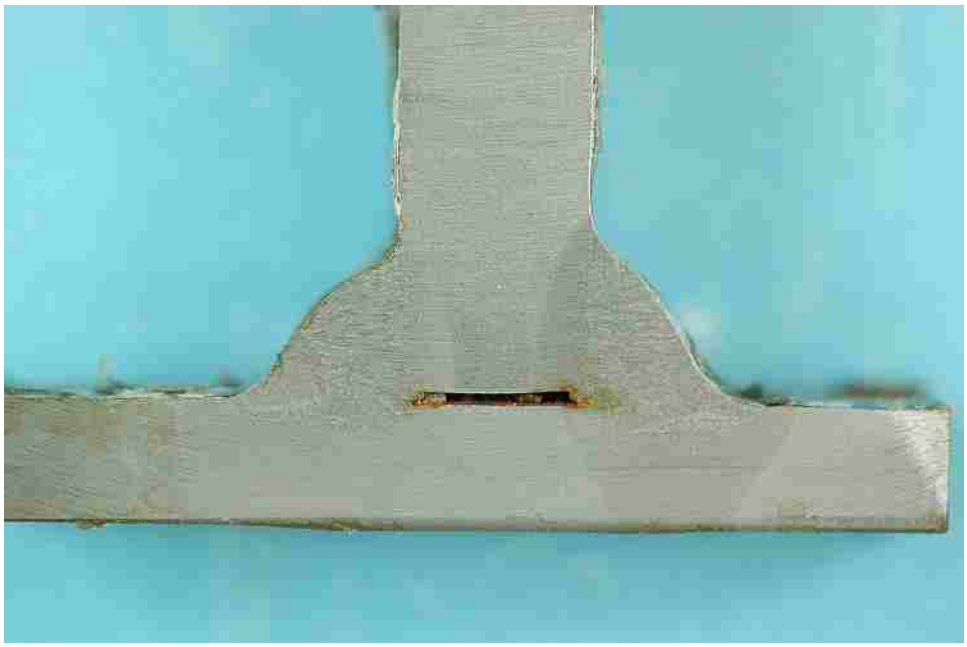

Figure 148 Macro-etched section FS_N_25

Figure 149 Macro-etched section FS_N_50

Figure 150 Macro-etched section FS_N_C

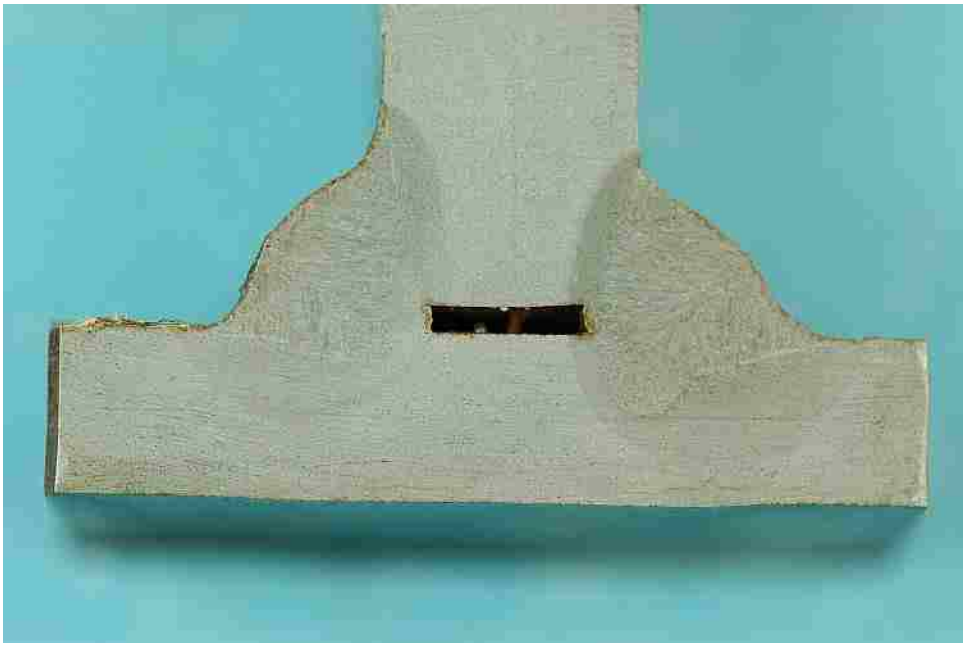

Figure 151 Macro-etched section FS_S_25

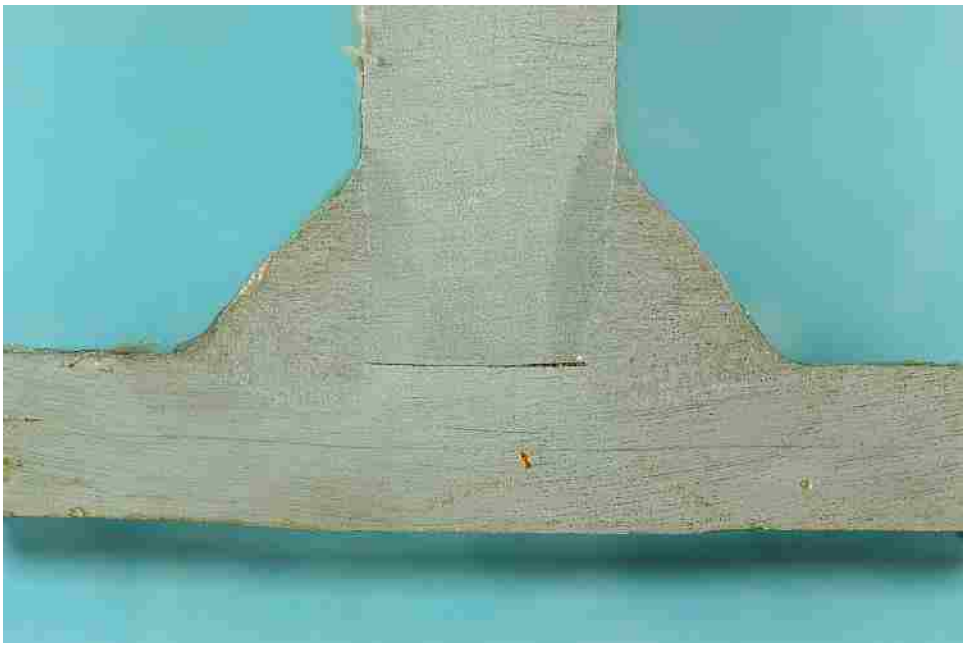

Figure 152 Macro-etched section FS_S_50

Figure 153 Macro-etched section FS_S_C

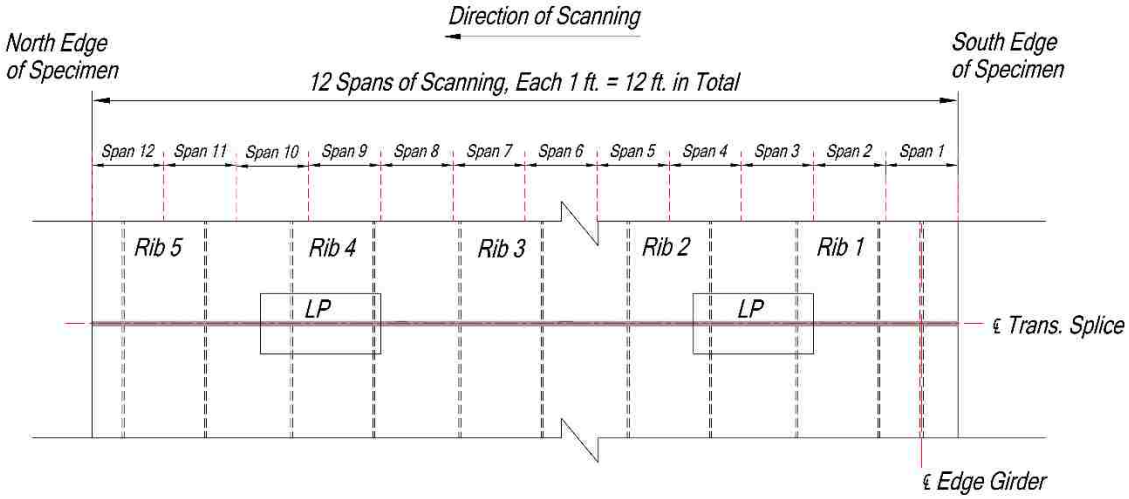

Figure 154 Schematic of PAUT scanning of the CJP deck weld

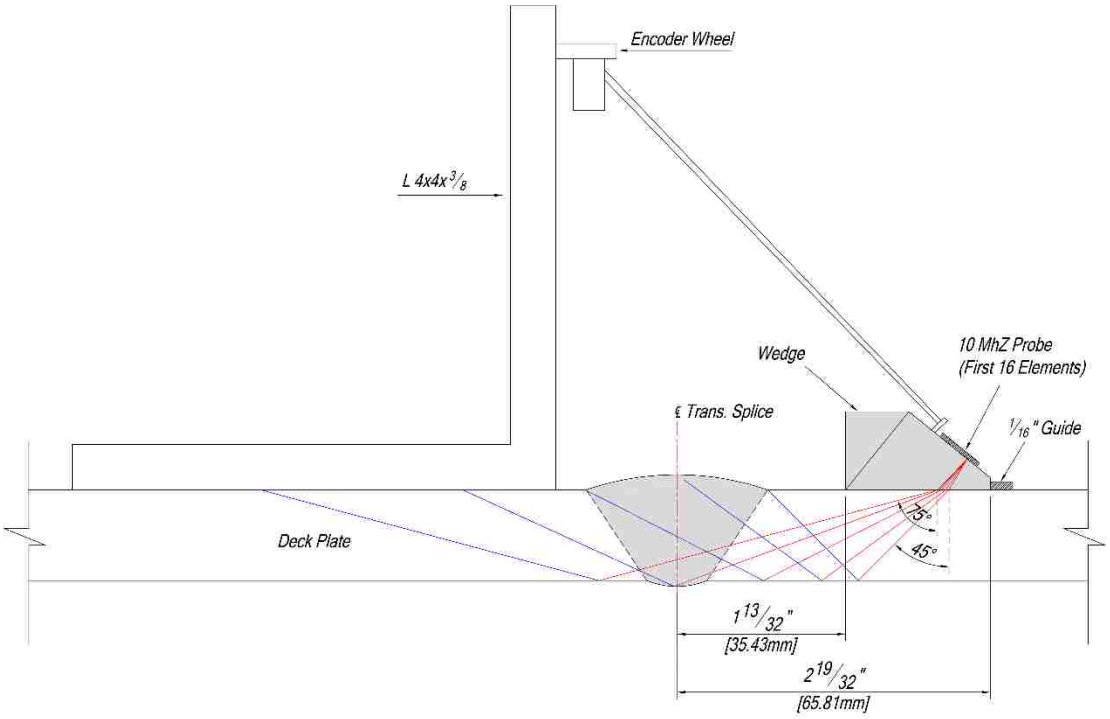

Figure 155 Schematic of the PAUT scan setup

Figure 156 Scan setup in the laboratory

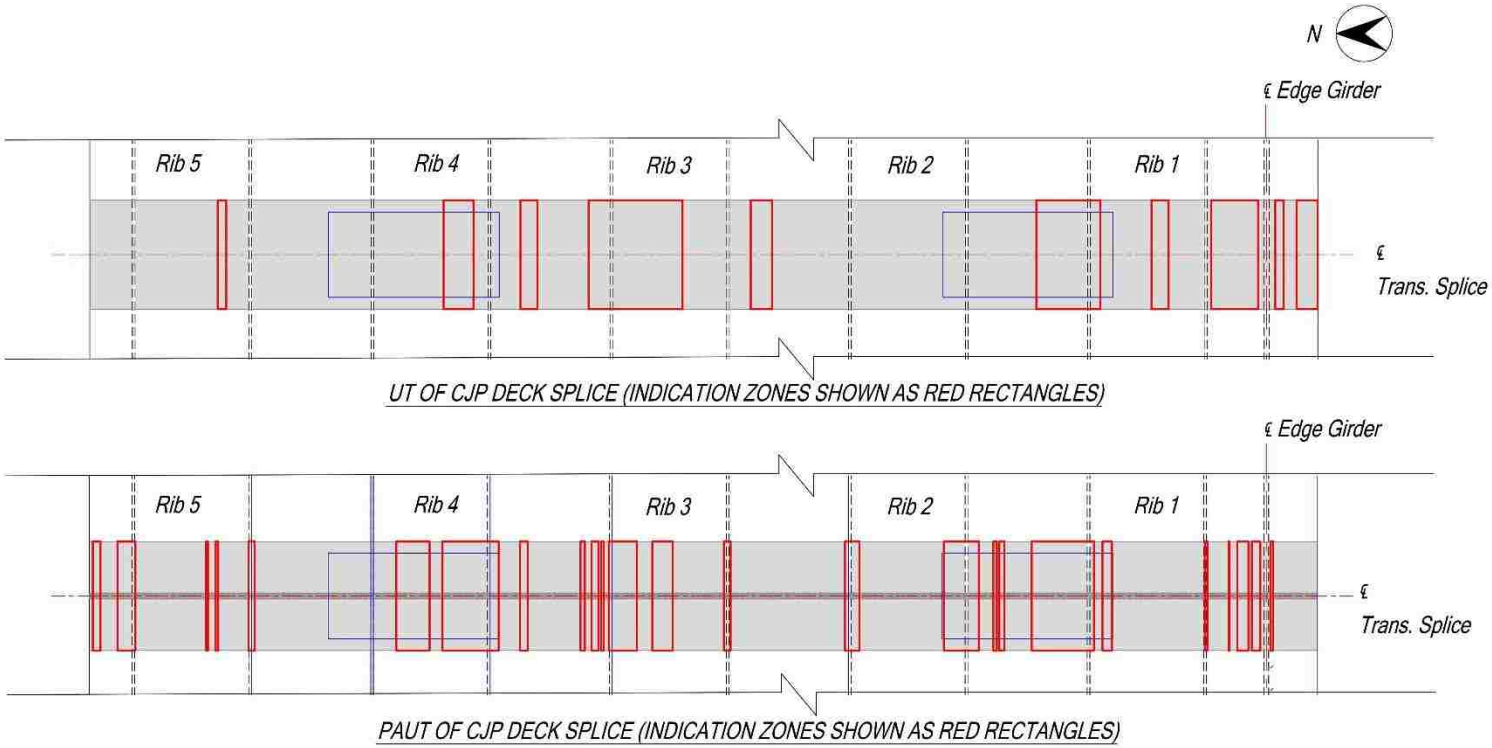

Figure 157 Comparison of UT and PAUT measurements on the plan view

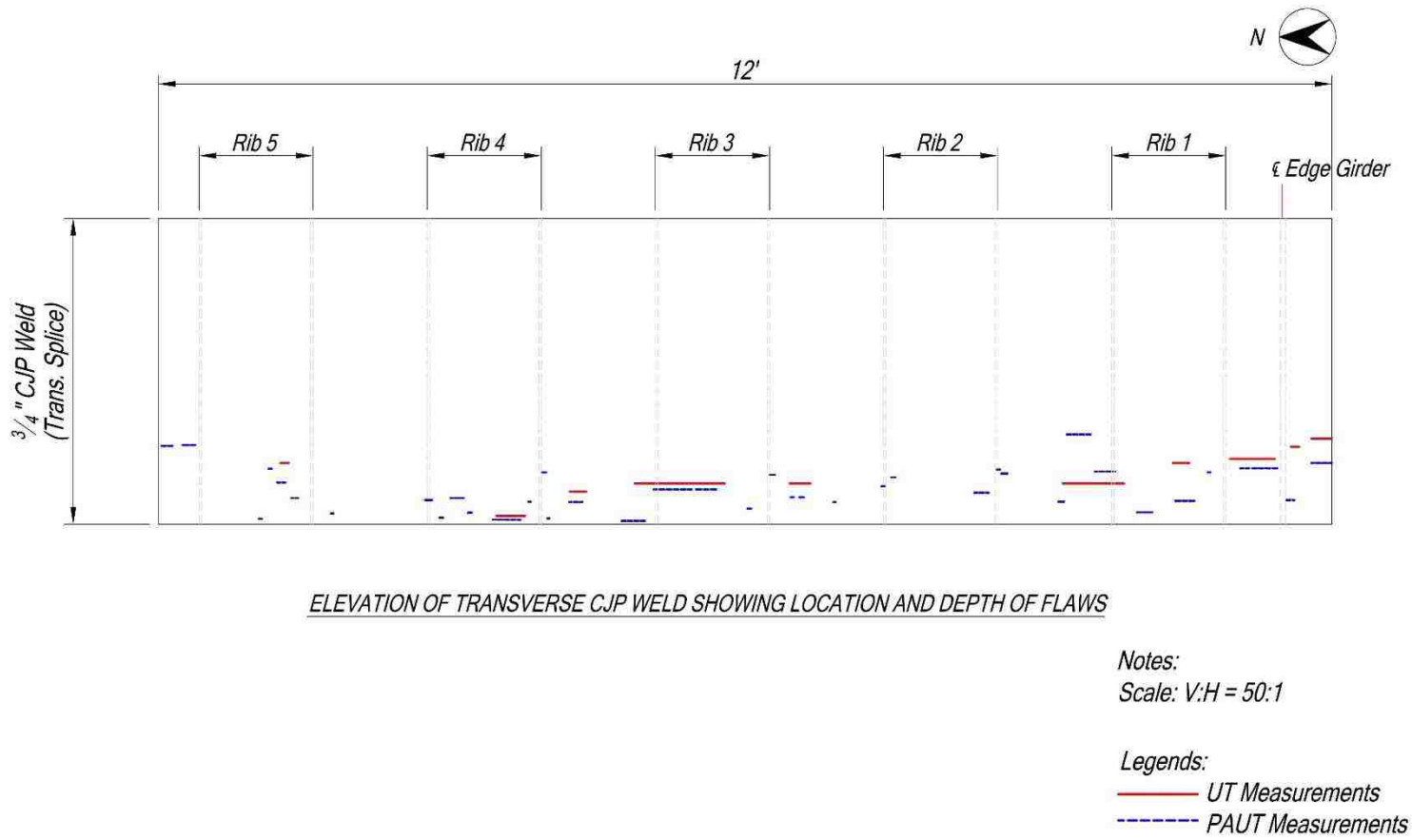

Figure 158 Comparison of UT and PAUT measurements on the elevation

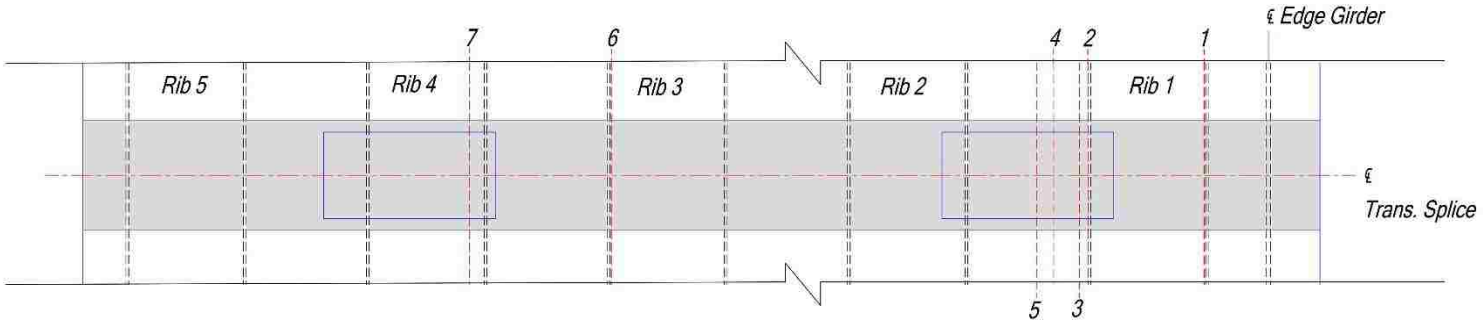

Figure 159 Sections for destructive evaluation

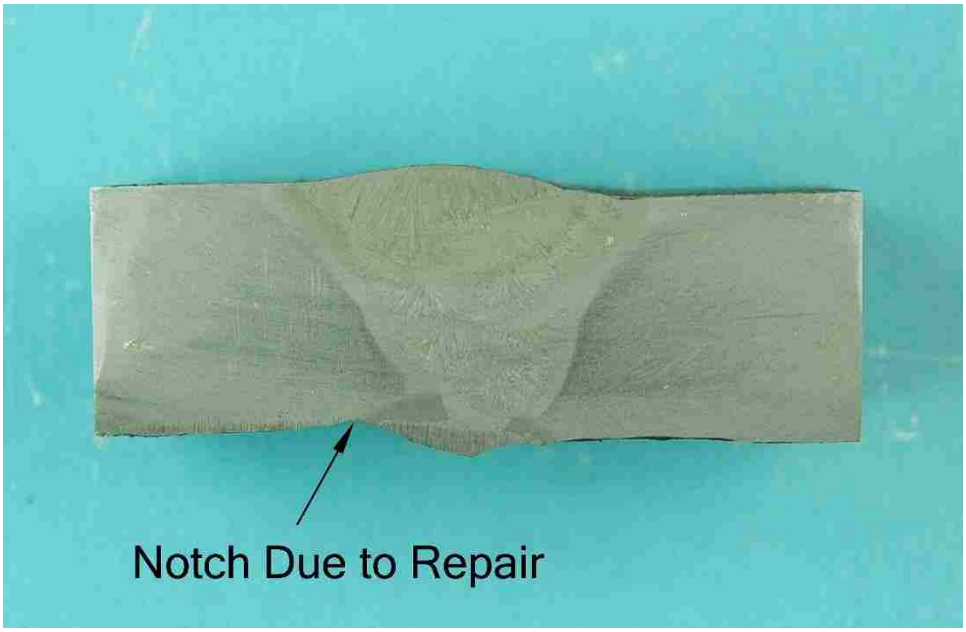

Figure 160 Macro-etched section 1 of CJP deck weld

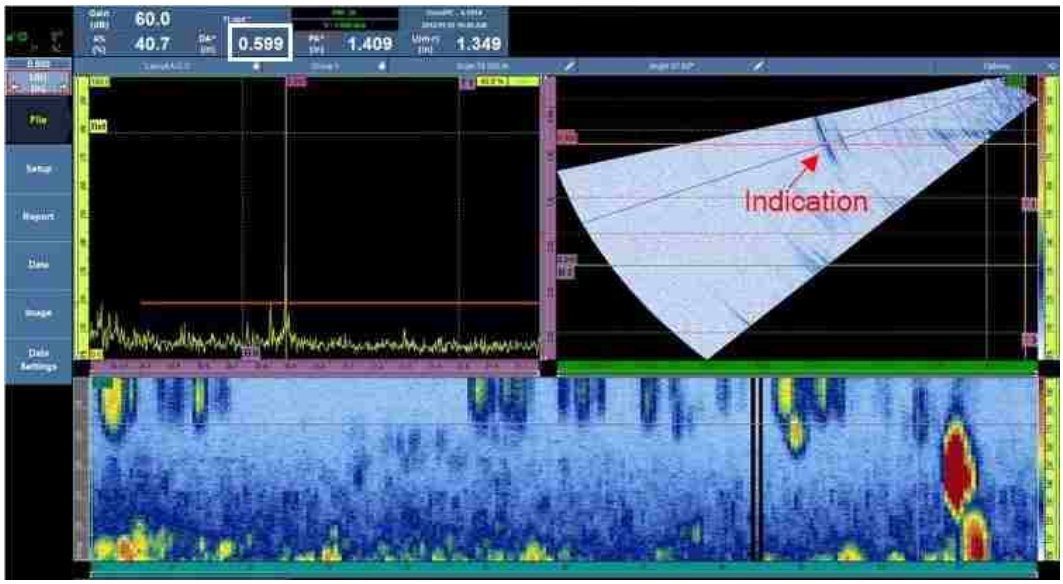

Figure 161 PAUT data for section 1 of CJP deck weld

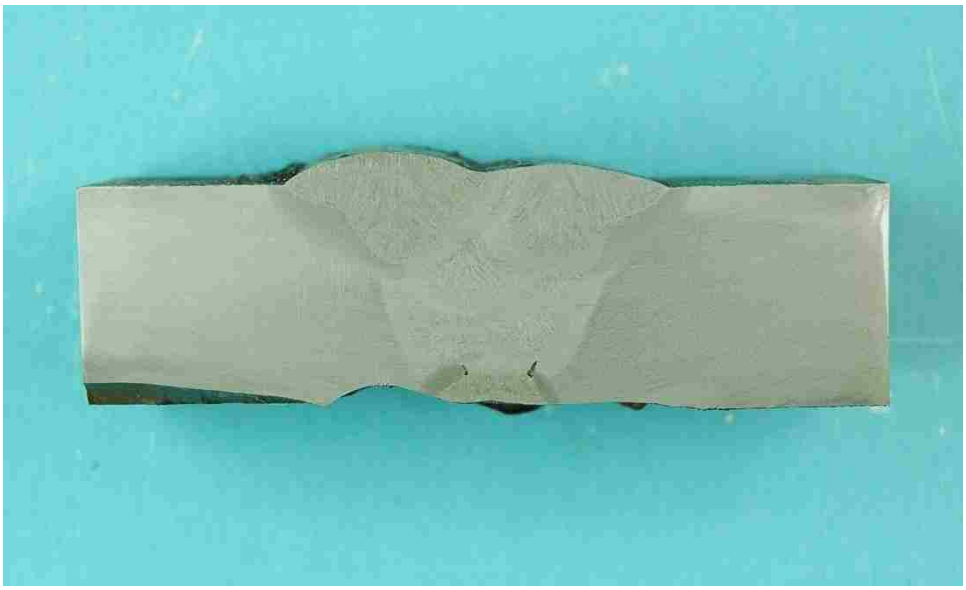

Figure 162 Macro-etched section 2 of CJP deck weld

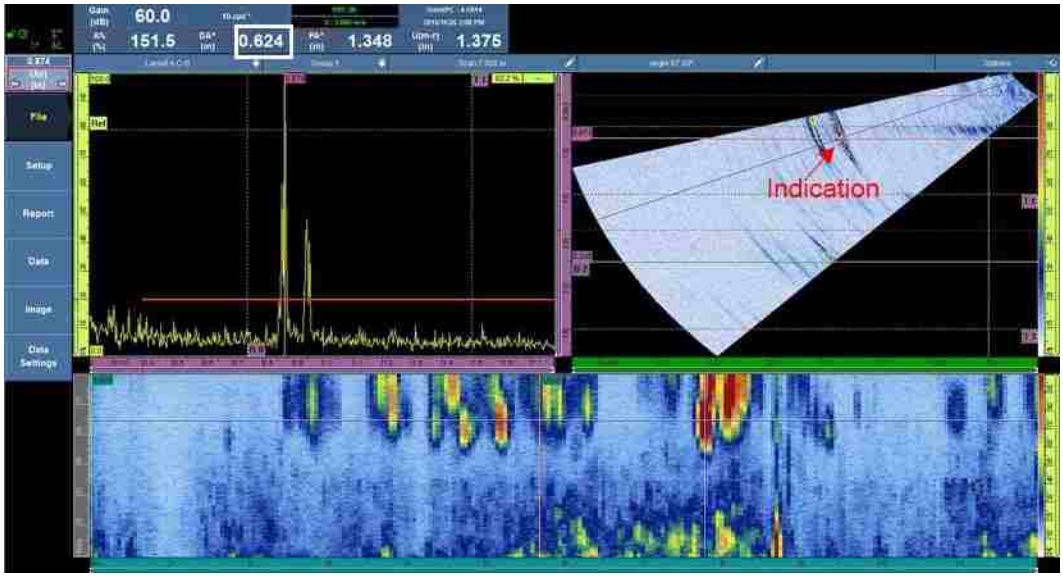

Figure 163 PAUT data for section 2 of CJP deck weld

Figure 164 Macro-etched section 3 of CJP deck weld

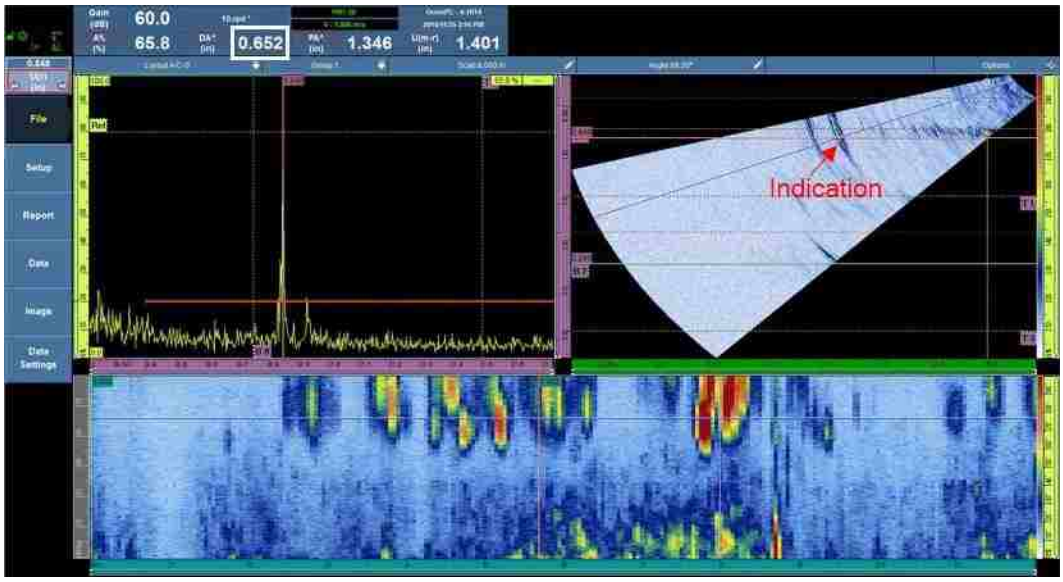

Figure 165 PAUT data for section 3 of CJP deck weld

Figure 166 Macro-etched section 4 of CJP deck weld

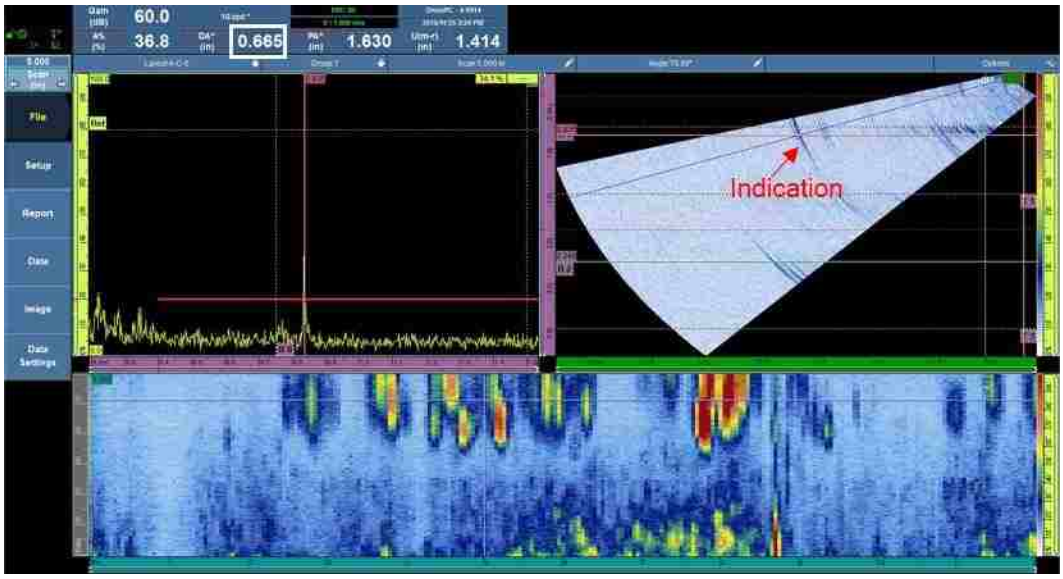

Figure 167 PAUT data for section 4 of CJP deck weld

Figure 168 Macro-etched section 5 of CJP deck weld

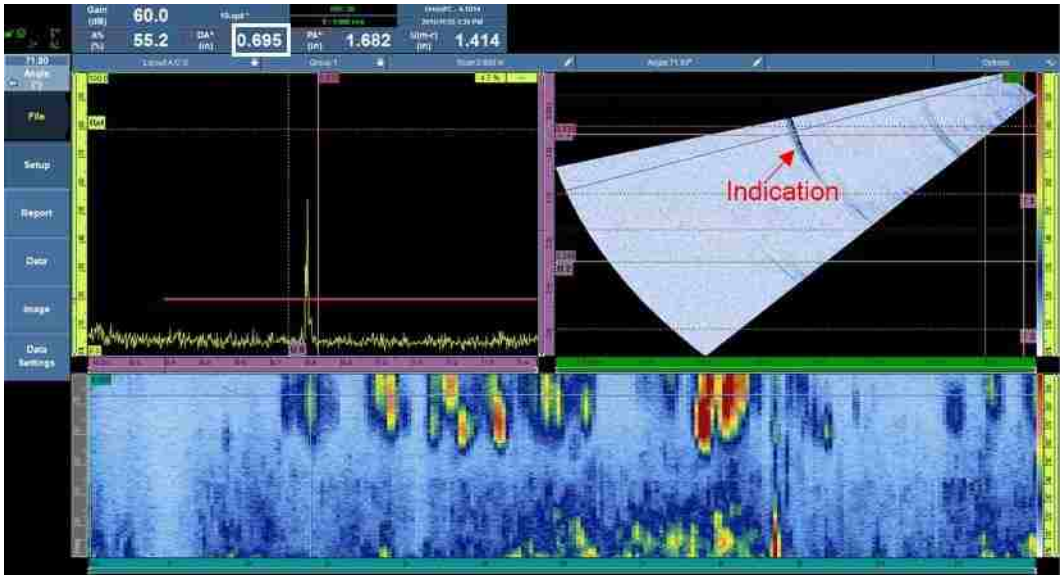

Figure 169 PAUT data for section 5 of CJP deck weld

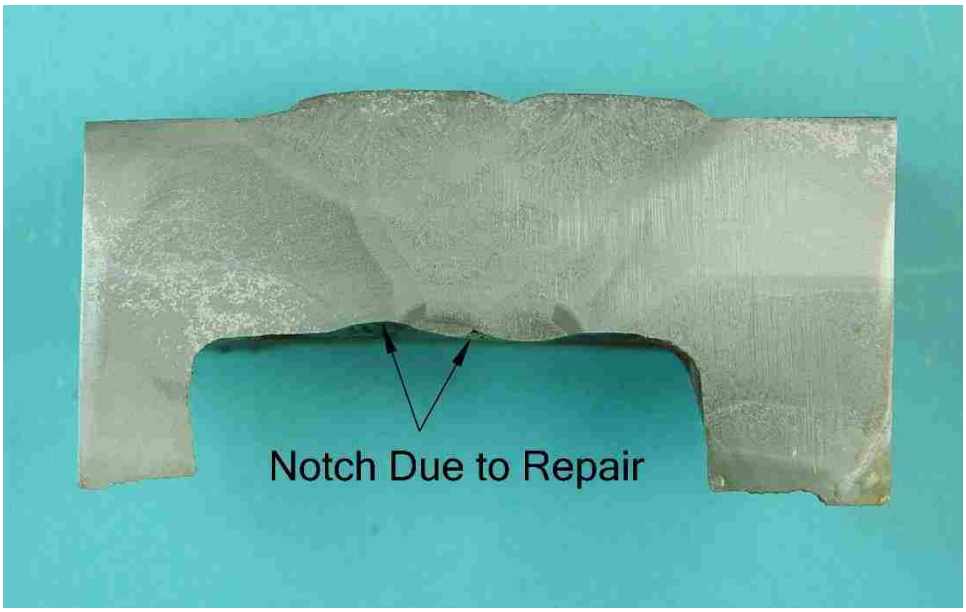

Figure 170 Macro-etched section 6 of CJP deck weld

Figure 171 Weld root section 6 of CJP deck weld

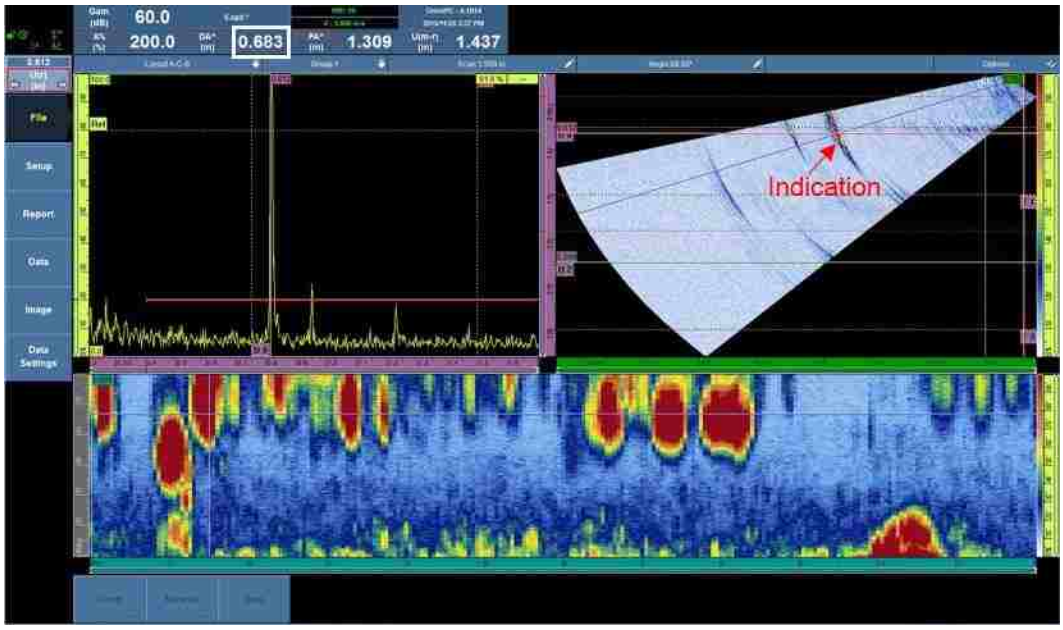

Figure 172 PAUT data for section 6 of CJP deck weld

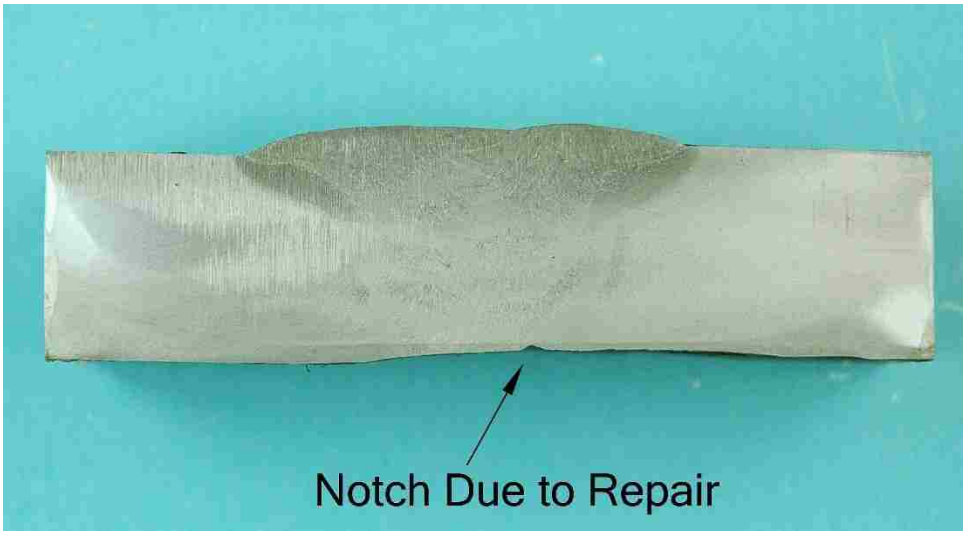

Figure 173 Macro-etched section 7 of CJP deck weld

Figure 174 Weld root section 7 of CJP deck weld

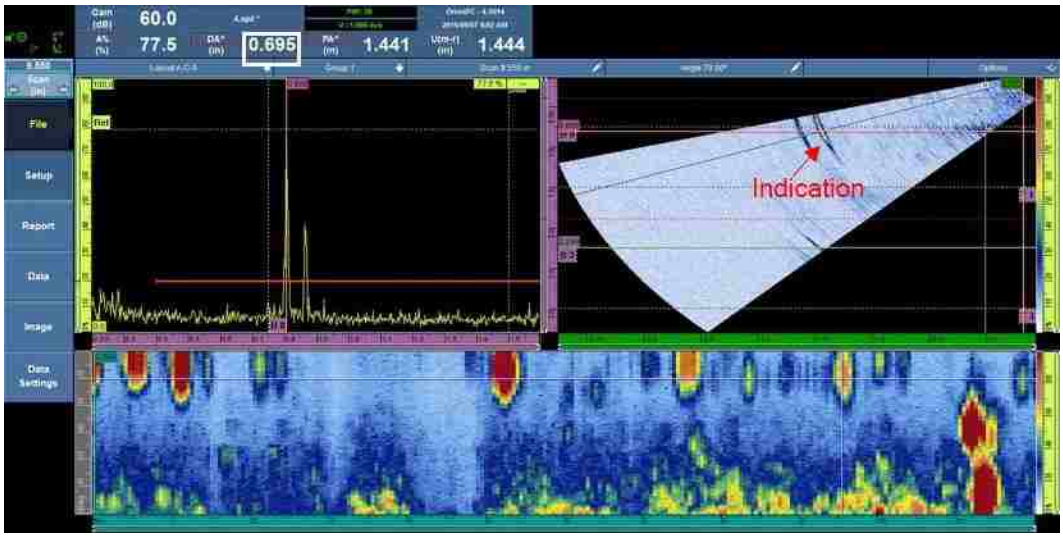

Figure 175 PAUT data for section 7 of CJP deck weld

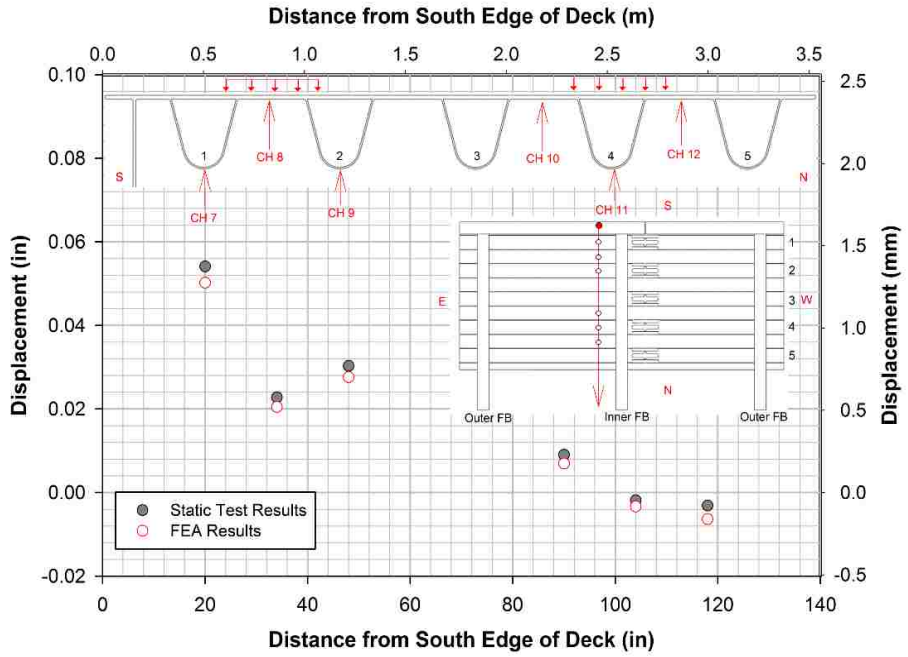

Figure 176 Comparison of vertical displacements at section Z-Z between static test and FEA

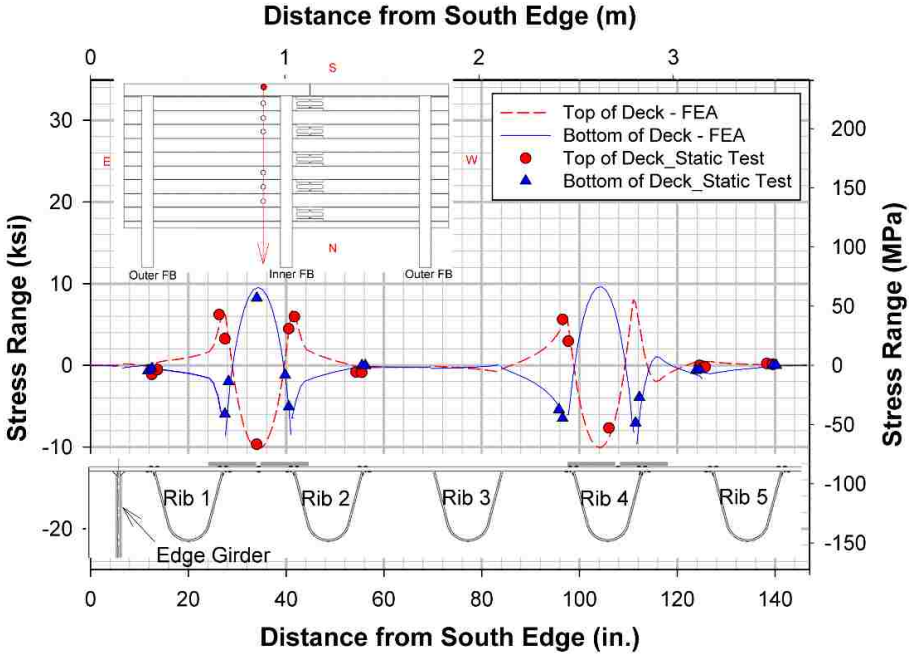

Figure 177 Comparison of transverse stress ranges at section Z-Z between static test and FEA

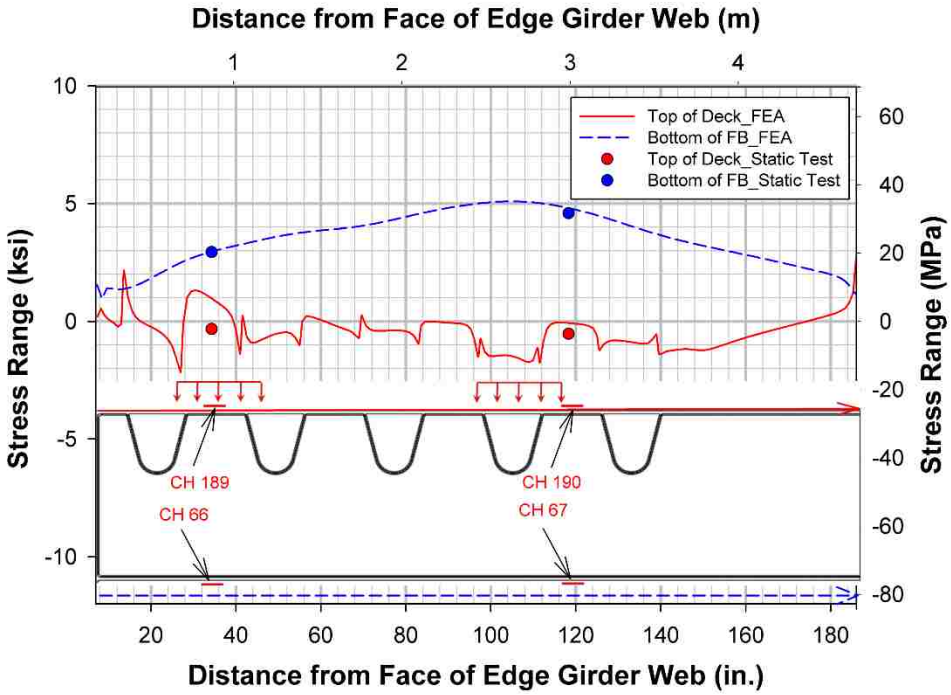

Figure 178 Comparison of transverse stress ranges at section Y-Y between static test and FEA

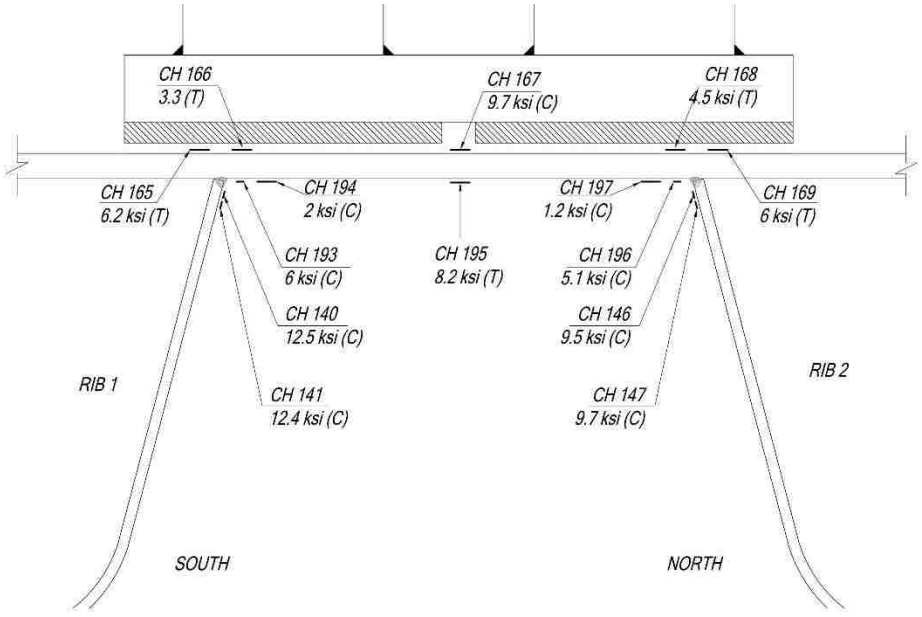

Figure 179 Measured stress ranges at the rib-to-deck plate connection at section Z-Z under south-east load pads

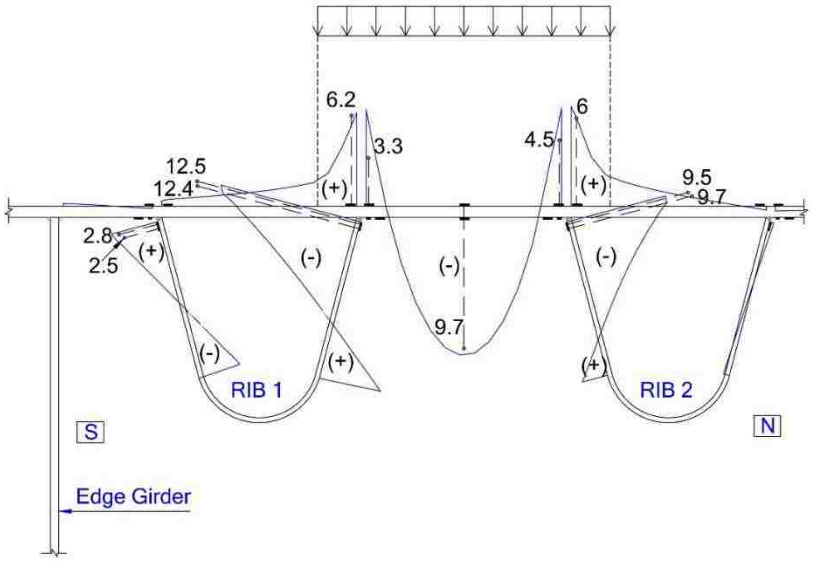

Figure 180 Transverse stresses on top of deck and outer face of rib wall from FEA at rib-to-deck plate connection at section Z-Z under south-east load pads with static test results plotted as dots

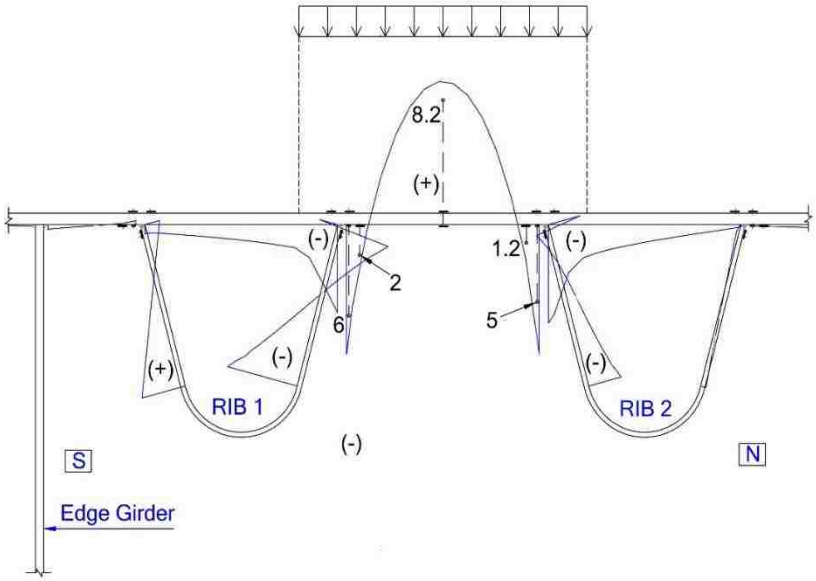

Figure 181 Transverse stresses on bottom of deck and inner face of rib wall from FEA at rib-to-deck plate connection at section Z-Z under south-east load pads with static test results plotted as dots

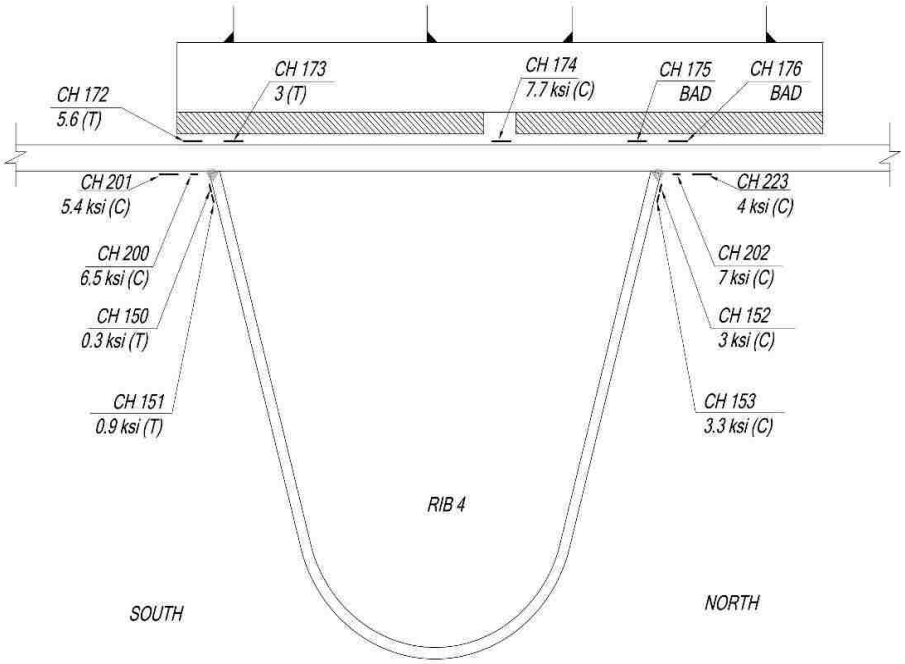

Figure 182 Measured stress ranges at the rib-to-deck plate connection at section Z-Z under north-east load pads

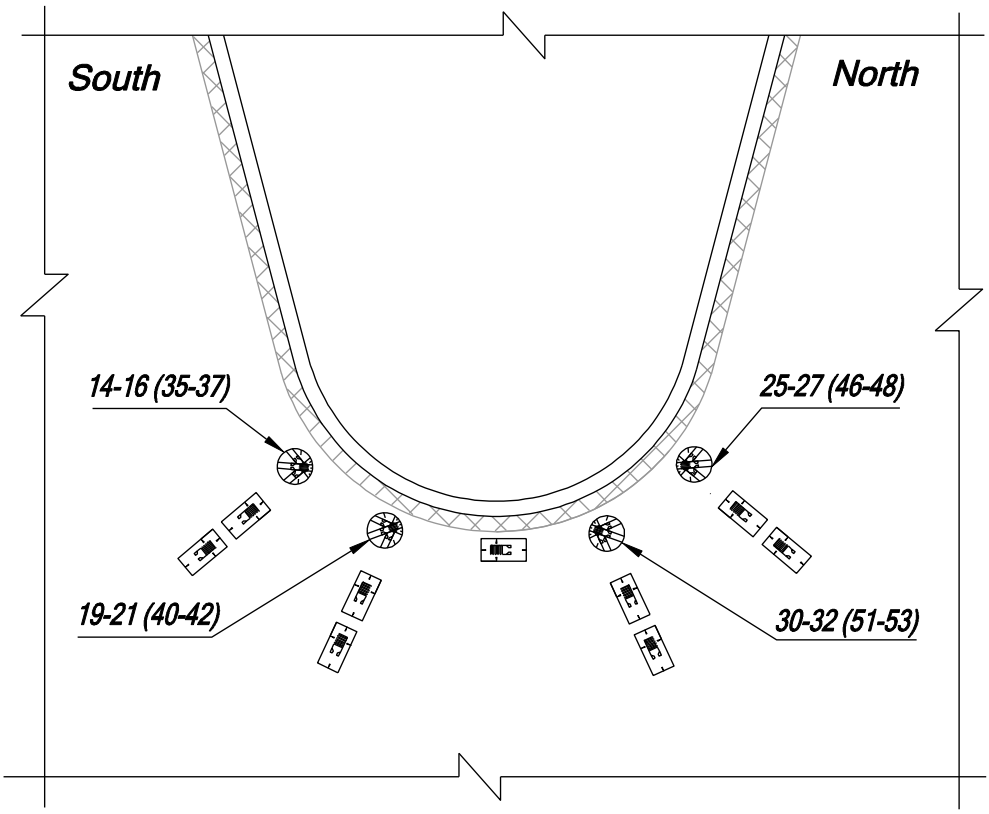

View looking west (showing east face); Gauges on the west face are identified in parenthesis

East Face		West Face	
CH	Measured Principal Stress (ksi)	CH	Measured Principal Stress (ksi)
14-16	7.96	35-37	6.18
19-21	9.76	40-42	8.21
25-27	-11.61	46-48	-10.23
30-32	-13.65	51-53	-11.09

Figure 183 Measured principal stresses at the rosette gauges on the inner FB web

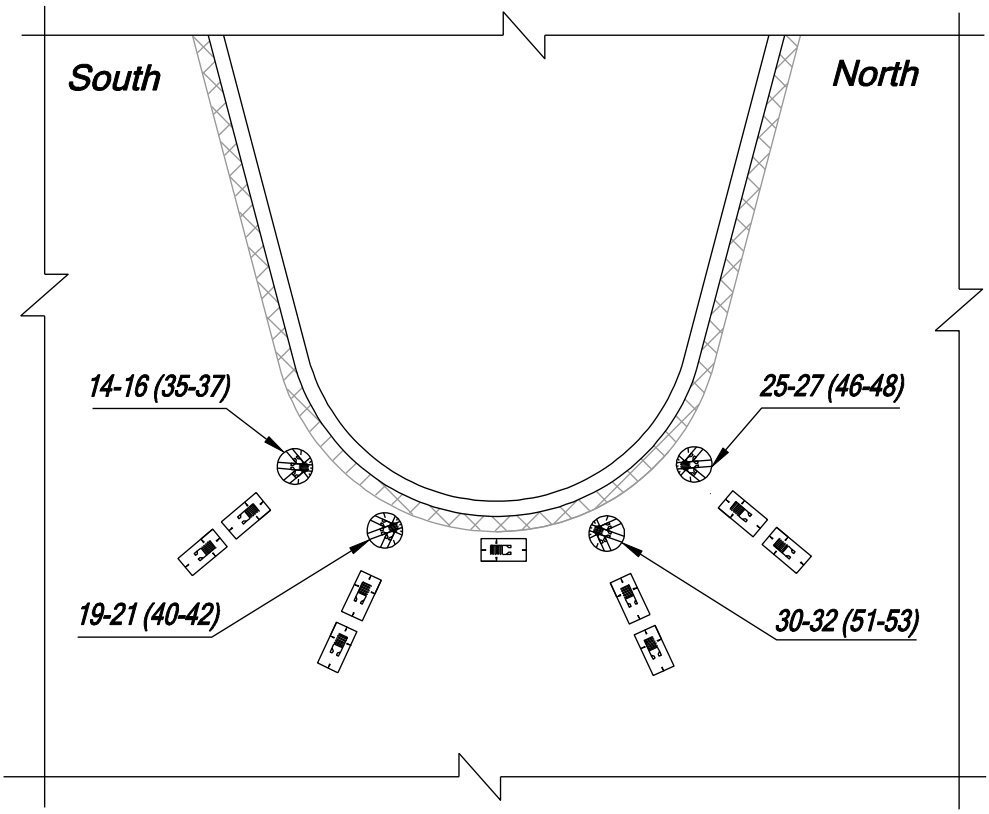

View looking west (showing east face); Gauges on the west face are identified in parenthesis

East Face			West Face		
CH	FEA Principal Stress Range (ksi)	Measured Principal Stress Range (ksi)	CH	FEA Principal Stress Range (ksi)	Measured Principal Stress Range (ksi)
14-16	8.67	7.29	35-37	6.38	5.7
19-21	10.23	8.98	40-42	8.25	7.57
25-27	-13.21	-10.67	51-53	-10.76	-9.43
30-32	-13.62	-12.51	46-48	-11.77	-10.19

Figure 184 Comparison of measured principal stress ranges at the rosette gauges on the inner FB web with the FEA results

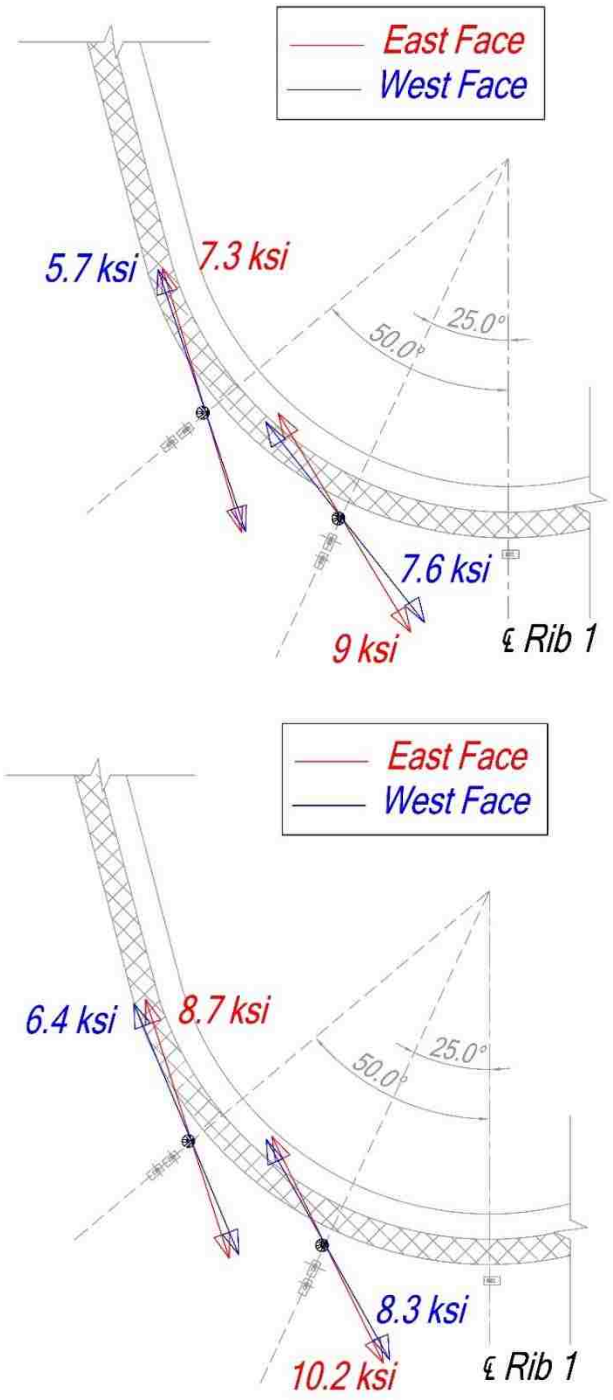

Figure 185 Comparison of the measured principal stress ranges at the rosette gauges on inner FB web to the south side of Rib 1 with FEA results (top figure is test results and bottom figure is FEA result)

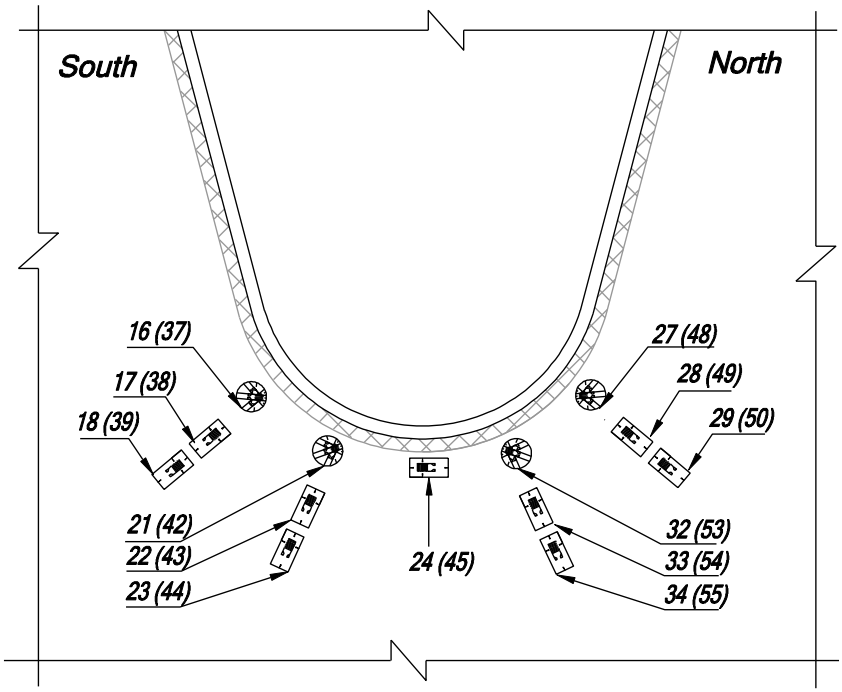

View looking west (showing east face); Gauges on the west face are identified in parenthesis

South of Rib 1			
East Face		West Face	
CH	Measured Value (ksi)	CH	Measured Value (ksi)
16	3.93	37	0.09
17	1.32	38	-1.83
18	1.37	39	-1.68
21	0.43	42	-2.01
22	-2.04	43	-3.59
23	-1.44	44	-2.38
24	0.45	45	-0.73

North of Rib 1			
East Face		West Face	
CH	Measured Value (ksi)	CH	Measured Value (ksi)
27	-6.89	48	-2.61
28	-2.75	49	-0.25
29	-2.74	50	-0.18
32	-3.28	53	0.07
33	-1.52	54	1.16
34	-2.14	55	-0.56

Figure 186 Measured stresses normal to the weld toe on the inner FB web

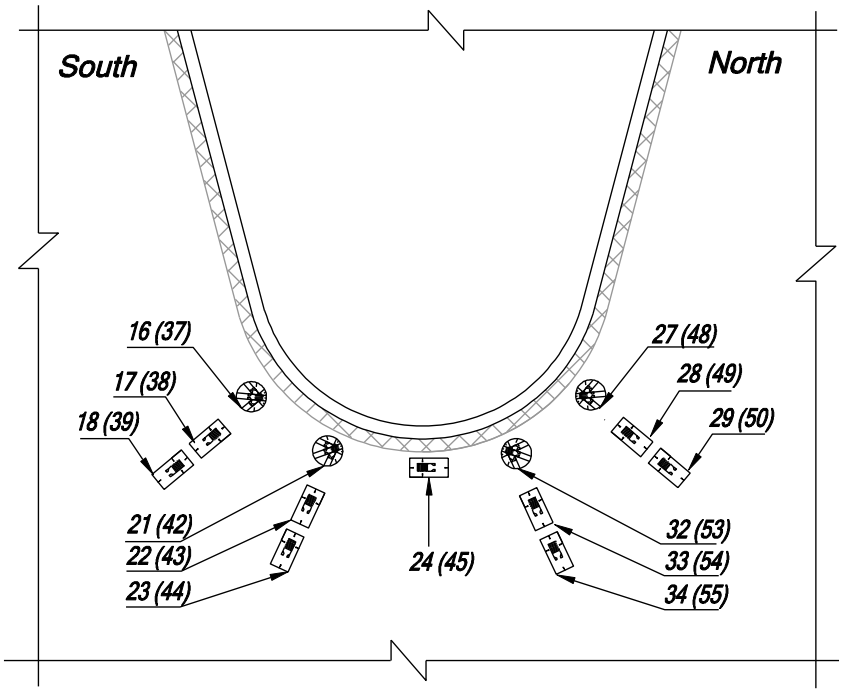

View looking west (showing east face); Gauges on the west face are identified in parenthesis

South of Rib 1			
East Face		West Face	
CH	Measured Range (ksi)	CH	Measured Value (ksi)
16	3.6	37	0.13
17	1.19	38	-1.66
18	1.13	39	-1.51
21	0.39	42	-1.82
22	-1.87	43	-3.25
23	-1.32	44	-2.17
24	0.43	45	-0.66

North of Rib 1			
East Face		West Face	
CH	Measured Value (ksi)	CH	Measured Value (ksi)
27	-6.31	48	-2.36
28	-2.52	49	-0.21
29	-2.54	50	-0.17
32	-2.95	53	0.1
33	-1.4	54	1.1
34	-1.99	55	-0.5

Figure 187 Measured stress ranges normal to the weld toe on the inner FB web

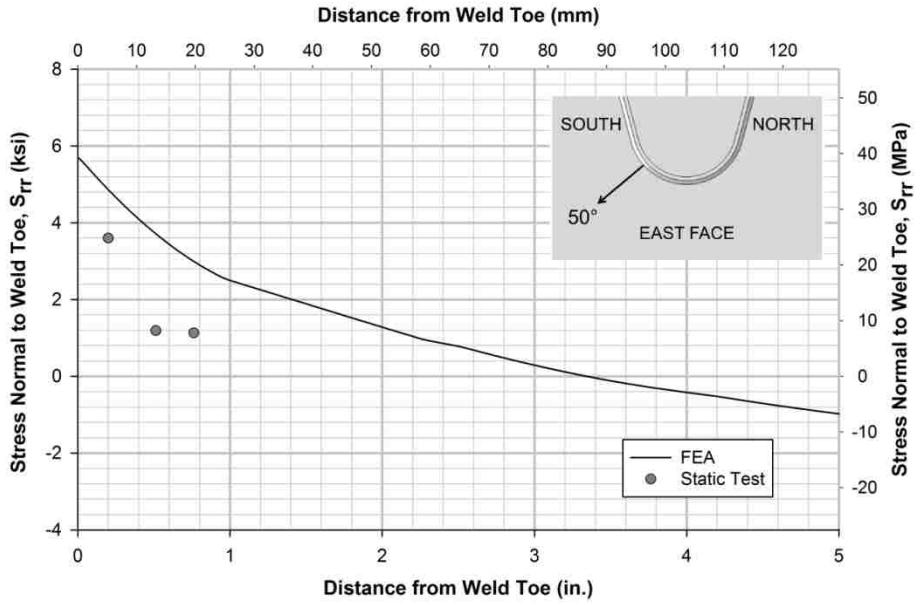

Figure 188 Radial stress range along 50 degree south path on east FB face

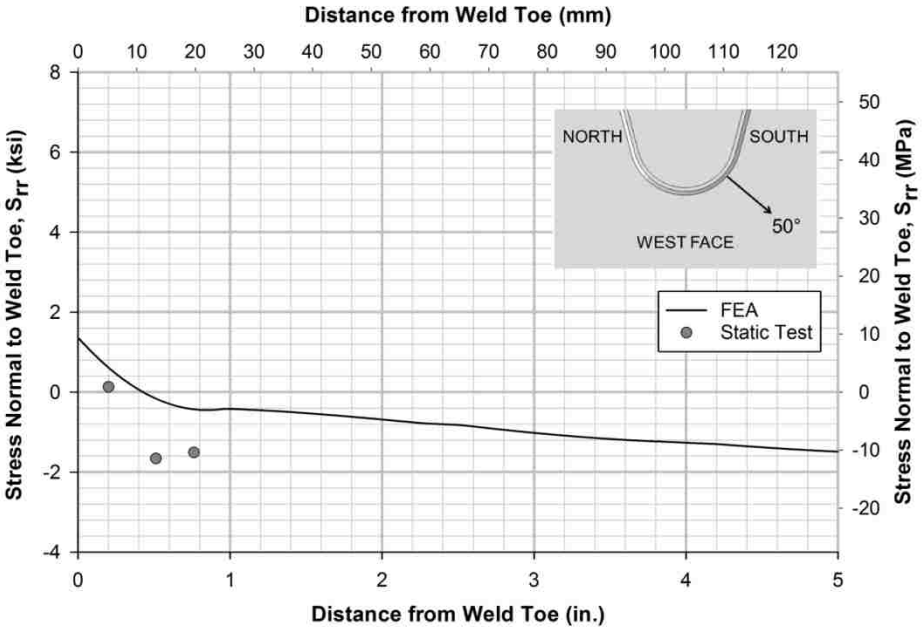

Figure 189 Radial stress range along 50 degree south path on west FB face

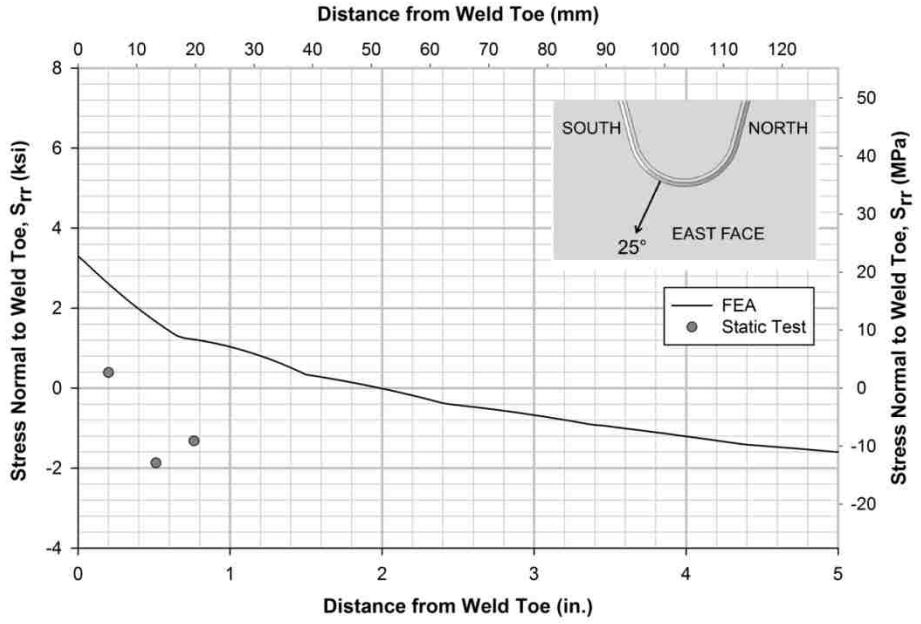

Figure 190 Radial stress range along 25 degree south path on east FB face

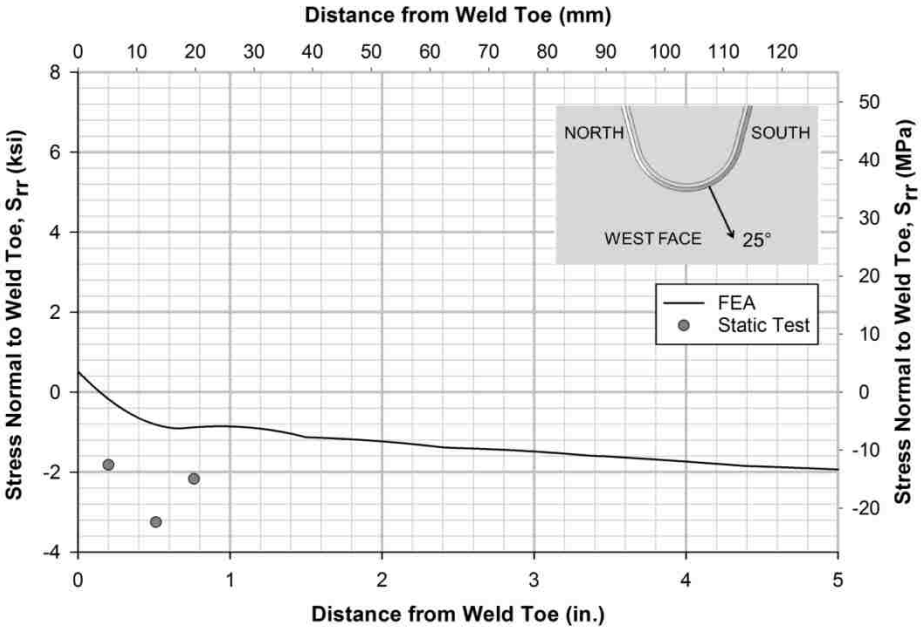

Figure 191 Radial stress range along 25 degree south path on west FB face

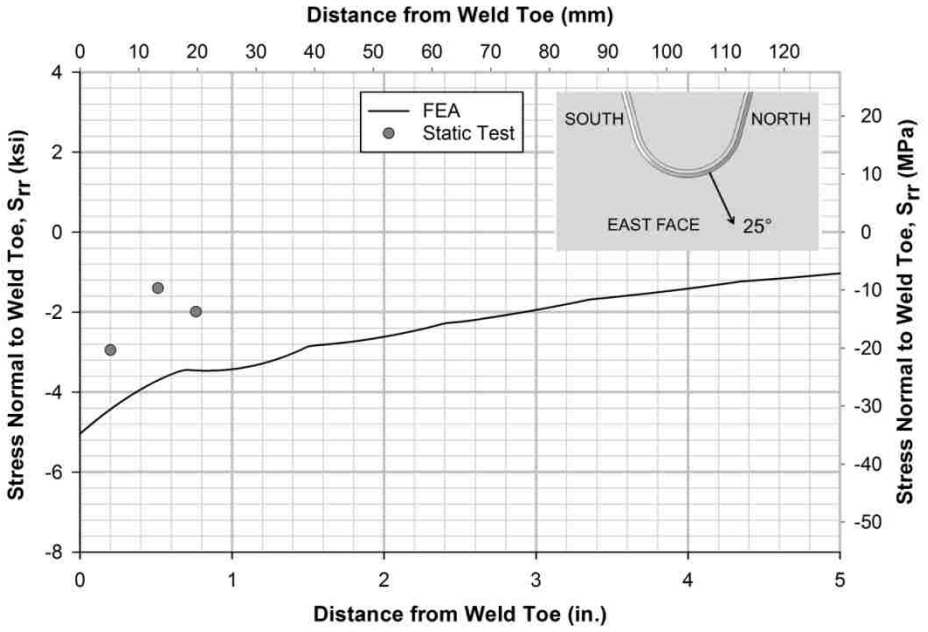

Figure 192 Radial stress range along 25 degree north path on east FB face

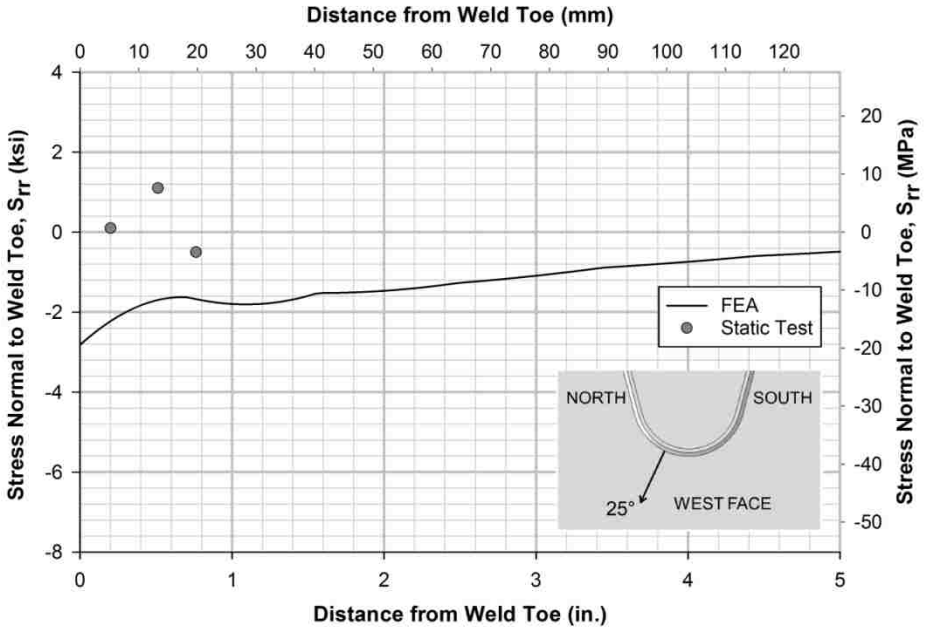

Figure 193 Radial stress range along 25 degree north path on west FB face

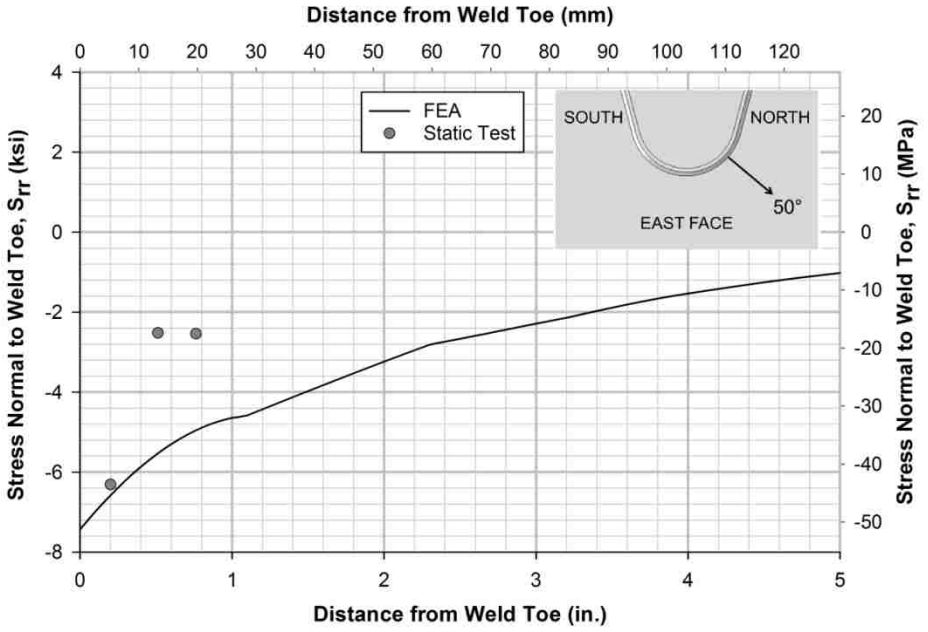

Figure 194 Radial stress range along 50 degree north path on east FB face

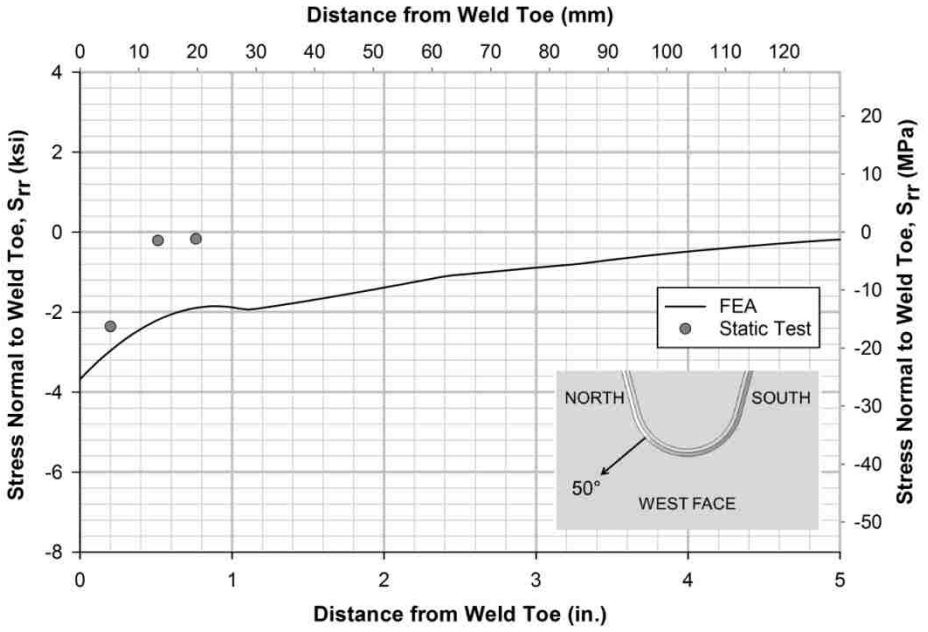

Figure 195 Radial stress range along 50 degree north path on west FB face

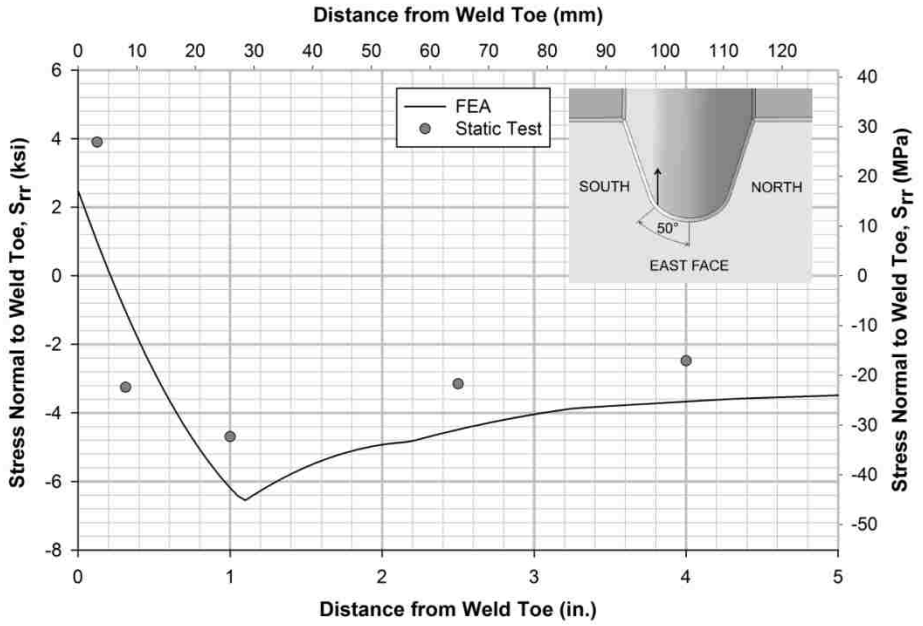

Figure 196 Radial stress range along 50 degree southeast path on rib 1

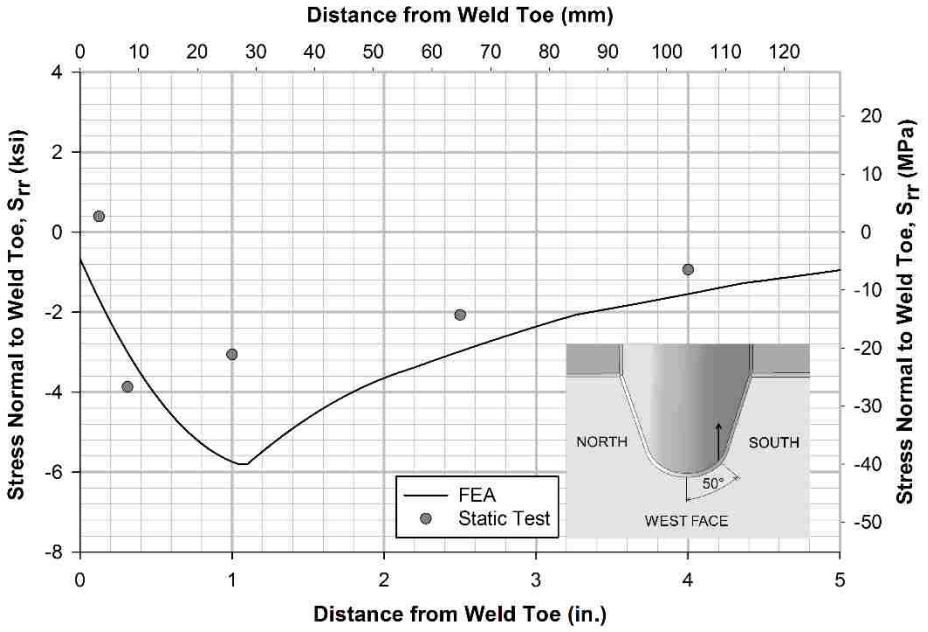

Figure 197 Radial stress range along 50 degree southwest path on rib 1

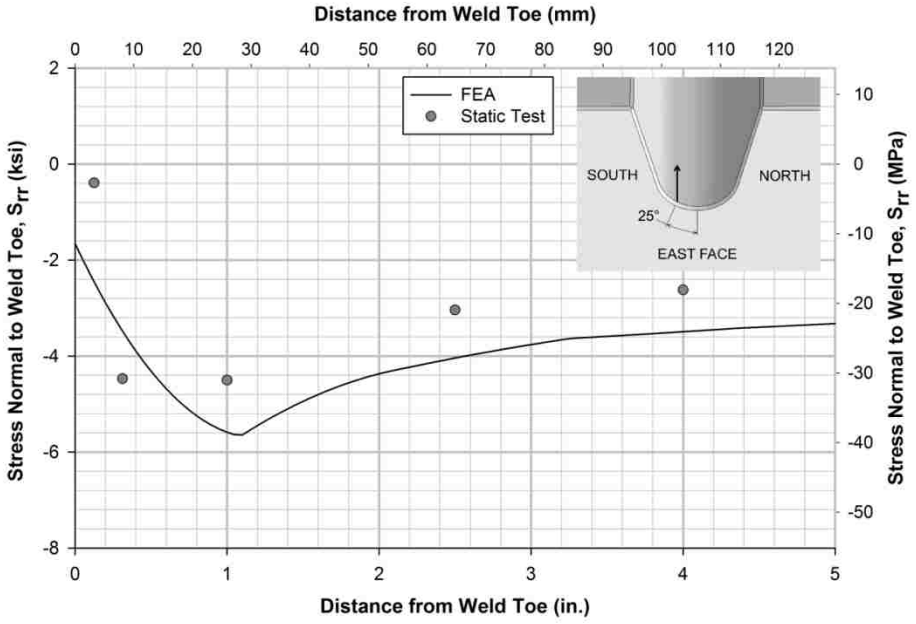

Figure 198 Radial stress range along 25 degree southeast path on rib 1

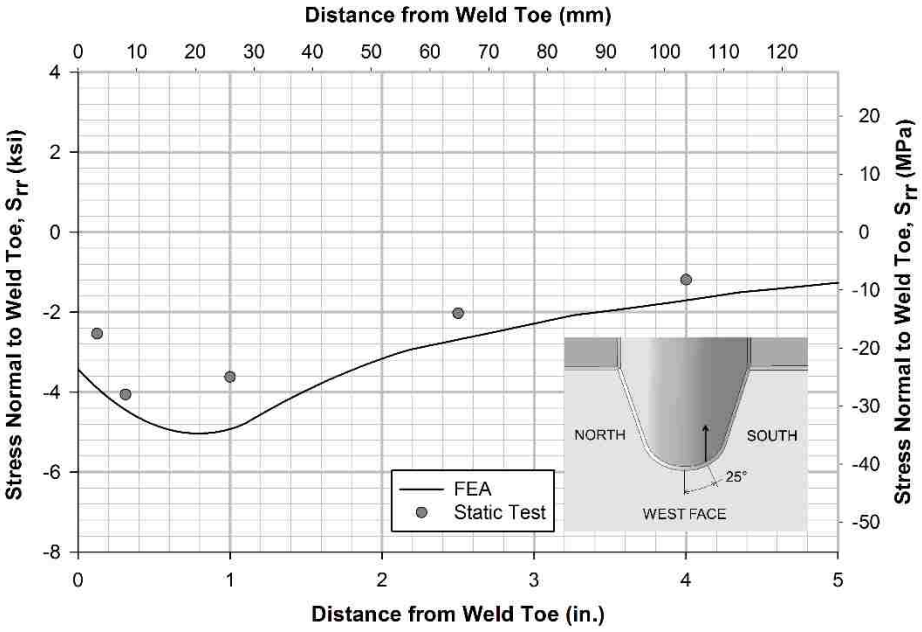

Figure 199 Radial stress range along 25 degree southwest path on rib 1

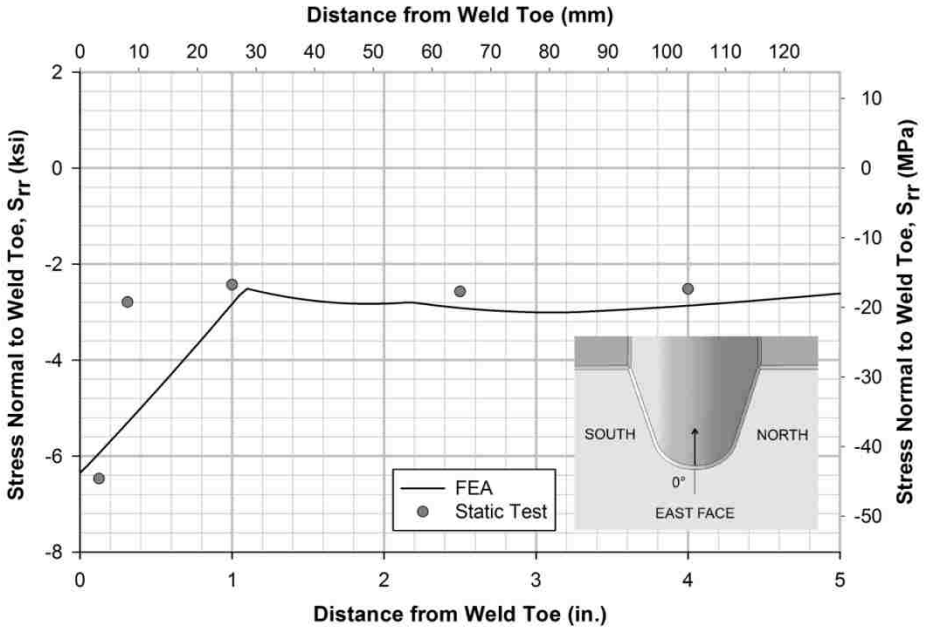

Figure 200 Radial stress range along 0 degree east path on rib 1

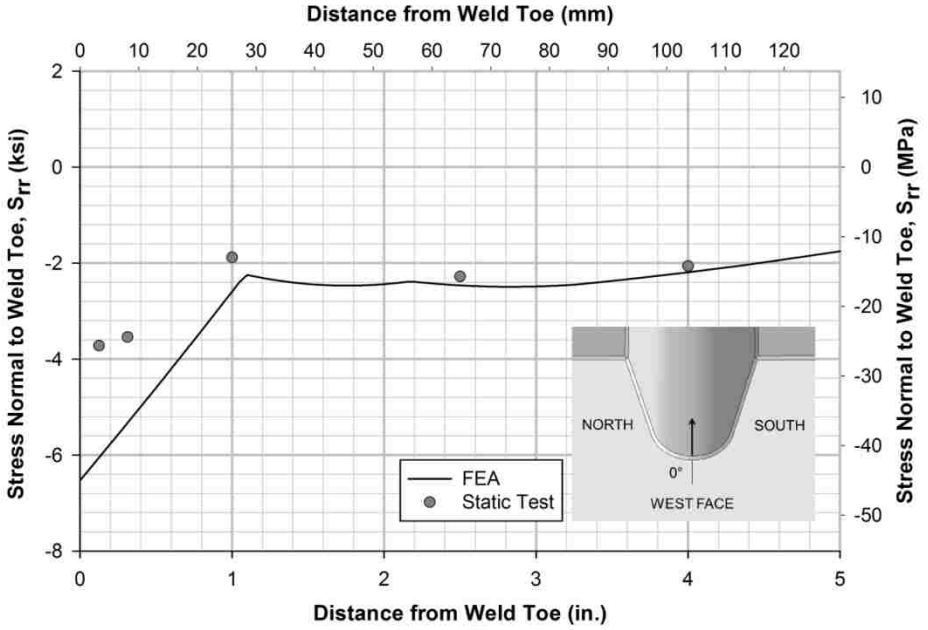

Figure 201 Radial stress range along 0 degree west path on rib 1

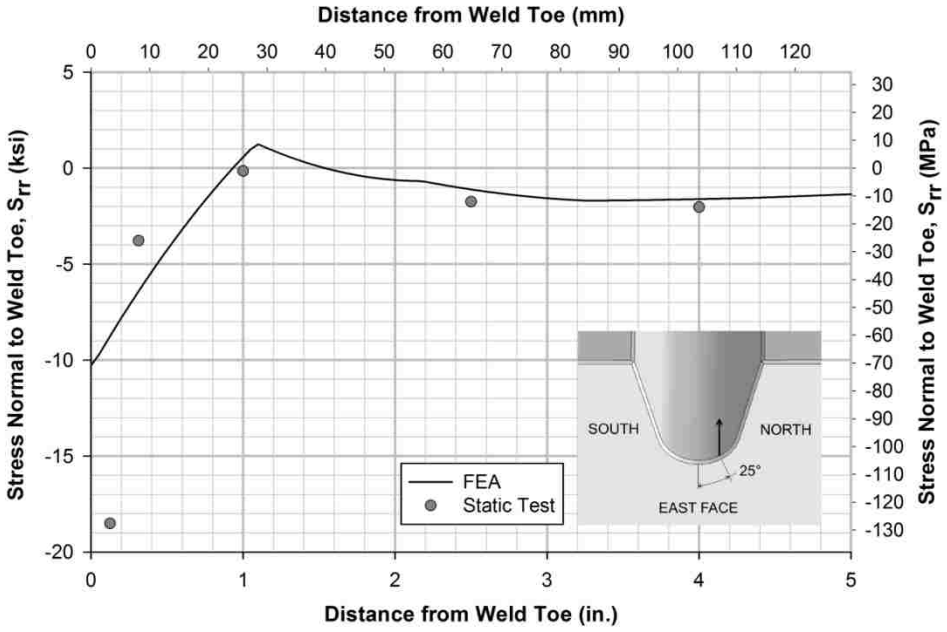

Figure 202 Radial stress range along 25 degree northeast path on rib 1

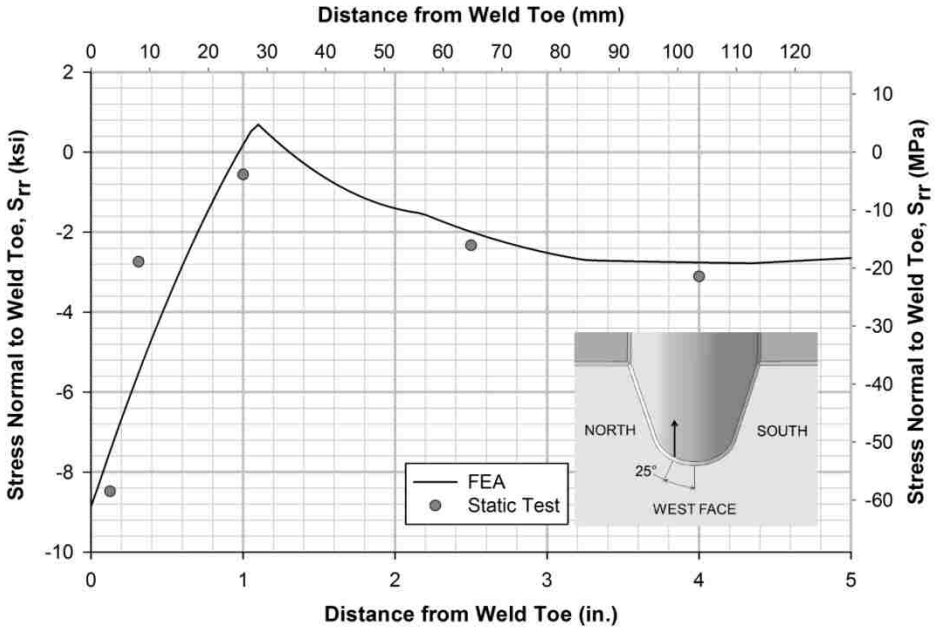

Figure 203 Radial stress range along 25 degree northwest path on rib 1

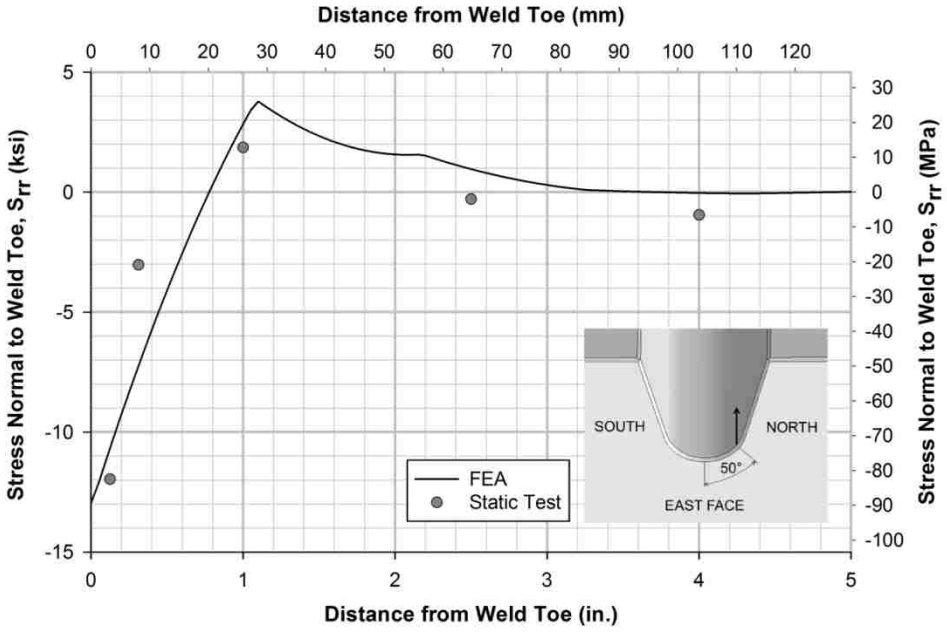

Figure 204 Radial stress range along 50 degree northeast path on rib 1

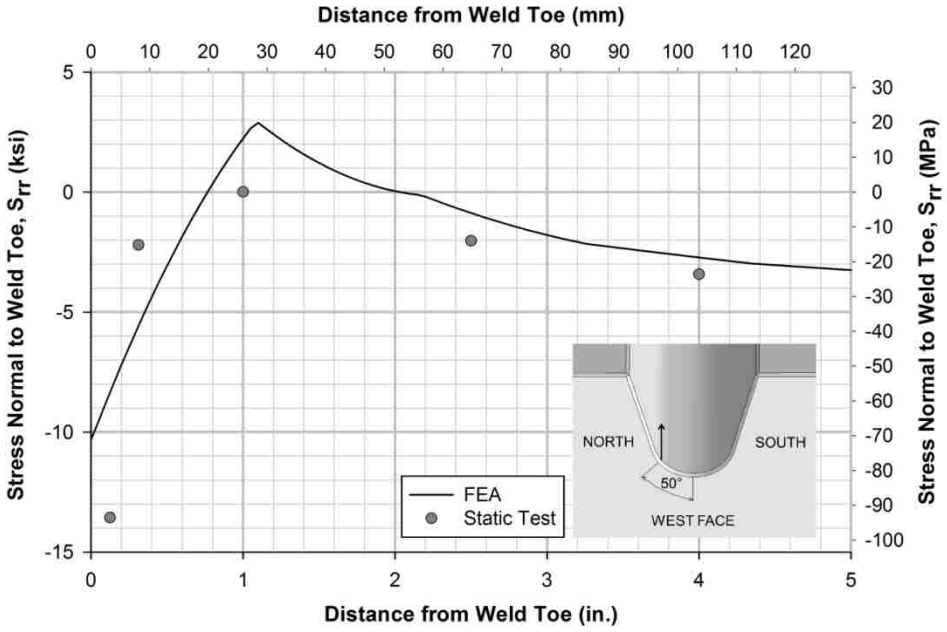

Figure 205 Radial stress range along 50 degree northwest path on rib 1

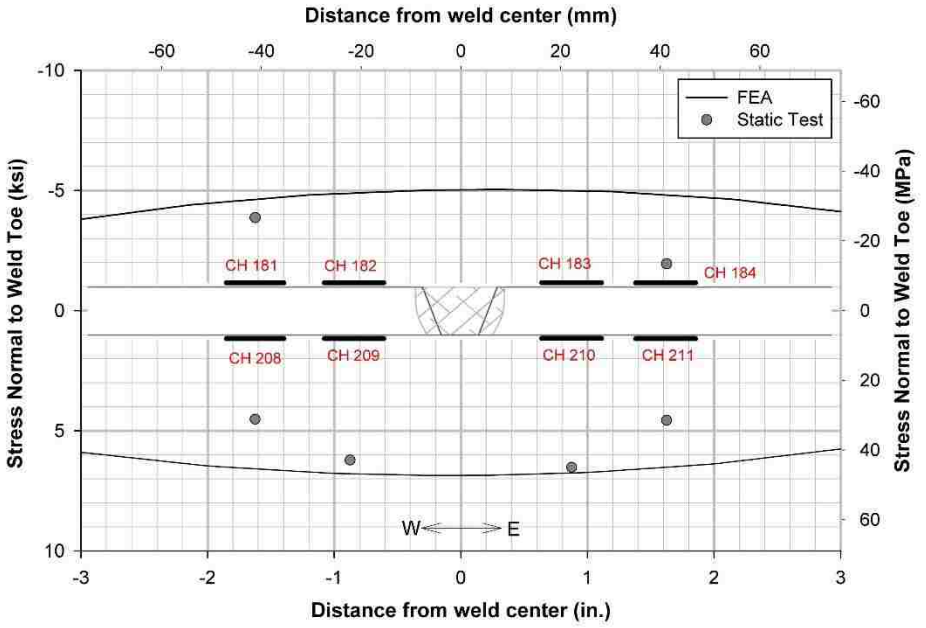

Figure 206 Stress ranges at the transverse deck splice under south-west load pads

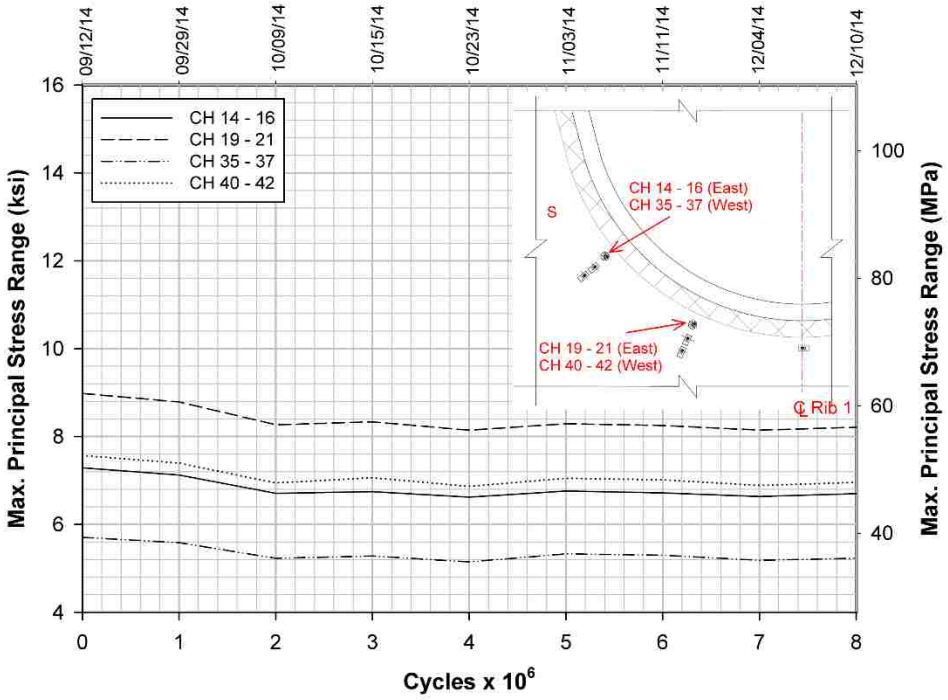

Figure 207 Changes in maximum tensile principal stress ranges at the rosettes on the inner FB web

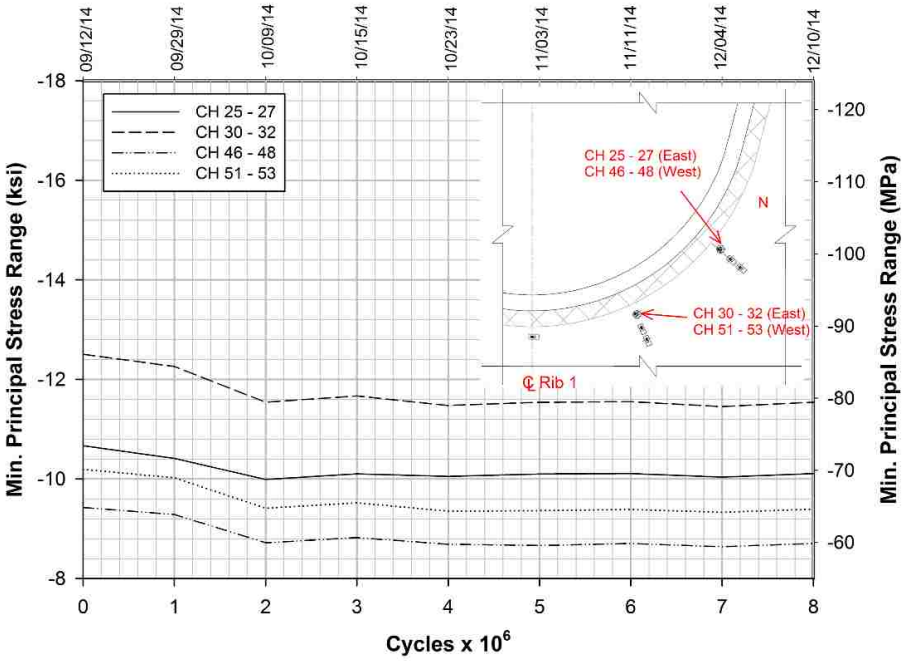

Figure 208 Changes in maximum compressive principal stress ranges at the rosettes on the inner FB web

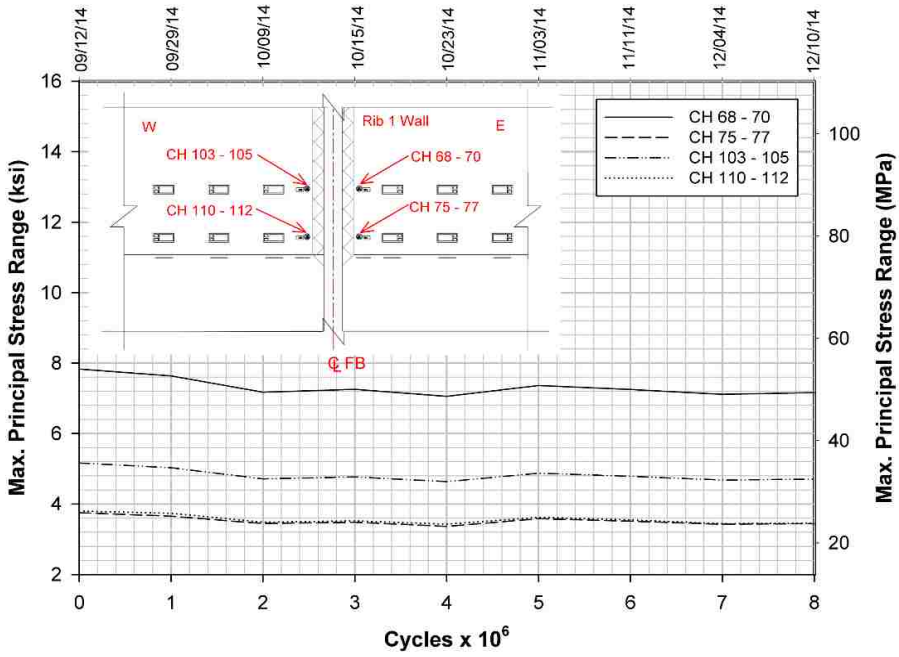

Figure 209 Changes in principal stress ranges at the rosettes on the south wall of Rib 1

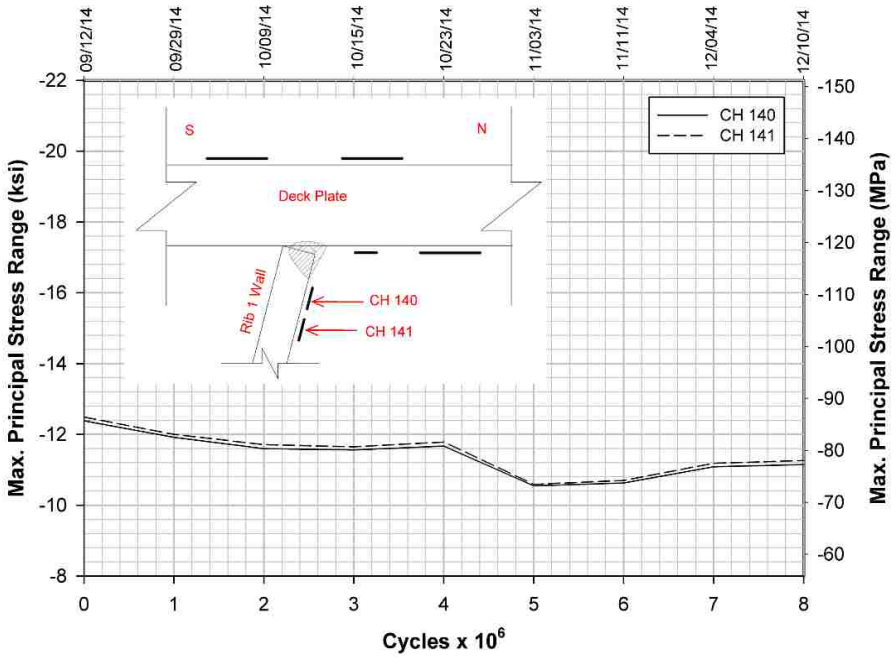

Figure 210 Changes in static test stress ranges at the gauges on north wall of Rib 1 near Rib 1-to-deck plate connection

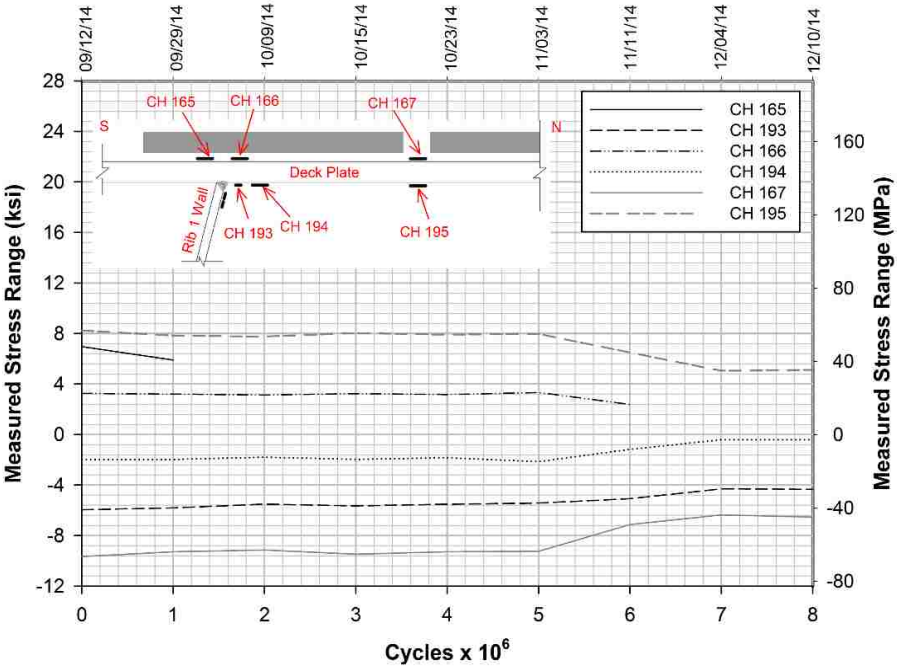

Figure 211 Changes in static test stress ranges at the deck plate gauges near Rib 1 at rib-to-deck plate connection

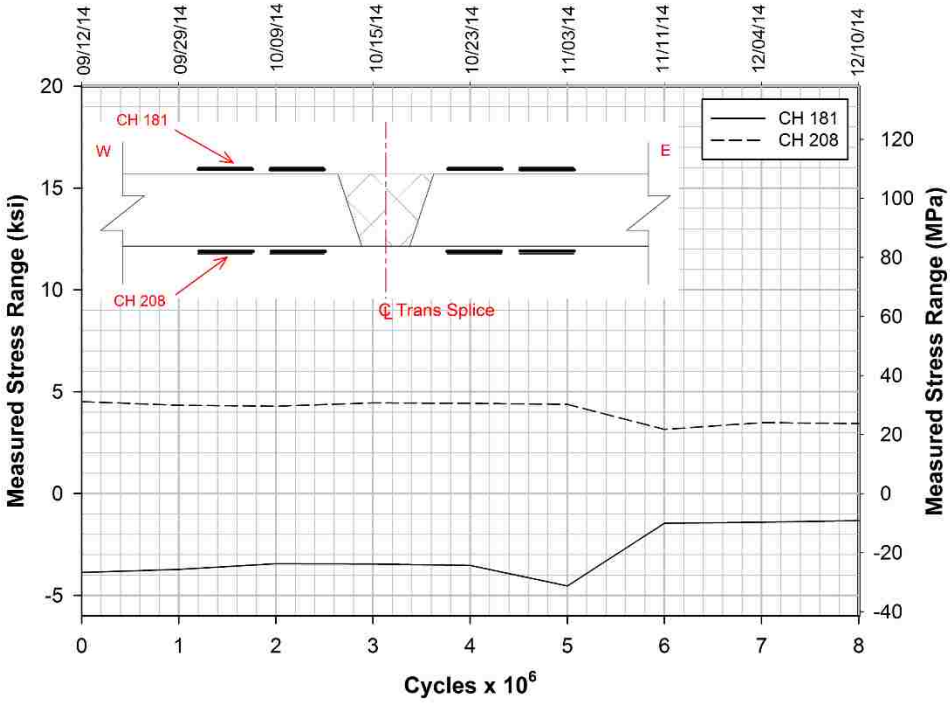

Figure 212 Changes in static test stress ranges at the gauges near the deck splice

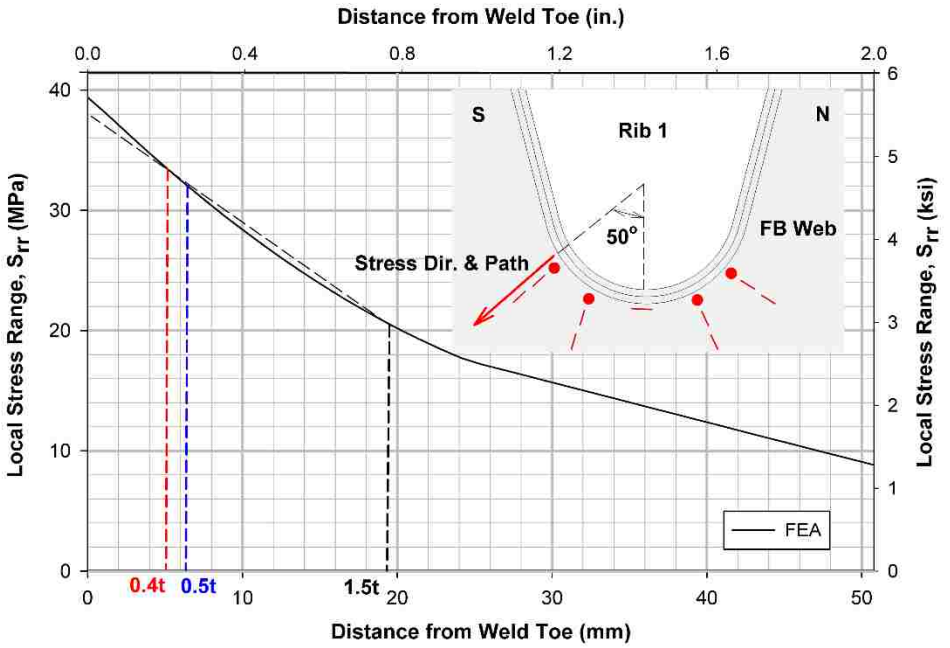

Figure 213 Reference points for extrapolation of stresses

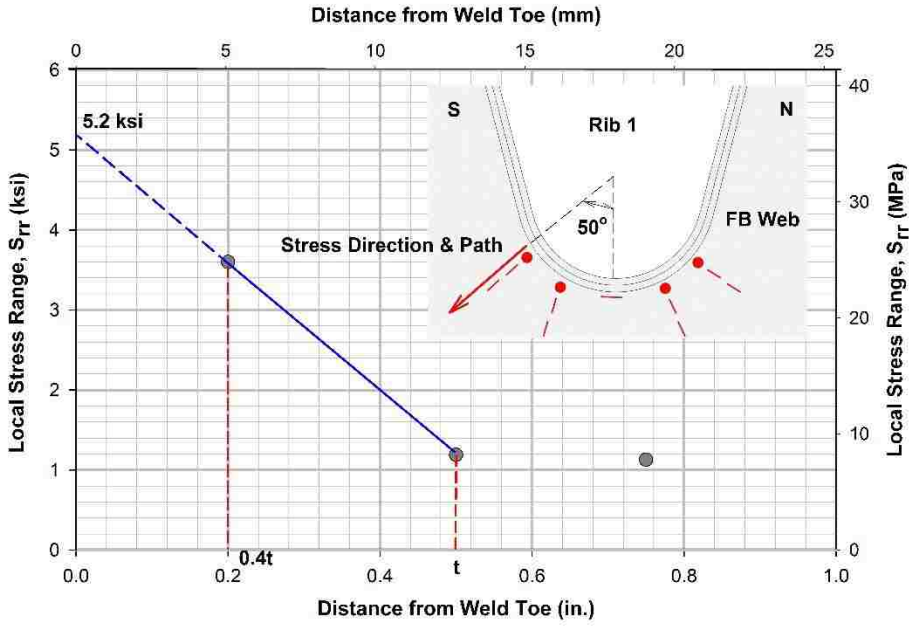

Figure 214 Method of extrapolation of stress to weld toe for rib-to-floor beam connection

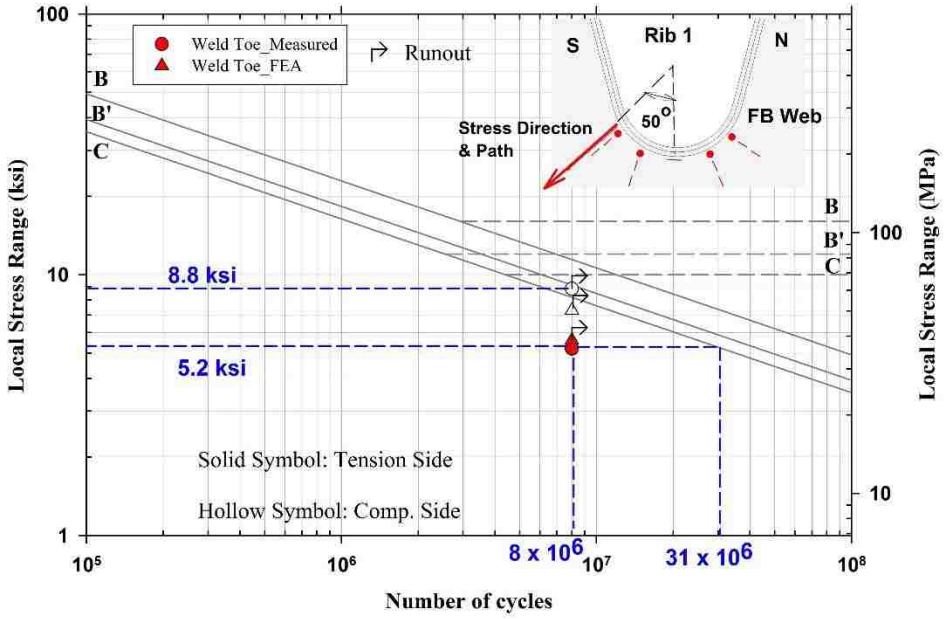

Figure 215 Assessment of fatigue performance of rib-to-floor beam connection against cracking from weld toe

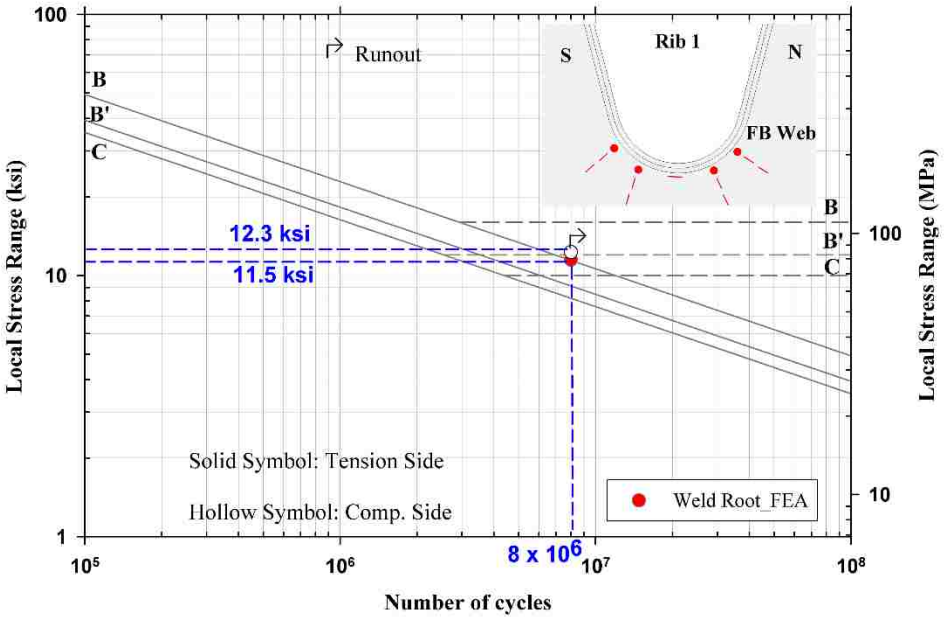

Figure 216 Assessment of fatigue performance of rib-to-floor beam connection against cracking from weld root

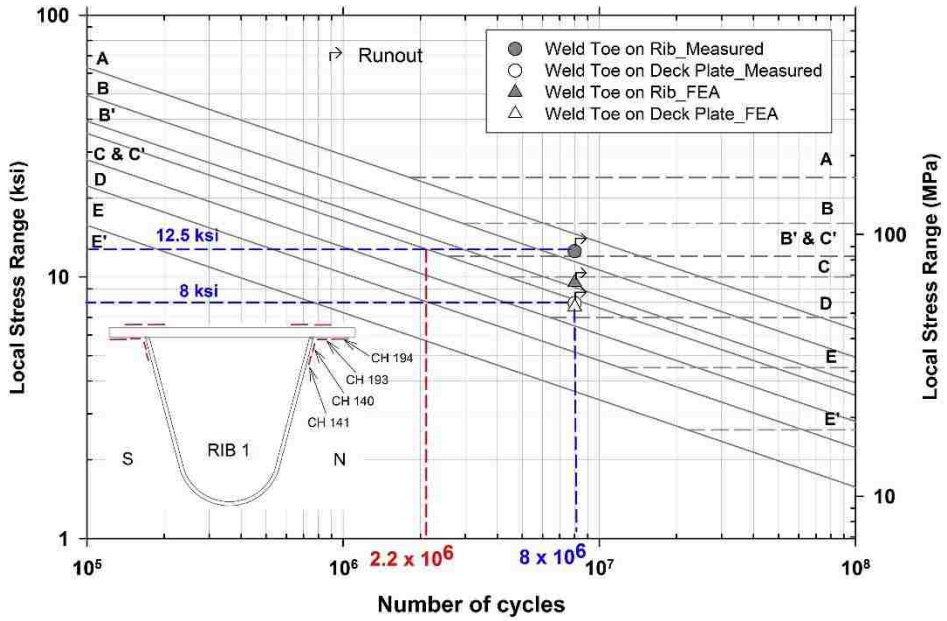

Figure 217 Assessment of fatigue performance of rib-to-deck plate connection at section Z-Z

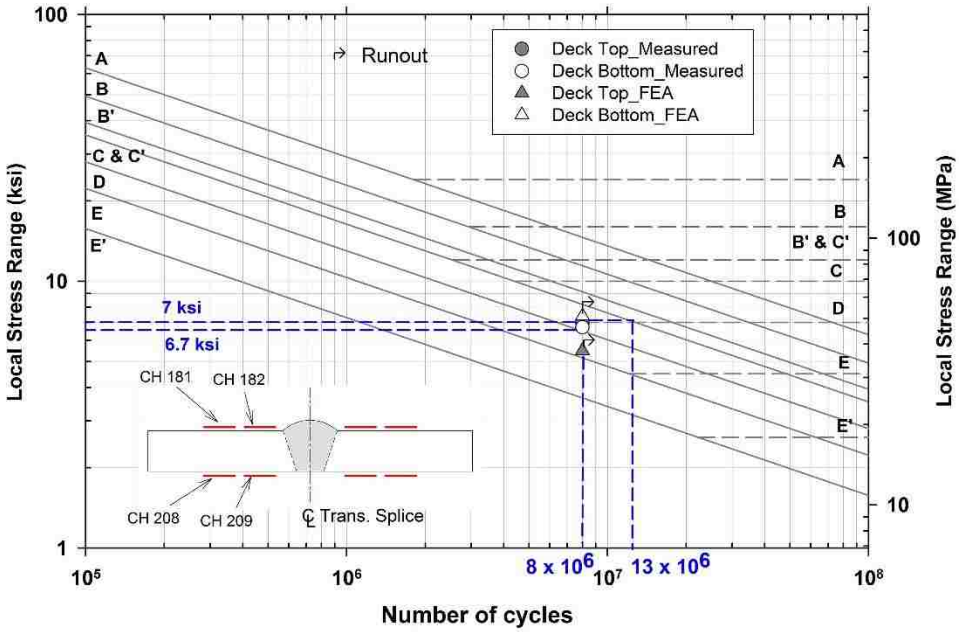

Figure 218 Assessment of fatigue performance of transverse CJP deck splice at section X-X

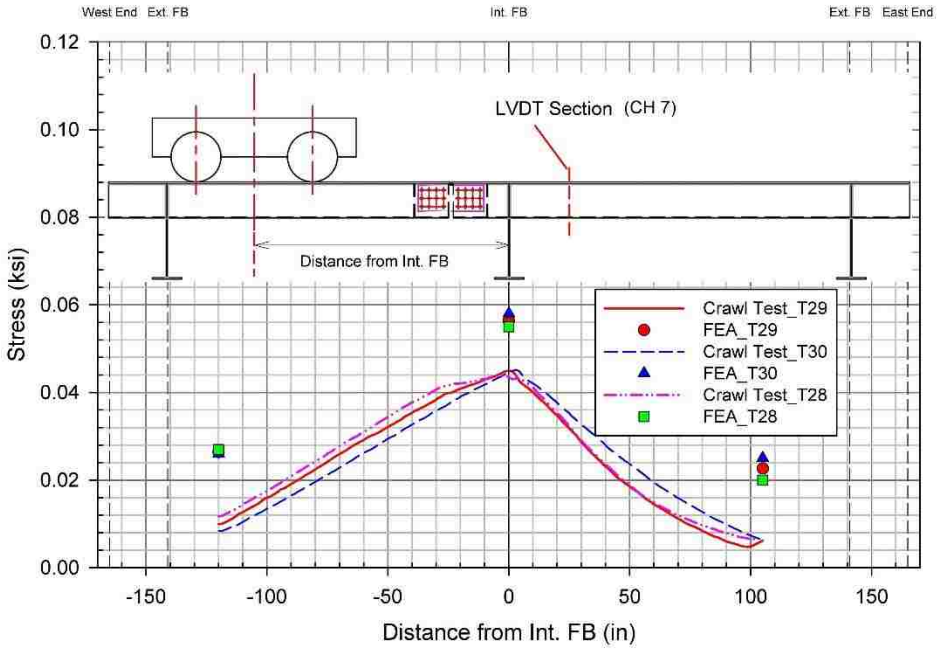

Figure 219 Displacement at LVDT under Rib 1 at section Z-Z (channel 7) for different crawl test positions

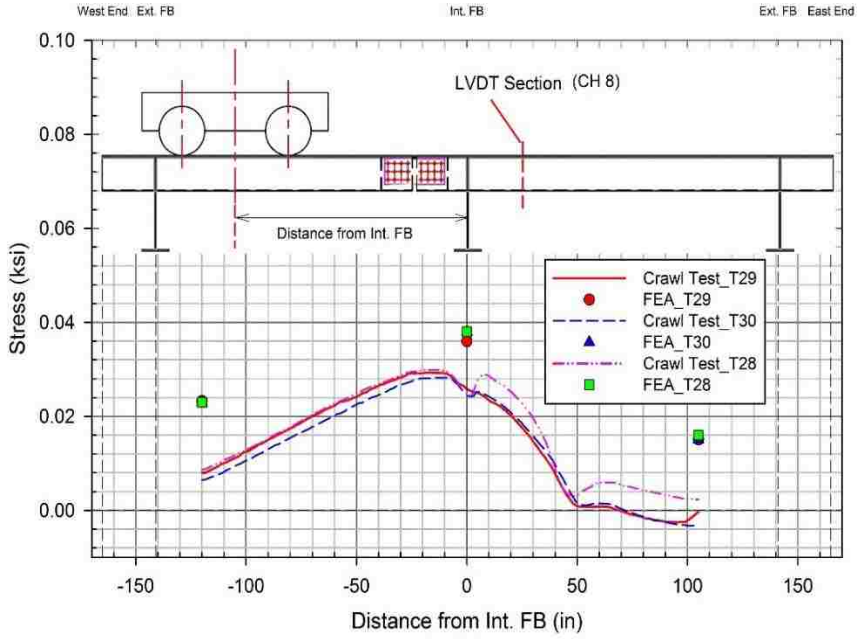

Figure 220 Displacement at LVDT under deck plate between ribs 1 and 2 at section Z-Z (channel 8) for different crawl test positions

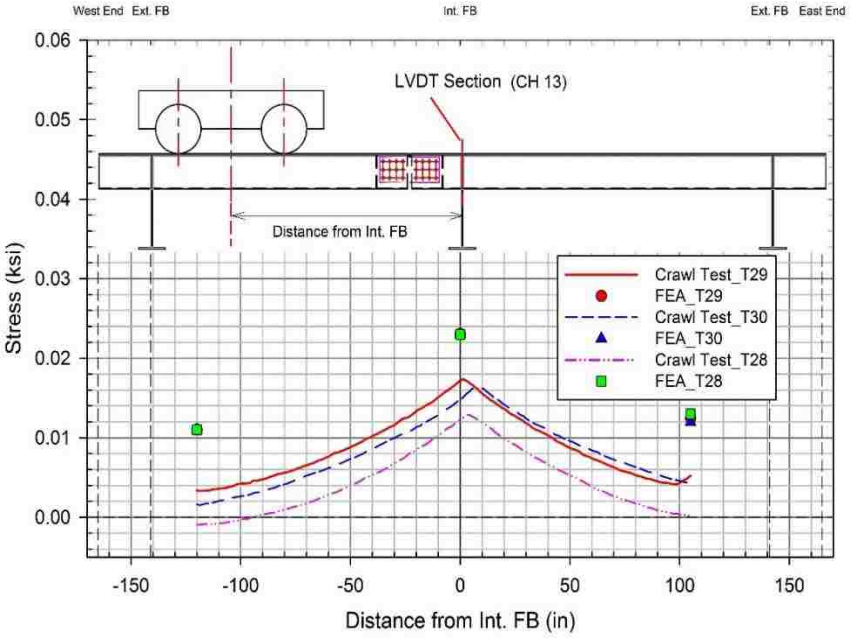

Figure 221 Displacement at LVDT under inner FB bottom flange at section Y-Y (channel 13) for different crawl test positions

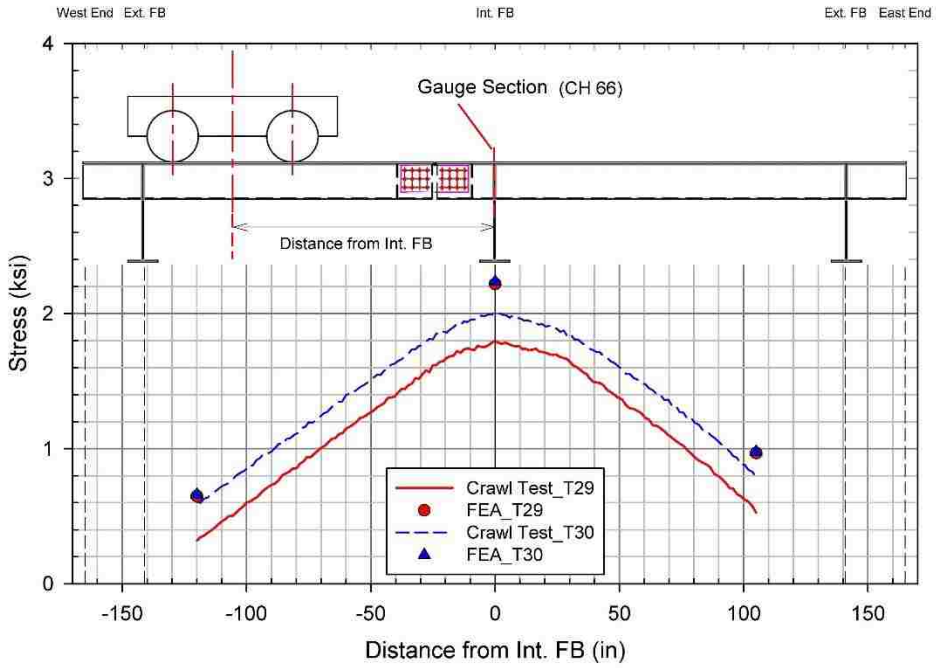

Figure 222 Transverse stress at bottom of inner FB (channel 66) at section Y-Y for different crawl test positions

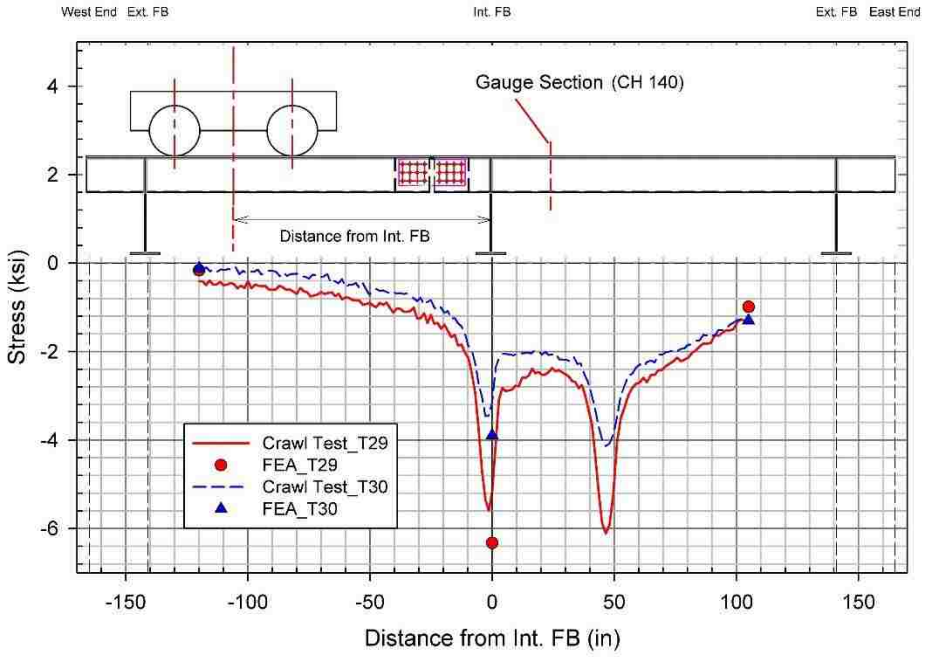

Figure 223 Transverse stress on the north wall of Rib 1 (channel 140) at section Z-Z for different crawl test positions

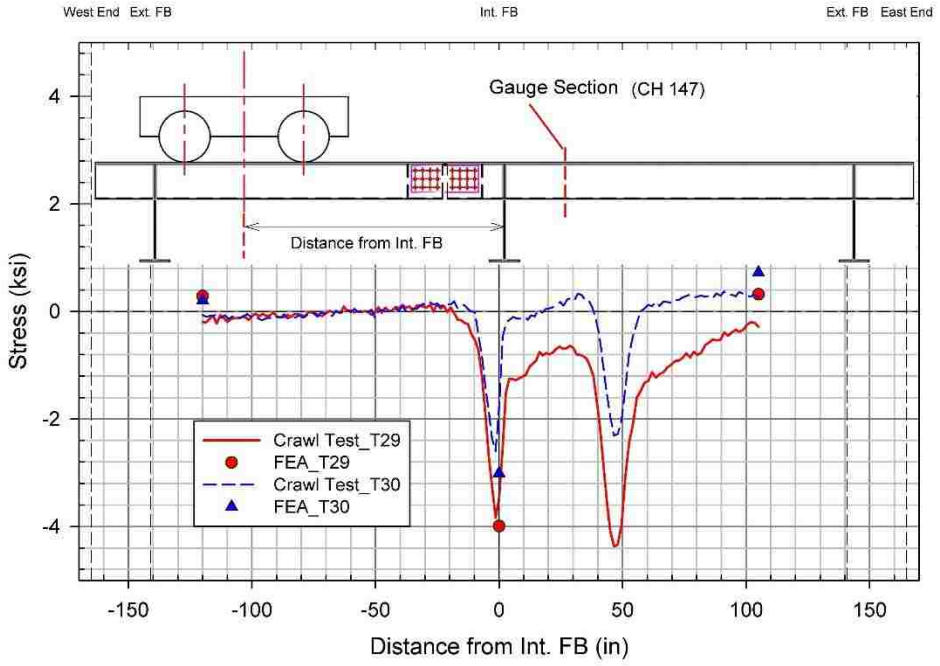

Figure 224 Transverse stress on the south wall of Rib 2 (channel 140) at section Z-Z for different crawl test positions

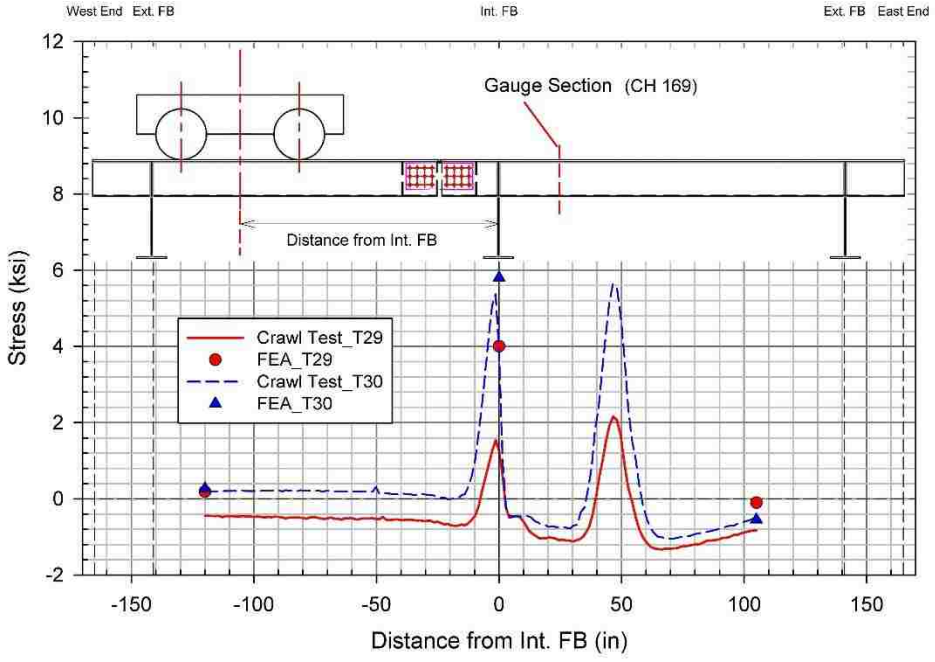

Figure 225 Transverse stress on top of deck plate to the south of Rib 2 (channel 169) for different crawl test positions

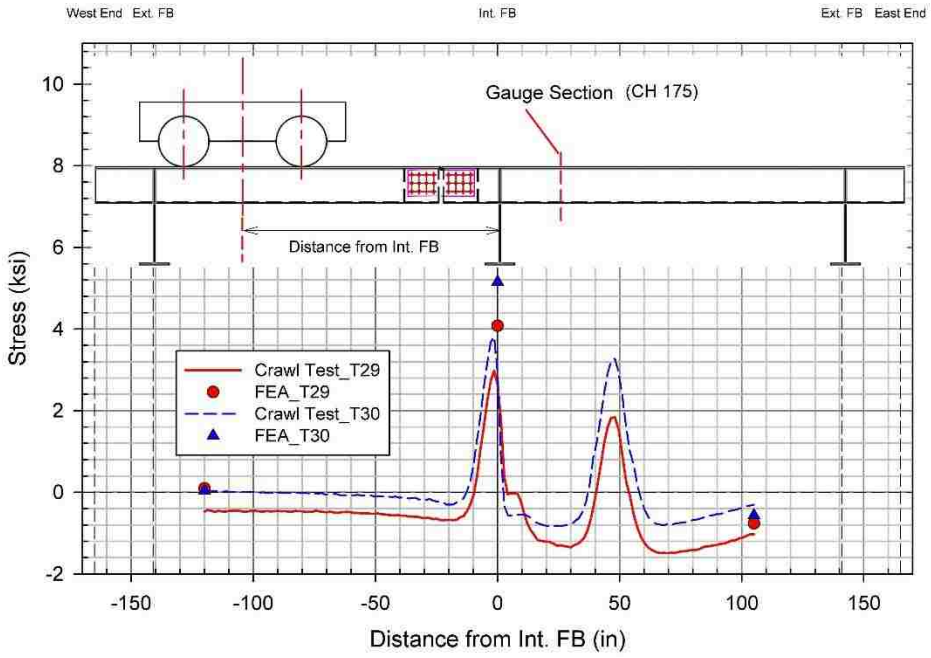

Figure 226 Transverse stress on top of deck plate to the north of Rib 4 (channel 175) for different crawl test positions

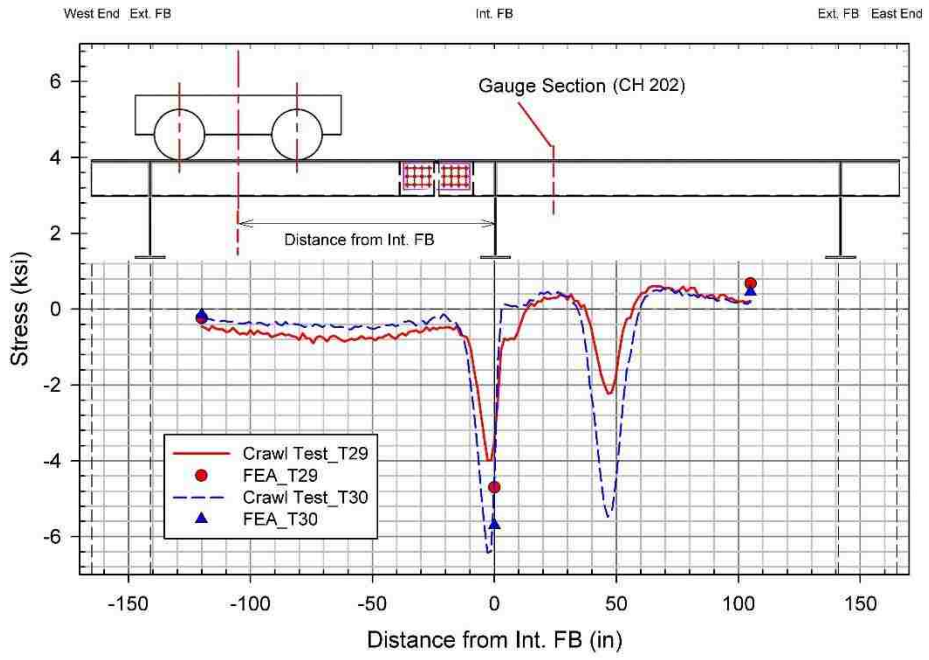

Figure 227 Transverse stress on underside of deck plate to the north of Rib 4 (channel 202) for different crawl test positions

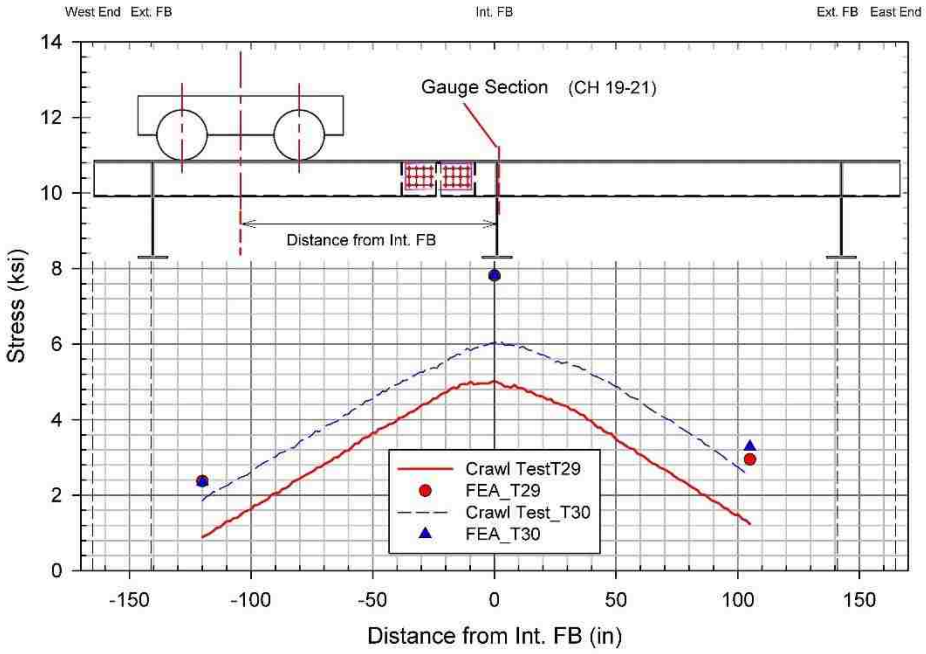

Figure 228 Principal stress at the south-east 25° rosette (channels 19-21) on the floor beam web for different crawl test positions

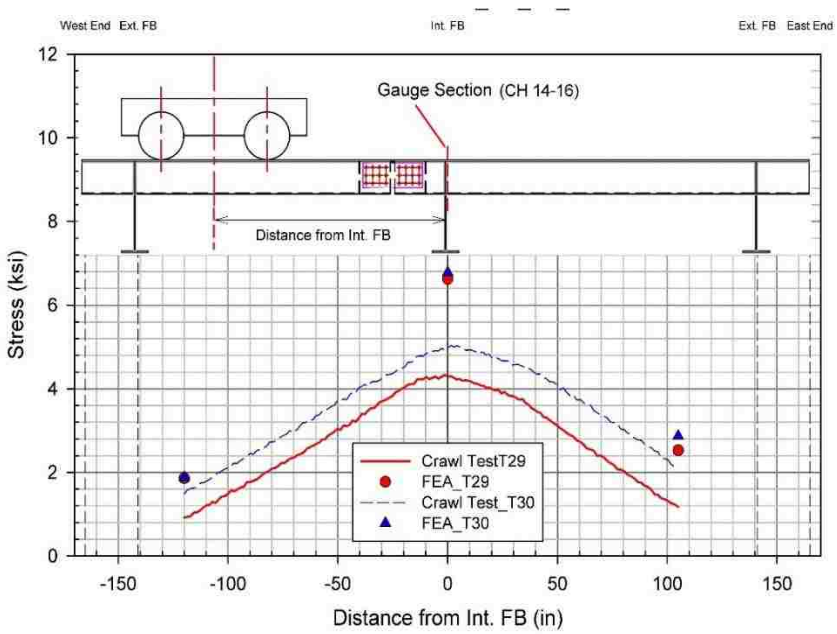

Figure 229 Principal stress at the south-east 50° rosette (channels 14-16) on the floor beam web for different crawl test positions

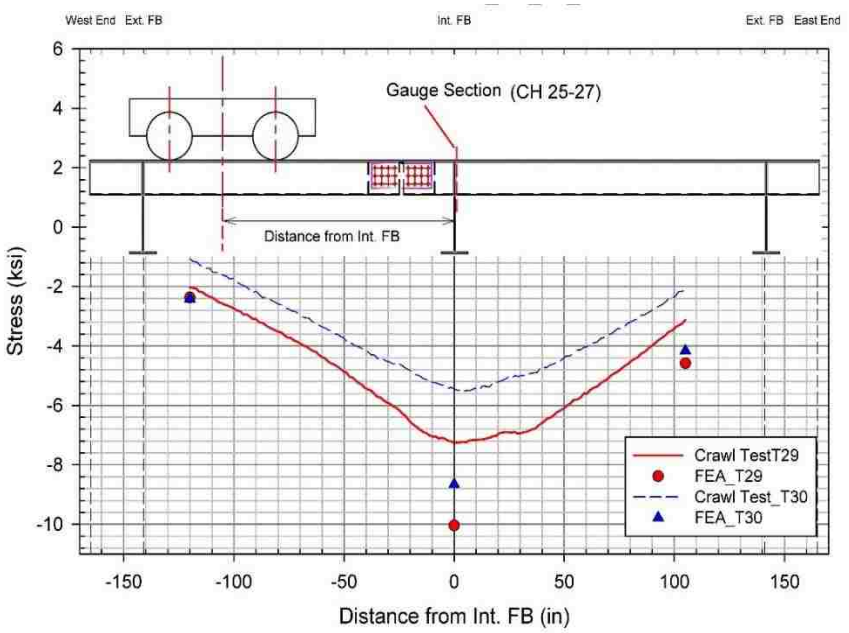

Figure 230 Principal stress at the north-east 50° rosette (channels 25-27) on the floor beam web for different crawl test positions

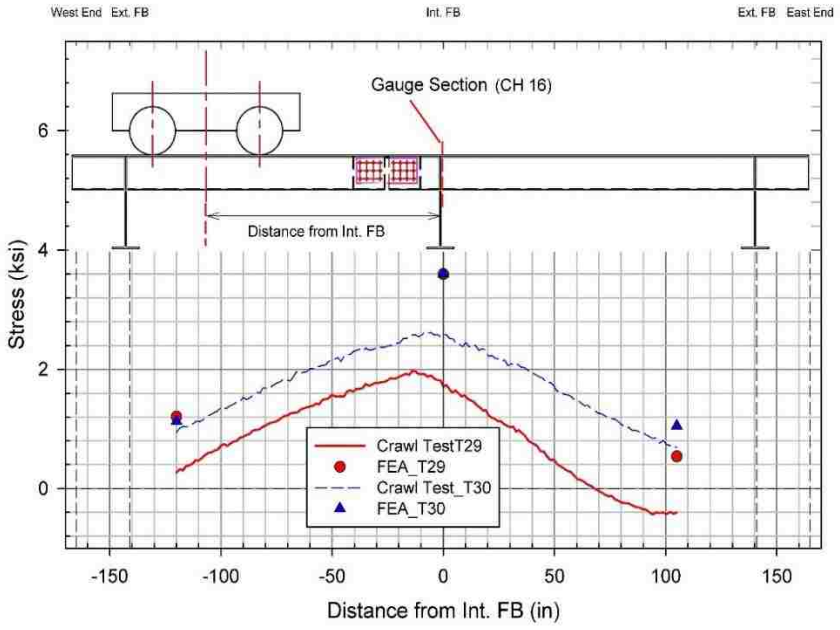

Figure 231 Stress normal to weld toe at the south-east 50° rosette (channel 16) on the floor beam web for different crawl test positions

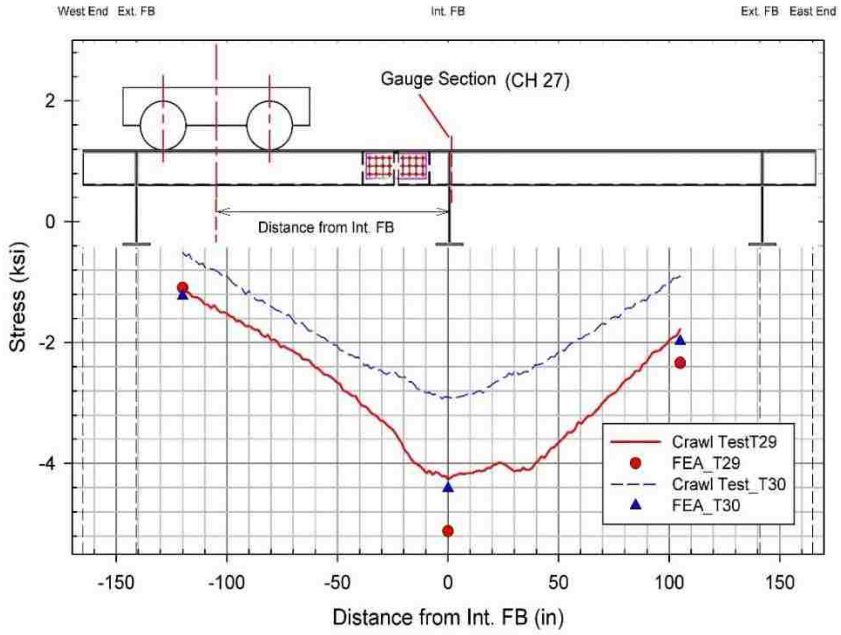

Figure 232 Stress normal to weld toe at the north-east 50° rosette (channel 27) on the floor beam web for different crawl test positions

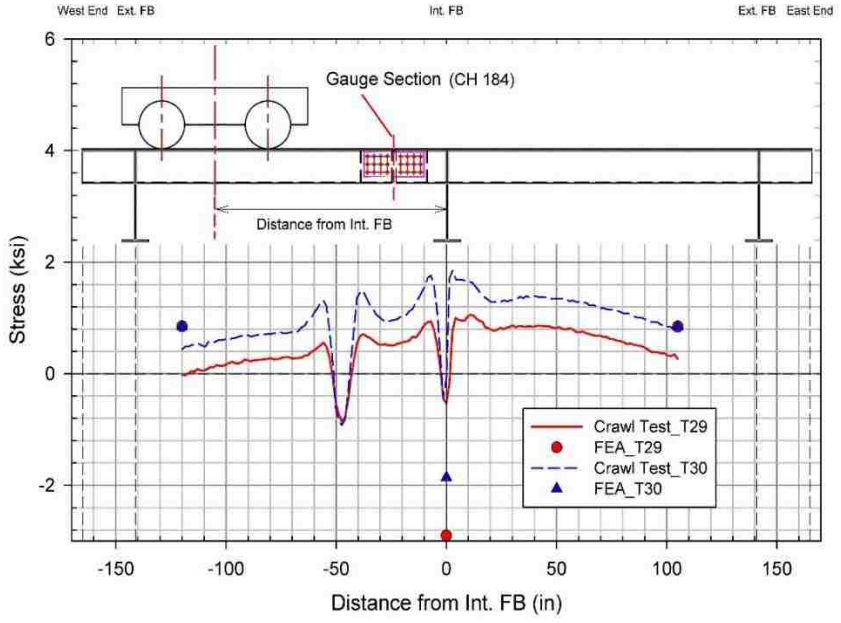

Figure 233 Longitudinal stress on top of deck plate below south-west wheel pair (channel 184) at the deck plate splice for different crawl test positions

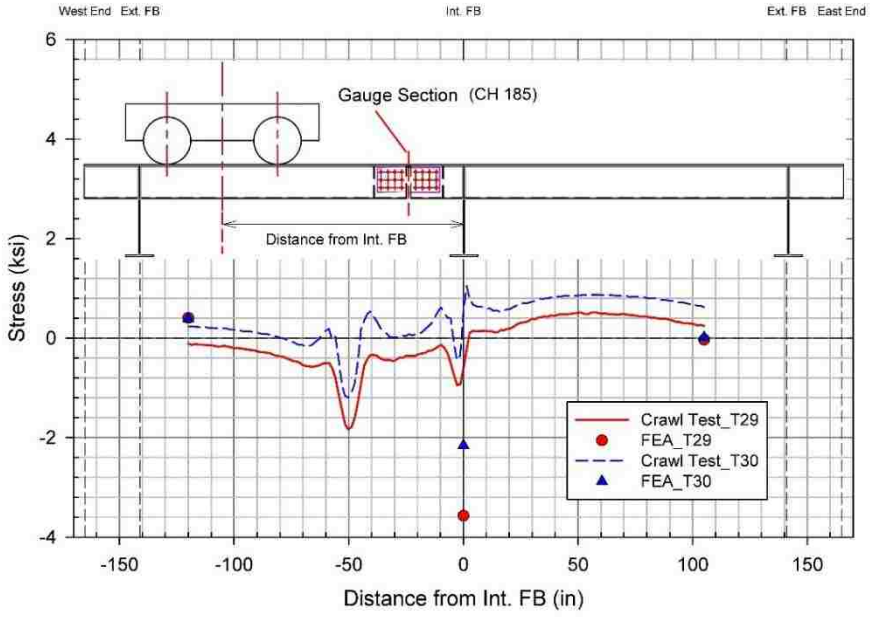

Figure 234 Longitudinal stress on top of deck plate below north-west wheel pair (channel 185) at the deck plate splice for different crawl test positions

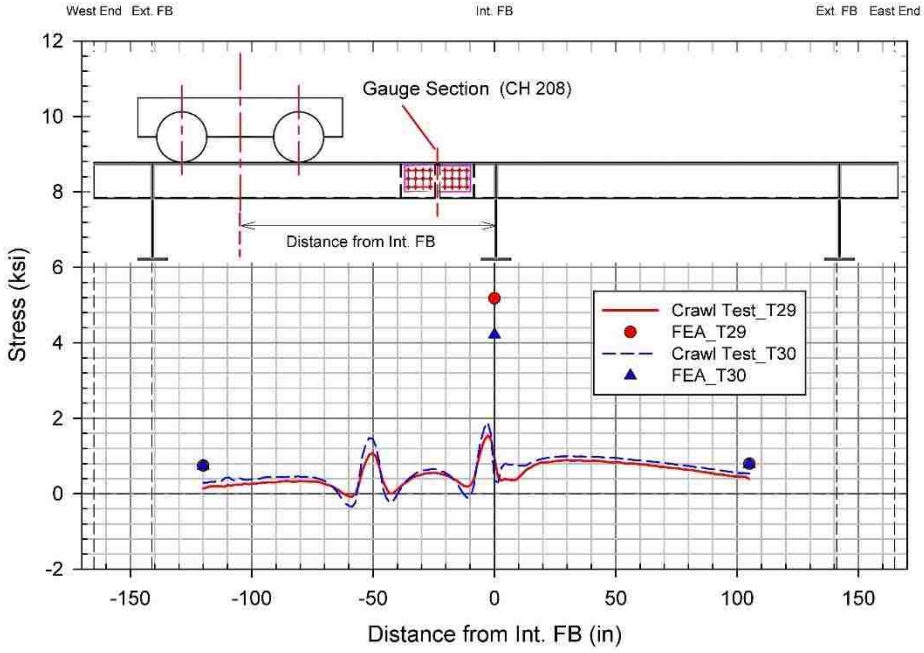

Figure 235 Longitudinal stress on underside of deck plate at the south-west wheel pair (channel 208) at the deck plate splice for different crawl test positions

REFERENCES

Alapati, R. S. D. (2012), Fatigue Evaluation of Replacement Orthotropic Deck for a Signature Bridge, M.S. Thesis, Department of Civil and Environmental Engineering, Lehigh University, Bethlehem, PA.

American Association of State Highway and Transportation Officials (AASHTO). LRFD Bridge Design Specifications. Washington D.C., 2012

Dassault Systèmes Simulia Corp, ABAQUS/Standard Version 6.12. Dassault Systèmes, Inc, Providence, RI, 2012. http://simulia.com/

Gajer, R.B., Patel, J., and Khazem, D. (1996). Orthotropic steel deck for the Williamsburg Bridge reconstruction. *Proceedings of the 14th ASCE Structures Congress*, 1, 491-498.

J.W. Fisher and S. Roy. "Fatigue of Steel Bridge Infrastructure." Structure and Infrastructure Engineering, Vol. 7 Nos. 7-8, (June 2010), pp 457-475, DOI: http://dx.doi.org/10.1080/15732479.2010.493304.

Kaczinski, M.R., Stokes, F.E., Lugger, P., and Fisher, J.W. (1997), Williamsburg Bridge orthotropic deck fatigue test. ATLSS Report No. 97-04, Bethlehem, PA: ATLSS Engineering Research Center, Lehigh University.

Kolstein, M.H. (2007), Fatigue Classification of Welded Joints in Orthotropic Steel Bridge Decks, Ph.D. Dissertation, T.U. Delft.

Kolstein, M.H., Leendertz, J.S., and Wardenier, J. (1995), Fatigue Performance of the trough to crossbeam connection in orthotropic steel bridge decks. *Proceedings of the Nordic Steel Construction Conference*, Malmo, Sweden, June 19-21.

Leendertz, J.S., Kolstein, M.H., and Wardenier, J. (1995), Numerical analyses of the trough to crossbeam connections in orthotropic steel bridge decks. *Proceedings of the Nordic Steel Construction Conference*, Malmo, Sweden, June 19-21.

Roy, S., and Mukherjee, S. (2015), *Design and Fabrication of Orthotropic Deck Details*, NJDOT Project Report, NJDOT, Trenton, NJ.

Roy, S., Fisher, J.W., Alapati, R.S.D., Manandhar, N.K., and Park, Y.C. (2012a), Laboratory fatigue evaluation of replacement orthotropic deck for a signature bridge. *Proceedings of the 2012 IABMAS*, Stresa, Lake Maggiore, Italy, July 8–12.

Roy, S., Park, Y.C., Manandhar, N.K., and Fisher, J.W. (2012b), Application of AASHTO fatigue design provisions for steel orthotropic bridge decks. *Proceedings of the 2012 World Steel Bridge Symposium*, Grapevine, TX, April 18–20.

Roy, S., Alapati, R.S.D., Manandhar, N.K., and Fisher, J.W. (2011a), Measurements of a steel orthotropic deck under crawl loading. *Proceedings of the 2011 ASCE Structures Congress*, Las Vegas, April 14–16.

Roy, S., Fisher, J.W., Alapati, R.S.D., Manandhar, N.K., and Park, Y.C. (2011b), Fatigue evaluation of orthotropic deck for a signature bridge. *Proceedings of IABSE-IASS Symposium*, London , September 20–23.

Roy, S., Fisher, J.W., and Alapati, R.S.D. (2010), Full scale laboratory testing of replacement orthotropic deck for the Verrazano Narrows Bridge. *Proceedings of the 2010 IABMAS*, Philadelphia, PA, July 11–15.

Tsakopoulos, P.A., and Fisher, J.W. (2005), Full-scale fatigue tests of steel orthotropic deck panel for the Bronx-Whitestone Bridge rehabilitation. Bridge Structures, 1(1), 55.

Tsakopoulos, P.A., and Fisher, J.W. (2003), Full-scale fatigue tests of steel orthotropic decks for the Williamsburg Bridge. Journal of Bridge Engineering, 8(5), 323-333.

VITA

Soham Mukherjee, son of Nupur Mukherjee and Suman Mukherjee, was born on October 28, 1986 at Kolkata, India. He received Bachelor of Engineering in Civil Engineering degree from Bengal Engineering & Science University, Shibpur (currently known as IIEST, Shibpur) in June 2008. After his bachelors, Soham worked in Foster Wheeler (part of Amec Foster Wheeler) and Larsen & Toubro until December 31, 2011. Soham started his graduate studies in the Department of Civil & Environmental Engineering, Lehigh University in January 2012. He worked as a graduate research assistant at ATLSS Engineering Research Center of Lehigh University from January 2012 and worked on a number of projects since. During his research at Lehigh, Soham has published 3 conference papers as first author and co-authored 1 conference paper, along with presenting his research at ASCE Structures Congress 2015, Portland, OR. He will receive his Masters of Science in Structural Engineering degree from Lehigh University, Bethlehem, PA in January 2016.